OUT-OF-PLANE STRENGTHENING OF UNREINFORCED MASONRY WALLS USING FRP

by

JAYA KASHYAP

BENG, HONS (CIVIL & STRUCTURAL), MSCENG (STRUCTURAL)

A THESIS SUBMITTED FOR THE DEGREE OF

DOCTOR OF PHILOSOPHY

SCHOOL OF CIVIL, ENVIRONMENTAL AND MINING ENGINEERING

FEBRUARY 2014

Table of Contents

Abstract

Unreinforced masonry (URM) structures constitute both a significant portion of the world's heritage buildings and a significant component of the modern residential building stock, and are particularly susceptible to damage from out-of-plane loads such as those generated by earthquakes (Ingham and Griffith 2011). Consequently, there is a considerable need for the development of economical and effective seismic strengthening techniques for URM construction. This study investigates the performance of near surface mounted (NSM) carbon fibre reinforced polymer (CFRP) strengthened clay brick masonry walls under monotonic and cyclic out-of-plane bending with particular attention to the FRP-to-masonry joint behaviour.

Fourteen NSM carbon FRP-to-masonry pull tests were conducted to study the FRP-to-masonry bond behaviour and to investigate the effect that variables such as cyclic loading and FRP strip dimensions have on the debonding resistance of a NSM FRP-to-masonry joint. The pull tests results were then incorporated into a large database of FRP retrofitted masonry pull test results by various researchers over the past 10 years. An empirical model was derived for the intermediate crack (IC) debonding resistance of FRP-to-masonry joints using a large set of test data from the open literature (Kashyap et al. 2012). Further, in order to predict the global load-slip response of FRP-to-masonry pull tests using various local bond-slip relationships two analytical procedures, namely a new generic numerical procedure and a closed-form mathematical solution, were developed which account for the partial-interaction response at the FRP-masonry interface (Kashyap et al. 2011).

Fifteen walls were tested in this study to investigate the behaviour of NSM CFRP retrofitted masonry walls under out-of-plane bending and investigate the IC debonding failure mechanism in them. Also, the effects of typical design variables such as reverse cyclic loading, axial pre-compression, FRP strip spacing and reinforcement ratio on the stiffness, displacement capacity and ultimate strength of FRP retrofitted masonry walls were studied. The test results demonstrated that NSM

CFRP strips designed to fail by IC debonding can provide an increase in strength of up to 20 times the strength of the corresponding unreinforced wall highlighting the effectiveness of the retrofitting scheme used. With respect to the test variables under investigation it was found that FRP strip spacing and reinforcement ratio strongly affect wall performance whereas cyclic loading and vertical pre-compression had little effect.

Finally, a simple design methodology has been developed for masonry walls retrofitted with vertical CFRP strips with IC debonding as the preferred failure mechanism. This design methodology will provide solutions for choosing the FRP strip dimensions (b_p and t_p) and spacing (S). Importantly, the methodology is generic in the sense that it can be used for any type of FRP material and both externally bonded (EB) and NSM retrofit techniques. It also enables the FRP retrofit to be optimised in terms of both the strip spacing and cross-section.

Overall, the results of this study show that the proposed NSM technique is structurally efficient and viable for seismic retrofitting of URM structures. Moreover, implementation of the proposed technique could have a significant impact in strengthening of masonry structures including conservation of the heritage buildings with considerable historical importance.

Statement of Originality

I, Jaya Kashyap certify that this work contains no material which has been accepted for the award of any other degree or diploma in any university or other tertiary institution and, to the best of my knowledge and belief, contains no material previously published or written by another person, except where due reference has been made in the text.

I give consent to this copy of my thesis when deposited in the University Library, being made available for loan and photocopying, subject to the provisions of the Copyright Act 1968.

I also give permission for the digital version of my thesis to be made available on the web, via the University's digital research repository, the Library catalogue, and also through web search engines, unless permission has been granted by the University to restrict access for a period of time.

Signature: _____

Date: _____

Publications

Journal Papers

Kashyap J, Griffith M, Mohamed Ali MS, and Oehlers D (2011). "Prediction of load-slip behavior of FRP retrofitted masonry." Journal of Composites for construction, 15(6):943–951.

Kashyap J, Willis CR, Griffith MC, Ingham JM, Masia M. (2012). "Debonding resistance of FRP-to-masonry joints", Engineering structures, 41(8):186–198.

Griffith MC, Kashyap J, and Mohamed Ali MS (2013). "Flexural displacement response of NSM FRP retrofitted masonry walls", Construction and Building Materials, 49:1032–1040.

Conference Papers

Kashyap J, Willis CR, and Griffith MC (2011). "Influence of spacing on flexural strength of FRP reinforced masonry walls," Proceedings, 9th Australasian Masonry Conference, Queenstown, New Zealand, 15 – 18 February.

Kashyap J, Griffith MC, and Mohamed Ali MS (2012). "Experimental study on flexural behaviour of FRP retrofitted masonry walls," Proceedings, FRP Composites in Construction (CICE) conference, Rome, Italy, 13-15 June.

Acknowledgement

I would like to express my deep and sincere gratitude to my supervisors: Prof. Michael Griffith and Dr. Mohamed Ali M.S., for their valuable guidance, encouragement, reviews of manuscript drafts and support over the course of my PhD. Their friendly discussions and valuable comments have been very helpful in preparation of this thesis. I also want to thank Prof. Michael Griffith for giving me the opportunity to undertake this PhD, and for his support and understanding during my maternity leave. I acknowledge Prof. Deric Oehlers and Dr. Craig Willis for their assistance. I also acknowledge the financial support of the Australian Research Council. I am also very grateful for the great efforts, timely co-operation and valuable advice of the Chapman laboratory staff during the experimental program. Sincere thanks are extended to the computing officer, Dr. Stephen Carr and the school administrative staff, for their help.

I wish to thank my fellow postgradutes for their assistance and friendship. Special thanks to my very good friends Li Li, Mina and Rupali, who have made this journey so much more enjoyable. I am very grateful to my family for their love and support over the years. Lastly, I would like to dedicate this thesis to my son, Krishna and my husband, Mahesh; without their amazing unwavering support, I would not have come this far. I wish to express my heartfelt thanks for their understanding, love and patience.

List of Figures

List of Tables

Notation

a	length of the micro-cracking region at the interface
a_d	magnitude of a corresponding to the beginning of macro-cracking
a_{de}	demand acceleration in units of acceleration due to gravity, g
a_{exp}	horizontal acceleration to cause F_{max}
a_u	maximum length of the interface that is softened
a_{URM}	horizontal acceleration to cause F_{URM}
A_{FRP}	total area of FRP used to retrofit a specimen
A_m	cross-sectional area of masonry
A_p	cross-sectional area of FRP plate
b_p	depth of FRP plate/strip
b_f	width of IC debonding failure plane
B	bond force
c	depth of neutral axis in a section
C	statistical coefficient
C_m	masonry compressive force
d_f	depth of IC debonding failure plane
ds/dx	slip strain/ relative slip between FRP and substrate at the interface
E	elastic Modulus of masonry
E_a	elastic modulus of adhesive
E_b	elastic Modulus of brick unit
E_m	elastic Modulus of mortar
E_p	elastic Modulus of FRP
$(EA)_m$	axial rigidity of masonry
$(EA)_p$	axial rigidity of retrofitting plate/strip
f_a	tensile strength of adhesive
f_c	cylinder compressive strength of concrete
f_d	design compressive stress
f_{mc}	compressive strength of masonry
f_{mt}	flexural tensile strength of masonry perpendicular to bed joints
f'_{mt}	characteristic flexural tensile strength of the masonry
f_{rupt}	rupture stress of FRP strip
f_{ut}	flexural tensile strength/ lateral modulus of rupture of brick units

F	applied load for wall
F_{max}	maximum applied load for wall
F_{IC}	applied load at the onset of debonding (wall test)
F_{URM}	unreinforced masonry bending capacity
g	equivalent accelerations
G_f	fracture energy/area beneath bond-slip curve
h_{crack}	crack height
H	wall height
k	interfacial ductility index
k_{mt}	bending moment capacity factor
k_p	perpend factor to allow for the degree of stretcher overlap
l_b	length of the brick unit
L	length of bonded region of the strip/plate
L_{eff}	critical bond length (or effective bond length)
L_{per}	perimeter of the debonding failure plane
m	statistical coefficient
M	moment
M_{ch}	horizontal bending capacity of a section of the masonry
M_{cv}	vertical bending capacity
M_d	design moment
M_{exp}	experimental moment capacity of wall
M_{URM}	bending moment capacity of unreinforced masonry section
M_{pred}	predicted moment capacity of wall
n	statistical coefficient
n_p	number of plates/strips
N	number of tests
N_a	applied axial load
N_s	self-weight of the wall
P	axial force in plate
P_{exp}	experimental IC debonding resistance/bond strength
P_{IC}	predicted IC debonding resistance/bond strength
P_L	axial force in the strip/plate at the crack face
P_{rupt}	tensile rupture capacity of FRP strip
S	horizontal spacing between the vertical FRP strips

S_{max} maximum horizontal strip spacing to avoid horizontal bending failure between strips

t_b/t_d thickness of failure plane surrounding FRP plate/strip

t_m thickness of masonry wall

t_p thickness of FRP plate/strip

u_m displacement of the masonry

u_p displacement of the FRP strip

w_d uniformly distributed lateral load

w_{exp} experimental lateral load capacity of wall

W wall width

x longitudinal position

z lever arm

Z_d section modulus of bedded area

Z_p lateral section modulus of the perpends

Z_u lateral section modulus of the masonry units

ρ reinforcement ratio

ρ_b balanced reinforcement ratio

η efficiency factor

Φ capacity reduction factor

δ interfacial slip

δ_1 slip at which τ_{max} occurs

δ_{max} slip at which macro cracking occurs

δ_L slip at the loaded end

Δ global slip (pull tests)/ mid-height wall deflection

ΔL incremental length along FRP strip (equal to strain gauge spacing)

Δ_s change in slip

Δ_{max} maximum slip at loaded end (pull test)

Δ_{ult} maximum mid-height wall deflection

ε strain

$\Delta\varepsilon$ change in strain over length ΔL

ε_{crack} cracking strain of the mortar

ε_{db} strain at onset of debonding

ε_{max} maximum experimental strain

ε_p interfacial strain of FRP plate/strip

ε_m interfacial strain of masonry

ε_{rupt} rupture strain of FRP plate/strip

σ_{exp} maximum experimental tensile stress

σ_m axial stress in masonry

σ_p axial stress in the FRP strip

σ_v axial stress applied to the walls

γ specific weight of masonry

τ interfacial shear stress

τ_b interfacial shear stress for brick

τ_{avg} average interfacial shear stress over the strip length ΔL

τ_m interfacial shear stress for masonry

τ_{mo} interfacial shear stress for mortar

τ_{max} maximum FRP-substrate interfacial shear stress

φ_f IC debonding failure plane aspect ratio

α $\dfrac{2(P_{IC}+N_s+N_a)}{\varepsilon_{db}E_m S}$, coefficient

β_o $\left(1/E_p + A_p/(EA)_m\right)$, constant

β_1 L_{per}/A_p, constant

β_2 $\beta_1\beta_0$, constant

λ $\sqrt{\dfrac{\tau_{\max}L_{per}}{\delta_{\max}(EA)_p}}$, constant

λ_1 $\sqrt{\dfrac{\tau_{\max}\beta_2}{\delta_1}}$, constant

λ_2 $\sqrt{\dfrac{\tau_{\max}\beta_2}{(\delta_{\max}-\delta_1)}}$, constant

λ_3 $\lambda_2\dfrac{(\delta_{\max}-\delta_1)}{\delta_{\max}}$, constant

List of Abbreviations

AFRP	Aramid fibre reinforced polymer
AS	Australian Standards
Bond-slip	Interfacial shear-stress/slip relationship
CFRP	Carbon fibre reinforced polymer
CI	Curvature incompatibility
COV	Coefficient of variation
EB	Externally bonded
FRP	Fibre reinforced polymer
GFRP	Glass fibre reinforced polymer
IC	Intermediate crack
LVDT	Linear variable differential transformer
MVG	Magnetic volt gauge
NSM	Near surface mounted
PI	Partial interaction
PE	Plate end
RC	Reinforced concrete
URM	Un-reinforced masonry
UV	ultraviolet

CHAPTER 1
INTRODUCTION

1.1. Background and significance of the research

Unreinforced masonry (URM) structures constitute both a significant portion of the world's heritage buildings and a significant component of the modern residential building stock, and are particularly susceptible to damage from out-of-plane loads such as those generated by earthquakes (Ingham and Griffith 2011; Ismail and Ingham 2012). Catastrophic out-of-plane flexural failures of URM (hereafter termed 'masonry') walls during seismic events worldwide (e.g. Newcastle, Australia in 1989; Northridge, California in 1994; Kocaeli, Turkey in 1999; L'Aquila, Italy in 2009; Christchurch, New Zealand in 2010, 2011) continue to highlight the need to strengthen these structures.

There is a broad range of strengthening techniques available today for enhancing the structural performance of masonry such as steel plate bonding, steel frame works, shotcrete jacketing and many others. But these traditional techniques have many disadvantages such as adding considerable mass to the structure, being labour intensive and time consuming, cause working space and access limitations and also impinge aesthetics of the building (Triantafillou 1998; Tan and Patoary 2004; Shrive 2005; Korany and Drysdale 2006). Hence, the use fibre reinforced polymers (FRPs) has gained much attention as a promising strengthening technique for reinforced concrete and masonry structures (Hamed and Rabinovitch, 2007; Willis et al. 2009a; Petersen et al. 2009; Milani and Lourenco 2013). Over the past decade or so, near surface mounted (NSM) FRP is emerging as a promising technology among the available FRP strengthening methods due to the advantages it offers over externally bonded (EB) FRP. The NSM FRP retrofitting technique (i.e. inserting FRP strips into grooves cut into the surface of a wall as shown in Figure 1-1(b)) provides significant advantages over externally bonded (EB) FRP Figure 1-1(a)) such as improved

aesthetics, reduced surface preparation and better protection from UV exposure and vandalism. Importantly, NSM FRP debonds at higher strains than EB FRP and thus leads to more efficient use of the FRP material (DeLorenzis and Teng 2006).

(a) EB **(b) NSM**

Figure 1-1: FRP retrofit techniques (cross-sectional view)

For a wall supported on all four sides and subjected to out-of-plane bending, the vertical bending of the wall is the weakest link (Willis et al. 2010). The use of vertically oriented NSM FRP to strengthen such walls, has been shown to significantly increase the vertical bending capacity and thus the ultimate wall capacity (Korany and Drysdale 2004; Willis et al. 2010). When using the NSM technique, the most efficient cross-section is a thin rectangular strip as its benefits, in terms of efficiency and construction time, are superior to those of other shapes such as bars (Seracino et al. 2007a).

Some of the common out-of-plane failure mechanisms of FRP strengthened masonry walls include flexural-shear cracking, FRP rupture, FRP debonding, and crushing of masonry in compression (Albert et al. 2001; Tumialan et al. 2003; Ghobarah and Galal 2005, Galati et al. 2006; Mosallam 2007). Among these debonding mechanisms, intermediate crack (IC) debonding is the preferred failure mechanism as it results increase in both moment capacity and sectional ductility. IC debonding involves progressive detachment of the NSM FRP strip which initiates at the location of intermediate flexural or flexural-shear cracks when the strip is subjected to large tension stress. If the FRP is perfectly attached to the masonry then theoretically the FRP strip requires infinite strain capacity in order to bridge the intercepting cracks. As such strain levels are not possible, debonding cracks will occur at the FRP-to-substrate interface and gradually propagate towards the strip ends (Oehlers and Seracino 2004; Liu et al. 2007) as long as the debonding strain is lower than the tensile rupture strain for the FRP.

Extensive reinforced concrete (RC) research has long shown that FRP can improve flexural behaviour (Teng et al., 2002; Oehlers et al., 2008). Whilst the application of NSM FRP strips appears to be a particularly viable retrofitting technique (Dizhur et al. 2010), limited research has previously been conducted on the application of this retrofitting technique to masonry structures. Further, the bond at the FRP-to-masonry interface which is a key factor affecting the flexural capacity is also one of the ill-understood areas. In addition, the effect of out-of-plane cyclic loading on the load-deformation behaviour of FRP retrofitted masonry members also warrants more attention. As a result, there is a significant need for more experimental and analytical investigations on NSM FRP retrofitted masonry walls before it can be confidently used for seismic retrofit of URM walls.

1.2. Scope and objectives of the research

This research is a part of a collaborative project between the Universities of Adelaide, Newcastle and Auckland which aims to develop an innovative and cost effective retrofit technique for masonry buildings which will not only significantly reduce the seismic risk posed to these structures but will also be architecturally unobstrusive. This study investigated the performance of NSM CFRP strengthened clay brick masonry walls under monotonic and cyclic out-of-plane bending with particular attention to the FRP-to-masonry bond behaviour. Thus, the following specific project aims were established.

Aim 1 – Characterise experimentally the bond-slip (τ-δ) behaviour between NSM FRP strips and clay brick masonry.

Aim 2 – Develop an analytical model to determine the IC debonding resistance of bonded joints and also develop mathematical/ numerical procedures, to predict the observed behaviour which accounts for the partial-interaction response at the FRP-masonry interface observed in Aim 1. Further, validate the accuracy of these models using past experimental results from literature and from tests conducted for Aim 1.

Aim 3 – Study the cyclic behaviour of NSM FRP strenthened masonry walls under out-of-plane bending through a series of experimental tests and investigate the effects

of other important variables such as FRP strip spacing, axial loading and FRP reinforcement ratio on the overall behaviour of FRP retroffited walls.

Aim 4 – Develop a design methodology for FRP strengthened masonry walls. Validate the accuracy of the design procedure using experimental results from Aim 3.

The outcomes of this project were expected to result in a deeper understanding of the shear bond stress-slip behaviour at the FRP-masonry interface; the behaviour of NSM FRP strengthened masonry walls; and an accurate method of analysis that will allow reliable and economic design to be undertaken. Thus, the research results should provide a structurally efficient and viable technique for seismic retrofitting of URM structures.

1.3. Overview of thesis

The research presented in this thesis has been divided into eight chapters: The contents of these chapters are briefly described in following sections.

1.3.1. Literature review

Chapter 2 presents an overview of the current state of the art for seismic strengthening of masonry walls subjected to out-of-plane bending. It discusses the need to retrofit masonry structures, comparision of traditional retrofit techniques with the proposed NSM FRP strengthening, different observed failure mechanisms in FRP retrofitted masonry walls with a specific focus on IC debonding. Also, it includes review on the behaviour of FRP-to-masonry bonded joints. Additionally, this section presents the assessment of existing bond strength models for their use with masonry against a large database of FRP retrofitted masonry pull test results by various researchers over the past 10 years. Furthermore, findings from previous experimental studies on the effect of important variables such as FRP strip spacing, reinforcement ratio, cyclic loading and pre-compression on the flexural response of FRP strengthened masonry walls are discussed. This chapter concludes by highlighting research gaps in the literature.

1.3.2. Bond behaviour

Bond behaviour is divided into two chapters (Chapters 3 and 4) and covers Aim 1 and Aim 2, respectively (refer to §1.2). Chapter 3 describes the experimental bond pull tests conducted on NSM CFRP-to-masonry joints. Variables that were expected to affect the bond behavior of FRP-to-masonry joints were considered such as FRP strip cross-section and loading (cyclic versus monotonic) type.

Chapter 4 presents the analytical models that were developed to describe the local behavior at the FRP-masonry interface. Firstly, the derivation of analytical models to determine the IC debonding resistance of bonded joints is presented. Then, empirical relationships for key parameters such as the fracture energy, G_f, and shear stress-slip (denoted as local bond-slip) relationship, τ-δ, are presented. Finally, two analytical procedures, namely a new generic numerical procedure and a closed-form mathematical solution, were developed to predict the global load-slip response of FRP-to-masonry pull tests using various local bond-slip relationships.

1.3.3. Flexural response of FRP strengthened walls

Flexural response of FRP strengthened walls, reported in Chapter 5 and Chapter 6 involved a series of NSM FRP reinforced masonry wall tests under lateral out-of-plane bending in order to achieve Aim 3 (refer to §1.2). In total, fifteen clay brick masonry wall tests were conducted to study the behaviour of NSM CFRP retrofitted masonry walls in flexure and investigate the intermediate crack (IC) debonding failure mechanism in them. Chapter 5 describes the test plan, setup and instrumentations details. Chapter 6 presents the results of experimental tests with discussion of the effects of different test parameters such as reverse cyclic loading, axial pre-compression, FRP strip spacing and reinforcement ratio on the stiffness, displacement capacity and ultimate strength of FRP retrofitted masonry walls.

1.3.4. Design methodology

Chapter 7 describes the development of a design methodology for FRP reinforced masonry walls under bending as part of Aim 4 (§1.2). This chapter also includes validation of the proposed design procedure through comparing with experimental test results.

1.3.5. Conclusions

A summary of the significant findings of this research and recommendations for future research are presented in Chapter 8.

CHAPTER 2
LITERATURE REVIEW

2.1. Introduction

URM buildings are most vulnerable to flexural out-of-plane failure (Figure 2-1) near the top of buildings due to a combination of lower vertical compression stress due to gravity loads and higher horizontal acceleration due to the earthquake. This endangers the gravity-load-carrying capability of a wall causing the most serious life-safety hazard for this type of construction (Bruneau 1994; Kuzik et al. 2003). Further, the inadequate out-of-plane bending strength of URM walls has been identified as the one of the major weak links in the seismic load path of URM (Klopp 1996; Doherty 2000).

a) 1989 Newcastle, Australia **b) 2010 Christchurch, New Zealand**

Figure 2-1: Examples of out-of-plane failures in URM buildings

Coburn and Spence (2002) state that in the 1990s, URM failures during earthquakes were responsible for the 60% of the lives lost (as referred in Erdal 2010). Recent catastrophic earthquakes in New Zealand (Christchurch, 2010, 2011), Haiti (2010),

Italy (L'Aquila, 2009) and China (Sichuan, 2008) have further demonstrated the significant earthquake damage possible in masonry structures.

Masonry structures are one of the oldest and most widespread forms of construction worldwide. However, many of these buildings were constructed before the development of formal design procedures and were detailed with little, if any, reinforcement to withstand wind and gravity loads. Typical masonry characteristics such as its heavy weight, brittle nature, large stiffness and high variability in material properties along with readily available failure planes in the form of well-defined joints makes these structures more susceptible to out-of-plane collapse even under low seismic loading (Wakabayashi 1986: Kuzik et al. 2003). More important, many of these masonry buildings have significant historical or cultural heritage value making it desirable to strengthen them. Masonry buildings may also require strengthening due to many other reasons such as increased life span demand, due to distress caused by environmental factors or past loading events, functional changes to use, or upgrading lateral strength to conform to modern code standards (Lillistone and Jolly 1998; Drysdale et al. 1994). Consequently, there is a considerable need for the development of economic and effective seismic strengthening techniques for URM construction.

2.2. Strengthening techniques

2.2.1. Traditional strengthening techniques

A variety of seismic strengthening techniques are available today for restoring lateral strength of masonry structures. An extensive review and comparison of various retrofitting techniques is given in ElGawady et al. (2004) and Chuang and Zhuge (2005). Some of the many traditional techniques include externally bonded steel plates; prestressing cables; surface treatment using ferrocement, shotcrete or, reinforced plaster; injecting grout or epoxy into pre-existing cracks or voids; structural repointing and confining the masonry with reinforced concrete tie columns and tie beams. Although these techniques have been proven effective, they also have

many drawbacks (Triantafillou, 1998; Tan and Patoary, 2004; Luccioni and Rougier, 2010) such as:

- being labour intensive and time consuming;
- cause working space and access limitations;
- have high construction costs and lack of reliability (450 buildings reinforced before the Northridge earthquake failed after it (ElGawady et al. 2005));
- adversely affect the architectural aspects of a structure;
- can add considerable weight to a structure which can significantly change its dynamic response and can require expensive upgrades to the foundation; and
- Corrosion of steel reinforcement.

The above mentioned disadvantages of the conventional retrofitting techniques make them excessively disruptive, visually intrusive, uneconomical for many practical applications and often undesirable for strengthening historical buildings which require special treatment (Korany and Drsydale 2006).

2.2.2. Strengthening with FRP

It is important that the seismic strengthening technique be cost effective, efficient and minimally disruptive to the occupants of the building (Erdal 2010), where URM structures have significant cultural heritage value, the technique also needs to be aesthetically acceptable. From a review of the existing literature, FRP composites have emerged as a viable and attractive retrofit alternative for construction application. FRPs are a composite material consisting of high strength fibres embedded in a resin matrix. The FRP reinforcement is either externally bonded (EB) to the surface of a wall or adhesively bonded into grooves cut into the surface of a wall (NSM) (discussed in more detail in §2.2.3).

FRPs have superior characteristics and several advantages with respect to traditional techniques (Ehsani et al.1999; Albert et al. 2001; Galati et al. 2005; Korany and Drsydale 2006; ACI 440.XR 2009; Carloni and Subramaniam 2012). These are:

- their high stiffness and strength-to-weight ratio so that an entire wall can be strengthened by treating only a fraction of wall surface area;

- they do not add significant weight to the structure so that the dynamic mass of the structure remains more or less unchanged;
- their small thickness and low specific weight offers ease of application and faster construction;
- they are flexible so they can be used in areas with limited access and are adaptable to curved and rough surfaces;
- they are non-corrosive and nonmagnetic with lower life-cycle maintenance costs; and
- minimal aesthetic impact making the NSM technique suitable for preservation of historical structures.

FRPs are readily available in several forms (Figure 2-2), such as sheets, strips, bars and tendons (for pre-tensioning or post- tensioning), reinforcing bars or meshes. The fibres are stronger in the longitudinal direction but are generally weak in lateral direction. Hence, when fibres are unidirectional such as in strips, tendons and bars, high strength and stiffness is achieved in that direction compared to others. In the case of sheets, fibres can be aligned orthogonally, at pre-defined angles or randomly to provide the desired orthotropic properties (Shrive, 2005).

Figure 2-2: Different FRP products (Tinazzi and Nanni 2000)

One of the factors which limit the use of FRP as a strengthening material is its high cost of production. However, it is important to consider that in the structural

strengthening field, major costs are associated with design, transportation and labor while material costs comprise only 20% of the total cost (Tinazzi and Nanni 2000). Moreover, its low installation and maintenance costs can make the FRP the most suitable option (Tinazzi and Nanni 2000).

Three types of FRP composites are commonly used for strengthening of structures: carbon-fibre-reinforced polymer (CFRP), glass-fibre-reinforced polymer (GFRP), aramid-fibre-reinforced polymer (AFRP). CFRPs have higher tensile strength, and higher modulus of elasticity (Table 2-1) due to which they are much more effective than laminates with lower stiffness such as GFRP (Triantafillou 1998; Korany and Drysdale 2006). GFRP is commonly preferred for masonry strengthening as its material costs are substantially less than carbon or aramid materials. However, CFRP is more suitable for sites where masonry will be subjected to sustained stresses, high alkalinity and high moisture or relative humidity. CFRP systems are more appropriate for these applications since compared to GFRP, they offer superior durability in moist environments, better resistance to wetting and drying, freezing and thawing, alkaline solutions, and creep rupture (Tumialan et al. 2009 and ACI 440.7R 2010).

Table 2-1: Mechanical properties of FRP composites (Teng et al. 2002)

Unidirectional FRP composite materials	Density (kg/m^3)	Longitudinal tensile modulus (GPa)	Tensile strength (MPa)
GFRP	1600-2000	20-55	400-1800
CFRP	1600-1900	120-250	1200-2250
AFRP	1050-1250	40-125	1000-1800

2.2.3. FRP application techniques

As mentioned in §2.2.2, two FRP application techniques that are commonly used for strengthening masonry structures are: externally bonded (EB) sheets or strips or NSM FRP bars or strips. Many studies have been conducted on masonry walls

reinforced with EB FRP whereas NSM FRP is a comparatively new retrofit technique. Although the EB FRP technique has been shown to improve the performance of masonry members, it has many disadvantages that may restrict its use under certain conditions, such as its: (1) adverse effect on the aesthetics of a structure; (2) high susceptibility to debond at low strain; (3) lengthy preparation of the substrate surface prior to installation of the FRP; (4) exposure to vandalism; and (5) possible interference with floor and/or pavement finishes (Vasquez and Seracino 2010).

Over the past decade or so, NSM FRP has gained attention as a viable strengthening technique as it offers many advantages over EB FRP. These include higher axial strain at debonding due to the increased bond surface area and confinement, protection from UV light and vandalism, minimally invasive, and reduced installation time. With the NSM technique, FRP strips can be inserted into grooves aligned vertically with the perpend joints or offset from the perpends so that the FRP is bonded to the bricks in every course of the cut into brick units only or alternating brick units and mortar joints. A study by Willis et al. (2009) concluded that positioning the strips through the perpend joints resulted in only a small reduction in bond strength, of the order of 10%. It should be noted that this level of strength reduction may be acceptable considering the beneficial effects such as the reduced aesthetic impact and ease of strip placement.

2.3. Failure mechanisms in FRP retrofitted masonry structures

Figure 2-3 shows the different failure mechanisms observed by previous experimental studies on FRP strengthened masonry walls subjected to out-of-plane loading. Some of the common failure mechanisms mentioned in the literature include intermediate crack (IC) debonding (Figure 2-3(a)), flexural-shear cracking (Figure 2-3(b)), FRP rupture (Figure 2-3(c)), perpend shear failure (Figure 2-3(d)), and crushing of brick in compression (Figure 2-3(e)) (Albert et al. 2001; Tumialan et al. 2003; Ghobarah and Galal 2004; Galati et al. 2006; Hamed and Rabinovitch 2007; Mosallam 2007).

(a) IC debonding

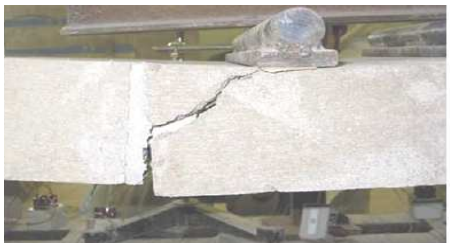

(b) FRP rupture

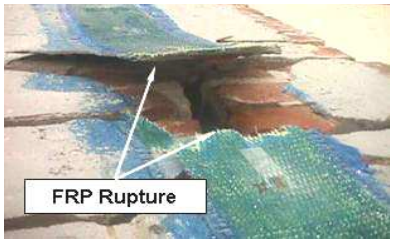

(c) FRP rupture

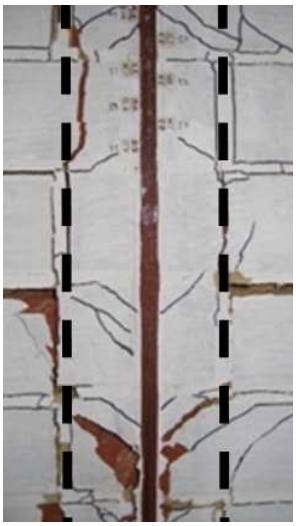

(d) Perpend Shear failure

(e) Compressive Failure

Figure 2-3: Observed failure modes in FRP strengthened masonry under out-of-plane loading

As discussed earlier in §1.1, debonding of FRP composites from masonry has been reported as one of the key failure mechanisms. The IC debonding mechanism can be idealised using a pull test. Figure 2-4(a) shows a masonry wall retrofitted with vertical FRP strips.

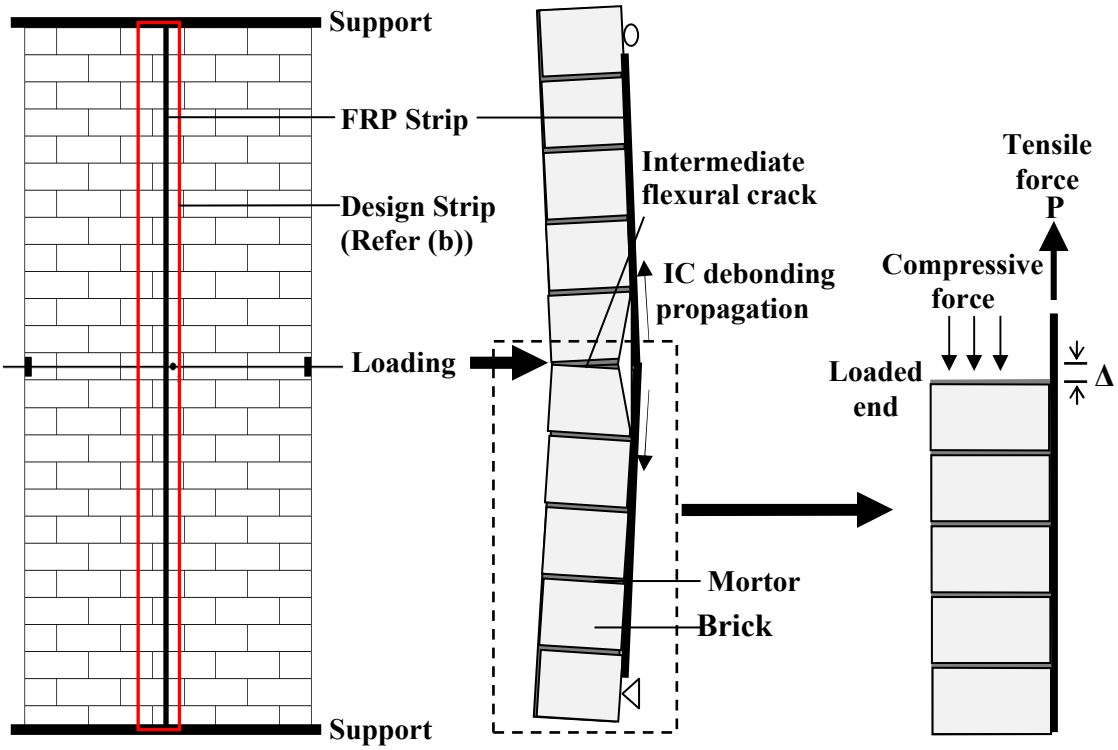

(a) FRP retroffited URM Wall (b) IC debonding in masonry wall (c) Pull test

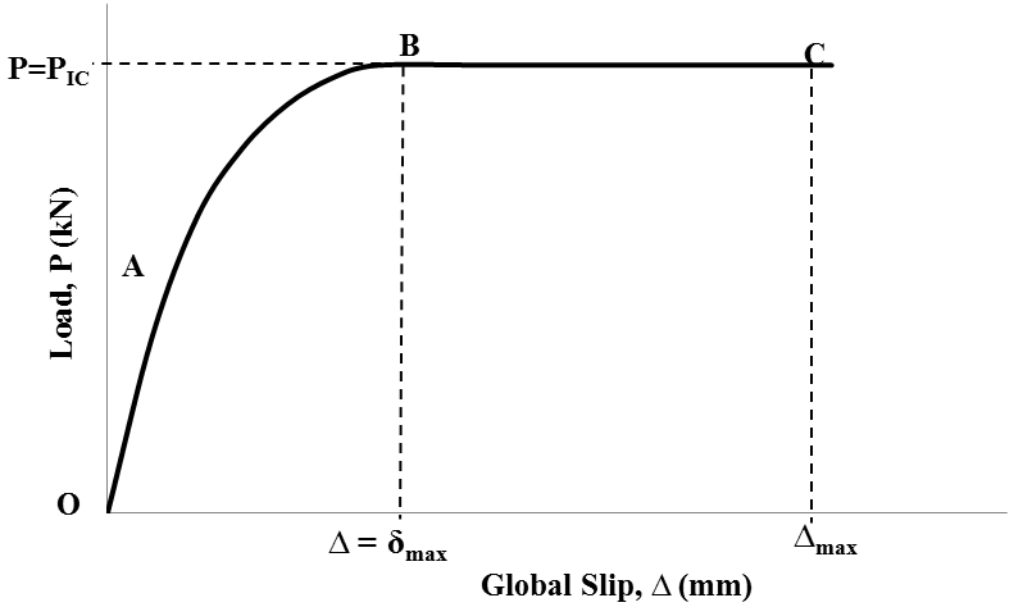

(d) Typical P-Δ response

Figure 2-4: Pull test simulating IC debonding

A design strip centered about an FRP strip can be represented as a masonry beam (wallette) with an FRP strip bonded to its tension face (Figure 2-4(b)). To simulate the IC debonding failure mechanism of such a beam, the monotonic pull test can be used whereby a tensile force (P) is applied to the FRP strip causing a slip (Δ) at the crack face as shown in Figure 2-4(c). The resulting P-Δ response (Figure 2-4(d)) is referred to as the global load-slip response.

Pull tests are useful, relatively inexpensive tests which can be used to investigate the effective bond length (which is the length of bonded FRP required to develop the maximum IC debonding load, P_{IC}), debonding strain and other factors impacting on the bond strength. These properties are required for the numerical analysis of FRP reinforced structures. Further, it has been shown that the debonding resistance obtained from FRP-plated pull tests is a lower bound to the IC debonding resistance in FRP strengthened structures due to effects of moment and crack distribution (Xia and Oehlers 2006; Liu 2005). Hence, to predict the behaviour of FRP strengthened masonry walls with potential flexural cracks occurring at the many closely-spaced mortar joints, the behaviour of the FRP-to-masonry joint needs to be studied in detail (Xia and Oehlers 2006; Petersen et al. 2009; Willis et al. 2009b).

2.4. Bond Behaviour of FRP strengthened structures

The global load-slip response depends on the interfacial bond characteristics between the FRP and the surrounding masonry substrate such as the interface shear stress, τ and the local interface slip, δ (Figure 2-5). The local τ-δ response is known as the local bond-slip behavior (Figure 2-5).

The behavior at the FRP-to-masonry interface is the means for transfer of load between the FRP and the substrate to develop composite action. The interfacial behavior affects the flexural capacity and other important aspects such as the width and spacing of cracks for a reinforced section. Hence, it is essential to quantify the interfacial bond-slip relationship for accurate modelling and understanding of debonding failures in FRP strengthened structures (De Lorenzis and Nanni 2002; Lu et al. 2005; Xia and Oehlers 2006; Ghiassi et al. 2012)

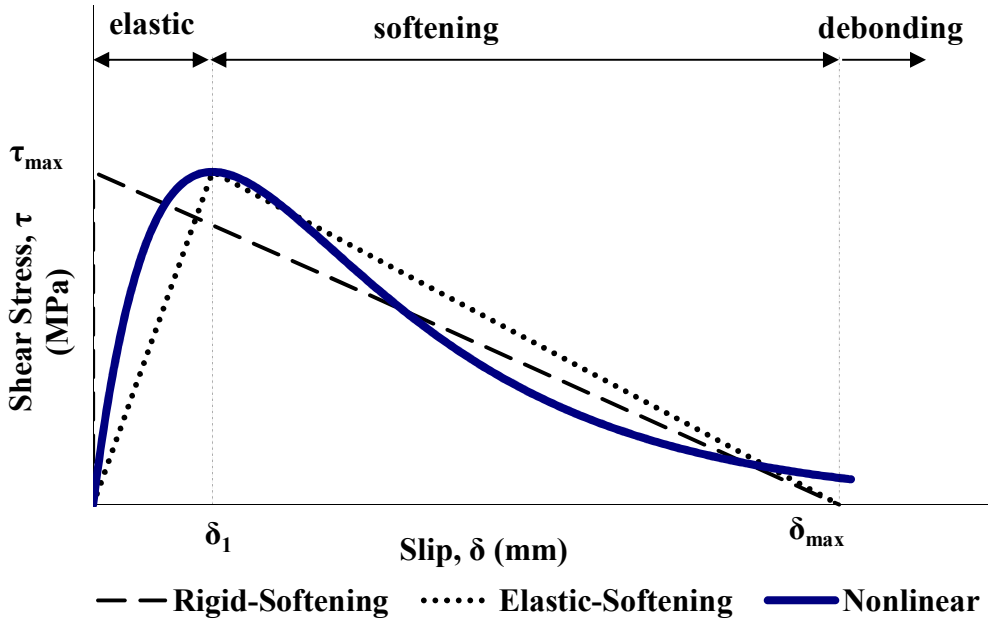

Figure 2-5: Local *τ-δ* characteristics

Extensive research is available in the literature on the bond between FRP and concrete (Teng et al. 2002; Oehlers et al. 2008) whereas the knowledge of the bond at the FRP-to-masonry interface is comparatively limited. It should be noted that while concrete is often considered to be a homogeneous material, masonry consisting of brick units and mortar joints is clearly heterogeneous. However, due to material similarity between concrete and masonry, such as low tensile strength and brittleness, the debonding mechanisms for retrofitted masonry have been found to be similar to those of retrofitted reinforced concrete (RC) members. Moreover, factors affecting the FRP-to-concrete bonded joint behaviour similarly influence FRP-to-masonry bonded joint behaviour (Xia and Oehlers 2006, Petersen et al. 2009). The use of FRP to improve the flexural resistance of RC members is now well established (e.g. Teng et al. 2002, Oehlers and Seracino 2004). Hence, in this study the research on the debonding mechanisms in plated RC structures has been used as the starting point for research on FRP retrofitted masonry structures.

2.4.1. Local bond slip model

Various local *τ-δ* relationships have been proposed for FRP-concrete bonded joints. These models have different shapes and large differences exist between them which

may be attributed to different retrofitting techniques and substrates used in these studies (Dai et al. 2005). Importantly a reliable local τ-δ model with an appropriate shape and interfacial fracture energy, G_f, are needed for the accurate analysis of debonding failures in FRP-strengthened structures (Lu et al. 2005; Ueda and Dai 2005). The interfacial fracture energy is equal to the area under the bond–slip curve and is needed to derive bond strength models. Moreover, for the calculation of some quantities such as maximum transferable load of a joint or bond strength, interfacial fracture energy can be used regardless of the shape of the bond–slip curve (Dai et al. 2005). The three significant parameters of a bond-slip model are the maximum bond stress (τ_{max}), the local slip at maximum stress (δ_1) and the maximum local slip at which the bond stress has reduced to zero (δ_{max}) (Figure 2-5).

Commonly idealised forms of local τ-δ models are rigid-softening, elastic-softening and non-linear. The rigid-softening model is characterized by a rigid-softening branch with the elastic stiffness tending to infinity whereas the elastic-softening interface characteristic linearly ascends before a maximum shear (τ_{max}) is reached at slip (δ_1), followed by a softening branch to zero residual stress at a slip of δ_{max} to accommodate the softening nature of the interface resistance (Figure 2-5). The main features of the nonlinear curve (Figure 2-5) are an initial ascending non-linear curve; a peak shear stress of τ_{max} which occurs at δ_1 followed by non -linear descending curve.

Xia and Oehlers (2006) concluded that the stiffness of the ascending branch of the local τ-δ relationship has a great influence on the initial stiffness and the ductility of the global load-slip curve of the FRP-masonry bonded joint (Figure 2-6). A smaller ascending stiffness results in a larger elastic region and more ductile load-slip response. However, it was observed that the various bond-slip curves with the same interfacial fracture energy all had the same ultimate strength capacity. Moreover, high fracture energy was found to improve the ultimate load and deformability of FRP-masonry bonded joints (Figure 2-6).

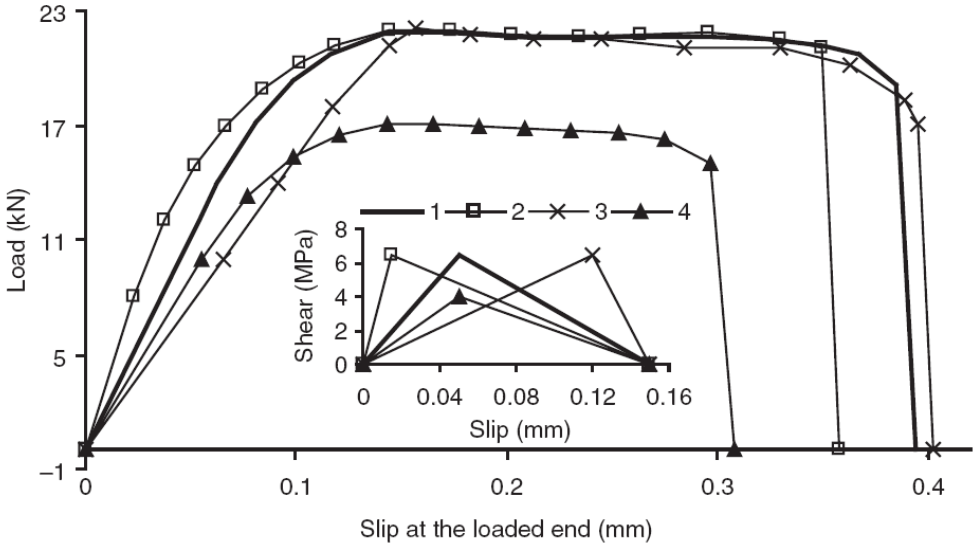

Figure 2-6: Effect of local τ-δ models on P-Δ response (Xia and Oehlers (2006)

2.4.2. Assessment of existing bond strength models

Discussion on existing bond strength models

Many theoretical models have been previously developed to predict the bond strength of FRP-to-concrete joints where the bond strength refers to the shear strength capacity of the FRP-to-substrate interface. A review of the existing models applicable to EB FRP-to-concrete bonded joints can be found in Lu et al. (2005), Kharbhari et al. (2006) and Sayed-Ahmed et al. (2009). A total of 24 FRP-to-concrete bond strength models from the literature were investigated in this study. These models are based on either empirical relations calibrated against experimental data or on fracture mechanics theories or combinations of the two. Some of these models involve parameters that are not applicable to masonry while for others, insufficient information was available to include the models in the reported analysis. Further, for the models proposed by some researchers (Challal et al. 1998, Bronsens and Van Gemert 1999, Dai and Ueda 2003 and Ueda et al. 2003) adhesive properties are needed. However, the properties of adhesives used are not always reported and hence, these models are not further discussed. Consequently, only 12 EB models were considered in this study (Tanaka (from Sayed-Ahmed et al. 2009), Hiroyuki and Wu 1997, Maeda et al. (from Chen and Teng 2001), Neubauer and Rostasy (from Sayed-Ahmed et al. 2009), Khalifa et al. 1998, Chen and Teng 2001, Yang et

al. (from Sayed-Ahmed et al. 2009), Monti et al. 2003, Iso (from Sayed-Ahmed et al. 2009), Sato (from Sayed-Ahmed et al. 2009), Lu et al. 2005 and Kharbhari et al. 2006 (extended from Nakaba et al. 2001). Analytical models specific to the NSM technique have been published by Blaschko (2003) and Seracino et al. (2007a). As Blaschko's model requires adhesives property data, it also could not be included in this analysis. Further, details of all these existing models for FRP-to-concrete joints are included in Appendix §A.1.

All of the above models are specific to a particular retrofitting technique, i.e. either EB or NSM. The first generic analytical model applicable to any adhesively bonded plate cross-section and material was developed by Seracino et al. (2007b) for predicting the IC debonding resistance, P_{IC}, using Eq. 2-1

$$P_{IC} = \sqrt{\tau_{\max}\delta_{\max}}\sqrt{L_{per}(EA)_p} \qquad \text{Eq. 2-1}$$

where the maximum interface shear stress, $\tau_{\max} = (0.802 + 0.078\varphi_f) f_c^{0.6}$;

the maximum interface slip, $\delta_{\max} = \dfrac{0.976\varphi_f^{0.526}}{0.802 + 0.078\varphi_f}$;

f_c is the cylinder compressive strength of the concrete;

$\varphi_f = d_f/b_f$, is the IC debonding failure plane aspect ratio and d_f and b_f are the lengths of the failure plane perpendicular and parallel to the surface of the substrate as shown in Figure 2-7;

L_{per} the perimeter of the debonding failure plane (Figure 2-7); and

$(EA)_p$ is the axial rigidity of the FRP strip.

The effective bond length, L_{eff}, is given by Eq. 2-2

$$L_{eff} = \frac{\pi}{2\lambda} \qquad \text{Eq. 2-2}$$

where, $\lambda = \sqrt{\dfrac{\tau_{\max} L_{per}}{\delta_{\max}(EA)_p}}$

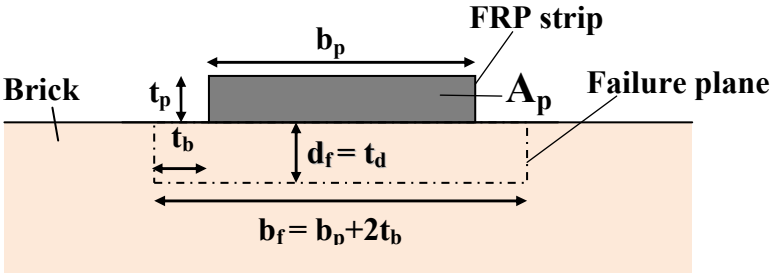

(a) EB

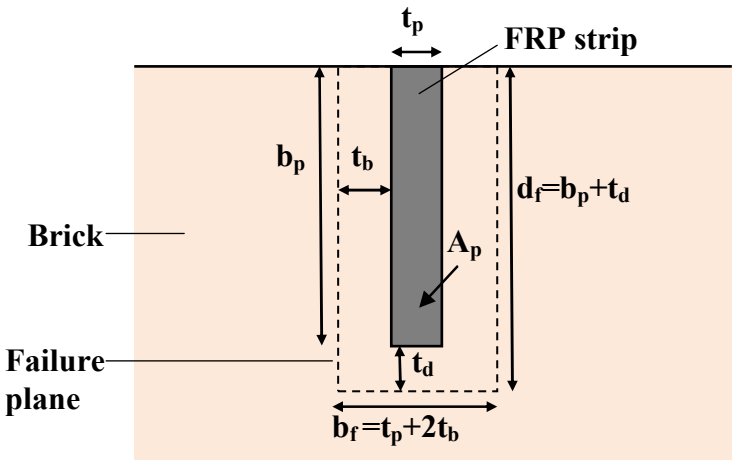

(b) NSM

Note: $t_d = t_b = 1$mm and failure plane, $L_{per} = b_f + 2d_f$

Figure 2-7: Failure plane for FRP retrofitted sections

From the current literature, only three theoretical models (Camli and Binici 2006, Willis et al. 2009b and Milani et al. 2009) are available for masonry to predict the debonding resistance of FRP-to-masonry joints. Moreover, the models proposed by Camli and Binici (2006) and Milani et al. (2009) are specific to the EB retrofitting technique. The generic model by Willis et al. (2009b) was adapted from the generic model of Seracino et al. (2007b) described earlier in this section using Eq. 2-1 and can be applied to both EB and NSM techniques. Details of all these existing models have been included in Appendix §A.1.

Existing pull test data

To assess the accuracy of the above mentioned bond strength models, a large database was developed containing the results of 223 FRP-to-masonry pull tests reported in the open literature for both EB and NSM FRP techniques. It should be

noted that other tests reported in the literature (e.g. Soric and `Tulin 1989, Carloni and Subramanium 2010, Capozucca 2009) had insufficient information (e.g. material and/or geometric properties) provided to allow meaningful analysis and comparison. It should be noted that of the 223 FRP-to-masonry pull tests available in the open literature, NSM tests account for only about 25% of the total. The database includes results from ten different experimental studies (De Lorenzis et al. 2000; Turco et al. 2003, Liu et al. 2005, Camli and Binici 2006, Xia & Oehlers 2006, Petersen et al. 2009, Konthesingha et al. 2009, Lam 2009, Willis et al. 2009b, and Oliveria et al. 2010). Results with failure modes other than IC debonding and bond lengths less than L_{eff} were excluded where L_{eff} was calculated using Eq. 2-2. Consequently, a dataset of 109 pull test results was available as shown in Appendix §A.2 (Table A-1). The range of experimental parameters included in the database are: 22.3 GPa < Ep < 230 GPa; 1.3 MPa < f_{ut} < 3.57 MPa and 0.02 < φ_f < 6.56 where the flexural tensile strength of the brick unit, f_{ut}, was not reported, it was calculated using Eq 2-3 assuming that the following relationship between between concrete tensile and compressive (f'_c) strength is also applicable to masonry units (MacGregor 1988).

$$\sqrt{f'_c} = \frac{f_{ut}}{0.53} \qquad \text{Eq. 2-3}$$

Comparison of existing bond strength models

Table 2-2 presents results that were used to evaluate the reliability and accuracy of the 15 existing models to predict the bond strength of the FRP-to-masonry pull tests given in the present test database (Table A-1, Appendix §A.2), based on the experimental test-to-predicted bond strength ratio (P_{exp}/P_{IC}). As can be observed in Table 2-2(a), the generic model by Willis et al. (2009b) under-predicts the bond strength on average by about ½ when both EB and NSM specimens are considered.

Table 2-2: P_{exp}/P_{IC} ratios for existing models

(a) for all specimens (N=109)						
Model	**mean**	**max**	**min**	**SD**	**COV**	**correlation**
Willis et al. (2009b)	1.50	2.39	0.67	0.46	0.30	0.92
(b) for EB specimens only (N=89)						
Model	**mean**	**max**	**min**	**SD**	**COV**	**correlation**
Kharbhari et al. (2006)	1.11	1.85	0.31	0.33	0.29	0.85
Lu et al. (2005)	1.20	1.85	0.79	0.29	0.24	0.89
Milani et al. (2009)	1.29	1.99	0.43	0.37	0.29	0.89
Maeda et al. (Chen & Teng 2001)	1.33	2.28	0.36	0.40	0.30	0.83
Chen & Teng (2001)	1.49	2.29	0.53	0.40	0.27	0.89
Willis et al. (2009)	1.64	2.39	0.67	0.43	0.26	0.88
Yang et al. (Sayed-Ahmed et al. 2009)	1.70	2.56	0.71	0.41	0.24	0.92
Camli and Binici (2006)	1.84	3.81	0.50	0.77	0.42	0.84
Iso (Sayed-Ahmed et al. 2009)	2.05	3.51	0.71	0.72	0.35	0.88
Monti et al. (2003)	2.10	4.23	0.88	0.90	0.43	0.93
Nebauer & Rostasy (Sayed-Ahmed et al. 2009)	2.26	4.43	0.91	0.95	0.42	0.92
Sato (Sayed-Ahmed et al. 2009)	2.34	4.96	0.18	1.28	0.55	0.71
Khalifa et al. (1998)	2.46	4.41	0.88	0.89	0.36	0.92
Hiroyuki & Wu (1997)	9.17	17.76	3.54	3.73	0.41	0.74
Tanaka (Sayed-Ahmed et al. 2009)	2.29	11.73	0.63	2.07	0.90	0.17
(c) for NSM specimens only (N=20)						
Model	**mean**	**max**	**min**	**SD**	**COV**	**correlation**
Willis et al. (2009b)	1.15	1.92	0.74	0.33	0.29	0.57
Seracino et al. (2007b)	1.41	3.20	0.64	0.57	0.41	0.26

Note: N is the number of specimens used to calibrate each of the models

Table 2-2(b) indicates that eight of the fifteen existing models applicable specifically for EB strips (Tanaka (from Sayed-Ahmed et al. 2009), Hiroyuki and Wu 1997, Neubauer and Rostasy (from Sayed-Ahmed et al. 2009), Khalifa et al. 1998, Iso (from Sayed-Ahmed et al. 2009), Sato (from Sayed-Ahmed et al. 2009), Monti et al. 2003 and Camli and Binici 2006) do not agree well with the experimental data, having either a mean value greater than or equal to 2 or a COV greater than 35%. It is worth noting that some of these models have also been identified by Chen and Teng (2001) and Lu et al. (2005) as being poorly performing models for FRP-to-concrete joints. Further, although the models by Chen and Teng (2001), Willis et al. (2009b) and Yang et al. (from Sayed-Ahmed et al. 2009), have a COV within the typical limit for masonry (i.e. 30%) and a relatively good correlation coefficient, these models significantly underestimate the bond strength.

Based on the data analysed in this study, only four models (Maeda et al. (from Chen and Teng 2001), Milani et al. 2009, Lu et al. 2005 and Kharbhari et al. 2006) out of the fifteen models applicable for EB can be considered to provide reasonable predictions of the debonding strength, having P_{exp}/P_{IC} less than 1.35 (Table 2-2 (b)). FromTable 2-2 (b) it can be observed that the models by Lu et al. (2005) and Kharbhari et al. (2006) provide particularly good estimates of the bond strength when compared to the other models. It is interesting to note that the generic model by Willis et al. (2009b) correlates better with the NSM test data (Table 2-2(c)) than with the EB test data (Table 2-2 (b)). Further, the NSM specific bond strength model by Seracino et al. (2007b) is also not reliable, with a large coefficient of variation (COV) and low correlation coefficient as shown in Table 2-2(c). From these results it can be seen that the existing bond strength models are inadequate for predicting the FRP-to-masonry joint test data considered in this study. This highlights the need for development of a new model that can more accurately predict the bond strength of FRP retrofitted masonry.

2.5. Previous Experimental Research on Flexural Strengthening of Masonry Walls

The review of previous research work conducted on FRP strengthened URM walls subjected to out-of-plane loading is presented in this section. In the past, laboratory-based and in-situ tests have been conducted on out-of-plane full scale or small scale models of wall panels and wall segments. Although in-situ testing of walls in real buildings provides more realistic boundary conditions, opportunities to do so are limited and construction of full-scale structures is expensive. Hence, simplified narrower wall panels tests are commonly used for realistic representation of the one-way bending portion of a masonry wall supported on all four sides and so were also adopted for this research.

Since 1997 researchers have been studying the use of the EB FRP technique to improve the out-of-plane performance of URM walls (Saadatmanesh 1997; Triantafillou 1998; Gilstrap and Dolan 1998; Ehsani et al. 1999; Velazquez-Dimas et al. 2000; Hamoush et al. 2001; Albert et al. 2001; Hamilton and Dolan 2001; Paquette 2001**;** Kuzik et al. 2003; Tumialan et al. 2003; Ghobarah and Galal 2004; Tan and Patoary 2004; Xia and Oehlers 2006; Mosallam 2007; Hamed and Rabinovitch 2007; Kiss et al. 2002, Vandergrift et al.2002 and Sayari et al. 2010). More recently, research into the use of NSM FRP has emerged as a promising strengthening technique for masonry walls. The experimental research on this technique includes that by: Turco et al. 2003; Bajpai and Duthinh 2003; Galati et al. 2005; Korany and Drysdale 2006; De Lorenzis 2000; Willis et al. 2009a; and Dizhur et al. 2010.

Out of the different modes of failure observed (§2.3) in these studies, debonding of FRP laminate from masonry substrate has been considered as the preferred failure mechanism (Schwegler et al. 1995; Velazquez-Dimas et al. 2000; Tumialan et al. 2003; Willis et al. 2009a). The ongoing research on FRP strengthened masonry walls shows that the FRPs are highly effective in increasing the flexural capacity, stiffness, and displacement ductility under out-of-plane loads. Past research has shown that

FRP strengthened walls can sustain lateral load of the order of five to fifty times that of the corresponding URM wall whereas deflections of about 1.2% to 5% of the wall height has been observed for retrofitted walls.

Different studies on out-of-plane bending of FRP strengthened masonry (Albert et al. 2001; Turco et al. 2003; Xia and Oehlers 2006;) have shown that the load-deflection response of strengthened walls can be characterized into two distinct phases: the first nonlinear phase represents the stiffness contribution of the masonry i.e. the result of the mortar reaching its tensile capacity and cracking while the second linear phase represents the stiffness contribution from the FRP where the cracks get progressively wider and the displacement at midspan increases until failure occurs when FRP completely debonds from the masonry. Despite the absence of a long post-peak plateau in the load- deflection response, FRP retrofitted walls can sustain large displacements and absorb energy through elastic deformations under both monotonic and cyclic loadings (Korany and Drysdale 2006). For example, the out-of-plane displacement of the FRP strengthened walls at peak strength was found to be 10 to 20 times greater than for the corresponding URM walls (Korany and Drysdale 2006).

The overall performance of an FRP retrofitted wall is greatly affected by the type of composite strip used. Based on four beam tests of URM masonry reinforced with EB FRP plates, Xia and Oehlers (2006) observed that increasing the FRP stiffness lead to higher ultimate load capacity and lower ductility. Velazquez-Dimas et al. (2000) recommended that narrow FRP strips are subjected to higher shear and hence, appropriate choice of composite strip and contact area is needed to avoid early delamination. Korany and Drysdale (2004) suggested using CFRP, which has much higher modulus of elasticity as the use of GFRP reinforcement resulted in much lower load capacity and energy absorption. It was also concluded that GFRPs can cause high deformability leading to a premature compression failure of the masonry units before the strength of the reinforcement is fully utilized. However, due to its lower costs, as compared with the other fibers, glass FRP is still widely used in many buildings (Christensen et al. 1996)

Previous research indicates that the design parameters that most strongly affect the strength and deflection capacity of retrofitted masonry walls include: boundary conditions; wall slenderness ratio (height-to-thickness); loading type; axial load, spacing and aspect ratio of FRP, single or double sided reinforcement and reinforcement ratio. The literature related to the parameters investigated in this study is presented in the following sections (§2.5.1 - §2.5.4).

2.5.1. Effect of FRP strip spacing

From the perspective of effective use of FRP material, strip configuration (dimension and spacing) should be such that it can efficiently utilize the tensile strength of the FRP material. Consequently, optimal spacing and dimensioning of FRP strips can enable FRP material costs to be minimized. The total amount of FRP used can be kept constant for a variety of strip spacings by altering the strip size.

There appears to be no scientific evidence for the recommendations on maximum or minimum spacing between two FRP strips or bars (Turco et al. 2003 and Tumialan et al. 2003). In order to avoid partial collapse of the wall, Tumialan et al. (2003) suggested that the maximum clear spacing should be set equal to the minimum of: ($2t_m$; l) where for block units: $l = l_b$, for brick units: $l = 2l_b$, t_m is the thickness of the wall being reinforced without including the wall veneer, if present, and l_b is the length of the masonry unit.

To date, a review of the studies shows that although different reinforcement spacings have been used for strengthening masonry walls, there has been no consideration of the effect of FRP strips/bars spacing on their flexural behavior. This research will investigate the influence of strip spacing on the flexural behavior of retrofitted walls, whilst maintaining a constant reinforcement ratio.

2.5.2. Effect of Cyclic loading

The cyclic flexural behavior of masonry walls reinforced with FRP has not been extensively investigated. The few experimental studies in the literature include

Ehsani et al. (1999), Velazquez-Dimas and Ehsani (2000), Albert et al. (2001), Kuzik et al. (2003) and Korany and Drysdale (2006).

Ehsani et al. (1999) and Velazquez-Dimas and Ehsani (2000) tested half-scale unreinforced brick walls retrofitted with vertical EB GFRP strips on both faces under reverse cyclic out-of-plane loading. All walls were simply supported at the top and bottom while the two vertical edges were unsupported. The test results showed a significant increase in the ultimate flexural strength and deflection as compared to the unreinforced wall. However, there was no comparison made between cyclic and monotonic behavior of the reinforced wall.

Albert et al. (2001) tested ten full-scale simply supported URM walls plated with EB FRP (glass and carbon) subjected to primarily monotonically increasing lateral out-of-plane loads. To study the effect of cyclic loading, one wall was reinforced on one side with carbon sheet and tested monotonically until fully cracked (MCST4), at which point additional carbon sheet fibre reinforcement was placed on the opposite side and the wall was tested again in the opposite direction with progressively increasing amplitudes of load-unload cyclic loading (MCST7-4). As shown in Figure 2-8, cyclic loading resulted in reduced first phase stiffness after each cycle but the original load-deflection envelope was maintained.

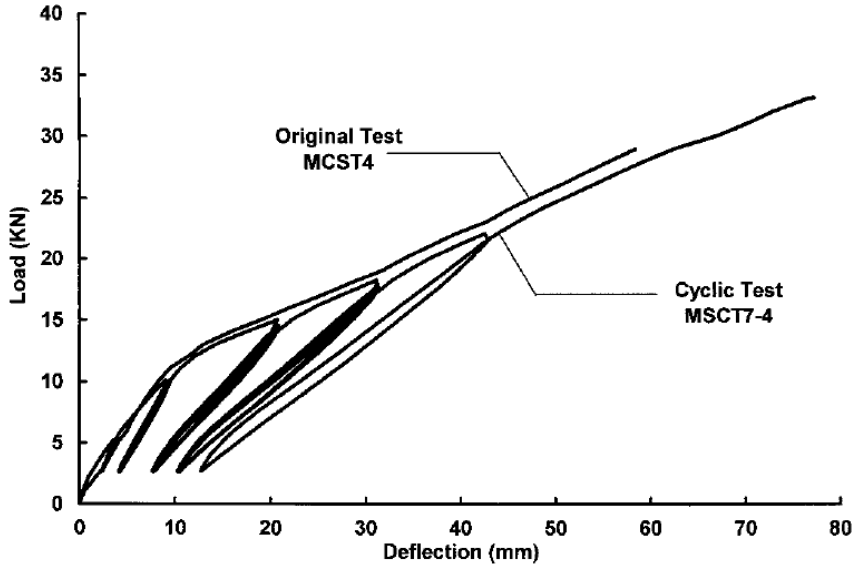

Figure 2-8: Load-deflection response showing the effect of cyclic loading (Albert et al. 2001)

Kuzik et al. (2003) extended the work of Albert et al. (2001) to include the behavior of eight full-scale lightly reinforced hollow concrete block masonry walls strengthened with GFRP sheets under fully reversed out-of-plane cyclic loading (Figure 2-9). The unloading/reloading paths for successive loading cycles were similar, indicating little degradation. Moreover, a "pinched" load-displacement response was observed which was similar to that of the monotonic loaded specimen tested by Albert et al. 1998. The authors reported that the walls maintained their structural integrity throughout the load versus deflection hysteretic responses.

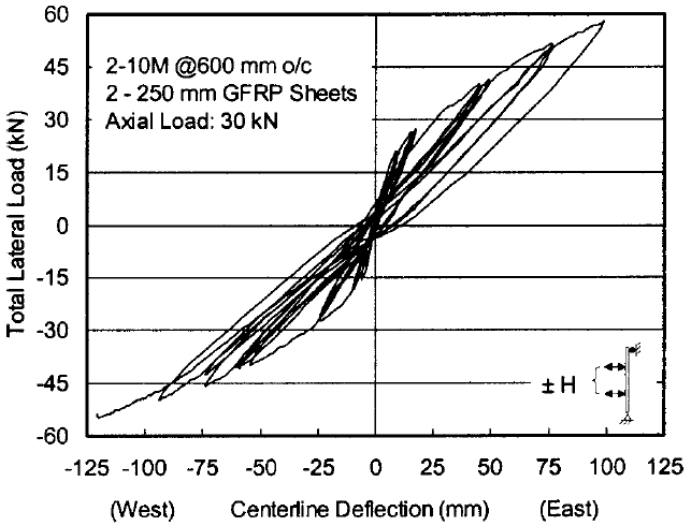

Figure 2-9: Typical load versus deflection hysteresis (Kuzik et al. 2003)

Five full-scale concrete masonry block walls with openings were tested by Ghobarah and Galal (2004). Firstly, the unreinforced walls were tested under uniformly distributed lateral pressure up to failure. These cracked walls were strengthened using CFRP laminate strips and then were subjected to cyclic out-of-plane pressure with hinged boundary conditions along the four edges of the wall. The strengthened walls were found to dissipate significant energy compared to the non-ductile behavior of the URM walls. From the study it was observed that, the permanent plastic deformation at the end of each loading-unloading cycle ranged between 20–30% of the maximum displacement reached. Upon reloading, a load reduction of about 5% on average was observed at the same displacement increment.

Korany and Drysdale (2006) investigated the effectiveness of the NSM carbon fiber composite cable (CFCC) in strengthening masonry walls under out-of-plane loading. Ten full scale clay brick wall panels were tested under monotonically increasing uniform lateral pressure using an airbag and three unreinforced control wall panels were also repaired with CFCC after initial testing and retested under unidirectional cyclic lateral load. At higher displacement levels, it was found that the static curve envelopes the cyclic test closely (Figure 2-10).

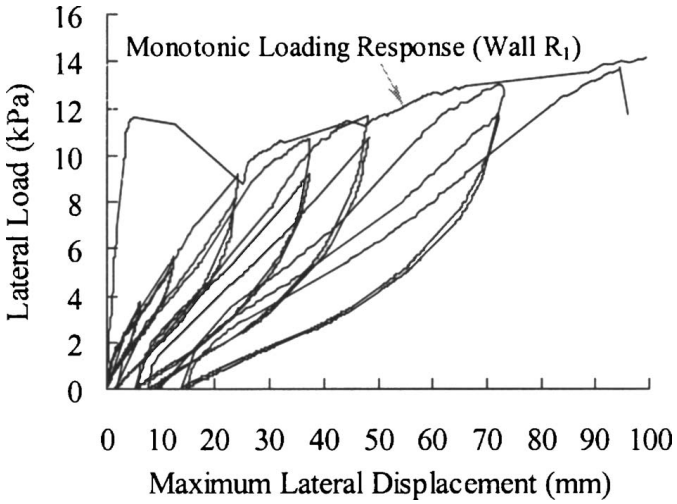

Figure 2-10: Influence of cyclic loading on lateral load-displacement response (Korany and Drysdale 2006)

After the loading-unloading cycles (Figure 2-10), only small permanent displacements were generated which was attributed to the elastic response of the FRP material. Furthermore, beyond the initial cracking point 10% load reduction was observed between the first and second cycle for the same displacement increment. The study concluded that cyclically loaded specimens had similar failure modes with slightly reduced strengths as compared to the specimens subjects to monotonic loading indicating that monotonic tests are suitable to evaluate the effectiveness of FRP in strengthening masonry walls.

Although, some studies have investigated the effects of cyclic loading on retrofitted masonry, only a few have focused on comparison of static and cyclic behavior under different test parameters such as axial load and reinforcement ratio. Moreover, only one study (Korany and Drysdale 2006) in the open literature has investigated the

behavior of NSM retrofitted masonry under cyclic loading. The present study will help to understand the behavior of clay brick masonry walls retrofitted with NSM CFRP strips subjected to reverse cyclic loading under varying axial loads, reinforcement ratios and spacings.

2.5.3. Effect of Axial loading

Gravity load-bearing masonry walls are subjected to applied axial loads from roof or upper level structures in addition to the self-weight of the wall itself. Applied axial loads are generally considered to strengthen and stiffen URM walls in their out-of-plane direction. However, there has been little research into the effects of axial load on FRP retrofitted members.

Albert et al. (2001) investigated the effects of moderate compressive axial load on full-scale URM walls plated with EB CFRP subjected to monotonically increasing lateral out-of-plane loads. The tests results showed that introduction of axial load affect the overall stiffness. For example, the study found that as the axial load introduces compression across the wall cross-section, debonding and cracking was delayed resulting in an increase in the first phase stiffness. However, there was a reduction in the second phase stiffness with increased axial loads. The study showed reductions of 10% and 21% for axial loads of 10 kN (0.04 MPa) and 30 kN (0.13 MPa), respectively.

Korany and Drysdale (2006) investigated the effect of axial loading on both unreinforced walls and masonry walls reinforced with NSM CFCC. For unreinforced walls, it was concluded that the stabilizing effect due to axial load resulted in an increase in both the cracking and residual strengths. Even higher cracking and ultimate strengths were achieved for the retrofitted walls by applying an axial load of 150 kN (0.28 MPa). The increase in the out-of-plane flexural strength due to pre-compression was comparable to the effect of increasing the reinforcement by 50%. This research also found that the displacement capacities at failure were lower for axial loaded walls.

The current literature provides no indication as to how axial load will affect the behaviour of NSM FRP-masonry. The effect of pre-compression on cyclic loaded walls also needs to be investigated. Therefore, this research also focused on how variations in axial loading affect the global load-displacement behavior of NSM FRP plated masonry walls under monotonic and cyclic lateral loading.

2.5.4. Effect of reinforcement ratio

The amount of reinforcement is an important factor in determining the FRP debonding strain and hence, is a key variable in the prediction of the flexural capacity of the debonding failure (Xia and Oehlers 2006). The flexural capacity of FRP strengthened masonry subject to out-of-plane loads is dependent on the failure mode which can be determined by comparing the FRP reinforcement ratio (ρ) to the balanced reinforcement ratio (ρ_b). The balanced reinforcement ratio represents the case of simultaneous crushing of masonry and IC debonding or tensile rupture of the FRP (Galati et al. 2005). Researchers have reported that $\rho>\rho_b$ will result in masonry crushing which is undesirable due to its brittle nature. However, in order to allow for the more ductile IC debonding failure, reinforcement ratio is a vital parameter.

Triantafillou (1998) tested four small-scale masonry wall specimens strengthened with EB CFRP laminates under one-way monotonic out-of-plane loading. Two specimens were tested for each of the two different reinforcement ratios used (0.21% and 0.42%). The test results showed that doubling the reinforcement ratio resulted in a 21% increase (on average) in strength.

Velazquez-Dimas and Ehsani (2000) tested seven half-scale EB GFRP retrofitted brick masonry walls under cyclic out-of-plane loading with the reinforcement ratio ranging from 0.6 to three times the balanced condition, ρ_b. The study concluded that for the short walls (slenderness ratio, H/t_m=14) no particular trend was observed between the deflection and reinforcement ratio. However, for the slender walls (H/t_m=28), deflection increased with the reinforcement ratio. Further, the test results indicated that for all stages of loading (i.e., cracking, delamination, and ultimate), load increased linearly with the amount of reinforcement up to $2\rho_b$. To avoid very

stiff behavior and improve the hysteretic response, it was recommended to limit the reinforcement ratio to $2\rho_b$.

Based on an experimental study on full-scale URM walls plated with EB FRP, Albert et al. (2001) concluded that the overall stiffness of a specimen was affected by the type and amount of FRP used. The test results showed that the slope of the second phase of the load-deflection response increased in proportion to the amount of reinforcement used. A study by Kuzik et al. (2003) on full-scale GFRP strengthened masonry walls concluded that varying the amount of GFRP sheets significantly affected the behavior of the walls. From the test results it was observed that the GFRP reinforcement governed the linear response of the bending moment-centerline deflection response. An increase or decrease in both the wall stiffness and its ultimate strength was controlled by an increase or decrease in the amount of GFRP reinforcement, respectively.

Tumialan et al. (2003) tested concrete and clay masonry walls retrofitted with different amounts of EB FRP laminates (0.04% to 0.19%). The study reported that large amounts of reinforcement (> 0.14% for clay masonry) resulted in shear failure of walls whereas for other lesser reinforcement ratios, walls failed by FRP rupture or debonding. It was also concluded that the crack widths were thinner as the amount of FRP reinforcement increased. Moreover, the test results showed that an increase in FRP reinforcement ratio increased the flexural capacity of walls, up to a limiting ratio, beyond which the member will become over-reinforced and the desired IC debonding mechanism will no longer govern.

Past studies have shown that reinforcement ratio not only affects the global load-displacement behavior but also the failure mode and hence, is a vital parameter in investigation of flexural behavior of masonry wall. It should be noted that past research has focused on EB FRP therefore, the effect of reinforcement ratio on NSM FRP strengthened masonry walls still needs to be investigated. One of the objectives of this research is to study how different reinforcement ratios influence the overall response of a masonry wall under out-of-plane loading while keeping the other test parameters such as spacing, axial load and loading type constant.

2.6. Research gaps

Experimental test results reported in the literature have demonstrated the effectiveness of FRP in improving the flexural out-of-plane response of URM walls. Whilst the application of NSM FRP strips appears to be a particularly viable retrofitting technique, limited research has been conducted on the application of this retrofitting technique to masonry structures. Further, the effect of out-of-plane cyclic loading on the load-deformation behaviour of FRP retrofitted masonry members also warrants more attention. In addition, limited testing has been conducted to study the effects of spacing between FRP strips, cyclic loading, applied pre-compression and reinforcement ratio on the flexural response of NSM FRP retrofitted masonry walls. As a result, there is a significant need for more experimental investigations on NSM FRP retrofitted masonry walls before it can be confidently used for seismic retrofit of URM walls.

Furthermore, it can be noted that a significant amount of data is available in the literature on the experimental and theoretical studies on the bond between FRP and concrete. While mathematical models and design equations related to the bond mechanisms, the bond strength, the interfacial fracture energy, the effective bond length and the bond stress-slip relationship are well established for FRP-concrete materials, understanding of the bond at the FRP-to-masonry interface is still relatively limited. Moreover, from the review of the large database presented in this study, it was revealed that of the 223 FRP-to-masonry pull tests available in the open literature, NSM tests account for only about 25% of the total. Furthermore, considering the limited available database and variability of available results due to different test set-up and material properties, different specimens geometry and test procedures, further experimental research is required.

Finally to better understand bond at the FRP-to-masonry interface there is a need for numerical investigations into the local shear bond-slip. Therefore, analytical models should be developed to predict the global load-slip response of FRP-to-masonry pull tests. To do this further development of explicit relationships for the bond-slip parameters for FRP-to-masonry (Aiello et al. 2007; Willis et al. 2009b) are needed.

From the current literature, only a few theoretical models are available for masonry to predict the debonding resistance of FRP-to-masonry joints. Importantly, as seen in §2.4.2 the existing bond strength models are inadequate for predicting the FRP-to-masonry joint test data considered in this study. Numerical investigations carried out by Milani (2010) and Milani and Bucchi (2010) on reinforced masonry walls and curved structures, respectively, suggest that application of existing FRP-to-concrete models to masonry is questionable. This further highlights the need for development of new model that can more accurately predict the bond strength of FRP retrofitted masonry and its application to complex realistic geometries.

CHAPTER 3
PULL TESTS EXPERIMENTAL STUDY

3.1. Introduction

This chapter presents the results of an experimental investigation of the behaviour of FRP-to-masonry joints. Fourteen NSM FRP-to-masonry pull tests were conducted to assess the effect of cyclic loading and FRP strip dimensions on FRP-to-masonry bonded joints. As mentioned in §2.4, limited research (33 tests) has been conducted on NSM FRP-to-masonry pull tests. Hence, these 14 tests add significantly to the relatively small existing NSM pull test database. §3.2 to §3.4 cover the description of the specimens, the material properties and the test setup. The chapter concludes with a discussion of the failure mode, FRP-masonry interface behavior, and the effects of cyclic loading and strip dimensions on bond behavior.

3.2. Test Plan

Fourteen NSM CFRP-to-masonry pull tests were conducted. Five different strip dimensions were used for the pull tests. These were chosen to match the strip dimensions used in the wall bending tests (discussed later in Chapter 5). Table 3-1 shows the details of the pull tests. The specimens were labeled using the notation shown in Table 3-1. The first term refers to the loading type (monotonic or cyclic); the second term denotes whether strain gauges were attached along the bonded length (NSG stands for no strain gauges and SG stands for strain gauges); the third and the fourth terms refer to the thickness, t_p and depth, b_p of the NSM FRP strip (Figure 2-7), respectively and the last term signifies the test number for cases where more than one specimen was tested with the same FRP strip configuration. The FRP strips were made up of multiple layers of 1.2 mm or 1.4 mm thick carbon FRP strips. As shown in Table 3-1, only P5 and P6 were subjected to cyclic loading while all the remaining specimens were monotonically loaded.

Table 3-1: Pull test plan

Test no.	Specimen notation	t_p (mm)	b_p (mm)
P1	M-SG-3.6-10-1	3.6	10.0
P2	M-SG-3.6-10-2	3.6	10.0
P3	M-SG-3.6-10-3	3.6	10.0
P4	M-SG-3.6-10-4	3.6	10.0
P5	C-SG-3.6-10-5	3.6	10.0
P6	C-SG-3.6-10-6	3.6	10.0
P7	M-NSG-4.2-10-1	4.2	10.0
P8	M-NSG-4.2-10-2	4.2	10.0
P9	M-NSG-7.2-10-1	7.2	10.0
P10	M-NSG-7.2-10-2	7.2	10.0
P11	M-NSG-4.8-7.5-1	4.8	7.5
P12	M-NSG-4.8-7.5-2	4.8	7.5
P13	M-NSG-4.8-5-1	4.8	5.0
P14	M-NSG-4.8-5-2	4.8	5.0

3.3. Material properties

The material properties for the masonry and CFRP strips are given in Table 3-2. These material properties are applicable for both the pull tests and the wall tests (discussed later in Chapter 5). Clay brick units with nominal dimensions of 230 x 110 x 76 mm were used. Masonry properties were determined based on material tests conducted in accordance with Standards Australia (2001). The mortar consisted of Portland cement, hydrated lime and sand in a ratio of 1:1:6 by volume. Material properties of the CFRP were obtained from the manufacturer's data sheet with the elastic modulus verified directly from pull test data. Details of the material tests have been included in Appendix §B.2.

Table 3-2: Material properties

Parameter	Mean	Standard Deviation	COV
Masonry Properties	**(MPa)**	**(MPa)**	
Flexural tensile strength of the masonry, f_{mt} (70 test specimens)	0.48	0.13	0.27
Compressive strength of the masonry, f_{mc} (21 test specimens)	17	2.95	0.17
Lateral modulus of rupture of the brick unit, f_{ut} (19 test specimens)	3.13	0.84	0.27
Elastic modulus of masonry, E (21 test specimens)	10700	2400	0.22
Elastic modulus of brick, E_b (21 test specimens)	19500	3700	0.19
Elastic modulus of mortar, E_m (21 test specimens)	2300	870	0.38
CFRP Properties			
Elastic modulus of FRP strip, E_p	$165x10^3$ MPa		
Ultimate tensile strength, f_{rupt}	2700 MPa		
Ultimate tensile strain, ε_{rupt}	0.0164		
Adhesive Properties			
Tensile strength, f_a	13.9 MPa		
Elastic modulus, E_a	6700 MPa		
Poisson's ratio, ν	0.31		

3.4. Specimen preparation and Test setup

Figure 3-1 shows details of the pull test specimen and test setup. Each pull test prism consisted of a five brick stack, with 10 mm mortar bed joints and an FRP-to-masonry bonded length of 420 mm to ensure full the effective bond was developed. The effective bond length (L_{eff}) is the minimum bonded length required to achieve the maximum possible debonding load, $P_{IC.}$ For detailed calculations refer to Appendix §C.1. To ensure IC debonding as the failure mode the specimens were designed against failure by FRP rupture (Appendix §C.1). The groove for the NSM strip was cut using a diamond blade saw and then filled with an epoxy adhesive after blowing the brick dust out with a high pressure air hose. The strip was cleaned with acetone to remove any foreign substances before being inserted into to the epoxy-filled groove

and allowed to cure for 7 days. The FRP strip was positioned flush with the masonry surface as shown in Figure 3-1(b) for all specimens. A layer of quick drying paste was applied to the top and bottom surfaces of the masonry prism to ensure that the load was transferred evenly using a manually controlled hydraulic ram. A solid steel plate with a small gap for the FRP to pass through was placed onto the top surface (loaded end) of the specimen. This restraining plate was used to apply approximately 1kN of pre-compression to settle the specimen at the early stages of loading.

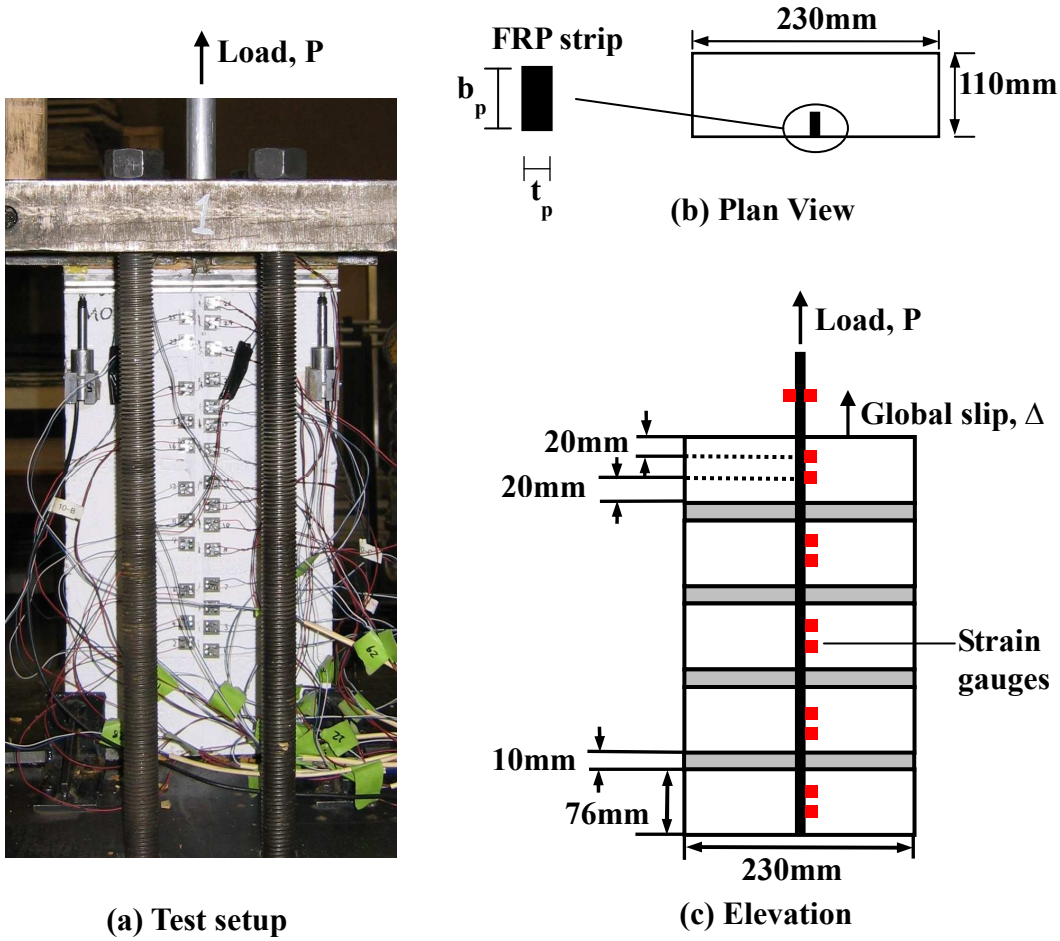

Figure 3-1: Pull test specimen details

Once the specimen was in place, a monotonic tensile load was applied using an Avery testing machine at a constant rate of approximately 2.5 kN per minute until failure, with 0.5 mm per minute as an upper bound for the displacement loading rate. For cyclic loading, one cycle of load consisted of increasing the load monotonically until the target load (displacement) was reached, then reducing the load to "zero" and

then reloading. Thus, the NSM strips of FRP were only loaded in tension. Each cyclic specimen was subjected to three cycles of load for each target displacement. Each test specimen had two strain gauges glued on the FRP strips at a position 25 mm away from the top brick unit at the loaded end to help align the FRP strip during testing and to confirm the manufacturer's value for the modulus of elasticity of the FRP. Six of the specimens were also strain gauged along the bonded length of the strip. These strain gauges were located 20 mm from the top and bottom edges of each brick unit to measure the strain profile along the FRP strip, as shown in Figure 3-1(c). The FRP strips were made up of multiple layers of 1.2 mm or 1.4 mm thick carbon FRP strips with the strain gauges sandwiched between the strips to minimize the negative effect that the presence of the strain gauges could have on the brick-FRP bond (Willis et al. 2009b). Two linear variable differential transformers (LVDT) placed at the top of the masonry prism measured the global slip (Δ) of the FRP strip at the loaded end.

3.5. Discussion of test results

The pull tests results are summarised in Table 3-3, where P_{exp} refers to the maximum experimental load and Δ_{max} refers to the maximum slip at the loaded end (i.e. slip at failure).

Table 3-3: Summary of pull test results

Test no.	Specimen No	P_{exp} (kN)	$P_{exp,}$ Group avg (kN)	Δ_{max} (mm)	E_p (GPa)
P1	M-SG-3.6-10-1	64.8	65.0	2.15	168
P2	M-SG-3.6-10-2	70.0		3.00	165
P3	M-SG-3.6-10-3	61.0		3.00	168
P4	M-SG-3.6-10-4	64.0		2.20	162
P5	C-SG-3.6-10-5	58.8	58.9	2.56	152
P6	C-SG-3.6-10-6	59.0		2.69	152
P7	M-NSG-4.2-10-1	59.0	56.2	2.20	169
P8	M-NSG-4.2-10-2	53.3		2.80	166
P9	M-NSG-7.2-10-1	59.0	67.2	2.30	162
P10	M-NSG-7.2-10-2	75.3		2.44	164
P11	M-NSG-4.8-7.5-1	60.5	59.4	3.49	163
P12	M-NSG-4.8-7.5-2	58.3		3.43	163
P13	M-NSG-4.8-5-1	41.0	44.8	2.36	163
P14	M-NSG-4.8-5-2	48.5		3.02	160

3.5.1. Failure mode

All specimens failed by IC debonding, which is characterised by the formation of wedges ('herringbone cracks') at the face of the prism along the bonded length (Figure 3-2(a)). The propagation of diagonal cracks in the masonry commenced from the loaded end and propagated to the unloaded end, indicating a gradual redistribution of the shear bond stress along the strip at the FRP-to-masonry interface. From the results it can be noted that the development of the crack pattern and debonding failure plane were similar to those seen in FRP-to-concrete pull tests, confirming the similarity between the load transfer mechanism of FRP-to-masonry joints and FRP bonded to concrete.

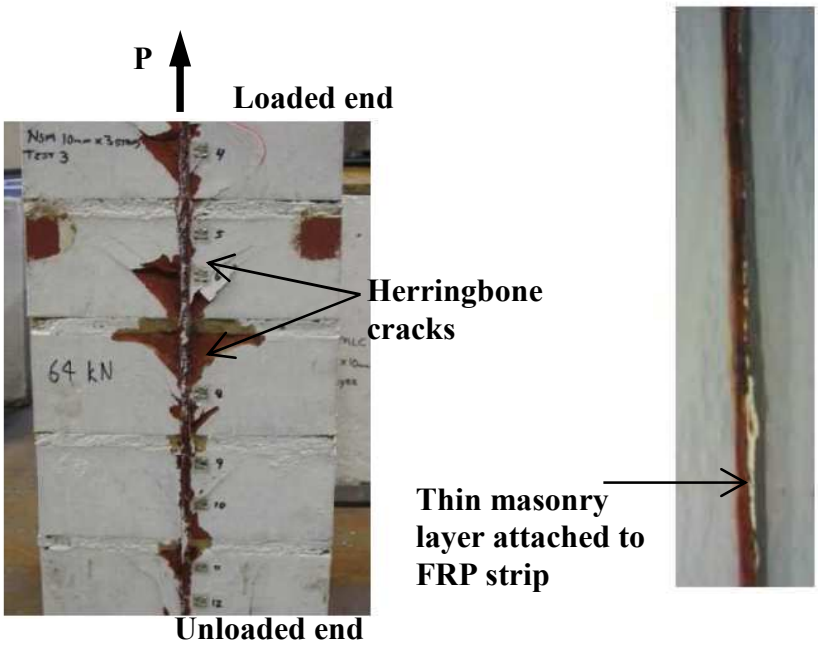

Figure 3-2: Debonding failure in pull test specimen

The load-slip (P-Δ) response at the loaded end is shown in Figure 3-3 for the four monotonically loaded specimens that contained 3.6x10 mm NSM strip (test specimens P1 to P4). For all four specimens, progressive damage in the FRP-to-masonry joints was indicated through reduced stiffness of the load-slip response with increasing load. Prior to failure, significant diagonal cracking had occurred in the masonry (Figure 3-2(a)) (step-wise through each brick unit, interrupted by the mortar

bed joints), demonstrating significant stress transfer into the masonry substrate and 'good' bond at the FRP-to-masonry interface. It should be noted that all the specimens were tested until failure. As the load dropped almost immediately to near zero after failure, the descending branch was not included in the experimental plots (Figure 3-3 - Figure 3-6).

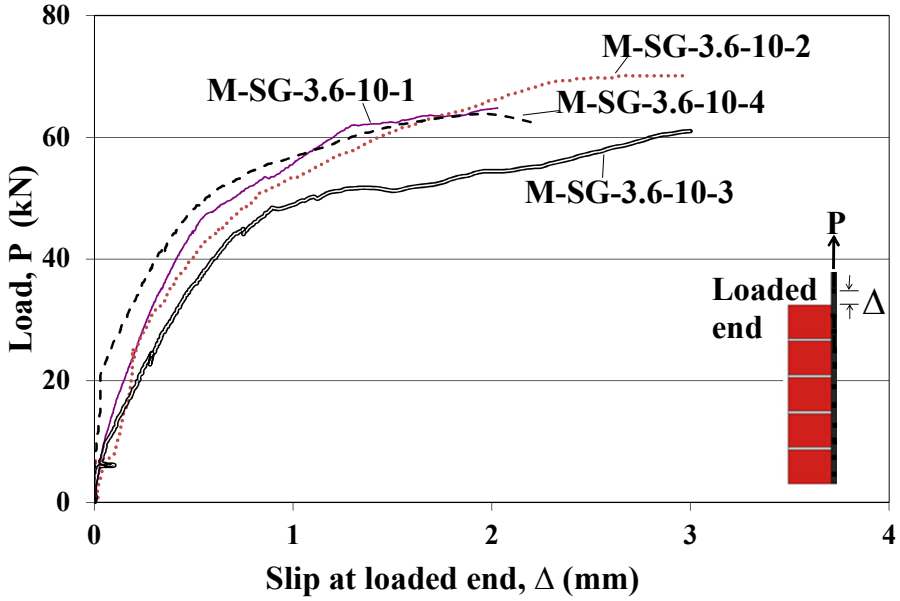

Figure 3-3: Load-slip response for monotonic specimens (P1 – P4) with 3.6 mm wide FRP strip

The ultimate failure plane was mostly within the masonry, near the masonry-to-adhesive interface as evidenced by a very thin layer of masonry being detached from the masonry prism as shown in Figure 3-2(b). This observation suggests that the bonding characteristics of FRP-to-masonry are closely related to the tensile strength of the masonry unit (f_{ut}) and are consistent with the findings reported by Seracino et al. (2007) for NSM FRP-concrete bond pull tests. From Figure 3-3 it is evident that there was reasonable consistency between the overall behaviour of these four pull test specimens.

3.5.2. Effect of cyclic loading

Figure 3-4 shows the effect of cyclic loading on load-slip behavior of FRP retrofitted masonry. The global load-slip (P-Δ) response of the two specimens subjected to cyclic loading (P5 and P6) (Figure 3-4) closely trace the average P-Δ curve for the

four monotonically loaded specimens (P1 – P4) shown previously in Figure 3-3. This observation suggests that cyclic loading does not significantly affect the overall behaviour of the FRP-to-masonry bond. The small reduction in strength that was observed after each loading-unloading cycle indicates that strength degradation of the bond was cumulative. Similar behaviour was observed in a study by Konthesingha et al. (2009). However, it was noted that these relatively small differences in strength and deformation capacity for the pull test specimens could also be due simply to material variability (30% is typical for masonry tests, e.g., Drysdale et al. 1994).

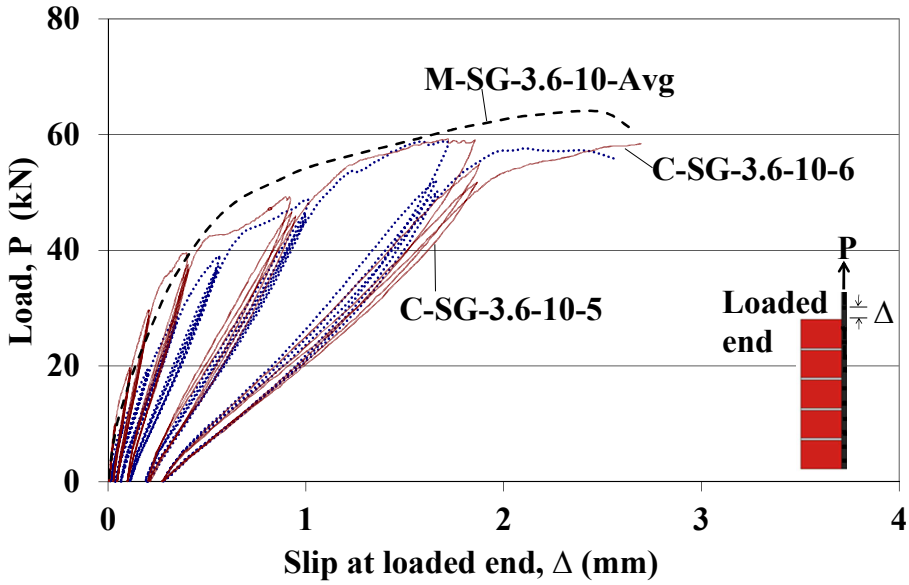

Figure 3-4: Effect of cyclic loading on load-slip response

3.5.3. Effect of FRP strip dimensions

As seen in Table 3-3 and Figure 3-5, no significant improvement in load-slip behaviour was observed when the thickness of the FRP strip, t_p, was varied from 3.6 mm to 7.2 mm (Specimen P7 –P10 and mean of P1 - P4). This was not too surprising since the "total bonded circumference/area" of the three configurations did not differ significantly. In contrast, increasing the depth of the FRP strip, (b_p) (measured into the masonry), was found to be effective in enhancing the debonding load (P_{exp}) (Figure 3-6). Considering the average value of P_{exp} (Table 3-3), increasing the depth from 5 mm to 7.5 mm resulted in about a 33% increase in the maximum

load (Figure 3-6). Most of this strength increase can be attributed simply to the 27% increase in the perimeter of the debonding failure plane, L_{per}, for specimens with a 7.5 mm deep strip (L_{per} = (4.8+2) mm + 2 x (7.5+1) mm = 23.8 mm) compared to specimens with a 5 mm deep strip (L_{per} = (4.8+2) mm + 2 x (5+1) mm = 18.8 mm). The remainder of the strength increase is probably due to more efficient confinement of the surrounding masonry for the deeper cut needed for the 7.5 mm strip.

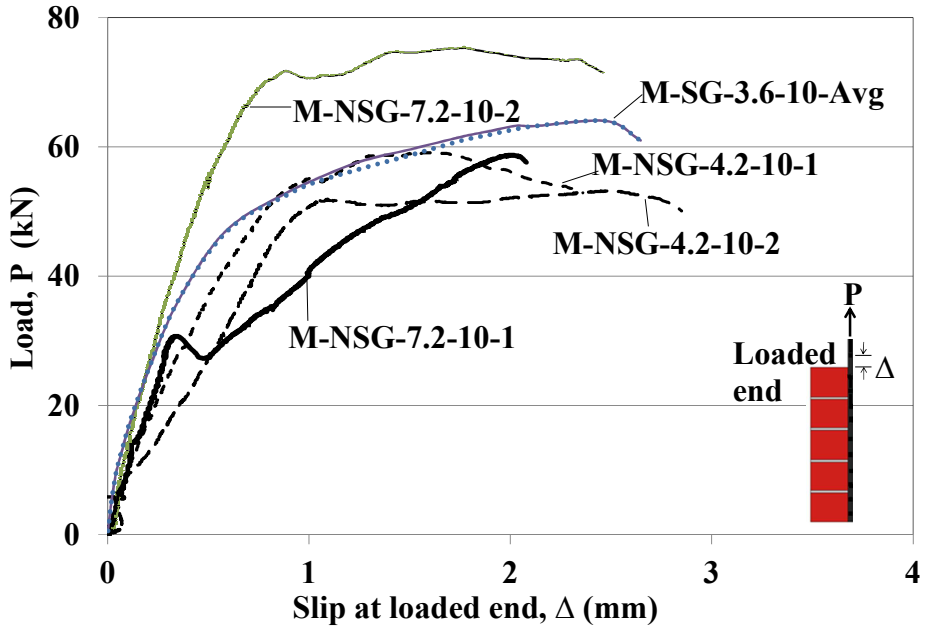

Figure 3-5: Effect of width of FRP strip on load-slip response

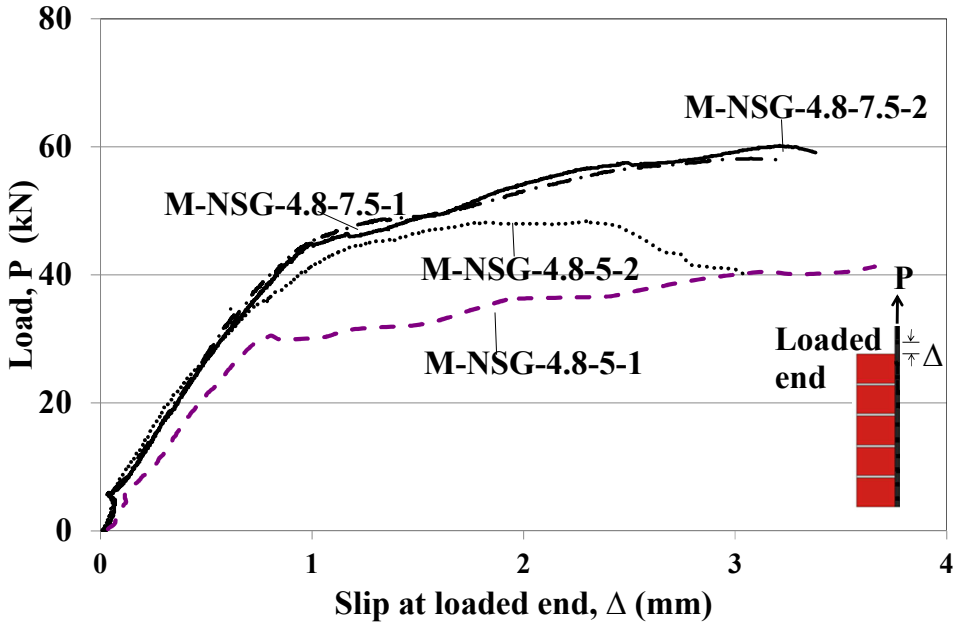

Figure 3-6: Effect of depth of FRP strip on load-slip response

3.5.4. Interface Behaviour

All six pull test specimens (Tests P1 – P6) showed similar trends in their strain and shear stress distribution . Hence, in this section the interface behavior is discussed in detail for only one specimen (P1). Results for the other 5 specimens (Tests P2 –P6) are included in the Appendix §C.2.

Axial strain distribution

A typical example of the axial strain distribution along an FRP strip with increasing load is shown in Figure 3-7 for specimen M-SG-3.6-10-1 (P1). The strain at the loaded end increased with increasing levels of applied load and eventually began to plateau out to a value of about 10,500 με at the maximum load P_{exp} of 64.8 kN.

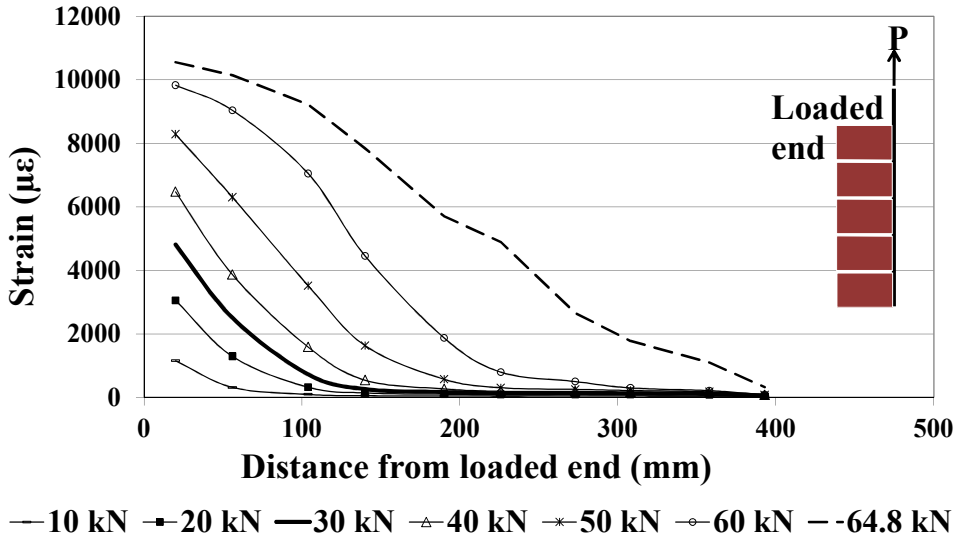

Figure 3-7: Typical FRP strain distribution (Specimen P1)

The strain plateau represents debonding at that point of the FRP strip, as there is no further significant change in strain, indicating little transfer of shear across the FRP-to-masonry interface. The position along the bonded length where the strain has reduced to near zero corresponds to the location at which the applied load has been entirely transferred from the FRP to the masonry through interface bond. This behaviour is evident in Figure 3-7 for loads up to 60 kN. At a load of 64.8 kN, it is evident that the strain is no longer zero at the last gauge and therefore, the force had not been fully transferred to the masonry over the bonded length between this point

and the loaded end, i.e. the debonding crack had propagated along the entire length of the FRP strip. At this point, the FRP could not resist any more load and shortly afterwards the specimen failed.

Shear stress distribution

Figure 3-8 shows the shear stress distribution for Test No.P1 (typical of all tests P1 - P6) along the bonded length for increasing load. The strain gauge data was used to study the force transfer mechanism from the FRP to the masonry through the shear bond stress acting at the FRP-masonry interface, for all the specimens with strain gauges, using Eq. 3-1.

$$\tau_{avg} = \frac{(\Delta\varepsilon)E_p b_p t_p}{(\Delta L)(2b_p + t_p)} \qquad \text{Eq. 3-1}$$

where, τ_{avg} = average shear stress over the length ΔL; $\Delta\varepsilon$ = change in strain over length ΔL; E_p = modulus of elasticity of the FRP strip; b_p = depth of strip; t_p = thickness of strip; and ΔL = incremental length along the FRP (equal to strain gauge spacing).

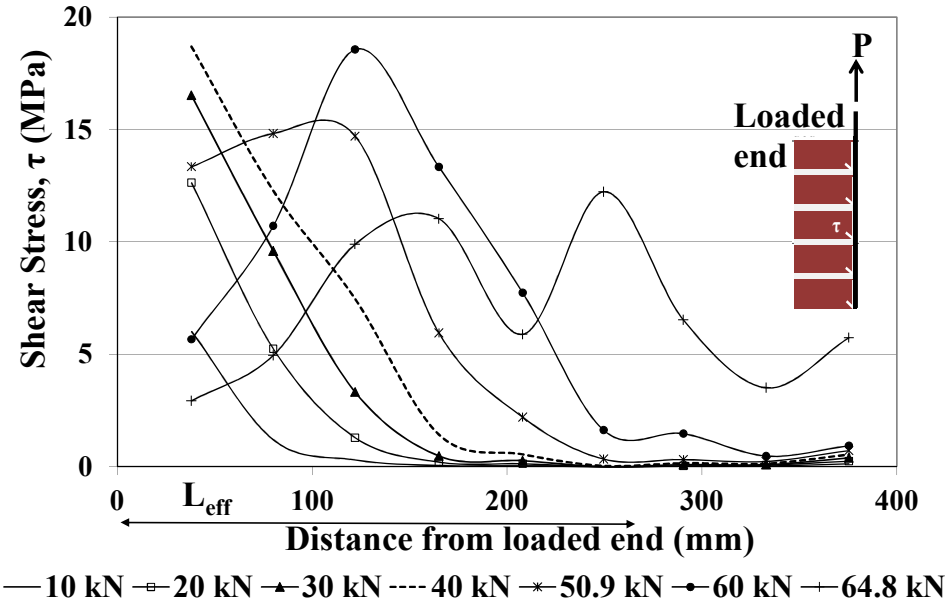

Figure 3-8: Typical interface shear-stress distribution (Specimen P1)

The shear stress at the loaded end initially increases with applied load until the maximum local bond shear stress is reached when the load is 40 kN. After this point there is a reduction in the magnitude of the shear stress as micro-cracking develops at the loaded end and begins to propagate along the FRP strip towards the unloaded end (Figure 3-8). With further loading, the location of the maximum shear stress shifts away from the loaded end, to the right in this case, as observed in FRP-to-concrete pull tests (Seracino et al. 2007a). The shear stress distribution also provides an experimental indication of the effective bond length, L_{eff}, (Figure 3-8) which is the length of bonded FRP required to develop the maximum IC debonding load (P_{IC}). The effective bond length ranged between 250 mm to 300 mm for all the specimens in this study.

Local Bond-slip behaviour

As mentioned in §3.4, six specimens (Tests P1 – P6) were strain gauged along the FRP strip. Figure 3-9 shows the local bond-slip response at various strain gage locations (measured from the loaded end).The differences between the local bond-slip response (Figure 3-9) for the six specimens was most likely due to: (1) the varying spacing between strain gauges, (2) the location of cracking relative to the strain gauges, and/or (3) the variation in the tensile strength of the bricks (f_{ut}). As shown in Figure 3-9, the load transfer mechanism at the FRP-to-masonry interface is similar to that of FRP-to-concrete (Seracino et al. 2007a) and can be represented in three stages, i.e. elastic, micro-cracking (softening) and macro-cracking (debonding). In the elastic stage, the shear-stress in the FRP-to-masonry interface increases until the peak shear stress, τ_{max}, is reached at local slip δ_1. This elastic stage is followed by a softening region as micro-cracking develops and the shear stress decreases to zero at a slip of δ_{max} beyond which macro-cracking occurs and the debonding interface is no longer capable of transferring force. An idealized bilinear model was fitted to the experimental data as shown by the dashed line in Figure 3-9. For the bilinear model, the peak shear stress, τ_{max} and corresponding slip, δ_1 were averaged from the experimental bond-slip curves whereas δ_{max} was back calculated using Eq. 2.1 with P_{IC} equal to the maximum experimental load, P_{exp}.The experimental values of the local bond-slip parameters ($\tau_{max,}$ δ_{max} and $\delta_{1)}$ for these specimens are summarised and

listed in Table 3-4 where τ_{max} is the maximum interfacial shear stress; δ_{max} is the maximum interfacial slip and δ_1 refers to the slip corresponding to the maximum load.

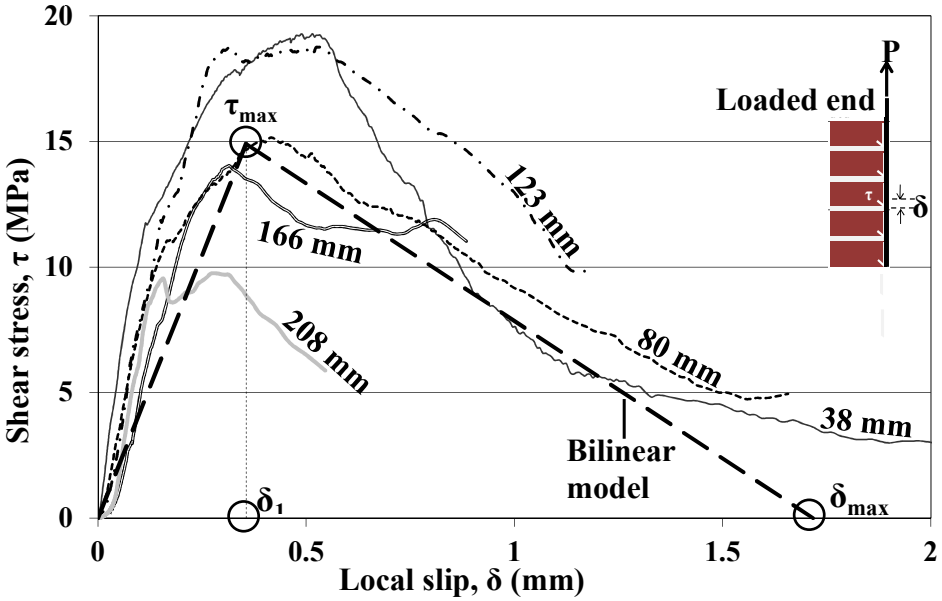

Figure 3-9: Local bond-slip relationship (Specimen P1)

Table 3-4: Bond-slip parameters for pull test

Specimen No	τ_{max} (MPa)	δ_{max} (mm)	δ_1 (mm)
M-SG-3.6-10-1	14.92	1.72	0.36
M-SG-3.6-10-2	15.16	1.97	0.43
M-SG-3.6-10-3	14.69	1.54	0.32
M-SG-3.6-10-4	14.53	1.70	0.55
C-SG-3.6-10-5	13.83	1.52	0.37
C-SG-3.6-10-6	14.98	1.42	0.45

3.6. Summary and closing remarks

Fourteen NSM FRP-to-masonry pull tests were conducted to assess the effect of cyclic loading and FRP strip dimensions on FRP-to-masonry joint behaviour. All specimens failed by "IC" debonding. The pull test results indicated that increasing the depth, b_p of the NSM FRP strips (measured perpendicular to the face of the

masonry) was more effective at enhancing the debonding resistance of a FRP-to-masonry joint than was increasing the thickness, t_p of the FRP strip because of the more substantial increase in L_{per} for specimens with a deeper strip as well as more efficient confinement provided by the surrounding masonry. From the two cyclic tests conducted, it appears that cyclic loading has only a minor effect on the bond.

CHAPTER 4
PULL TESTS NUMERICAL STUDY

4.1. Introduction

This Chapter presents the results of a numerical investigation into the local bond behaviour at the FRP-masonry interface. First, a new analytical model is derived to give a lower bound prediction of the IC debonding resistance of FRP-to-masonry joints from a large database of FRP retrofitted masonry pull test conducted by various researchers over the past 10 years. Next, empirical expressions are developed for the key local bond-slip parameters such as peak interface shear-stress, τ_{max} and maximum local slip, δ_{max}. The new model is then compared with fifteen existing theoretical bond strength models reported in the open literature.

Two analytical procedures, namely a new generic numerical procedure and a closed-form mathematical solution, are developed to predict the global load-slip (P-Δ) response of FRP-to-masonry pull tests using empirical expressions for the local bond-slip parameters developed in the first part of this chapter. The analytical results from both models have been validated against the test data. The chapter concludes with recommendations regarding the influence of the heterogeneous nature of masonry and the effect of the bond-slip parameters on the global load-slip response of FRP-to-masonry pull tests.

4.2. Empirical model

From the assessment of the existing bond strength models presented in §2.4.2, it was seen that there is a need for a new model to accurately predict the bond strength of FRP-to-masonry joints. The generic model of Seracino et al. (2007b) for defining P_{IC} was considered as the starting point for development of a new model. Seracino et

al.'s (2007b) model for concrete is a function of the cylinder compressive strength, f_c, which was originally incorporated to represent the principal tensile stress that resulted in the interface debonding cracks. The corresponding material property for masonry is the flexural tensile strength of the masonry unit, f_{ut} which is a value used widely in design and so is readily available for use in an expression of P_{IC}.

It is known that the debonding strain is higher for a NSM strip than for an EB strip due to its large bonded surface area and better confinement. Therefore, to account for the type of retrofitting technique (i.e. EB or NSM) it was assumed that $\tau_{max}\delta_{max}$, which is twice the fracture energy, G_f (area under the local bond-slip curve), is a function of the geometric property, φ_f of the FRP strip (defined earlier in §2.4.2). Since the debonding cracks are initiated within the masonry, $\tau_{max}\delta_{max}$ was assumed to also be a function of the tensile strength of the masonry, f_{ut} (Seracino et al. 2007b). Hence, the following expression can be written:

$$\tau_{\max}\delta_{\max} = C\varphi_f^m f_{ut}^n \qquad \text{Eq. 4-1}$$

4.2.1. New Generic Model

In order to derive values for *C*, m and n in Eq. 4-1, a value of $\tau_{max}\delta_{max}$ was calculated for each test specimen in the pull-test database by substituting P_{exp} into Eq. 2-1 and solving for $\tau_{max}\delta_{max}$. A statistical analysis was then undertaken to determine optimal values for the constants C, m and n using the data for 109 specimens from the database (Table A-1, Appendix §A.2) and the 14 new pull test results (Table 3-3). The parameters C and m were determined from linear regression, with n varied incrementally until the lowest coefficient of variation was identified, as shown in Figure 4-1.

Eq. 4-2 was obtained from this process and is represented graphically in Figure 4-2. The data points clustered on the left end of the graph are results for EB test specimens and those on the right end are for NSM test results.

$$(\tau_{\max}\delta_{\max})_{Generic} = 3.94\varphi_f^{0.38} f_{ut}^{0.94} \qquad \text{Eq. 4-2}$$

By substituting Eq. 4.2 into Eq. 2-1, a generic expression was derived for the IC debonding resistance, P_{IC}, given by Eq. 4-3 in terms of the conventional design parameters, f_{ut}, for masonry and the other standard parameters for an FRP section.

$$(P_{IC})_{Generic} = 1.99\varphi_f^{0.19} f_{ut}^{0.47} \sqrt{L_{per}(EA)_p} \quad \text{Eq. 4-3}$$

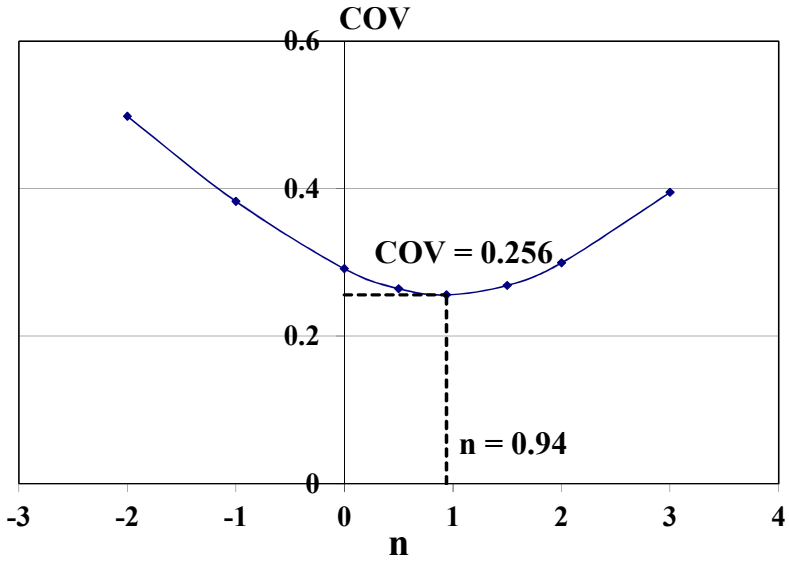

Figure 4-1: Determining exponent of f_{ut} (n) by comparison with COV

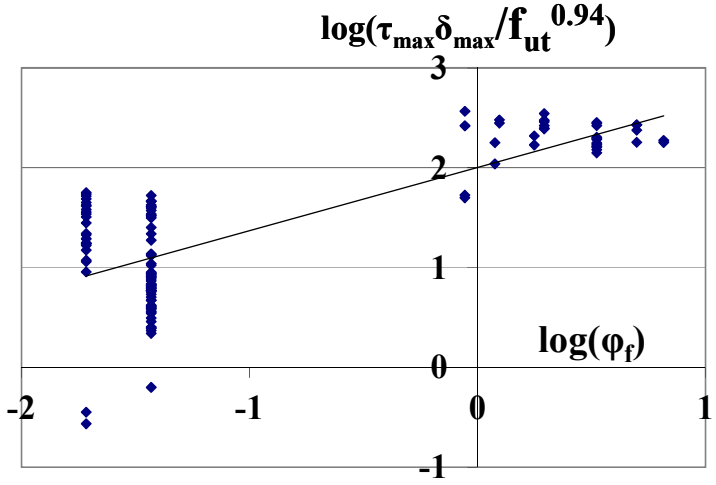

Figure 4-2: Statistical analysis for key bond-slip parameters

The predictions of the new generic model Eq. 4-3 compared with the 123 test results of the present database (Table 3-3 and Table A-1) are shown in Figure 4-3. A value greater than one for the test-to predicted bond strength ratio (P_{exp}/P_{IC}) (i.e. above the

line in Figure 4-3) signifies a conservative (under-) estimate of bond strength. As shown in Table 4-1(a), the experimental and the predicted bond strengths agreed reasonably well with mean, COV, and linear regression correlation coefficient of the test-to-predicted strength ratios being 1.036, 25.6% and 0.922, respectively.

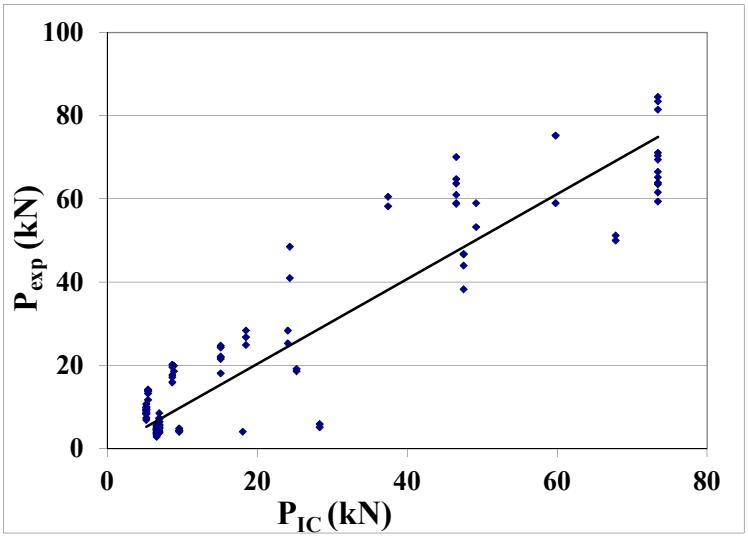

Figure 4-3: Comparison of P_{exp} and P_{IC} using new generic model

Table 4-1: Bond strength ratios P_{exp}/P_{IC} for new models

Model	Mean	Median	Max	Min	SD	COV	Correlation
a) All specimens (N = 123)							
New Generic (Eq. 4-3)	1.04	1.03	1.63	0.38	0.27	0.26	0.92
(b) EB Specimens only (N = 89)							
New EB specific (Eq. 4-5)	1.03	1.01	1.54	0.57	0.25	0.24	0.88
New Generic (Eq. 4-3)	1.03	1.05	1.56	0.38	0.27	0.27	0.88
(c) NSM Specimens only (N = 34)							
New NSM specific (Eq. 4-7)	1.01	1.01	1.27	0.67	0.14	0.13	0.73
New Generic (Eq. 4-3)	1.02	0.98	1.63	0.73	0.23	0.23	0.61

Note: N is the number of specimens used to calibrate each of the models

Although Eq. 4-2 is valid for both EB and NSM pull tests, it was considered important to further investigate the EB and NSM specimens separately to identify the sensitivity of the new generic P_{IC} expression (Eq. 4-3) to consideration of the database in subsets, and whether further improvements of the new generic model could be achieved.

4.2.2. New EB Specific Model

When considering a model specific to EB FRP strips, 89 tests results were available out of the total of 109 tests listed in Table A-1. This subset of the data was used to determine $\tau_{max}\delta_{max}$ giving Eq. 4-4 for calculating the bond strength of EB FRP strips in masonry. The same method used for generic equation was applied to calibrate the constants *C,* m and n (Eq. 4.4) for 89 EB test results giving Eq. 4-4 and Eq. 4-5. The statistics of the P_{exp}/P_{IC} ratios for the EB specific model is given in Table 4-1(b).

$$(\tau_{\max}\delta_{\max})_{EB} = 187.40\varphi_f^{1.69} f_{ut}^{1.80} \quad \text{Eq. 4-4}$$

$$(P_{IC})_{EB} = 13.69\varphi_f^{0.84} f_{ut}^{0.90} \sqrt{L_{per}(EA)_p} \quad \text{Eq. 4-5}$$

The correlation coefficient for the EB model is 0.88 and the mean value is close to one (Table 4-1(b)), which demonstrates that the 'EB specific' bond strength model predicts the trends of the test data reasonably well. Further, it was noted that the values of the constants *C*, m and n in the new generic expression (Eq. 4-3) and the EB expression (Eq. 4-5) are significantly different in spite of the commonly assumed form for the relationship between fracture energy and aspect ratio and masonry unit tensile strength. Moreover, when the new generic model (Eq. 4.6) was used to predict the bond strength for only EB specimens from the database, the correlation coefficient was only slightly lower and the COV was only slightly higher than for the 'EB specific' model as shown in Table 4-1(b). Hence, while the EB specific model provides reasonable estimate of the bond strength, it does not appear to be any more accurate or reliable than the new generic model.

4.2.3. New NSM specific model

In a similar fashion, the 34 NSM specimens from the database (Table 3-3 and Table A-1) were used to calibrate the constants *C*, m and n in Eq. 4-1 in order to define a bond strength model specific to the NSM technique. The final expression is given by Eq. 4-7.

$$(\tau_{\max}\delta_{\max})_{NSM} = 6.94\varphi_f^{-0.24} f_{ut}^{0.94} \quad \text{Eq. 4-6}$$

$$(P_{IC})_{NSM} = 2.63\varphi_f^{-0.12} f_{ut}^{0.47} \sqrt{L_{per}(EA)_p} \quad \text{Eq. 4-7}$$

From Table 4-1(c) it can be observed that the average value of the P_{exp}/P_{IC} ratio for the NSM model (Eq. 4-7) is close to one and the COV is about 0.133. Further, by comparing the generic (Eq. 4-3), EB (Eq. 4-5) and NSM (Eq. 4-7) models it can be noted that the constants *C*, m and n were significantly different for each model, possibly reflecting the difference between the EB and NSM applications. It is interesting to note that there is a negative (-) exponent on φ_f in Eq. 4-6 and Eq. 4-7. This exponent is small in magnitude which possibly implies that the FRP strip aspect ratio does not strongly affect the bond performance. Due to the relatively small size of the data set available (N = 34), there seems to be scope for further improvements in Eq. 4-6 and Eq. 4-7 as the NSM bond tests data set increases. Moreover, the results for the new generic model, when applied to only NSM specimens, were only slightly less accurate than those obtained using the 'NSM specific' model' (Table 4-1(c)). Given the versatility of the new generic expression over the NSM specific expression, the new generic expression is preferred.

4.2.4. New local bond-slip model

The parameters, τ_{max} and $\delta_{max,}$ from the pull test data are the principal parameters for the numerical investigation of FRP strengthened structures and are needed to calculate the critical bond length, L_{eff} (Eq. 2-2). Hence, the statistical analysis was extended to determine an empirical expression for $\tau_{max.}$ Reported values of τ_{max} (for 20 tests) were plotted against φ_f and the data was analysed using power regression. The resulting expression for τ_{max} is given by Eq. 4-8 and is graphically represented in

Figure 4-4. There is good agreement between the experimental and the predicted values of τ_{max} with mean of 1.01 and a correlation coefficient of 0.89. Note, that τ_{max} and δ_{max} are functions of both the masonry unit tensile strength and the aspect ratio of the FRP strip. This conclusion differs from that reported by Seracino et al. (2007b) for concrete where δ_{max} was expressed as a function of the aspect ratio only. It should be noted that the above expressions for τ_{max} (Eq. 4-8) and δ_{max} (Eq. 4-9) are based on a relatively small data set (N = 20) so that in spite of the good statistical correlation of the regressed curve in Figure 4-4, there is potential for alternate expressions and further improvements as the data set increases.

$$\tau_{\max} = 8.83\varphi_f^{0.15} f_{ut}^{0.2} \qquad \text{Eq. 4-8}$$

Eq. 4-2 can then be divided by Eq. 4-8 to generate the following expression for δ_{max}:

$$\delta_{\max} = 0.45\varphi_f^{0.23} f_{ut}^{0.74} \qquad \text{Eq. 4-9}$$

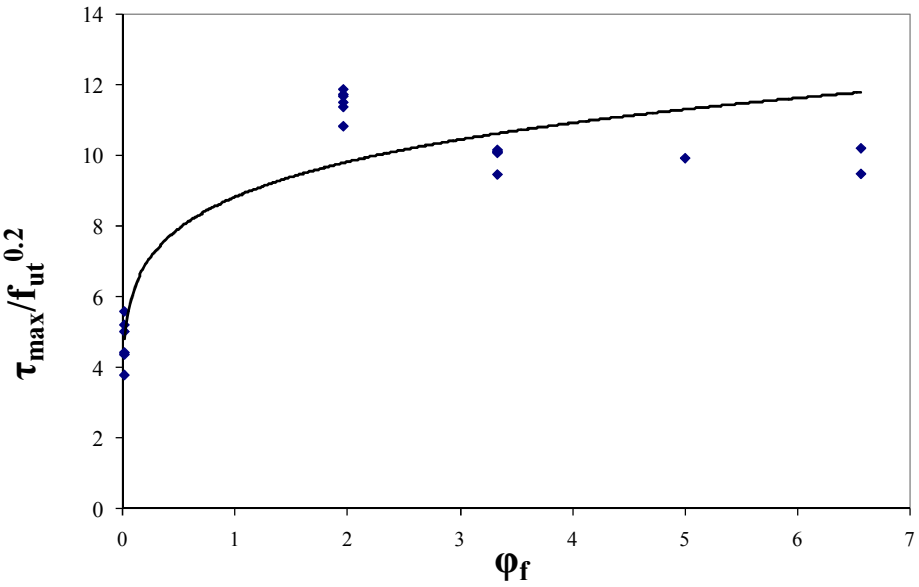

Figure 4-4: Statistical analysis for τ_{max}

4.2.5. Comparison of existing bond strength models and new generic model

In this section, predictions by the existing bond strength models (§2.4.2) and the new models developed in this study (§4.2.1 to §4.2.3) were compared. Figure 4-5 compares the model by Willis et al. (2009b) with the new generic model (Eq. 4-3),

considering results from both NSM and EB specimens given in the complete test database of 123 specimens. It is clear that the new generic model is more accurate than the model by Willis et al. (2009b) suggesting that equations developed for concrete (e.g. Eq. 2 1) cannot be applied directly to masonry by simply substituting f'_c with the corresponding tensile masonry strength (f_{ut}).

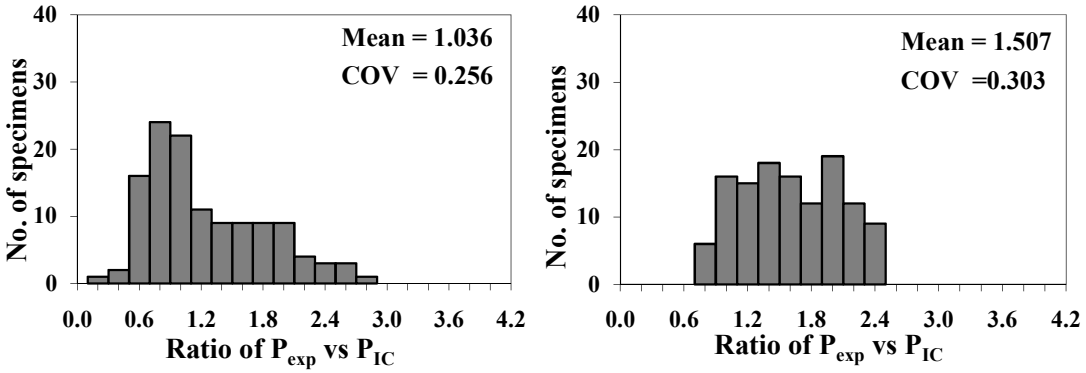

(a) New generic model **(b) Willis et al. (2009b)**

Figure 4-5: Effectiveness of bond strength models for all specimens

For the EB specimens the new generic model gives better estimates of the bond strength, with a mean value for the P_{exp}/P_{IC} ratio being close to unity and a COV value of approximately 25% (Table 4-1(b)). From Figure 4-6 it can be seen that the new generic model (Figure 4-6(b)) is more accurate as compared to the four best performing existing models (Figure 4-6(c-f)) mentioned previously. While the model by Lu et al. (2005) gives results that are close to the new generic model, the new generic model is chosen due to its simple form. Figure 4-7 gives similar comparisons between the new generic model (Figure 4-7(b)) and pre-existing expressions (Figure 4-7(c and d)) applicable to NSM specimens. It was concluded that the new generic model is more accurate than the existing models with reasonably low COV values (of about 25%).

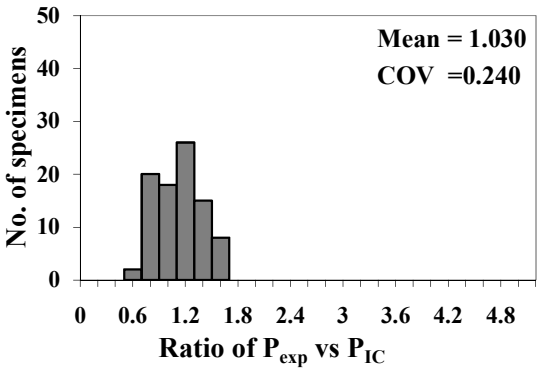

(a) New EB specific model

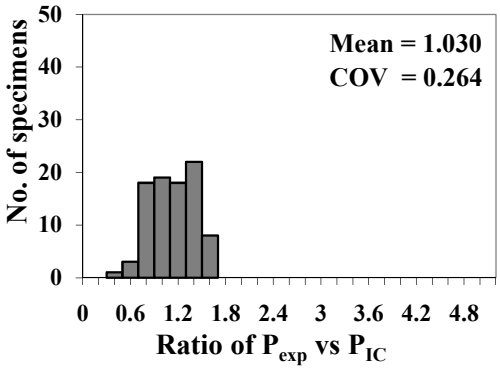

(b) New generic model

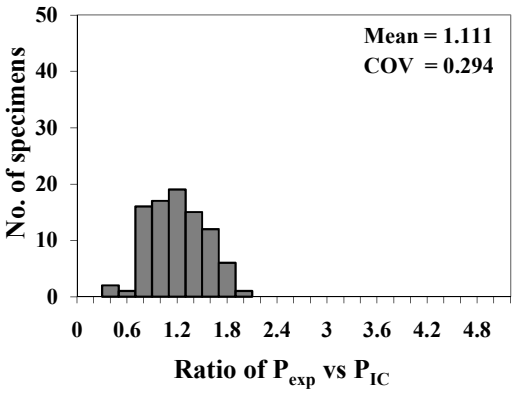

(c) Karbhari et al. (2006)

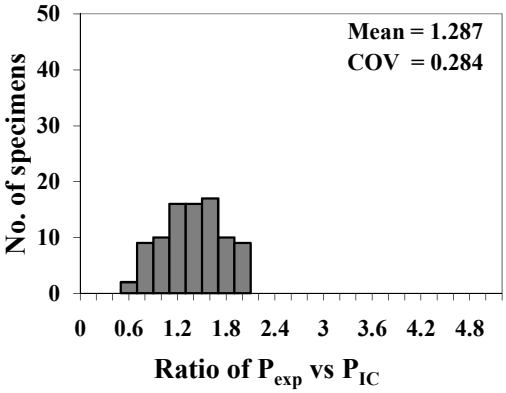

(d) Milani et al. (2009)

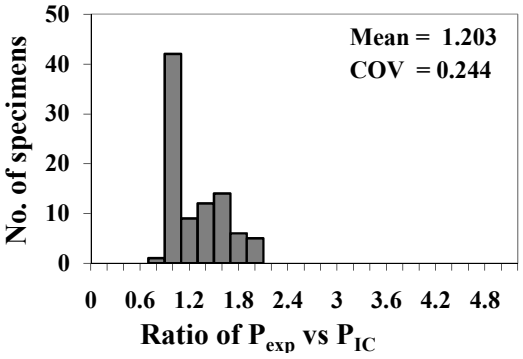

(e) Lu et al. (2005)

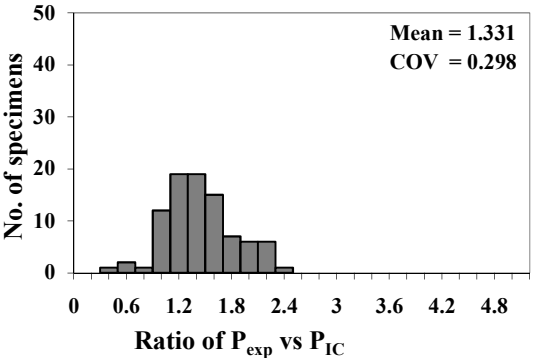

(f) Maeda et al. (Chen and Teng, 2001))

Figure 4-6: Effectiveness of bond strength models for EB specimens

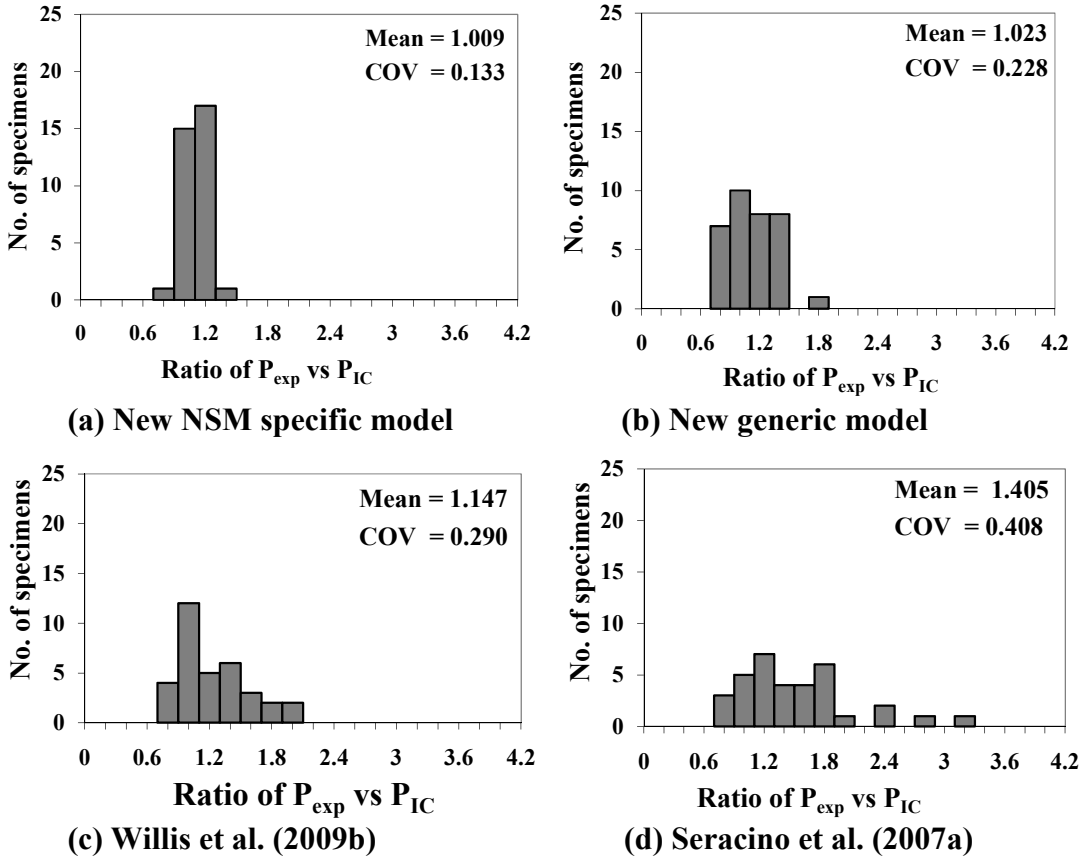

Figure 4-7: Effectiveness of bond strength models for NSM Specimens

4.3. Modelling of FRP-to-Masonry Pull Tests

Two analytical procedures, i.e. a numerical procedure and a closed-form mathematical solution were developed to predict the global load-slip response of FRP-to-masonry pull tests. These procedures account for the slip-strain (*ds/dx)* that is the relative slip between the FRP and adjacent substrate at the interface and hence, are expected to accurately model the true behaviour of retrofitted members.

4.3.1. Input data for modelling

The analytical procedures use the material and geometrical properties of the FRP and masonry, and the local bond-slip (τ-δ) models as input data. The key parameters (i.e. maximum interface shear stress, τ_{max} and maximum interface slip, δ_{max}) for the analysis were calculated using Eq. 4-8 and Eq. 4-9 from §4.2.4. Interestingly, a value of $\delta_1 = 0.33$ for the slip corresponding to the maximum interface shear stress was

found to be fairly consistent for all the pull tests reported above. Hence, this value was used for all the subsequent analyses reported in this study. However, the applicability of this value for a wider range of masonry, FRP and epoxy adhesive types requires further investigation.

Further, different τ-δ models (discussed in §2.4.1)**,** such as rigid-softening, elastic-softening and non-linear, were used as input data to study their effect on load-slip behaviour of FRP-to-masonry bonded joints. As observed in Figure 2-5, the ascending branch of the rigid-softening model is much stiffer in comparison to the elastic-softening and the non-linear model which affects the initial slope of the global P-Δ response and hence, the accuracy of the numerical results (Xia and Oehlers 2006). It has been stated by some researchers (Yuan et al. 2004; Haskett et al. 2008) that the local τ-δ relationship for FRP-to-concrete is accurately modelled by an elastic-softening model. However, it was considered important to investigate the accuracy of the prediction versus complexity of the different τ-δ models for FRP-to-masonry interface.

4.3.2. Numerical Model

Model description

Figure 4-8 gives a schematic representation of the iterative procedure used in the analysis. The numerical procedure is generic as it can accommodate any: local τ-δ characteristic, type and shape of axial reinforcement, length of embedment of FRP, and cross-sectional area of the substrate. Also, it does not depend on strain gauge data along the bonded strip which in some cases can affect the bond at the FRP-to-masonry interface. The procedure uses the local τ-δ model as input data and is driven by displacement-control (i.e. increments of strain are applied for which a guess of the slip is made for each iteration). The procedure is based on the numerical procedure developed by Haskett et al. (2008) to study bond along steel reinforcing bars embedded in concrete. It has been suitably modified for its application to masonry to account for its heterogeneous nature.

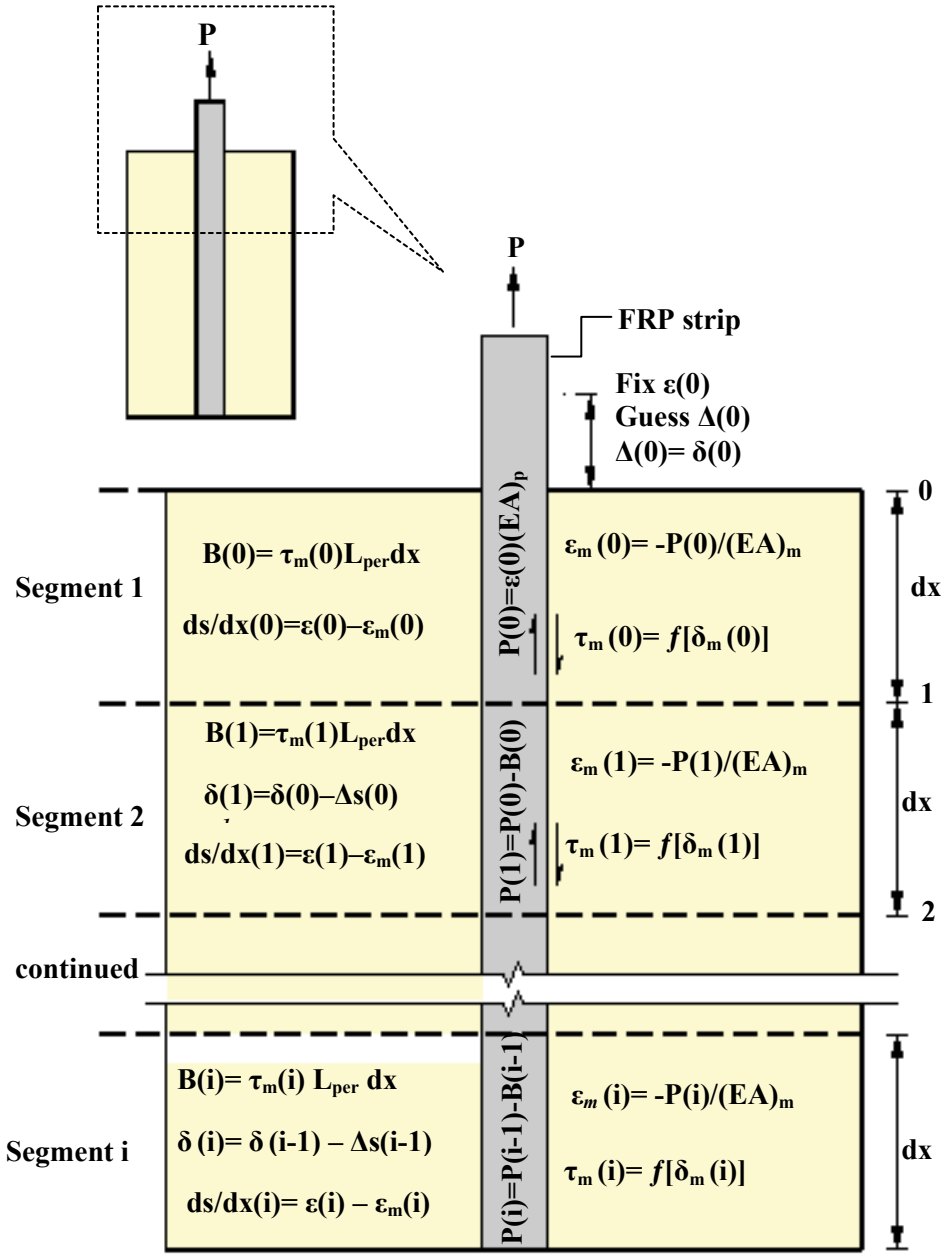

Figure 4-8: Schematic of the homogeneous numerical model for pull test

The following algorithm is used for the numerical procedure shown in Figure 4-8:

- A tensile strain in the FRP is fixed at the loaded end at Position 0, $\varepsilon_p(0)$ and, hence the force in the FRP, $P(0)$, can be determined from the σ-ε relationship of FRP. The corresponding compression strain in the masonry is $\varepsilon_m(0) = -P(0)/(EA)_m$, where $(EA)_m$, is the axial rigidity of the masonry (E_m being the elastic modulus of masonry and A_m being the cross-sectional area of masonry).

- For this fixed strain, $\varepsilon_p(0)$, and force, $P(0)$, a slip at the loaded end, $\Delta(0) = \delta(0)$, is guessed.
- The bond stress, $\tau_m(0)$, corresponding to the guessed slip is derived from local τ-δ model for masonry.
- The bond force acting over the first segment length, dx is given by $B(0) = \tau_m(0)\, L_{per} dx$, where $L_{per} = 2d_f + b_f$, is the perimeter of the failure plane and d_f and b_f are the lengths of the failure plane perpendicular and parallel to the masonry surface, respectively, which are assumed to lie 1mm away from the surface of the FRP strip (as shown previously in Figure 2-7).
- Therefore, the load in the FRP at the end of the first segment is $P(1) = P(0) - B(0)$.
- The corresponding strain in the FRP is $\varepsilon_p(1) = P(1)/(EA)_p$, where $(EA)_p$, is the axial rigidity of the FRP (E_p is the elastic modulus of FRP and A_p is the cross-sectional area of FRP) and the corresponding strain in the masonry at the end of the first segment is $\varepsilon_m(1) = -P(1)/(EA)_m$.
- The slip strain in the first segment is $ds(0)/dx = \varepsilon_p(0) - \varepsilon_m(0.)$.
- By integration, the change in slip over the first segment is $\Delta s(0) == \int \frac{ds(0)}{dx} \cdot dx$.
- Hence, the slip at the beginning of the second segment is $\delta(1) = \delta(0) - \Delta s(0)$.

This procedure is repeated over the subsequent segments until the two boundary conditions at the unloaded end are achieved that is, both slip-strain and slip are zero. It should be noted that these conditions are applicable for infinite bond length. In case of finite bond lengths, the boundary condition is ε = 0 at the free end. An example has been included in the Appendix §D.2 to illustrate the numerical procedure. This procedure was also followed for a heterogeneous simulation of the brick and mortar components of masonry by using separate moduli of elasticity and τ-δ bond characteristics for the segments spanning the mortar joints and brick units, respectively. The numerical procedure was carried out using a segment length of 1 mm (refer to Appendix §D.2 for sample calculations). From the analysis, it was noted that the segment length does not influence the accuracy of the load-displacement response to a great extent. The difference in load/displacement ranges between 0 - 8% for segment lengths of 1 mm to 10 mm for the sample specimen

considered in this study. It is however recommended that smaller segment length should be considered for analysis.

Homogeneous and heterogeneous numerical procedures

The PI numerical procedure used in this study investigated the use of a homogeneous analysis (Figure 4-8) with masonry material properties and a heterogeneous analysis with disparate material properties for the mortar and brick unit (Figure 4-9).

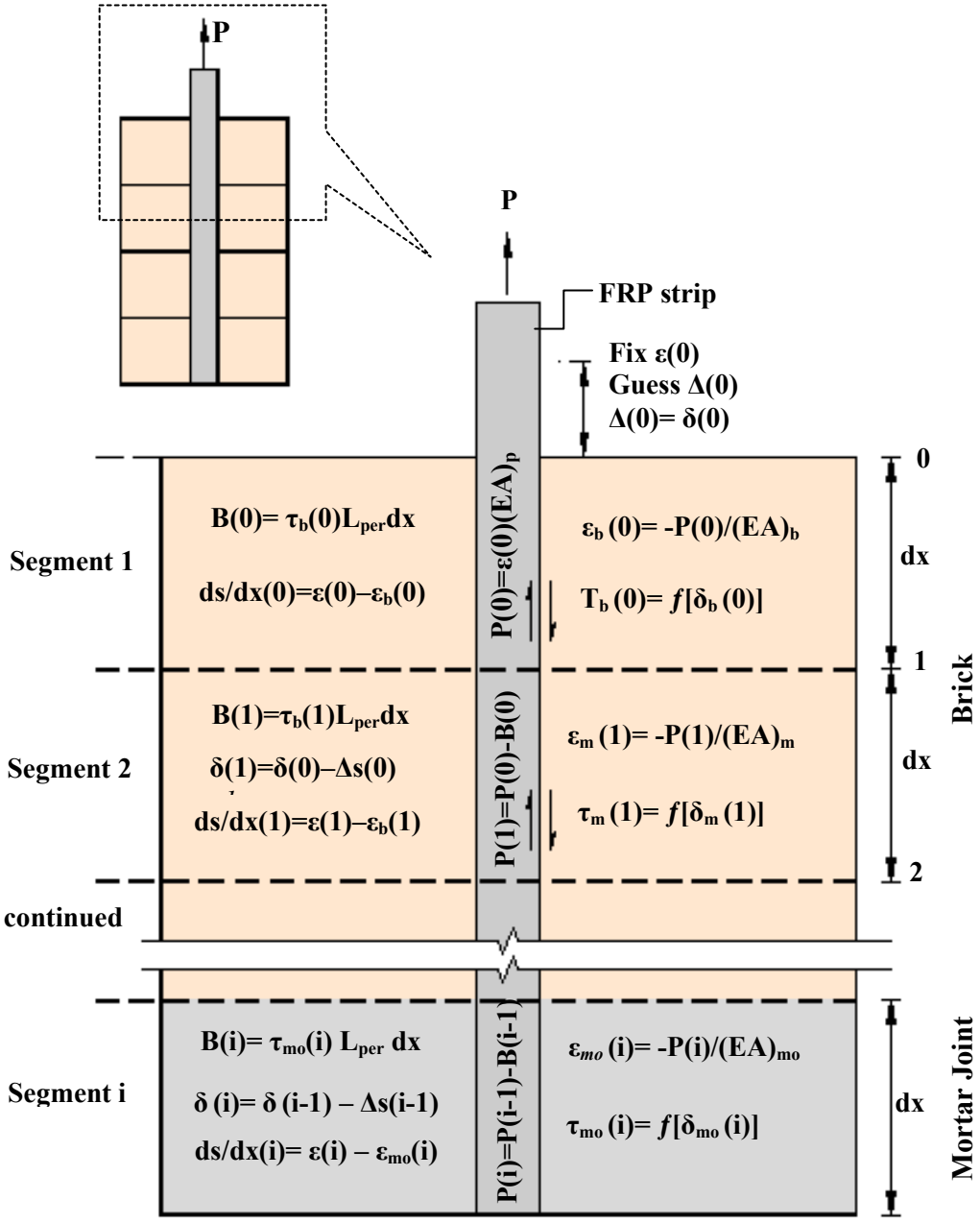

Figure 4-9: Schematic of the heterogeneous numerical model for pull test

While the heterogeneous analysis is a true reflection of the mortar and brick matrix that is masonry, it is much more numerically intensive in the sense that more elements are needed and different τ-δ relationships are used to account for the different mortar-FRP and brick-FRP bond. Hence, results from this study highlight the importance of the FRP-to-mortar bond τ-δ on the global P-Δ behaviour. In this study the effect of the heterogeneous nature of masonry was accounted for in two ways: (i) using separate bond-slip models for FRP-to-brick and FRP-to-mortar (Figure 4-10), and (ii) assigning zero shear bond strength to the FRP-to-mortar joint. The load-displacement responses using the above methods were then compared with that from the homogeneous simulation.

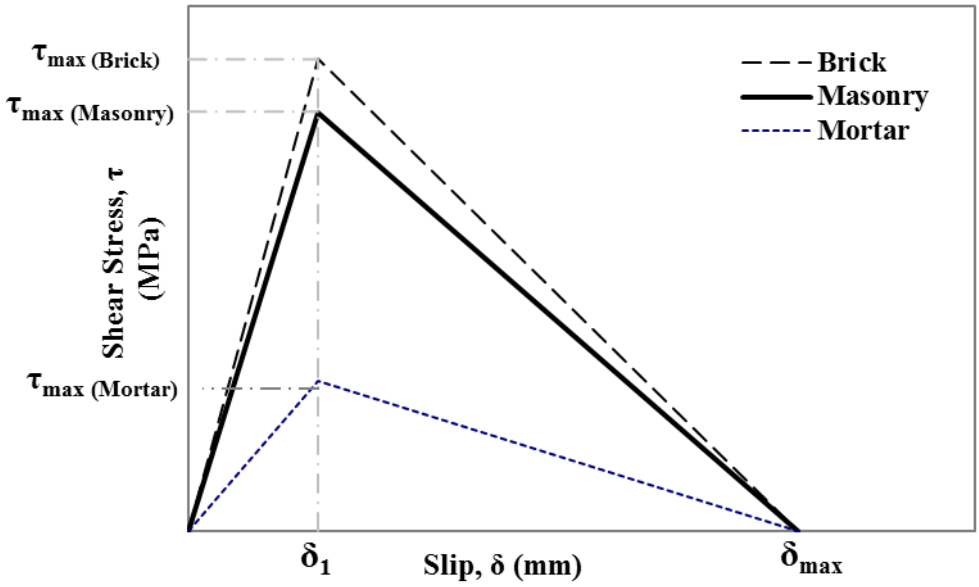

Figure 4-10: Local elastic-softening τ-δ relationship fornumerical models

For the heterogeneous procedure, the magnitude of δ_{max} and δ_1 (for both mortar and brick unit) were kept the same as for the homogeneous procedure owing to a lack of evidence in the literature. Given the dominant role that the brick unit bond appears to play in the response, it was not expected that this assumption for δ_{max} would be critical. The influence of the choice for δ_1 is even less critical as the bond strength is known to a property of $\tau_{max}\delta_{max}$. On the other hand, research by Petersen et al. (2009) reported τ_{max} values for mortar and brick units in the order of 4.5 and 13 MPa,

respectively. Hence, a ratio of one-third for the mortar to brick unit shear stress was adopted for τ_{max} in this study (Figure 4-10). As the individual brick unit is stronger than the masonry with "smeared" material properties (for typical modern clay-brick masonry), the τ_{max} value for the brick unit was increased slightly over the value used in the homogeneous model and a value of one third of that was used for the mortar τ_{max}. Although, these results were specific to the mortar and FRP aspect ratio used by Petersen et al. (2009), still provided a more realistic estimate for the distinct τ-δ characteristics where none previously existed.

4.3.3. Mathematical model

Model description

The derivation of the governing equation of the stress transfer problem for plated prisms involves four unknown fields which are: the axial stresses $\sigma_p = \sigma_p(x)$ in the FRP and $\sigma_m = \sigma_m(x)$ in the masonry; the axial strains $\varepsilon_p = \varepsilon_p(x)$ in the FRP and $\varepsilon_m = \varepsilon_m(x)$ in the masonry; the interface shear stress across the bonded length $\tau = \tau(x)$; and the interface slip $\delta = \delta(x)$ which is the difference between the axial displacement u_p of the FRP and u_m of the masonry. Based on the approach of Yuan et al. (2004) and Wu et al. (2002), the generic governing equations for the stress transfer problem for FRP -masonry prisms can be written as:

$$\frac{d\sigma_p}{dx} = \frac{\tau L_{per}}{A_p} \qquad \text{Eq. 4-10}$$

and

$$\sigma_p A_p + \sigma_m A_m = 0 \qquad \text{Eq. 4-11}$$

where, Ap and A_m are the cross-sectional areas of the FRP and masonry, respectively and L_{per} is perimeter of the failure plane.

The constitutive equations for the two adherents can be written as

$$\sigma_p = E_p \varepsilon_p = E_p \frac{du_p}{dx} \qquad \text{Eq. 4-12}$$

and

$$\sigma_m = E_m \varepsilon_m = E_m \frac{du_m}{dx}$$ Eq. 4-13

where, E_p and E_m are the Young's Moduli of the FRP and masonry, respectively.

The slip at the interface (δ) is the difference between the slips of the adherents u_p and u_m, i.e. $\delta = u_p - u_m$ and differentiating twice, we get

$$\frac{d^2\delta}{dx^2} = \frac{d^2u_p}{dx^2} - \frac{d^2u_m}{dx^2}$$ Eq. 4-14

Substituting Eq. 4-10 and the derivative of Eq. 4-12 into Eq. 4-14 leads to

$$\frac{d^2\delta}{dx^2} + \frac{d^2u_m}{dx^2} - \frac{\tau L_{per}}{E_p A_p} = 0$$ Eq. 4-15

Differentiating Eq. 4-11 and Eq. 4-13 once and using Eq. 4-10 yields

$$\frac{d^2u_m}{dx^2} = -\frac{\tau L_{per}}{E_m A_m}$$ Eq. 4-16

Substituting Eq. 4-16 into Eq. 4-15 leads to the governing differential equation

$$\frac{d^2\delta}{dx^2} - \beta_2 \tau = 0$$ Eq. 4-17

where, $\beta_2 = \beta_1 \beta_0$, $\beta_1 = L_{per} / A_p$, $\beta_0 = \left(1/E_p + A_p/(EA)_m\right)$, $(EA)_m$ is the axial rigidity of the masonry substrate, 'x' is the distance from the unloaded end and $\tau = f(\delta)$ is the interface shear-stress/slip function.

Similarly, differentiating slip with respect to x once and using Eq. 4-11 to Eq. 4-13 will result in the following expression for axial stress, σ, in the FRP strip.

$$\sigma = \frac{d\delta}{dx}\frac{1}{\beta_0}$$ Eq. 4-18

The governing Eq. 4-17 can be solved by using an appropriate relationship for local τ-δ along with the boundary conditions of zero slip and slip strain at the unloaded end of the FRP strip (refer to Mohamed Ali et al. (2008). While the rigid-softening model and elastic-softening model solutions have been discussed previously in Mohamed Ali et al. (2008), their application to a strongly heterogeneous material such as masonry has never been studied before. Thus, this study presents the closed

form solutions for these two models as well as that for the non-linear model that governs the behaviour of the FRP strip in a pull test for the various stages of τ-δ and crack propagation (Figure 4-11 and Figure 4-12). An example has been included in the Appendix §D.3 to illustrate the mathematical procedure.

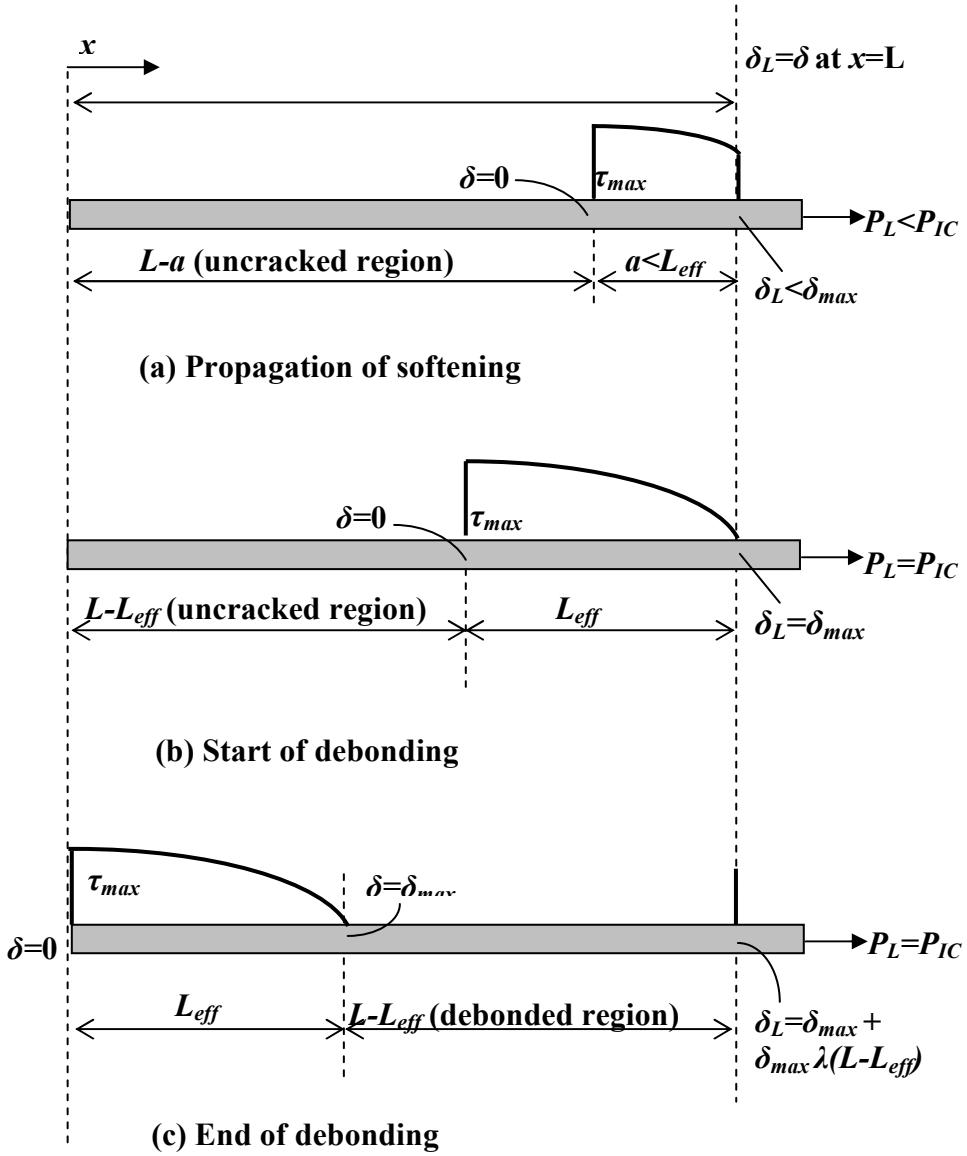

Figure 4-11: Bond-slip and crack propagation stages for rigid-softening model (Mohamed Ali et al. 2008)

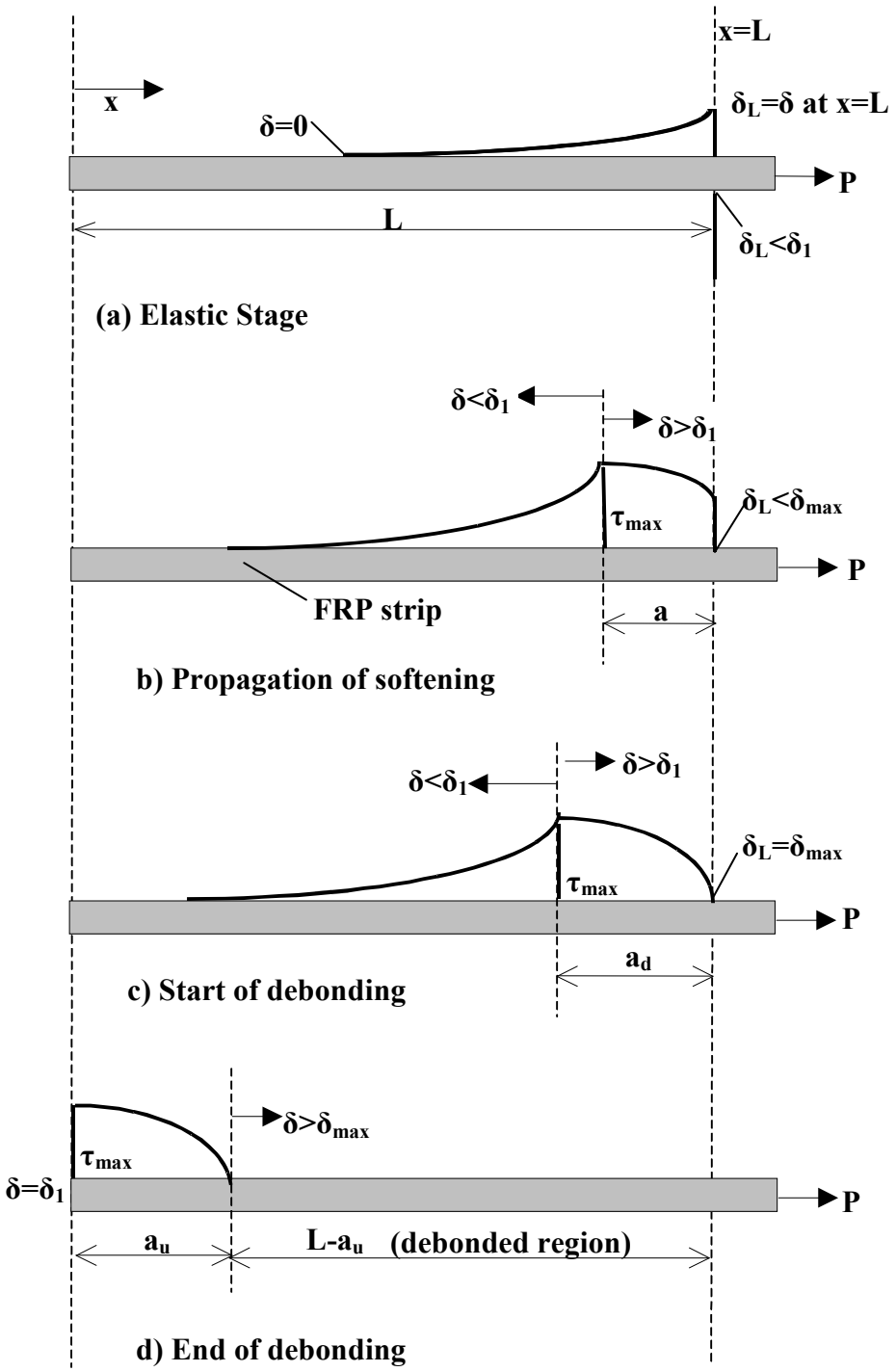

Figure 4-12: Bond-slip and crack propagation stages for rigid-softening model (Mohamed Ali et al. 2008)

Solution for different bond-slip models

Rigid-softening model

(i) ***For the softening stage and start of debonding stage*** (Figure 4-11(a) and (b)) **(**$\delta \leq \delta_{max}$):

The generic expression for the relationship between the axial load in the FRP strip, P, and the slip at the loaded end, Δ, for the rigid-softening model (Figure 2-5) is given by Eq. 4-19 (Mohamed Ali et al. 2008). The model assumes that the entire interface is rigid and neglects any elastic deformation. Therefore, the softening stage solution given by Eq. 4-19 can be represented by segment OB in Figure 2-4(d). At the end of this stage at point B, the debonding stage begins ($\delta = \delta_{max}$) and corresponds to first attainment of the peak load (P_{IC}).

$$P = \frac{\tau_{\max} L_{per}}{\lambda} \sin\left(\arccos\left(\frac{\delta_{\max} - \Delta}{\delta_{\max}} \right) \right) \qquad \text{Eq. 4-19}$$

where, $\lambda = \sqrt{\frac{\tau_{\max} L_{per}}{\delta_{\max} (EA)_p}}$

(ii) End of debonding stage (Figure 4-11(c)) ***(*$\delta > \delta_{max}$***):***

When the bonded length is greater than the effective bond length (L_e) and peak load is attained, the debonding crack propagates further towards the unloaded end with the load remaining constant (shown as segment BC in Figure 2-4(d)). This debonding results in uniform strain over the debonded region and continued increase in the ultimate slip at the loaded end (Eq. 4-20). Therefore, P= P_{IC} and

$$\Delta = \delta_{\max} + \delta_{\max} \lambda (L - L_{eff}) \qquad \text{Eq. 4-20}$$

where, $L_{eff} = \frac{\pi}{2\lambda}$

Elastic-softening model

The generic expression for the relationship between the axial load in the FRP strip, P, and slip at the loaded end, Δ, from initial application of load to complete debonding for the elastic-softening τ-δ model is given by Eq. 4-21 to Eq. 4-28 (Mohamed Ali et al. 2008).

(i) For the elastic stage (Figure 4-12(a)) *($0<\delta<\delta_1$):*

This stage is represented by the ascending branch of the elastic-softening model (Figure 2-5). Eq. 4-21 gives the linear P-Δ solution during the elastic stage corresponding to segment OA in Figure 2-4(d).

$$P = \frac{\Delta \lambda_1 A_p}{\beta_0 \cot(\lambda_1 L)} \qquad \text{Eq. 4-21}$$

where, $\lambda_1 = \sqrt{\frac{\tau_{\max} \beta_2}{\delta_1}}$ and the other terms are as defined previously.

(ii) For the softening stage (Figure 4-12(b)) *($\delta_1<\delta<\delta_{max}$):*

This stage is represented by the descending branch of the elastic-softening model (Figure 2-5) as represented by segment AB in Figure 2-4(d) and at the end of this stage debonding starts (i.e. $P = P_{IC}$).

$$\Delta = (\delta_{\max} - \delta_1)\left[\frac{\lambda_2}{\lambda_1}\tanh(\lambda_1(L-a))\sin(\lambda_2 a) - \cos(\lambda_2 a)\right] + \delta_{\max} \qquad \text{Eq. 4-22}$$

$$P = \left(\frac{\tau_{\max}\beta_1 A_p}{\lambda_2}\right)\left[\frac{\lambda_2}{\lambda_1}\tanh(\lambda_1(L-a))\cos(\lambda_2 a) + \sin(\lambda_2 a)\right] \qquad \text{Eq. 4-23}$$

where, a is length of the interface in the softening zone and $\lambda_2 = \sqrt{\frac{\tau_{\max}\beta_2}{(\delta_{\max} - \delta_1)}}$.

The softening length can be only be obtained by iterative solution of Eq. 4-22. However, for infinitely long bond lengths,

$$P_{IC} = \frac{\tau_{\max} L_{per}}{\lambda_3} \qquad \text{Eq. 4-24}$$

where, $\lambda_3 = \lambda_2 \dfrac{(\delta_{\max} - \delta_1)}{\delta_{\max}}$,

$L_{eff} = a + \dfrac{1}{2\lambda_1} \ln \dfrac{\lambda_1 + \lambda_2 \tan(\lambda_2 a)}{\lambda_1 + \lambda_2 \tan(\lambda_2 a)}$,

and

$a = \dfrac{1}{\lambda_2} \arcsin\left[0.97 \sqrt{\dfrac{\delta_{\max} - \delta_1}{\delta_{\max}}} \right]$.

(iii) Start of debonding stage **(**Figure 4-12(c)) *($\delta = \delta_{max}$):*

At this point, corresponding to point B in Figure 2-4(d), debonding starts when the softening zone is fully developed ($a=a_d$) as given by:

$$a = a_d = \frac{1}{\lambda_2} \arctan\left(\frac{\lambda_1}{\lambda_2}\right) \qquad \text{Eq. 4-25}$$

$$P_{IC} = \left(\frac{\tau_{\max}\beta_1 A_p}{\lambda_2}\right)\left[\frac{\lambda_2}{\lambda_1}\tanh\left(\lambda_1\left(L - \frac{1}{\lambda_2}\arctan\left(\frac{\lambda_1}{\lambda_2}\right)\right)\right)\cos\left(\arctan\left(\frac{\lambda_1}{\lambda_2}\right)\right) + \sin\left(\arctan\left(\frac{\lambda_1}{\lambda_2}\right)\right)\right] \qquad \text{Eq. 4-26}$$

(iv) For the softening debonding stage (Figure 4-12(d)) *($\delta > \delta_{max}$):*

When debonding starts, the model predicts that the elastic component of the axial force is reduced resulting in a slight decrease in load. This stage is represented by segment BC in Figure 2-4(d) where

$$P = \frac{(\delta_{\max} - \delta_1) A_p \lambda_2}{\beta_0} \qquad \text{Eq. 4-27}$$

$$\Delta = \frac{P\beta_0 (L - a)}{A_p} + \delta_{\max} \qquad \text{Eq. 4-28}$$

where, $a = a_u = \pi / 2\lambda_2$.

Non-linear model

The attraction of the non-linear τ-δ relationship (originally proposed by Dai et al. (2005, 2006) is that it can be represented by a single mathematical expression (Eq. 4-29) and hence, results in a single solution for the entire debonding process. The relationship depends only on the maximum shear bond stress, $\tau_{\max}$ and the interfacial

fracture energy, G_f. It should be noted that for consistency, G_f was kept the same as for the rigid-softening and elastic softening models. In this application, the non-linear τ-δ relationship takes the form (Kashyap et al. 2011)

$$\tau = 2G_f k e^{-k\delta}(1-e^{-k\delta}) \quad \text{Eq. 4-29}$$

where, the interfacial ductility index, $k = 2\tau_{\max}/G_f$.

Substituting Eq. 4-29 into the governing differential equation (Eq. 4-17) results in the expression

$$\frac{d^2\delta}{dx^2} = 2\beta_2 G_f k e^{-k\delta}(1-e^{-k\delta}) \quad \text{Eq. 4-30}$$

Recognising that $\frac{d^2\delta}{dx^2} = \frac{d}{dx}\left(\frac{d\delta}{dx}\right) = \frac{d}{d\delta}\left(\frac{d\delta}{dx}\right)\frac{d\delta}{dx} = \frac{1}{2}\frac{d}{d\delta}\left(\left(\frac{d\delta}{dx}\right)^2\right)$ and substituting into Eq. 4-30 leads to the expression

$$d\left(\left(\frac{d\delta}{dx}\right)^2\right) = 4\beta_2 G_f k e^{-k\delta}(1-e^{-k\delta})d\delta \quad \text{Eq. 4-31}$$

Integration of Eq. 4-31 and taking the square root gives,

$$\frac{d\delta}{dx} = \sqrt{2\beta_2 G_f (1-e^{-k\delta})^2 + c_1} \quad \text{Eq. 4-32}$$

Using the following boundary condition for specimens with long bond length (i.e., for $L > L_e$), the value of constant c_1 is zero. Thus, with zero slip strain and slip at x = 0, $\frac{d\delta}{dx}\Big|_{x=0} = 0$ and $\delta\big|_{x=0} = 0$, Eq. 4-32 becomes

$$\frac{d\delta}{dx} = \sqrt{2\beta_2 G_f}(1-e^{-k\delta}) \quad \text{Eq. 4-33}$$

Substituting Eq. 4-33 into Eq. 4-18 gives the stress in the FRP as a function of the local slip, δ:

$$\sigma = \sqrt{2\beta_2 G_f}(1-e^{-k\delta})\frac{1}{\beta_0} \quad \text{Eq. 4-34}$$

Eq. 4-34 can be used to write the following generic expression for the relationship between the axial load in FRP strip at the onset of IC debonding, P_{IC} and slip at the loaded end, Δ for the non-linear model. (Kashyap et al. 2011)

$$P_{IC} = A_p \sqrt{2\beta_2 G_f}(1 - e^{-k\Delta})\frac{1}{\beta_0} \qquad \text{Eq. 4-35}$$

4.3.4. Comparison of results from numerical procedure, closed-form mathematical solution and experimental data

The predicted P-Δ behaviour using the numerical procedure and closed-form mathematical solutions was verified by comparing with results from FRP-to-masonry pull tests. In this section, results of the parametric study on a NSM CFRP-to-masonry pull test specimen (P8) are included as an example. The *τ-δ* parameters for this specimen were calculated using Eq. 4-8 and Eq. 4-9 according to the procedure described in the previous section. The masonry material properties used for this test specimen are those given in Table 3-2.

Influence of τ-δ characteristics on load-slip response

Figure 4-13 and Figure 4-14 show the *P*-Δ plots from the predictive procedures using three different *τ-δ* models, i.e. rigid-softening, elastic-softening and non-linear. These demonstrate that the *P*-Δ response varies depending on the shape of the *τ-δ* characteristics and the key parameters used. As can be seen from Figure 4-13 and Figure 4-14, the results from the numerical procedures and mathematical solutions agreed reasonably well with the experimental load-slip behaviour. The peak load (i.e. the maximum debonding resistance, P_{IC}) was quite similar for all three *τ-δ* models as the fracture energy, G_f, i.e. the area under the *τ-δ* characteristic, remained constant. There was little difference (about 2-3%) between the predicted and experimental values of peak load. However, for this specimen, the predicted P-Δ response using elastic-softening *τ-δ* model gave better correlation with the overall experimental result as compared with the rigid-softening and non-linear *τ-δ* models which tend to over-estimate the *P*-Δ response at serviceability. This is due to the fact that both of

these models have stiffer ascending branches for their τ-δ models than the elastic-softening does.

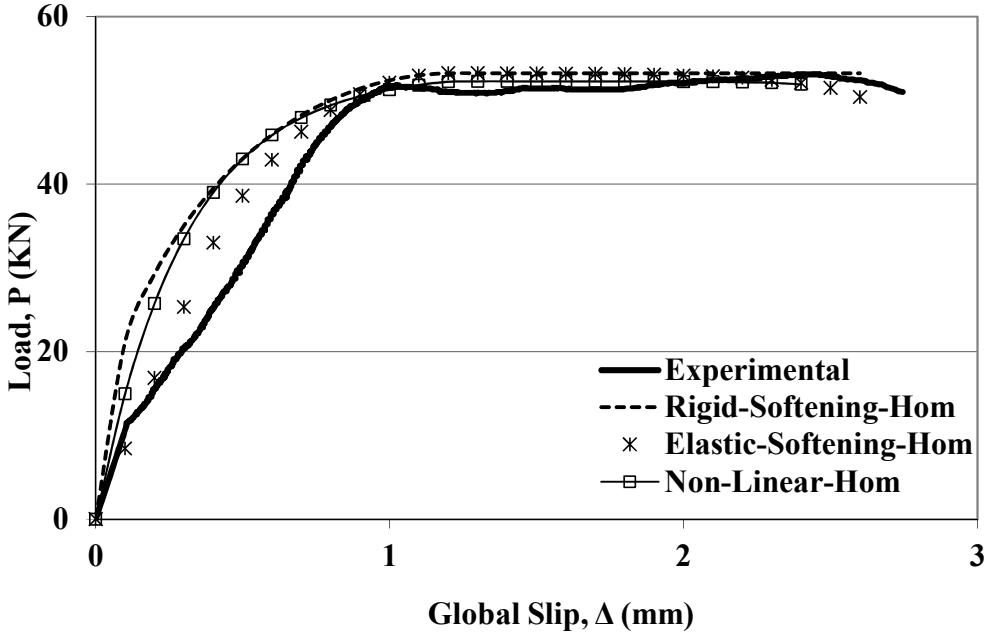

Figure 4-13: Experimental and numerical analysis *P*-Δ curves (P8) for different τ-δ characteristics

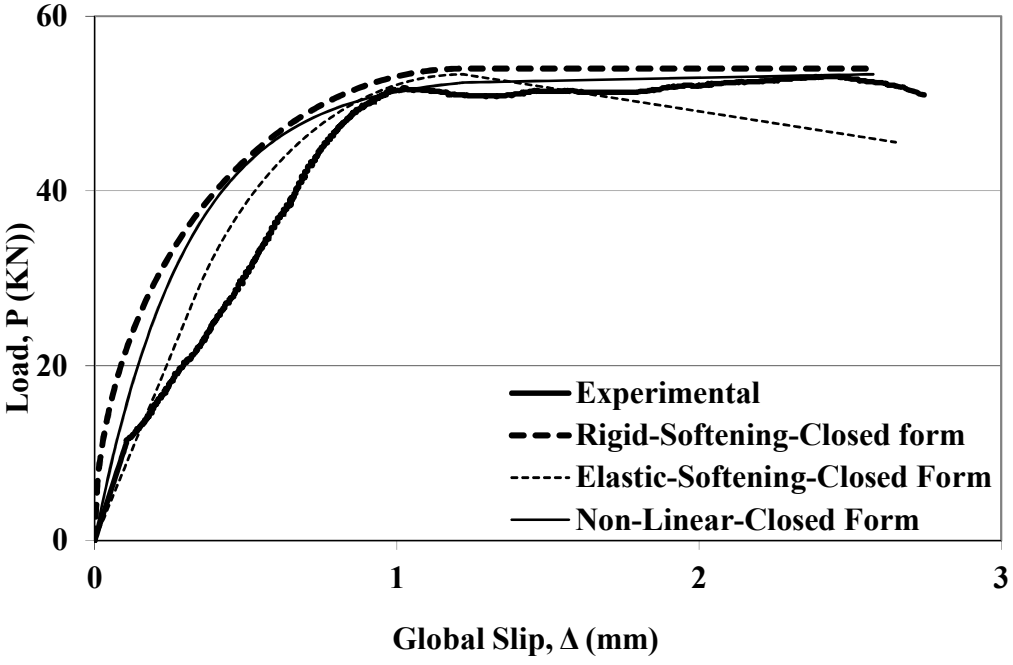

Figure 4-14: Experimental and closed-form P-Δ curves (P8) for different τ-δ models

One noticeable difference was in the initial slope of the global P-Δ response. As expected, using the rigid-softening and non-linear models resulted in a much stiffer initial slope of the P-Δ curve due to the rigid/stiffer ascending branch of the respective τ-δ models. This signifies that the stiffness of the ascending branch has great influence on the initial slope of the P-Δ curves. Further, the ultimate slip was also predicted with good accuracy for all three τ-δ models. The difference between the predicted and the experimental values for the ultimate slip varied between 5 to 12% for numerical procedures and 3-6 % for closed-form solutions which could be attributed to the material variability at the FRP-to-masonry interface.

Influence of heterogeneous nature of masonry

Figure 4-15 shows the results from the homogeneous and heterogeneous numerical procedure using elastic-softening τ-δ model. The P-Δ response for different τ-δ characteristics using heterogeneous analysis was similar to the homogeneous analysis.

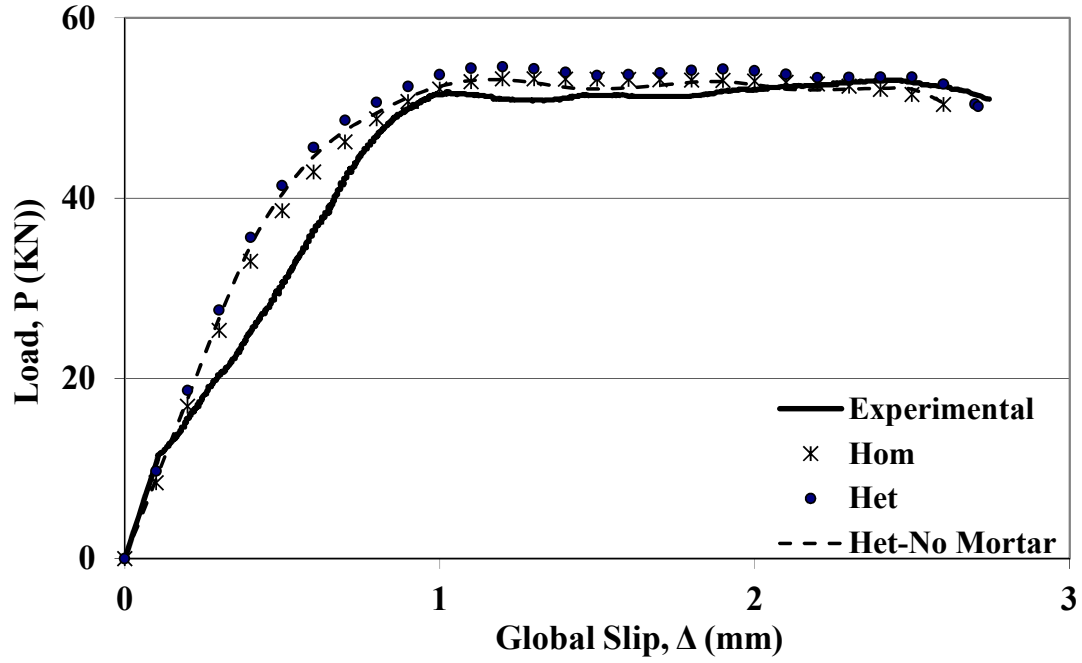

Figure 4-15: Experimental and numerical analysis P-Δ curves for elastic-softening τ-δ model

A slight reduction (about 2%) in the peak load was observed when the homogeneous procedure is used compared to the heterogeneous procedure (Figure 4-15). Furthermore, for the heterogeneous procedure, ignoring the mortar contribution only marginally affects the P-Δ response which could be attributed to its low strength. Consequently, for a heterogeneous simulation, the mortar τ-δ can be ignored. Similar trends were observed for the rigid-softening and non-linear τ-δ characteristics.

4.4. Summary and closing remarks

A new generic model that is applicable to both EB and NSM techniques was derived to predict the IC debonding resistance of FRP-to-masonry joints using a large set of test data from the open literature. For the range of experimental parameters investigated as part of this study, the predicted values from the new model correlate reasonably well with the experimental values. Further, empirical expressions were developed for the key local bond-slip parameters such as peak interface shear-stress and maximum slip.

A set of numerical and mathematical procedures that predict the pull test behaviour for FRP retrofitted masonry were developed using the empirical expressions for bond-slip parameters developed in §4.2.4. For the available test data, the numerical and closed-form mathematical solutions accurately predicted the experimental behavior. The difference between the peak loads from the homogeneous and the heterogeneous numerical procedures was observed to be negligible. Hence, for simplicity the homogeneous procedure can be used for pull test analysis. For both predictive procedures, the elastic-softening τ-δ model gave better correlation with the experimental results than the rigid-softening and non-linear models for the overall *P*-Δ response. However, the peak load (P_{IC}) only varies slightly when using either the rigid-softening or non-linear model.

CHAPTER 5
WALL BENDING TESTS - SETUP AND INSTRUMENTATION

5.1. Introduction

A series of NSM CFRP reinforced masonry wall tests were conducted under lateral out-of-plane bending. These tests investigated the use of the NSM technique to increase the bending strength of URM walls. Major gaps were identified in the literature (§2.5) relating to the influence of cyclic loading, axial pre-compression, reinforcement ratio and FRP strip spacing on the FRP-to-masonry bond. Hence, wall tests were conducted to study:

- Behaviour of NSM CFRP retrofitted masonry walls in flexure and investigate the IC debonding failure mechanism in them; and
- The effects of reverse cyclic loading, axial pre-compression, FRP strip spacing and reinforcement ratio on the stiffness, displacement capacity and ultimate strength of FRP retrofitted masonry walls.

In this chapter the test plan, setup, and instrumentation details are described. The test results are presented and discussed in Chapter 6.

5.2. Test Plan

Fifteen NSM CFRP reinforced walls were subjected to out-of-plane bending. The test parameters that were varied included: FRP strip spacing, reinforcement ratio, single/double sided FRP mounting, axial pre-compression and cycling loading. Table 5-1 shows the details of the walls tested in this research.

Table 5-1 - Out-of-plane bending test plan

Wall *S/C	Wall Dimensions		Strip Size		# of Strips **O/D	Strip spacing^ ^(mm)	Axial loading (MPa)	ρ*** = A_{FRP}/A_{Wall} (%)
	W (mm)	H (mm)	t_p (mm)	b_p (mm)				
1S	355	1710	3.6	10	1D	355	0	0.092
2S	355	1710	3.6	10	1D	355	0	0.092
3C	355	1710	3.6	10	1D	355	0	0.092
4S	230	1710	3.6	10	1D	230	0	0.142
5S	1070	2310	7.2	10	1O	1070	0	0.061
6S	1070	2310	4.8	7.5	2O	535	0	0.061
7S	1070	2310	3.6	10	3O	357	0	0.092
8S	1070	2310	4.8	5	3O	357	0	0.061
9S	1070	2310	3.6	10	1O	1070	0	0.031
10S	1070	2310	4.2	10	2O	535	0.1	0.071
11C	1070	2310	4.2	10	2D	535	0	0.071
12C	1070	2310	4.2	10	2D	535	0.1	0.071
13C	1070	2310	4.2	10	2O	535	0	0.071
14S	1070	2310	4.2	10	2O	535	0.2	0.071
15C	1070	2310	4.2	10	2D	535	0.2	0.071

wall thickness t_m = 110 mm for all walls
* S – monotonic static loading; C – quasi-static cyclic loading
**O – strips on one side; D – strips on both sides
***ρ – Reinforcement Ratio
^ – strip spacing refers to horizontal spacing between vertically oriented strips

Walls 1-4 were conducted as pilot tests in order to ensure the test setup would function satisfactorily. The test wall width was increased for walls 5-15 in order to study variable strip spacing. As shown in Table 5-1, walls 5, 6 and 8 were used to investigate the influence of strip spacing on the flexural behaviour of NSM FRP retrofitted walls. The effects of axial loading on wall response under monotonic loading was investigated by tests on walls 6, 10 and 14 with the same repeated under cyclic loading with walls 11, 12 and 15. The effect of cycling loading was investigated under three axial load conditions i.e. with no axial load (walls 1-3 and walls 6 & 12), under 0.1 MPa (walls 10 and 12) and under 0.2 MPa (walls 14 and 15). The effect of reinforcement ratio was studied through walls 4, 5, 7 and 9. Wall

13 was unique in the sense that it was tested with cyclic loading even though it only had NSM reinforcement on one face of the wall.

5.3. Specimen Design

Each wall test specimen consisted of a single leaf clay brick masonry wall with nominal dimensions as shown in Table 5-1. These walls were constructed by professional brick layers using the materials specified in §3.3. The unreinforced walls were left to cure for a minimum of 28 days before retrofitting with NSM CFRP. The FRP strips were aligned vertically through the brick units offset by 52 mm from the perpend joints (except for wall 4) as this provided the most efficient increase in ultimate strength (Willis et al. 2009b). This also allowed strain gauging of FRP in adjacent bricks so that data could be recorded on either side of a crack (i.e. mortar joint) and provided the closest possible representation of an FRP strip through a homogeneous material. The FRP was obtained from the manufacturer in rolls of 1m wide sheeting, 1.2 mm (walls 1-9) or 1.4 mm (walls 10-15) thick. All strips were fabricated by cutting and gluing the required number of individual strip elements together and spanned for the full length of the specimen. It should be noted that the 1.4 mm thick strip was used for walls 10-15 only because of the unavailability of the strip with 1.2 mm thickness. The FRP retrofitting scheme was designed using full interaction theory to ensure that IC debonding was the critical failure mode, rather than FRP tensile rupture or masonry crushing (refer to calculations included in Appendix §E.1). The groove for the NSM strip was cut using a diamond blade saw and then filled with an epoxy adhesive after blowing the brick dust out with a high pressure air hose. The strip was cleaned with acetone to remove any foreign substances before being inserted into to the epoxy-filled groove and allowed to cure for 7 days. The FRP strip was positioned flush with the masonry surface as shown in Figure 5-1 and Figure 5-2 for all specimens.

The first four wall tests (walls 1-4) were conducted with 1710 mm high and 110 mm thick masonry walls (Figure 5-1). Walls 1-3 were 355 mm wide and wall 4 was 230 mm wide. All four walls were reinforced on both faces with vertical NSM CFRP strips. The FRP strip was placed along the centerline of the flexural face, hence for

wall 4 (Figure 5-1(a-ii)), the strip went alternately through brick units and perpend joints in adjacent courses, while for walls 1-3, the FRP strip ran through the brick units in every course of brickwork (Figure 5-1(a-i)). This allowed for investigation of the influence of perpend joints in bond and a different reinforcement ratio on the flexural behavior of retrofitted masonry wall.

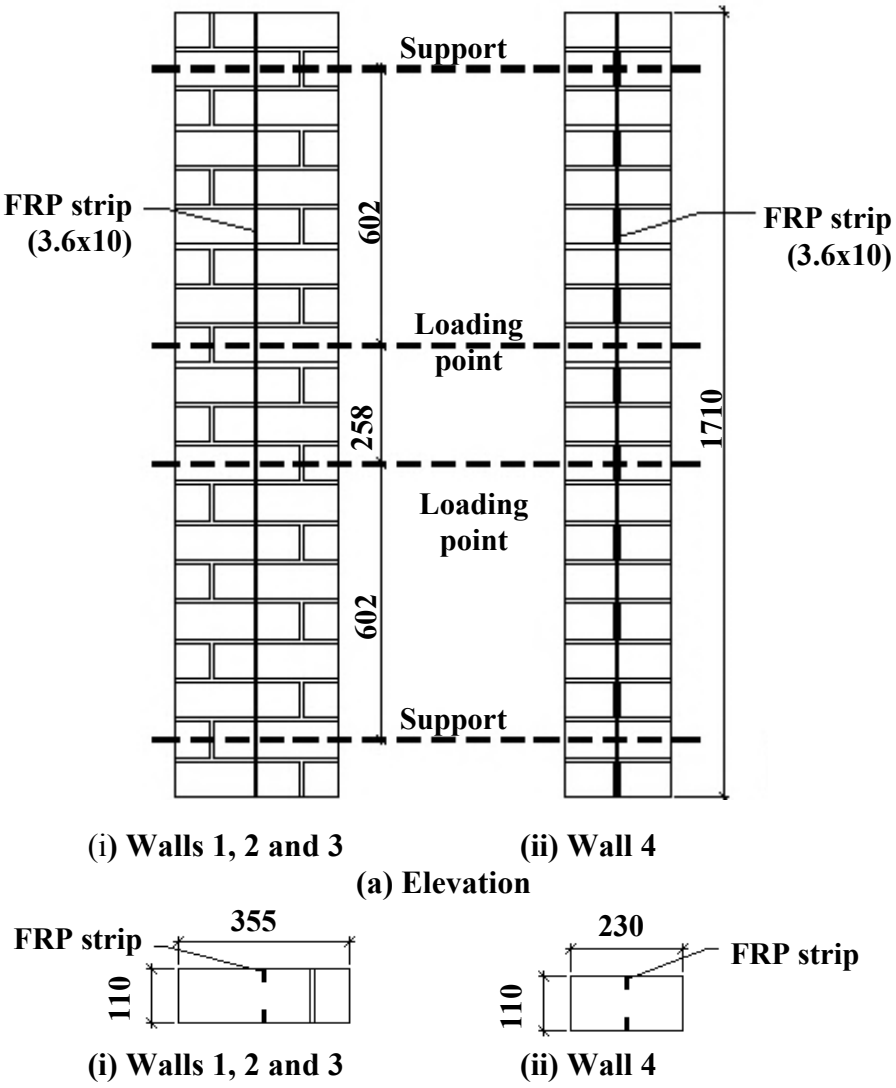

Figure 5-1: Specimen details – walls 1-4

The FRP strip arrangements and wall dimensions for walls 5-15 are shown in Figure 5-2. Walls 5-15 were 2312 mm tall, 1070 mm wide and 110 mm thick. These dimensions were chosen to give a more realistic representation of the one-way vertical bending portion of a masonry wall supported on all four sides as well as to

study the influence of strip spacing. It should be noted that from wall 5 onwards, specimens subjected to monotonic loading had the FRP reinforcement placed only on the "tension face" (Figure 5-2(b)) as it was thought that due to the small reinforcement ratios being used, the absence of FRP on the compressive face would not result in a significant difference in behavior as well as saving time and money. However, as can be seen in (Figure 5-2(c)), the cyclically loaded specimens were reinforced on both sides (except for wall 13).

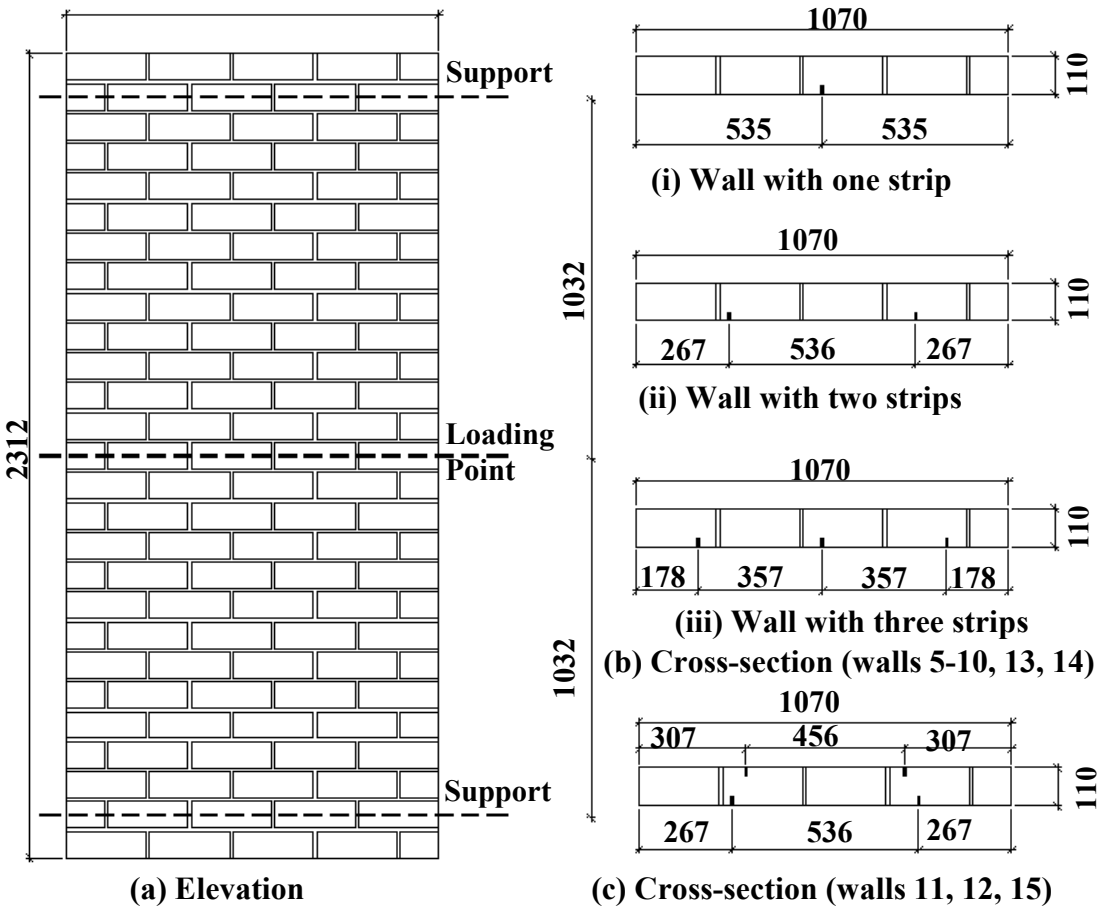

Figure 5-2: Specimen details –walls 5-15

A vertical crack was observed on the compressive face (back face) directly behind the FRP strips on tension face (front face) for wall 10. This was thought to be due to the plane of weakness caused by the FRP strip on the opposite side. To avoid further complications due to the vertical crack interacting with the FRP strip, the spacing of the FRP on the back face was reduced by approximately 40mm. Therefore, for walls

11, 12 and 15 the centre-to-centre strip spacing was 535mm on the front face and 456mm on the back face (Figure 5-2(c)).

5.4. Test Setup

The setup used for the wall tests is shown in Figure 5-3 and Figure 5-4.

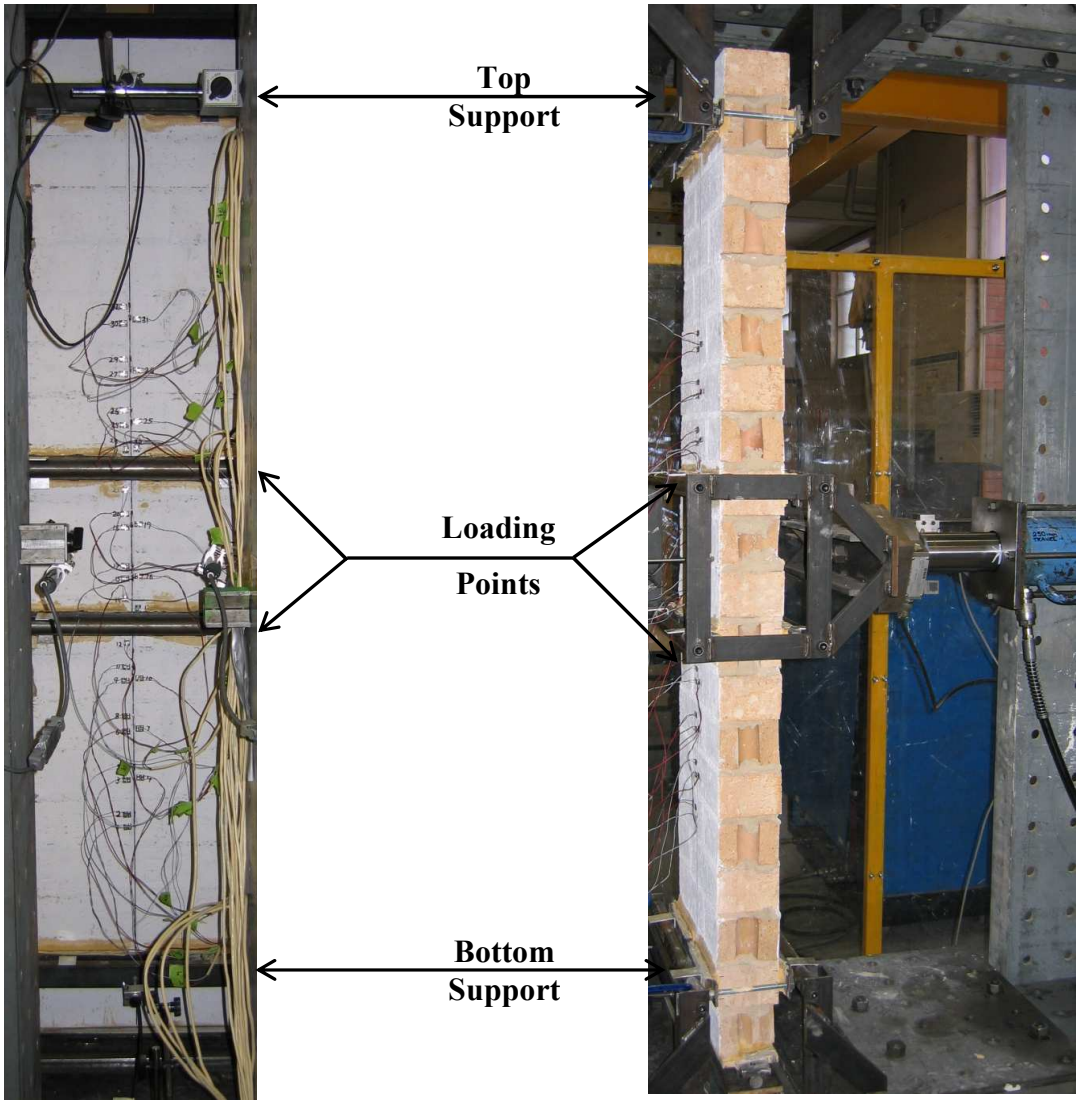

a) Front view **b) Side-view**

Figure 5-3: Out-of-plane bending test setup for walls 1-4

The walls were simply-supported along their top and bottom edges with roller supports at the second course from the top and bottom of the walls. Walls 1-4 (Figure 5-3) were subjected to four-point loading using a hydraulic ram whereas walls 5- 15

specimens were tested under three point loading (Figure 5-4). In every test, the ends of the FRP strips were untrapped (Figure 5-5) so that the final failure occurred once debonding propagated sufficiently close to the unloaded end so that there was not enough bonded length left to maintain the tension force in the FRP strip.

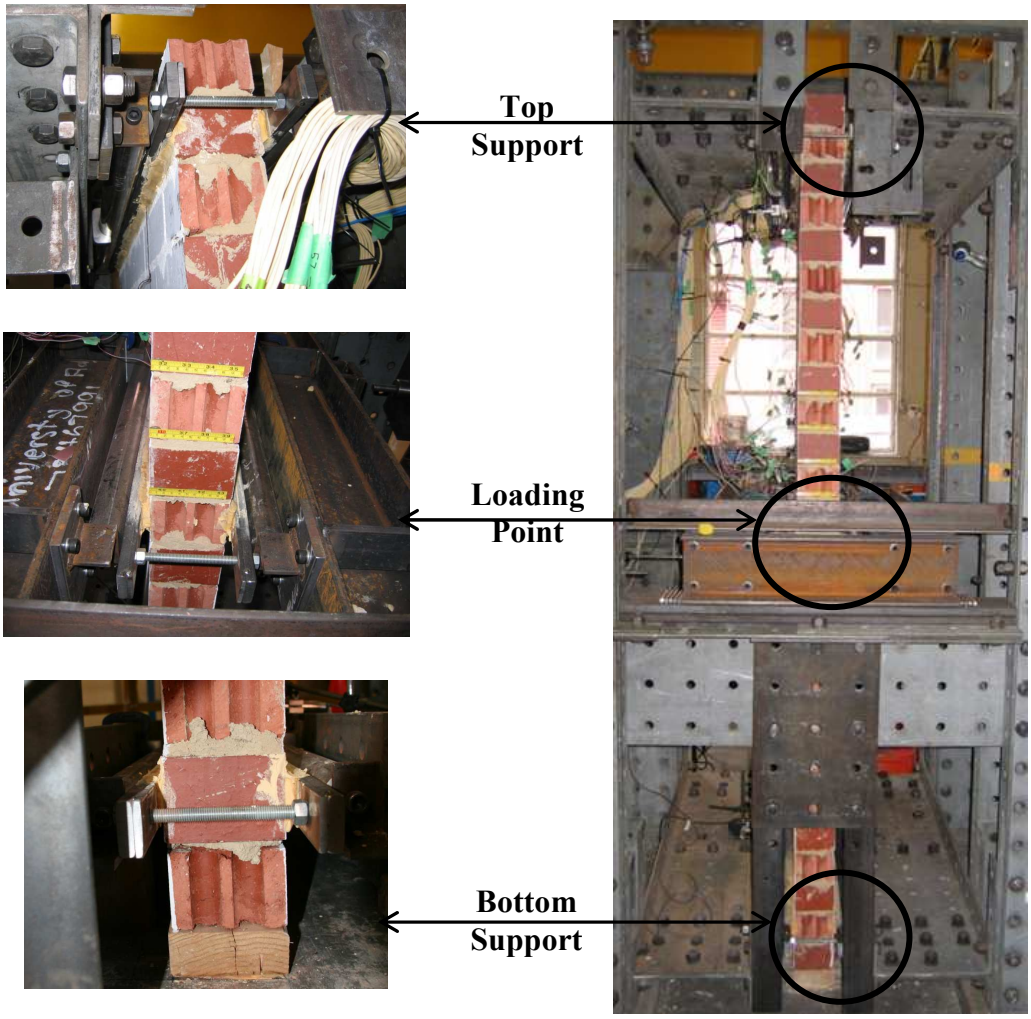

Figure 5-4: Out-of-plane bending test setup for walls 5-15

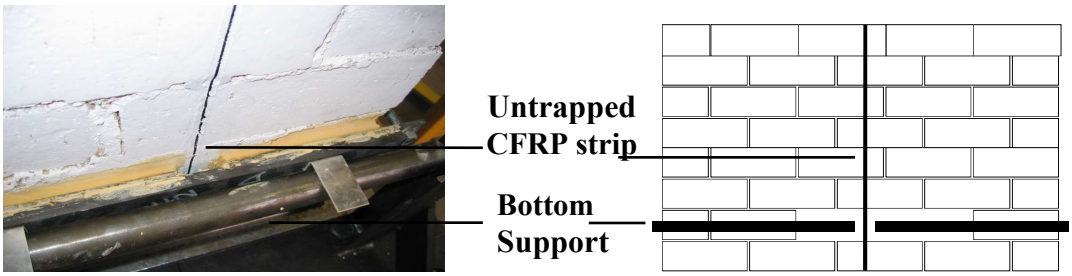

Figure 5-5 Untrapped FRP strip at the support

For each static test, the load was applied uniformly across the specimen width at their mid-height and in one direction such that the strain gauged FRP strip was in tension. The quasi-static load was applied slowly using a manually operated hydraulic jack until failure. For cyclic loading, the test arrangement used for static tests was modified such that a reaction frame was constructed on both sides of the specimen with the centre course of bricks clamped on each side (Figure 5-6), allowing the hydraulic ram to push and pull the specimen back and forth. The cyclic tests were conducted by loading the walls in increments of 10-30% of the estimated ultimate deflection, as determined from the corresponding monotonic static test. This was done to collect data for a sufficient number of load cycles in order to compare with the monotonic test results. For each displacement increment two to three cycles were conducted with each cycle consisting of: 1) monotonically loading the wall in the positive direction until the target displacement is reached and then reducing the load to "zero"; 2) monotonically loading the wall in the negative direction until the target displacement is reached and then reducing the load to "zero".

Figure 5-6: Cyclic loading setup

5.5. Axial Pre-compression

A vertical pre-compression (of 0.1 MPa or 0.2 MPa) was applied to walls 10, 12, 14 and 15 (Table 5-1) using the test arrangement shown in Figure 5-7. A total of 527 kg (W = 5.17 kN) was required to reach the desired 0.1 MPa axial load at top of the

wall. This was doubled to 1,054 kg (W = 10.34 kN) to apply 0.2 MPa to the wall. In order to apply these axial loads to walls, two steel hanger beams were placed along the top of the wall and the required weights were hung from free end of these beams. The steel hanger beams were supported by a steel bar used to apply the vertical reaction as a point load to allow control over the length of the lever arm used to magnify the load. Timber plates and a layer of rubber were matted underneath the steel bar to uniformly distribute the vertical load onto the wall (Refer to Figure E-4 for more details).

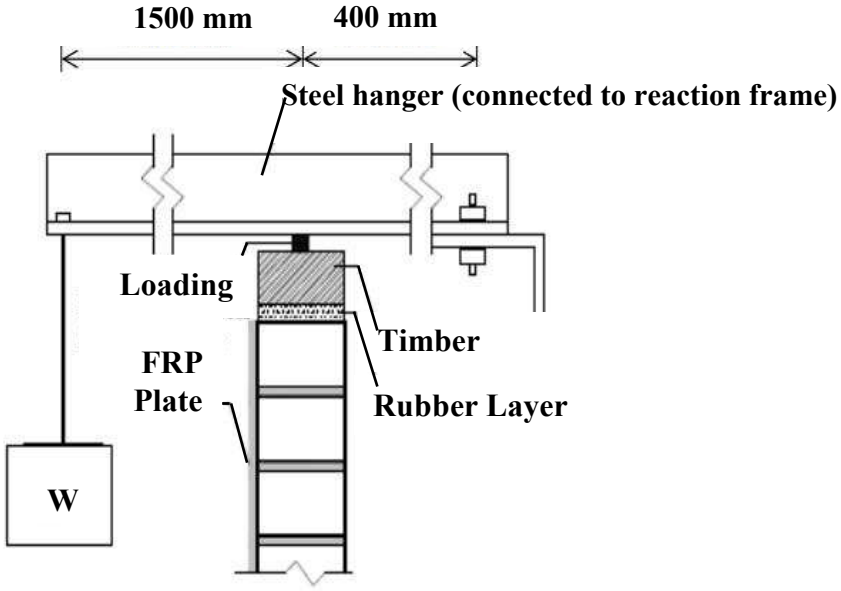

Figure 5-7: Axial loading arrangement

5.6. Instrumentation

To better document the wall response, instrumentation consisting of strain gauges, magnetic voltage gauges (MVGs) and LVDTs were used. The instrumentation was used to collect information about the global load-displacement response of the wall; strain and shear stress distribution within a single brick and over the entire height of the wall; crack formation and opening/closing along with width and height of cracks. As the experimental study progressed, as more understanding was gained which enabled the instrumentation to be varied to better target the data necessary to document specific wall responses.

5.6.1. Strain gauge setup

Strain gauges were used to record the change in axial strain in the reinforcement from which the progression of debonding along the strip could be monitored. Strain gauges were glued in between the FRP strip layers so as to not interfere with the bonded surface area at the FRP-to-masonry interface. The number and the position of strain gauges used for each wall varied depending on the cost and availability of data acquisition channels and on the test variables involved such as loading type, strip configuration, axial pre-compression. For the pilot tests (walls 1-4) 32 data acquisition channels were used and this number was increased to 64 for the remaining walls to gain more knowledge of the wall behavior. The strain gauge arrangement for walls 1-3 is shown in Figure 5-8.

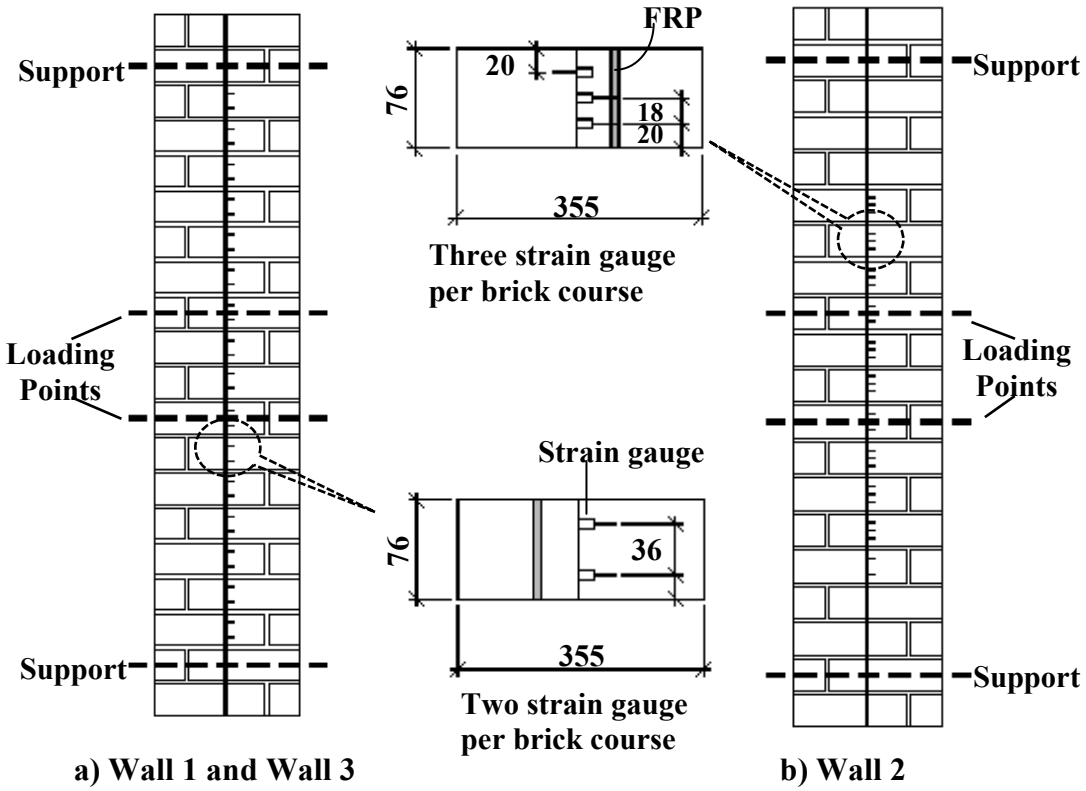

Figure 5-8: Strain gauge arrangement for walls 1 –3

For walls 1-4, only the tension face FRP strip was strain gauged due to data acquisition system limitations. As shown in Figure 5-8(a), for wall 1 and wall 3, two strain gauges per brick were positioned in the central sixteen courses, as this was the range where debonding was expected to occur. The strain and shear stress

distribution plots for these two walls revealed that the important features within the brick unit were missing (refer §6.2.1 and §6.2.3 for details). To improve the resolution of the experimental strain and shear stress plots for wall 2, three strain gauges per brick were placed on the central ten courses (Figure 5-8(b)). However, the strain and stress distribution plots still suffered from a lack of peaks at crack locations and hence, the peak shear stress value was still uncertain. (refer §6.2.2 for details). Hence, it was realized that the number of strain gauges per brick needed to be further increased to get a more realistic picture of the shear stress distribution. Consequently, for wall 4, four bricks on the tension face were instrumented (i.e. avoiding the loading points and perpend joints) with seven strain gauges per brick (Figure 5-9).

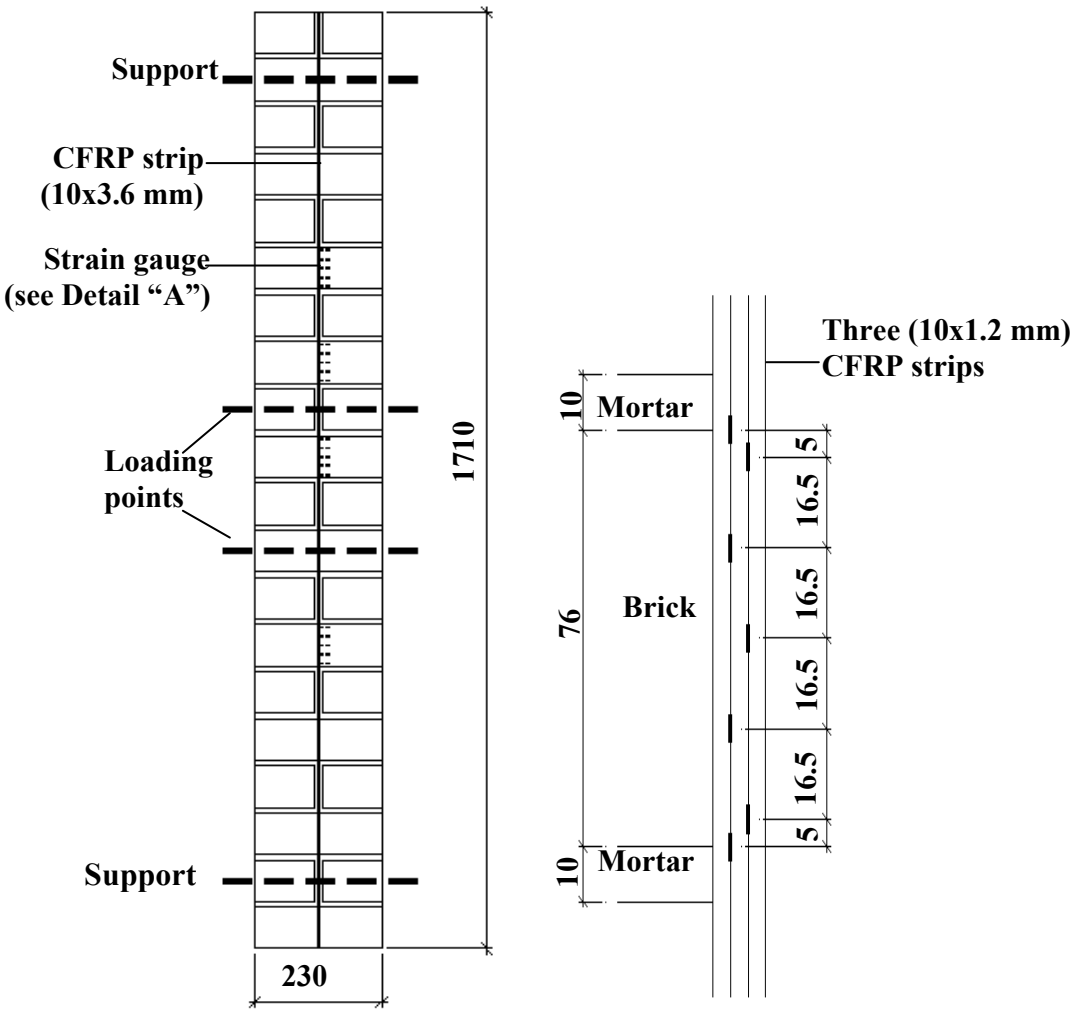

a) Wall 4 **b) Strain gauge arrangement - Detail "A"**

Figure 5-9: Strain gauge arrangement for wall 4

From the ('pilot') tests on the first four walls, a large degree of symmetry was noted in the recorded strains for the top and bottom half of the test specimens (Figure 5-10). Consequently, in future tests only the strips in the top half of the walls were strain gauged.

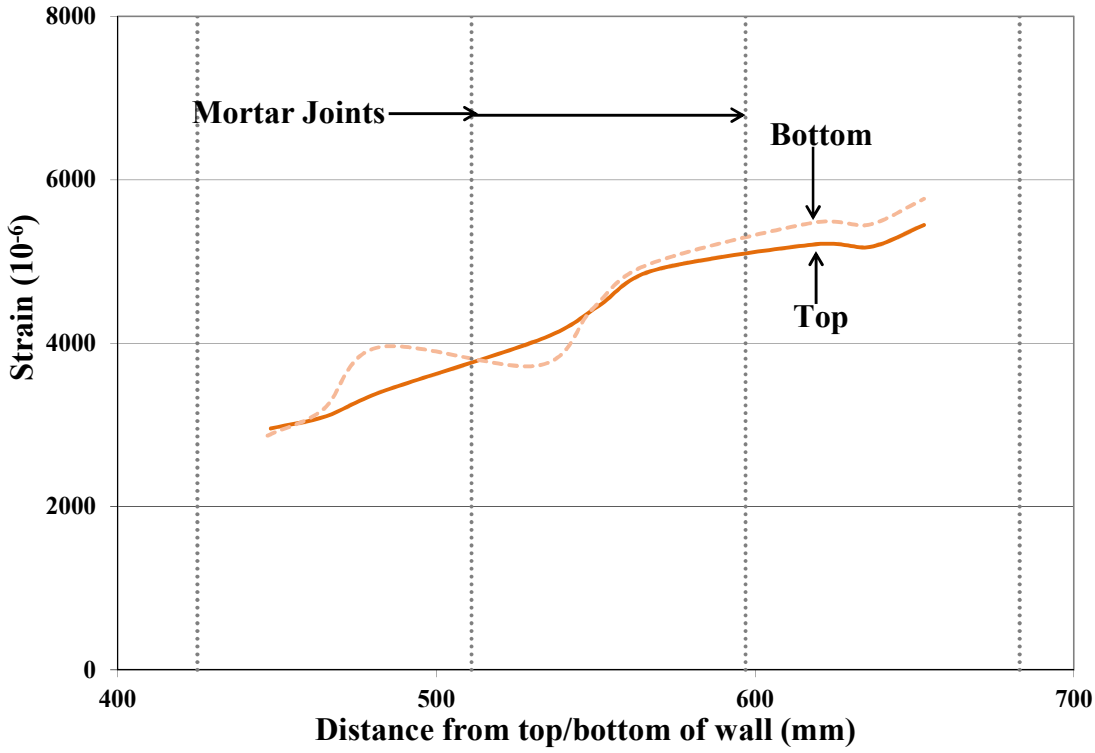

Figure 5-10: Comparison of strain above and below wall mid-height

For walls 5-15, strain gauge positions were chosen based on the number of FRP strips and loading type. Further, lateral symmetry was assumed for walls with two or three strips. Hence, for walls reinforced with two strips, only one strip was instrumented whereas, for walls with three strips, the centre strip and one outer strip were instrumented. Due to the different test configurations adopted for each specimen and the limitation of 64 number of data acquisition channels available, the number of strain gauges used per brick as either three or five. As shown in Figure 5-11, the position of three gauges was such that they corresponded to the middle three of the five gauge configuration on a brick unit. For specimens reinforced with one FRP strip and subjected to static loading (walls 5 and 9), five strain gauges per brick were used (Figure 5-12). As wall 7 and wall 8 were reinforced with three strips,

the central and one of the two outer strips were instrumented with three strain gauges per brick (Figure 5-13).

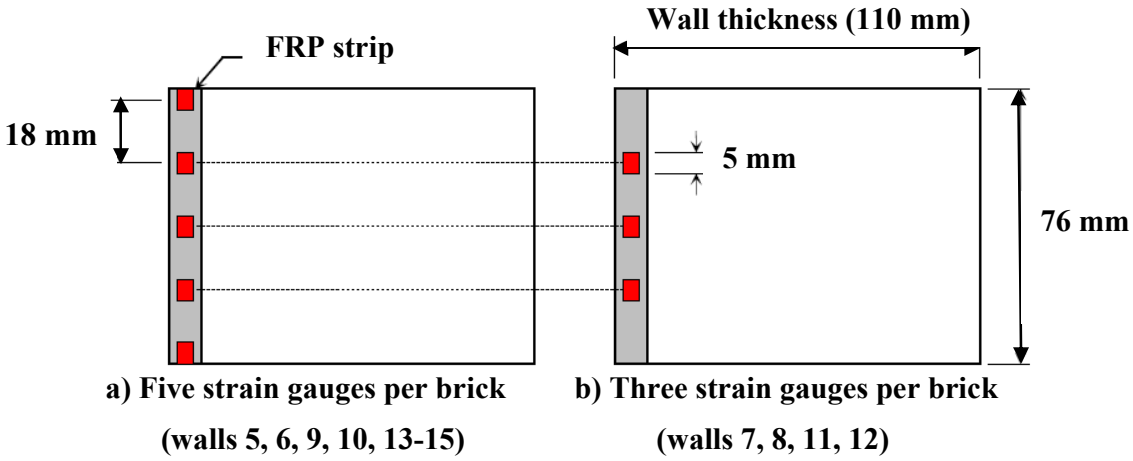

Figure 5-11: Strain gauge location within brick unit

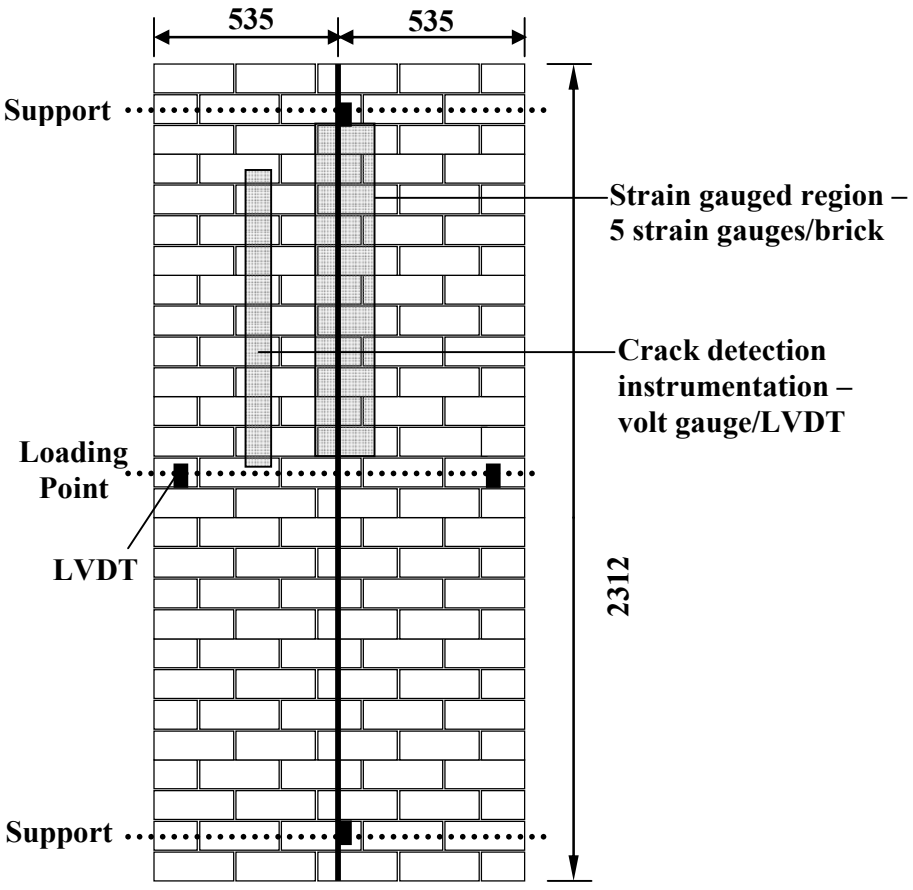

Figure 5-12: Instrumentation for walls reinforced with one strip (walls 5, 9)

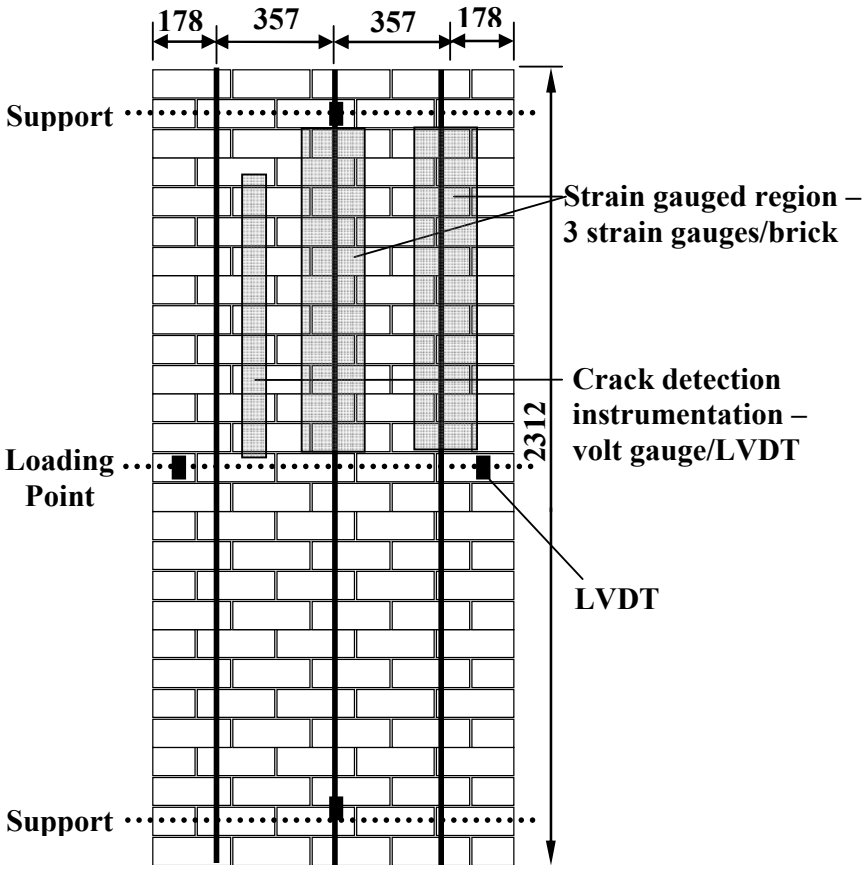

Figure 5-13: Instrumentation for walls reinforced with three strips (walls 7, 8)

Further, for monotonically loaded walls with two strips (walls 6, 10, 14), only one strip was instrumented with 5 strain gauges per brick, as shown in Figure 5-14(a). Walls 11-12 were subjected to cyclic loading and had two strips on both faces so, top half of alternate strips on each face were strain gauged with three gauges per brick (Figure 5-14(b)). As shown in Figure 5-15, similar strains were recorded from the strips on the front and back faces of the wall, (refer to §6.2.11 for details). Consequently, for wall 15 only one strip on one face was strain gauged as it allowed for five strain gauges per brick giving more detailed strain and stress profile information. Further, for some wall tests extensive cracking was noted in the lower half of the wall. Thus the difference in strains between the top half and lower half of the walls were also investigated in W-15 by placing strain gauges for the three bricks above and below the central brick. As mentioned in §5.2, wall 13 was subjected to cyclic loading with reinforcement only on one face so the strain gauge setup was similar to static tests (Figure 5-14(a)).

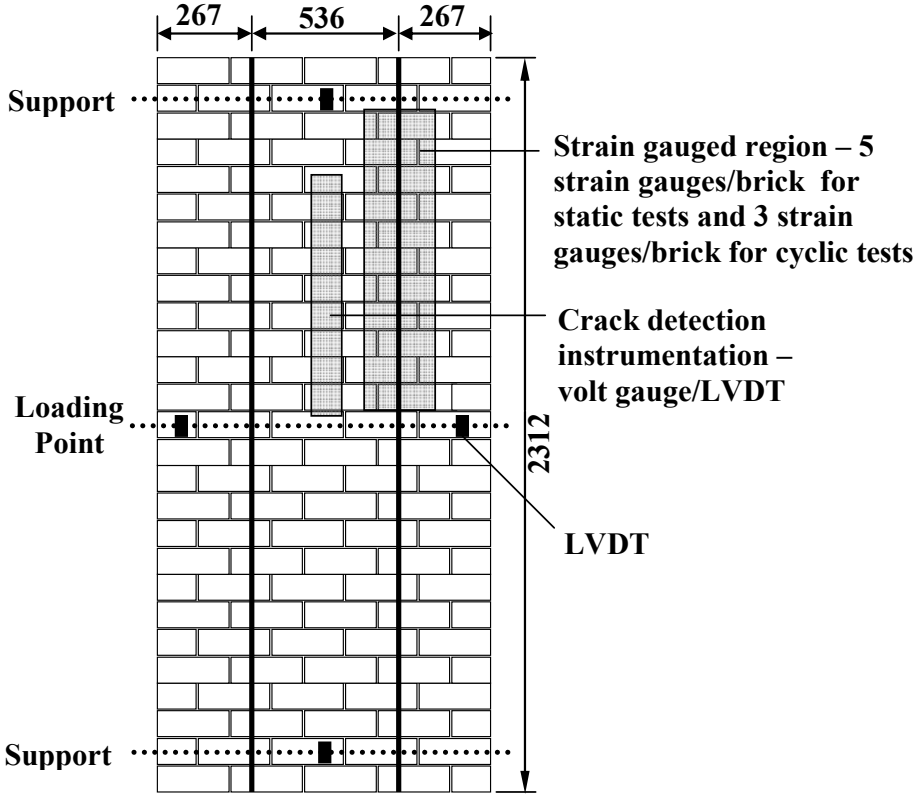

a) Front of the wall (walls 6, 10-15)

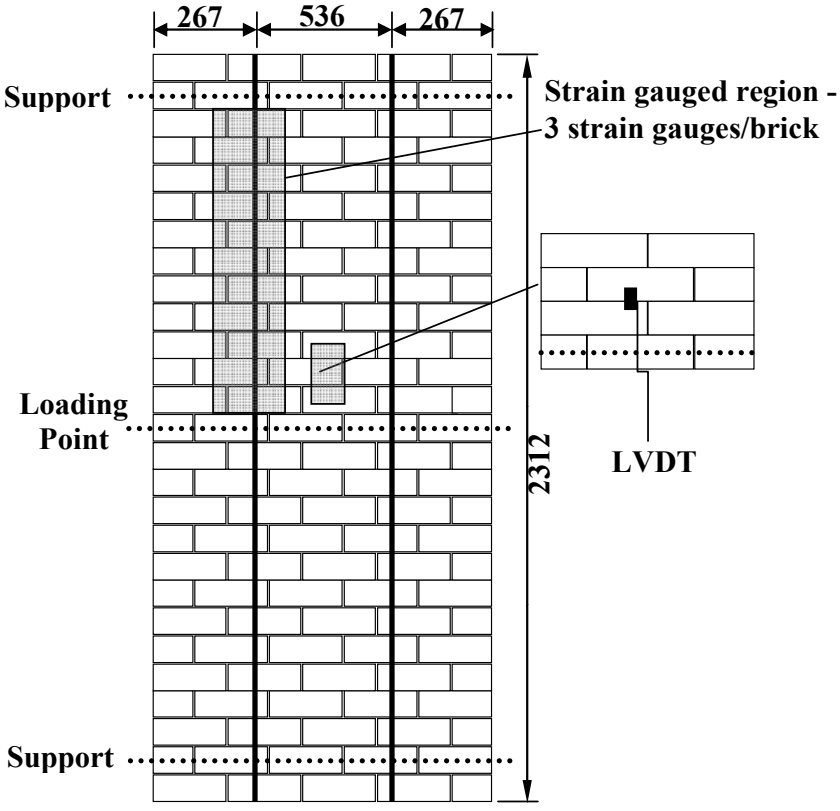

b) Back of the wall for cyclic tests (walls 11, 12)

Figure 5-14: Instrumentation for walls reinforced with two strips

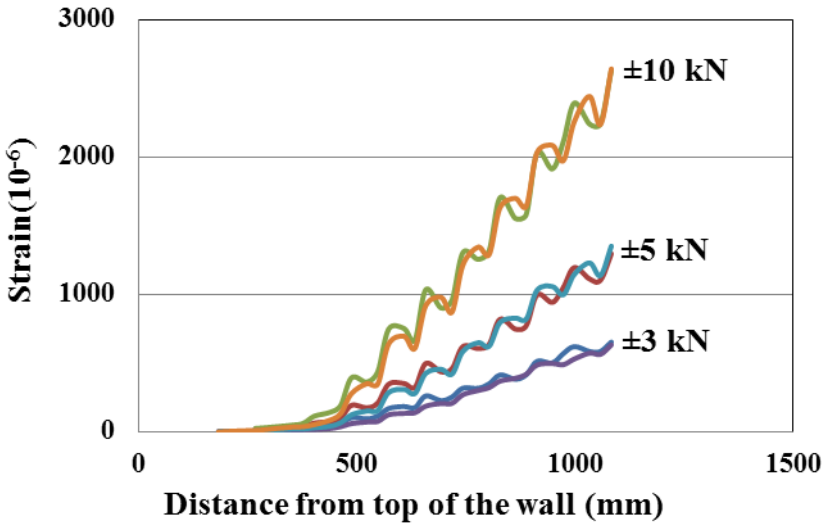

Figure 5-15: Strain comparison between front and back strip

5.6.2. LVDT and other instrumentation

Load-displacement data is crucial for understanding wall behaviour. To monitor the global displacement five LVDTs were placed at different positions on each wall (Figure 5-13 and Figure 5-14). To measure the mid-span displacement, three LVDTs were placed at the mid-height of the wall, one in the centre and two on either side to document if any lateral rotation (twisting) of the wall occurred. The remaining two LVDTs were positioned at the top and bottom supports to account for any support support movement, should it occur, during testing.

To successfully model the wall displacement behaviour, the discrete rotations at flexural cracks within the wall must be accounted for. To get crack information such as crack width, crack initiation and closure, MVGs, LVDTs and strain gauges were placed across mortar bed joints in the upper half of the specimen (Figure 5-16 and Figure 5-17). To record the onset of cracking at the bed-joints in the walls, MVGs (Figure 5-16) were used for walls 5-8. Two MVGs were trialled successfully for the first time for crack detection in wall 5. Thus, the number was increased to ten for walls 6-8.

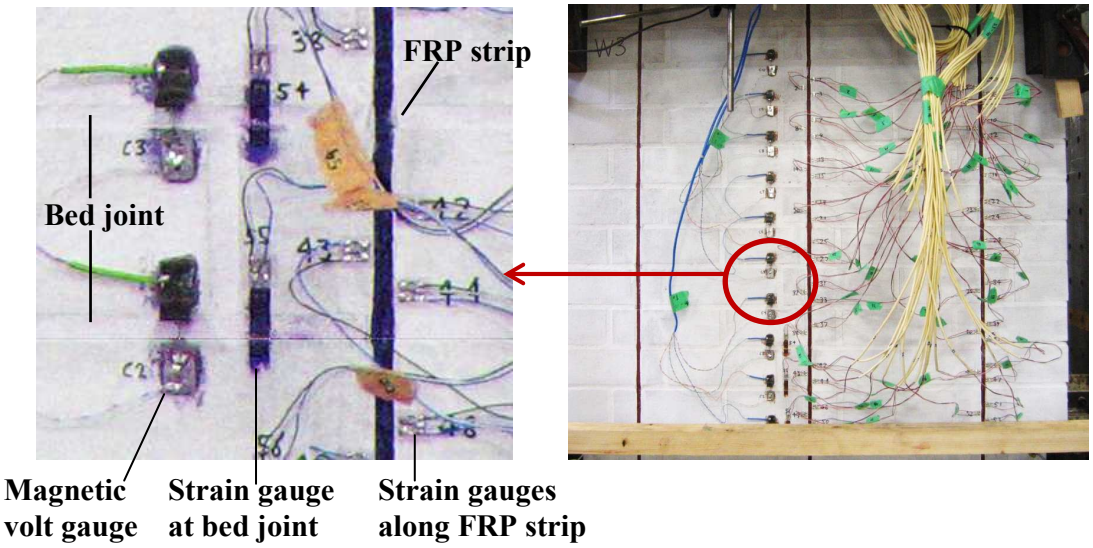

Figure 5-16: Use of volt gauge and strain gauge for crack detection

Although, volt gauges and strain gauges could detect the cracks with reasonable accuracy, there was still some uncertainty in the ability of the gauges to detect the first opening of cracks. Therefore, volt gauges were replaced with more sensitive LVDTs (Figure 5-17) to gain a better understanding of the wall behaviour as they could record the crack width along with more accurate recording of crack initiation. Three LVDTs were first trialled along the bed joint on the tensile face of wall 10 and then for walls 11-15, six LVDTs were used. For cyclic tests, 5 LVDTs were placed on the front face of the wall and only 1 on the back face.

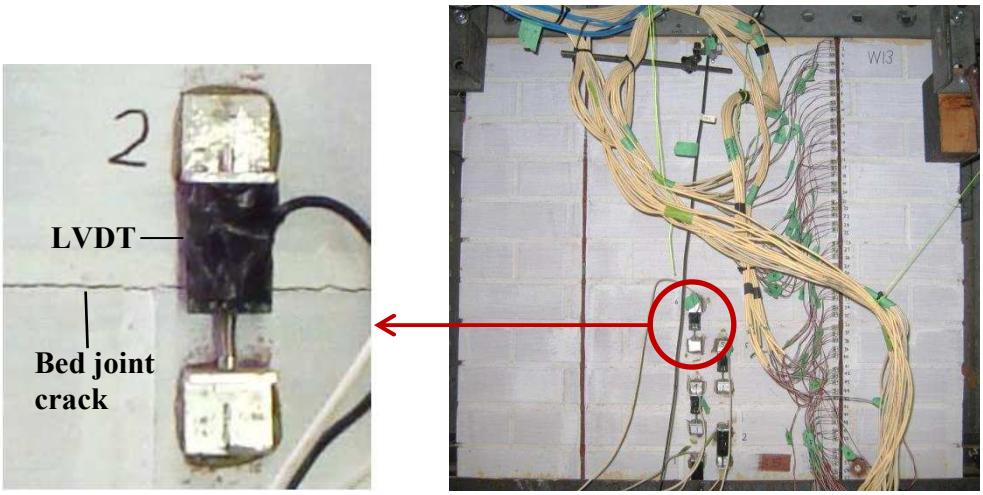

Figure 5-17: Use of LVDT for crack measurement

In addition to the above mentioned instrumentation, rulers were glued to the sides of the wall in order to give manual readings for crack details such as the depth and width of the crack, as shown in Figure 5-18. This helped in the visual analysis of the cracking formation. Also, during testing many photographs were taken along with the video recording for most of the tests. All the crack formation data recorded using visual observation, strain gauges, MVGs and LVDTs was finally compared and validated against each other.

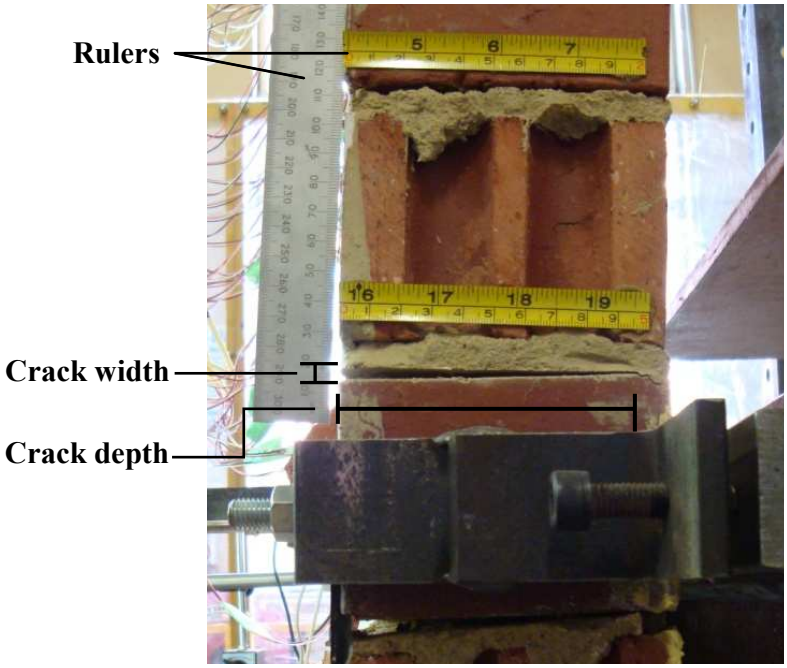

Figure 5-18: Use of Rulers to estimate crack height

CHAPTER 6
WALL BENDING TESTS RESULTS

6.1. Introduction

This chapter presents the test observations and results from fifteen wall tests. The description for each wall tests includes a discussion of: (1) the load versus deflection response; (2) axial strain and stress distribution in the FRP strips; and (3) failure mode descriptions. The chapter concludes with a discussion of the effects of different parameters on the flexural behaviour of NSM FRP reinforced masonry walls.

6.2. Test results

6.2.1. Wall 1

Wall 1 was 355 mm wide (corresponding to 1.5-brick unit lengths) and was tested under four point monotonic loading as shown in Figure 6-1. The wall was reinforced with one NSM FRP strip having cross-sectional dimensions of 3.6 mm (i.e. three 1.2 mm layers adhered together) x 10 mm which corresponds to a reinforcement ratio of ρ = 0.092%. Axial strain data along the FRP strip, the applied load and displacements at the mid-span and supports were recorded during testing. During this first test data it was observed that the bottom wall support moved (in the order of 10 mm), thus the maximum displacement, Δ_{ult} for wall-1 is not reported. The supports were bolted in all of the subsequent wall tests to prevent similar movement. The maximum strain recorded in the FRP strip during this test was ε_{max} = 9837 $\mu\varepsilon$ which occurred when the applied load was at its maximum value of F_{max} = 18.6 kN. This was 60% of the rupture strain, $\varepsilon_{rup.}$

The ultimate failure was due to a combination of IC debonding of the FRP strip and masonry crushing. During this test hairline cracks became visible in the bed joints

near the constant moment region just above and below the loading points, at approximately 5-8 kN of load. As the load was increased, the existing cracks widened, developing into the herringbone cracking pattern shown in Figure 6-1 along the FRP strip. The orientation of the herringbone cracks with respect to the primary flexural crack indicates that debonding propagated away from the primary crack towards the supports, that is from the region of high to low moment.

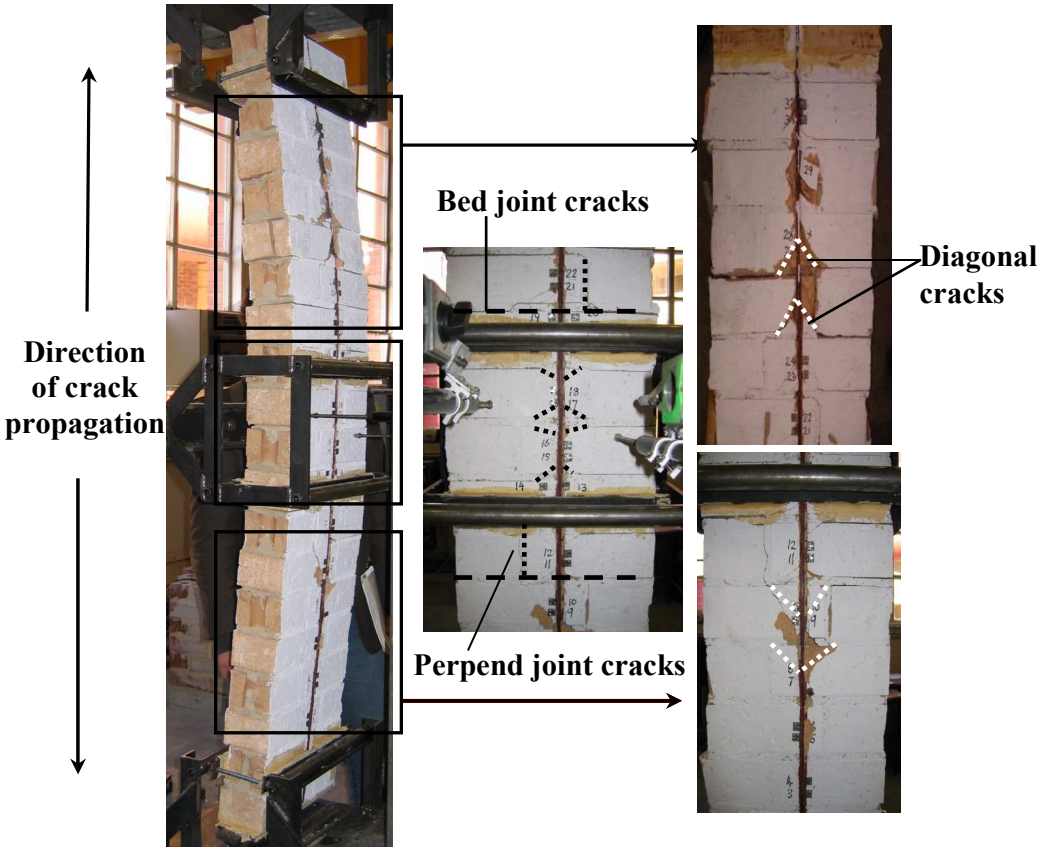

Figure 6-1: IC debonding failure in wall 1

Extensive cracking in the masonry was eventually also observed outside the constant moment region as debonding slowly propagated towards the unloaded ends of the FRP strips near the supports. At failure, wedges formed from diagonal cracks exploded off the tension face of the wall. Further, as shown in Figure 6-2, major cracks were also observed within a few bricks near the loading points resulting in lengthwise/width wise splitting of the brick units. Importantly, from the cross-sectional analysis, it was found that the strain at the extreme compression face (0.0018) calculated using the maximum recorded strain in FRP, exceeded the masonry crushing strain (0.0016) (see Appendix §E.3.1 for calculations) which is in

agreement with the observation that at maximum load there was some evidence of crushing of the brickwork on the compression face of the wall. For wall 1, the failure occurred above the top loading plate which was probably due to the fact that the lower compressive stresses in the top half of the wall would increase the chance of IC debonding in this half. After failure, clay brick masonry residue was still attached to the FRP strip showing that debonding occurred within the brick material at the FRP-to-masonry interface.

Figure 6-2: Failure on compression face of test specimen

The load-displacement response for wall 1 is shown in Figure 6-3 where it can be seen that there was a change in the stiffness at a very early stage of loading, approximately 2 kN, which is when the primary flexural crack occurred at the wall mid-height. This point also corresponds to the unreinforced masonry bending capacity, F_{URM} as shown by the dotted line in Figure 6-3 after which point the load is supported by the FRP strip. It should be noted that the vertical bending capacity of 18.6 kN for wall 1 was approximately 14 times higher than its unreinforced bending capacity, F_{URM} of 1.3 kN. Despite the relatively low reinforcement ratio of 0.092%, this demonstrates the substantial increase in strength that is possible with this retrofitting scheme.

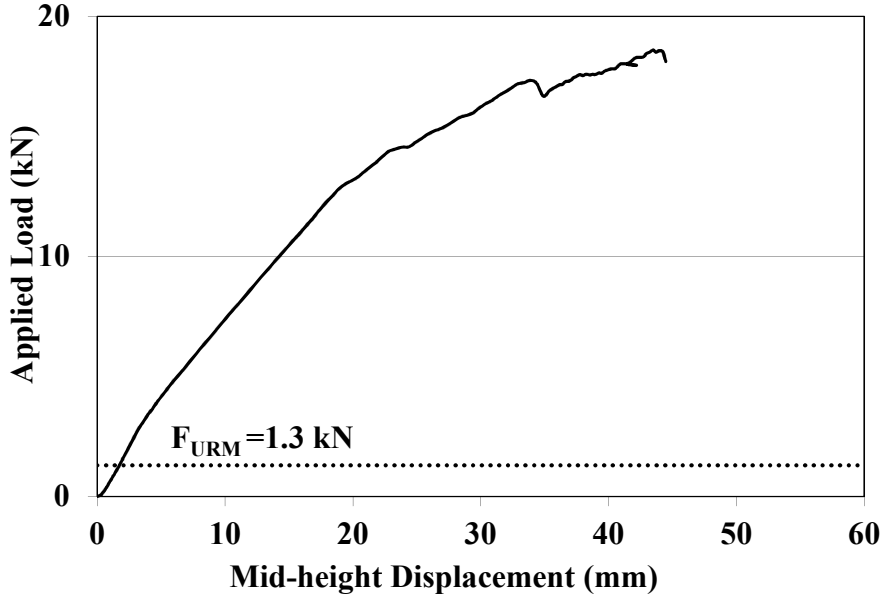

Figure 6-3: Load-displacement* response for wall 1
***Note: Displacement is indicative only as supports moved during test.**

As mentioned in §5.6.1, wall 1 was instrumented with two strain gauges per brick. Figure 6-4 shows the strain distribution for wall 1. From the literature review (Gravina and Smith, 2008), it was expected that troughs in the strain distribution would occur between cracked sections and that sharp peaks in strain would occur at crack locations. However, due to the fact that there were only two strain gauges per brick, only one shear stress value per brick could be calculated. Hence, these features could not be captured from the strains recorded for wall 1.

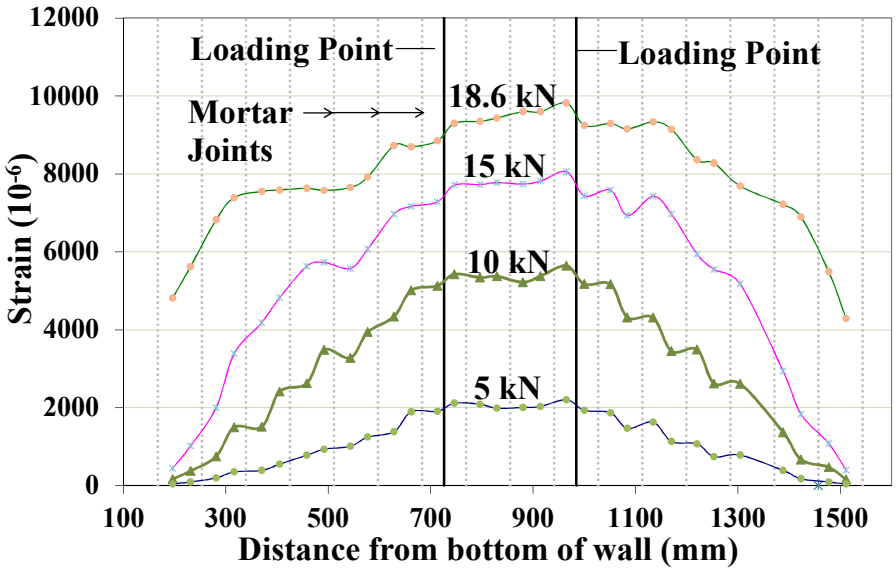

Figure 6-4: Strain distribution for wall 1

6.2.2. Wall 2

Wall 2 was a repeat of the monotonic test for wall 1 but this time with the bottom support movement prevented. The overall response of wall 2, including failure mode, was similar to wall 1 with maximum recorded values of ε_{max} = 9987 με (61% of ε_{rup}) and F_{max} = 18.5 kN. In addition, the maximum wall deflection, Δ_{ult} was recorded as 36.6 mm. The load displacement plot for wall 2 is shown in Figure 6-5.

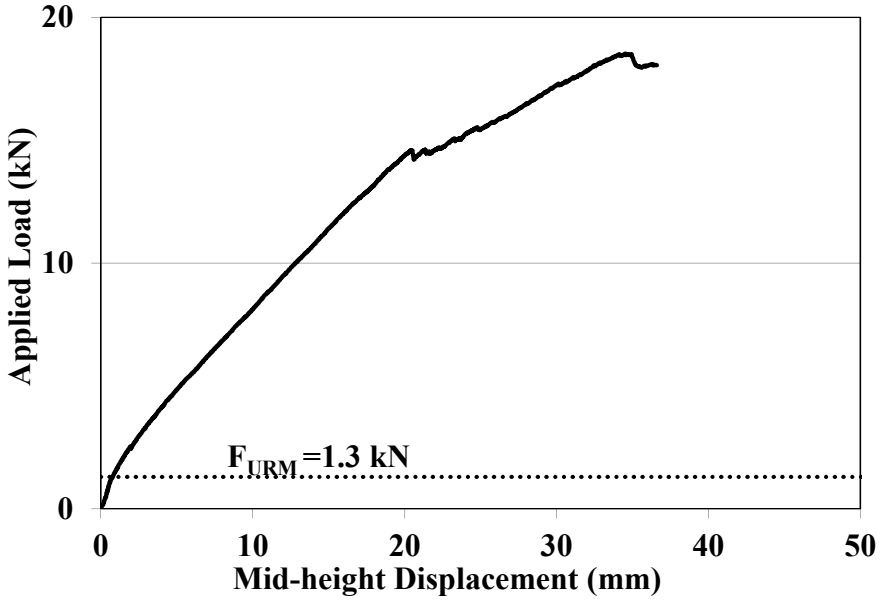

Figure 6-5: Load displacement plot for wall 2

The main difference observed in the response of wall 2 (compared to wall 1) was that it was slightly stiffer, no doubt due to the absence of the support movement that occurred in test 1. Similar to the wall 1 test, at a load of 2 kN load the primary crack occurred in the wall at mid-height causing a slight reduction in stiffness. The response under further loading was more or less linear until masonry crushing began at about 15 kN which further contributed to a notable loss of stiffness. From the cross-section analysis for wall 2 using the maximum FRP strain from the test data, the compressive strain was estimated to be 0.0018 which exceeded the masonry crushing strain of 0.0016 (see Appendix §E.3.2).

In order to improve the resolution in the plots of strain and shear stress distribution, the FRP strip in wall 2 had three strain gauges per brick. As seen in the strain distribution plot for wall 2 (Figure 6-6), due to the presence of a third strain gauge

the expected troughs in the strain distribution near the middle of the brick were recorded. This change in strain corresponds to a stress reversal in the shear bond slip between the FRP strip and the masonry. While there is lack of information for the expected peaks in FRP strain immediately adjacent to crack locations, extrapolation from the centre of the brick units out towards the mortar joints suggest that peaks should occur at cracked sections (Figure 6-6).

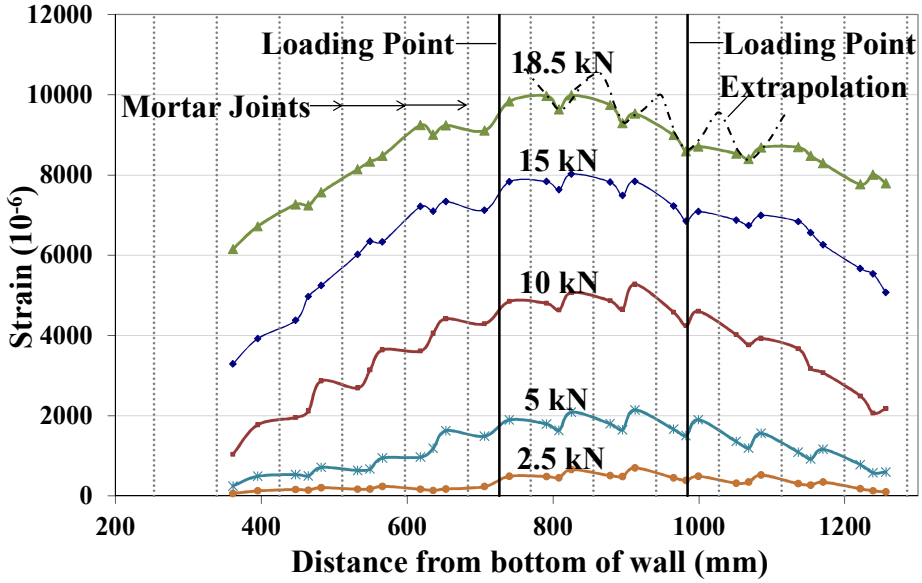

Figure 6-6: Strain distribution for wall 2

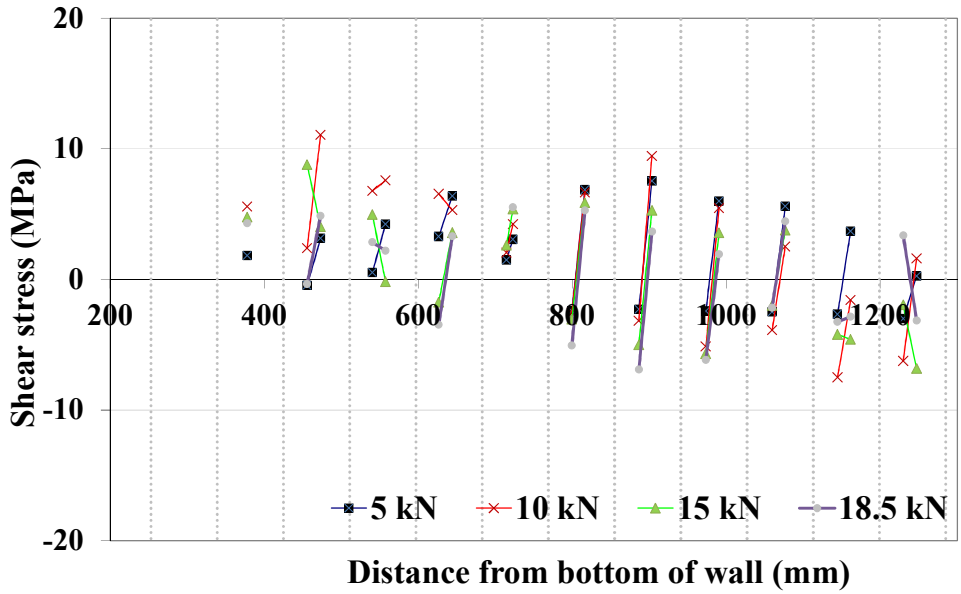

Figure 6-7: Shear stress distribution for wall 2

As wall 2 had three strain gauges per brick, two shear bond stress values could be calculated per brick to give an indication of the distribution as well as magnitude of the shear bond stress along the FRP strips as shown in Figure 6-7. From Figure 6-7, it can be observed that shear stress reversals occur within the brick unit due to cracks that are formed at the mortar joints. Further, it can be noted that high shear stress were recorded at early stages of loading, especially near the loading points, with values reducing towards the supports. The limited numbers of data points for shear stress were not especially helpful for analysing wall behaviour. It was interesting to note that the maximum shear stress was calculated as 11 MPa. This was similar to the 10.8 MPa value calculated from the pull test for a strip with similar dimensions.

The difference in strip behaviour in the top half and bottom half of the wall was investigated by comparing strains above and below mid-height for wall 2 (Figure 6-8). As shown in Figure 6-8, the differences were found to be minimal and were put down to experimental variability. This indicates that similar debonding processes occurs in the top and bottom half of the wall and as discussed earlier, debonding progresses from mid-height of the wall towards the supports. This verifies that the strain data recorded above mid-height is representative of the strains below mid-height.

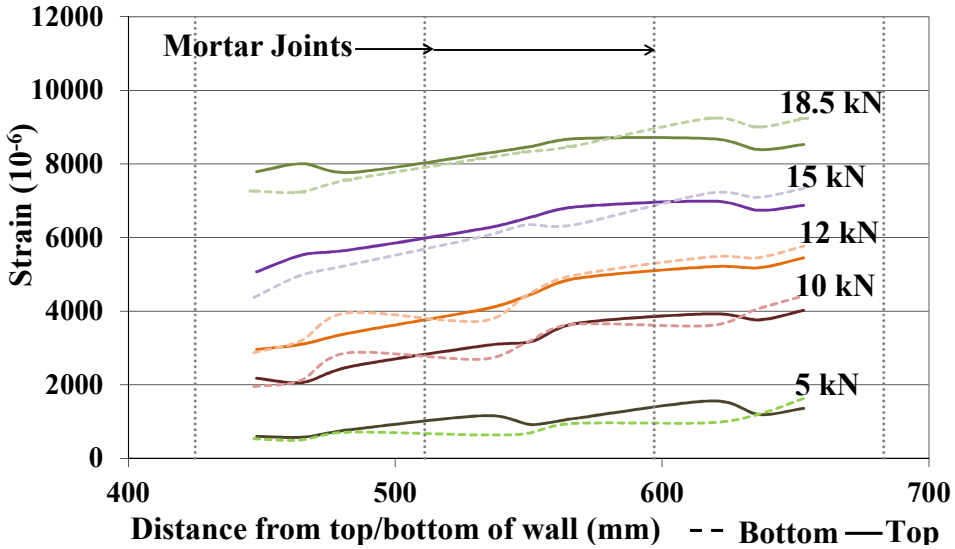

Figure 6-8: Comparison of strain below and above mid-height for wall 2

6.2.3. Wall 3

The test configuration for Wall 3 was similar to that for walls 1 and 2, the main difference being that Wall 3 was subjected to reverse cyclic loading. Wall 3 had recorded values of ε_{max} = 8298 με (approximately 50 % of ε_{rup}); F_{max} = 15.6 kN and Δ_{ult} = 30.3 mm. Similar to walls 1 and 2, debonding commenced outside of the constant moment region where higher slips were generated. As the load approached the peak load, severe diagonal cracking was followed by masonry crushing on both faces of the wall. Hence, final failure was due to a combination of IC debonding and masonry crushing (as for walls 1 and 2). From the cross-sectional analysis, it was found that the maximum compressive strain (0.0015) was very close to the masonry crushing strain (0.0016) (Refer Appendix §E.3.3 for calculations).

The global load-displacement response for wall 3, shown in Figure 6-9, closely follows the load-displacement envelope of the monotonic tests (walls 1, 2), suggesting that cyclic loading has only a small effect on the response of a CFRP NSM strengthened masonry wall. The level of cycle-to-cycle degradation was relatively small. The greatest energy dissipation occurring in wall 3 was generally observed in the first cycle of each increment of displacement due to the formation of new cracks, as seen in Figure 6-9. Compared to monotonic loading, reverse-cyclic loading reduced the strength and the displacement capacity by an average of 16% and 17%, respectively.

As mentioned in §5.6.1, wall 3 was instrumented with only two strain gauges per brick. Hence, the strain profile for wall 3 did not provide much information about the wall behaviour. Therefore, strain and shear stress distributions of wall 3 are not discussed here.

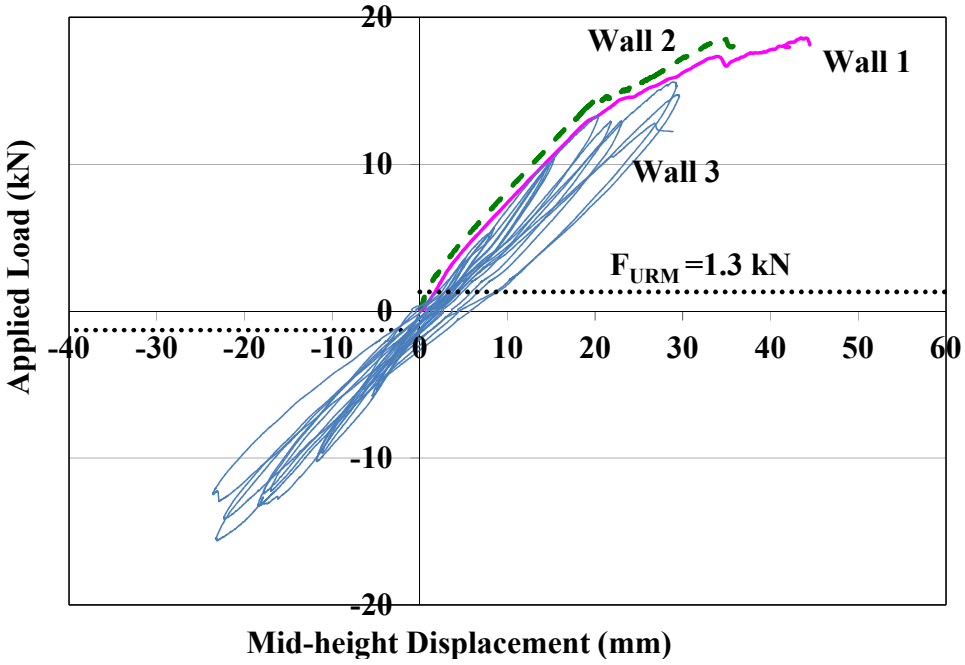

Figure 6-9: Load-displacement response for wall 3

6.2.4. Wall 4

The test configuration of Wall 4 was similar to walls 1 and 2, the main difference being that Wall 4 was 230 mm wide with a reinforcement ratio of 0.142% compared to 0.092% used in walls 1 and 2. The main objective for testing wall 4 was to get detailed strain and stress distributions by using seven strain gauges per brick. This wall had recorded values of ε_{max} = 8298 με; F_{max} = 15.6 kN and Δ_{ult} = 30.3 mm. As can be seen in Figure 6-10, wall 4 failed due to a combination of IC debonding and masonry crushing due to the higher reinforcement ratio used in this wall.

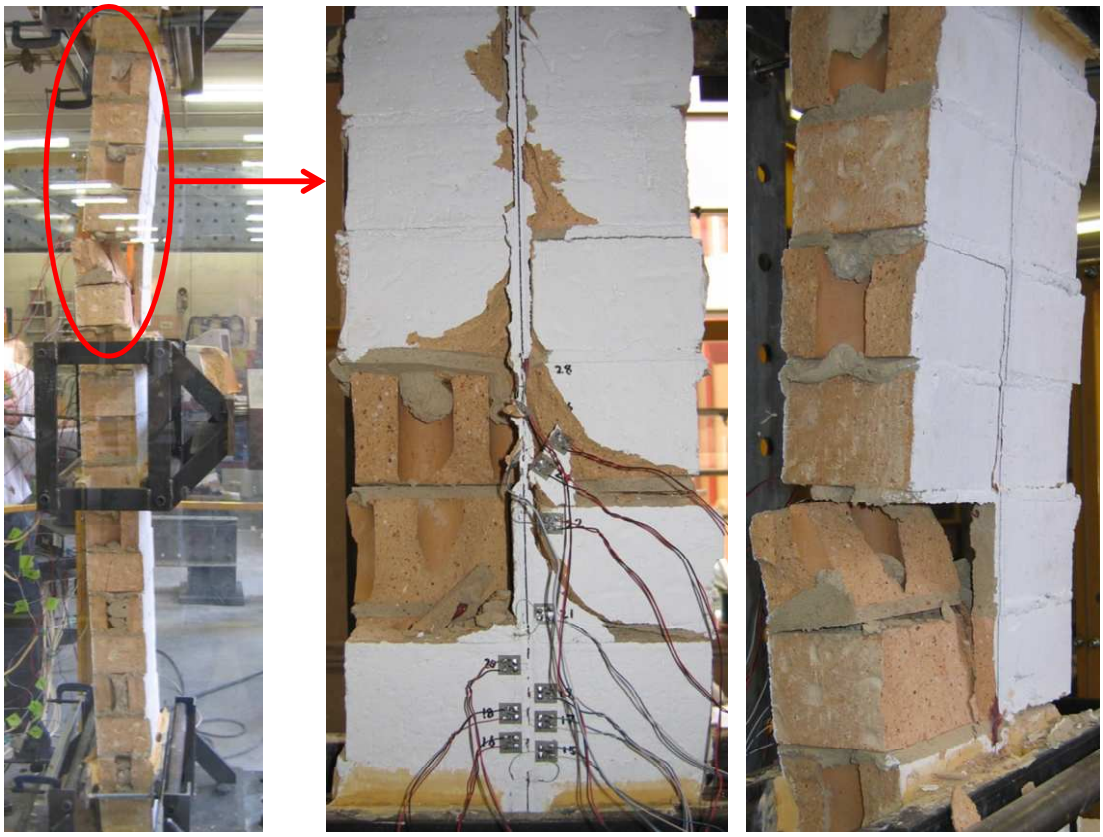

(a) Side view **(b)Tension face** **(c) Compression face**

Figure 6-10: Failure mechanism in wall 4

Some masonry residue was attached to the FRP strip indicating that debonding was at FRP-to-masonry interface. However, IC debonding did not develop fully particularly in the lower half of the wall. Along with the mortar joints, some cracks appeared at the perpend joints which continued through to the adjacent brick. It was noted that due to the comparatively high reinforcement ratio, the wall exhibited severe masonry crushing as the load approached its peak. Extensive cracking in the masonry was concentrated near the upper loading point with failure occurring just above the top loading plate (Figure 6-10). This was in agreement with the cross-sectional analysis results which indicated that the strain on the compression face (0.0018) exceeded the masonry crushing strain (0.0016) (see Appendix §E.3.4).

From Figure 6-11, it can be noted that the load-displacement response of wall 4 was similar to that of walls 1-3. Importantly, even though the reinforcement ratio of wall 4 was higher compared than walls 1-3, the peak load achieved was lower. This was thought to be because of the lower bond strength due to FRP strip passing through

perpend joints and premature failure of wall due to crushing. Consistent with the idea that the bond strength was lower in wall 4, the maximum tensile strain recorded for wall 4 was only 8189 με which corresponds to 50% of the rupture strain.

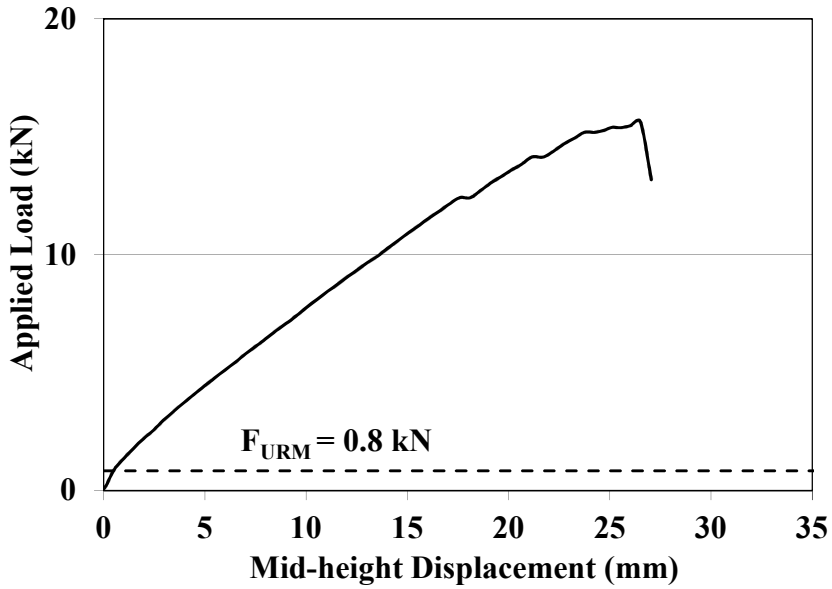

Figure 6-11: Load-displacement response of wall 4

Figure 6-12 and Figure 6-13 show the strain profile and shear stress distribution for wall 4, respectively. To improve the resolution of strain distribution, four bricks in wall 4 were heavily instrumented with seven strain gauges per brick. As expected from the extrapolation of wall 2 results (Figure 6-6), higher strains at the crack locations did occur (Figure 6-12). It can be noted that flexural cracks occurred at almost all mortar joints at early stages of loading due to the low brick-mortar tensile strength. This is indicated by strain being maximum at crack locations as tension is resisted solely by the FRP at cracks. However, the strain in between the cracks (i.e. bed joints) decreases as both the FRP and the masonry can resist the tensile strain.

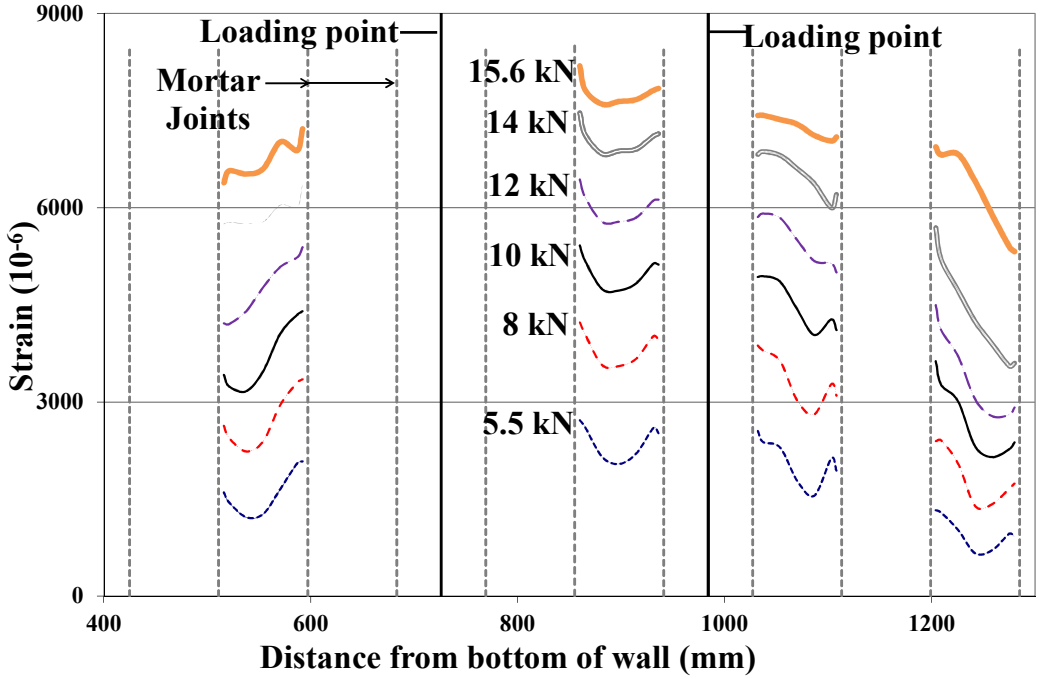

Figure 6-12: Strain distribution for Wall 4

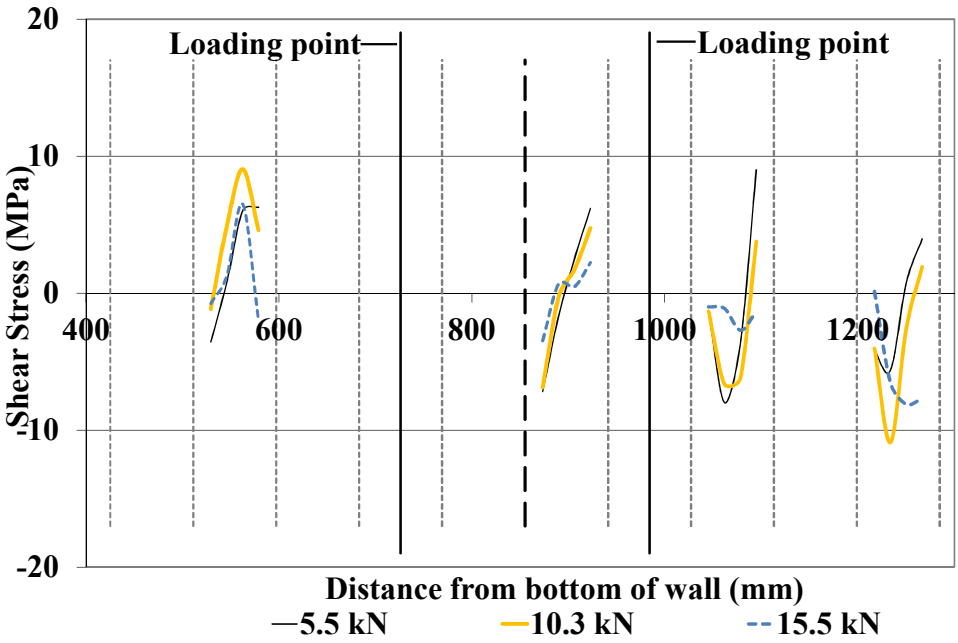

Figure 6-13: Shear stress distribution for wall 4

As the load gradually increased and reached its peak, the strain near the loading points outside constant moment region changed to linear distribution signifying unidirectional slip which is due to sufficient difference in the forces in the FRP at adjacent crack locations. This enables large enough slip to form and allow the debonding failure at the interface. This is in agreement with the experimental

observations, where with increasing loads orientation of the cracks became uniform towards the support and the debonding failure occurred in the shear spans where changes in moment exist. It is interesting to note that in the constant moment region, although the maximum strain exists in this region there is no such change in the strain profile probably as forces in the FRP at the adjacent crack locations are opposite in direction and similar in magnitude.Note that as only alternate bricks were strain gauged for wall 4 due to the FRP strip passing through perpend joints, a continuous stress profile could not be calculated. Nevertheless, it can be seen from Figure 6-13 that at early stages of loading the shear stress reversals occur within each brick due to cracks formed at the mortar joints. Also, due to the additional strain gauges used for this wall a more realistic picture of wall behaviour including signs of micro-cracking and softening at the interface could be captured.

6.2.5. Wall 5

This wall was the first tested as part of a group of walls that were used to investigate the effect of FRP strip spacing (walls 5, 6 and 8 - §6.3.2) and reinforcement ratio (walls 5 and 9 - §6.3.5). Wall 5 had the nominal masonry dimensions of 1070 x 2310 x 110 mm (width x height x thickness). Wall 5 was retrofitted on one face with one FRP strip having cross-sectional dimensions of 7.2 mm (i.e. six 1.2 mm layers adhered together) x 10 mm, corresponding to $\rho = 0.061\%$. The maximum recorded values for Wall 5 were $\varepsilon_{max} = 6998\ \mu\varepsilon$; $\Delta_{ult} = 49.2$ mm and $F_{max} = 17.1$ kN. However, the maximum strain recorded during the tests was only 42% of the rupture strain, indicating that the FRP was not used very efficiently.

Figure 6-14 shows the test specimen at failure. As can be seen, the main failure mode was IC debonding although IC debonding did not fully develop in the top half of the wall. In this region, the diagonal cracks that were formed at initial loading then intersected with the perpend joints at the end of the bricks on each side of the FRP strip (perpend shear failure) (Figure 6-14 (b)). This defined a new plane of weakness with the cracks in the perpends continuing in a vertical line through the brick units above each perpend joint. At this point, the vertical in-plane shear strength of the

masonry was unable to carry any more force so the strip and the masonry commenced to fail with fairly large pieces of brickwork attached.

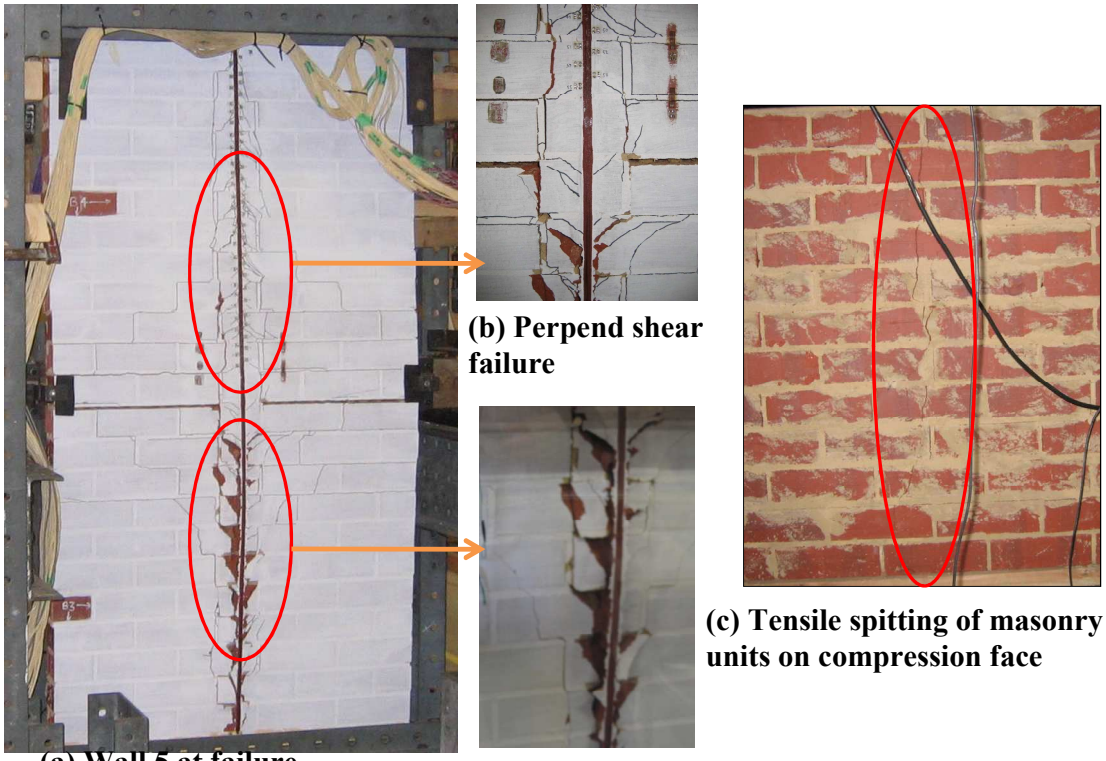

(a) Wall 5 at failure

(b) Perpend shear failure

(c) Tensile spitting of masonry units on compression face

(d) Curvature incompatibility

Figure 6-14: Failure pattern for wall 5

Another potential failure mechanism for which some early signs were observed was tensile splitting of the masonry units along a vertical line on the compression face of the wall opposite the FRP strip (Figure 6-14(c)). It is thought that this can be avoided by keeping the compression face strain well below the masonry crushing strain of 0.0016. From the cross-section analysis for wall 5 using the maximum FRP strain from the test data, the compressive strain was estimated to be 0.0010 (Appendix §E.3.5).

At final failure, the FRP strip popped out of the tension face of the bottom half of the wall (Figure 6-14(d)). By virtue of the large FRP cross-section used in wall 5, the force in the strip so was high that it may have contributed to the onset of perpend shear failure and tensile splitting cracks on the compression face. Therefore, it

appears that the use of the larger size strip and spacing used in this wall made it more susceptible to the above mentioned failure mechanisms other than IC debonding.

As seen from the load-displacement response of wall 5 (Figure 6-15), debonding initiated at approximately 10-12 kN after which the reduction in strength and stiffness of the member became more apparent. The IC debonding resistance (P_{IC}) from the corresponding pull test (with similar strip dimensions) was used to predict the applied load at the onset of debonding, F_{IC} (refer Appendix §E.4.1 for calculations). The cross-sectional analysis indicated that for wall 5 debonding would initiate at about 12 kN which is in agreement with the experimental observation.

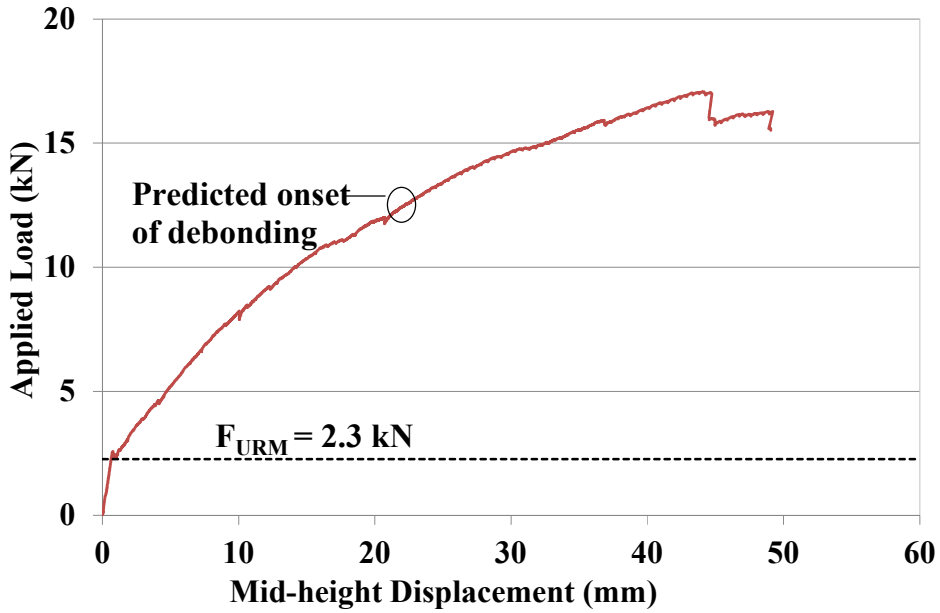

Figure 6-15: Load displacement response for wall 5

Figure 6-16 and Figure 6-17 show the strain and shear stress distributions, respectively, for wall 5. It can be noted that flexural cracks, indicated by peaks in the strain profile, occurred at mortar joints as early as 2.5 kN of loading. As the load approaches the peak load, the mid-height region shows a nearly constant strain profile indicating full debonding in that region.

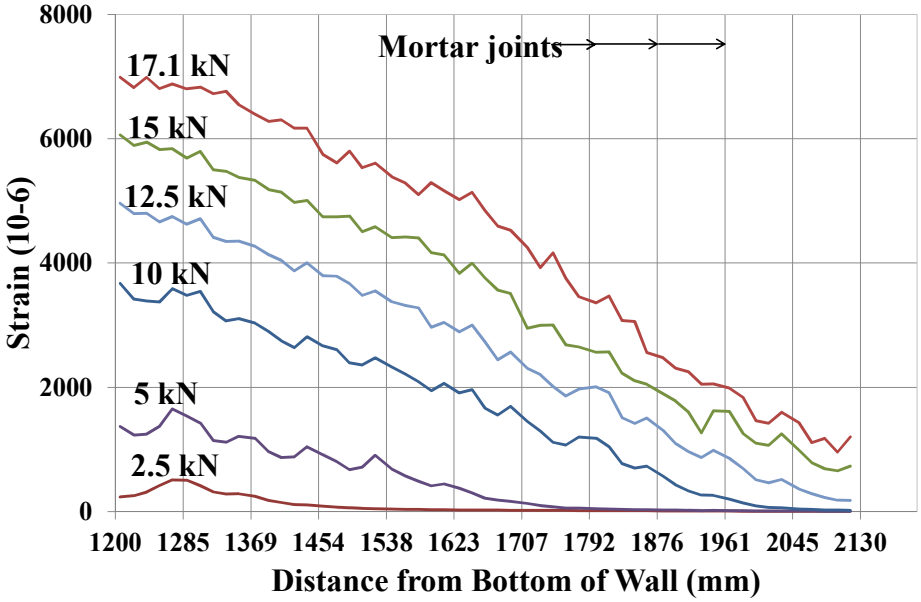

Figure 6-16: Strain distribution for wall 5

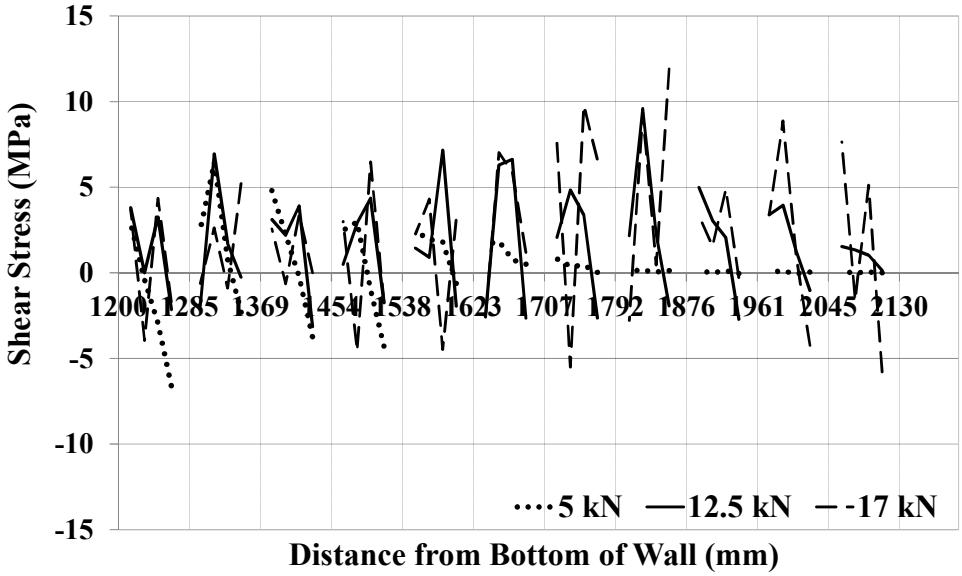

Figure 6-17: Shear stress distribution for wall 5

Figure 6-17 shows the shear stress distribution for the top half of wall 5. The maximum bond stress was calculated to be 12 MPa and was lower than the 14.8 MPa calculated from the pull test with similar strip size (P1-P4). As seen in Figure 6-17, at early loading shear stress reversals can be observed near the wall mid-height whereas the bricks near the support had not yet been fully engaged. As the load approached its peak value of 17 kN, the shear stress near the wall mid-height reduced. However, the stress does not reduce to zero (corresponding to full debonding) at the peak load due to a residual friction component of shear stress. As expected, the maximum shear

stress shifts towards the support as load increased confirming that debonding propagated the from mid-height towards the wall supports.

As mentioned in §5.6.2, MVGs and strain gauges were placed across mortar bed joints for the first time in wall 5 to try and detect the onset of cracking. Figure 6-18 shows the crack development using the MVGs and strain gauges. It can be noted that the loads corresponding to cracking initiation from the strain gauges and MVGs are reasonably consistent. The small variations between the two readings can be attributed to the propagation of crack from one point to another and to the slight offsets between the position of the strain gauges and MVGs.

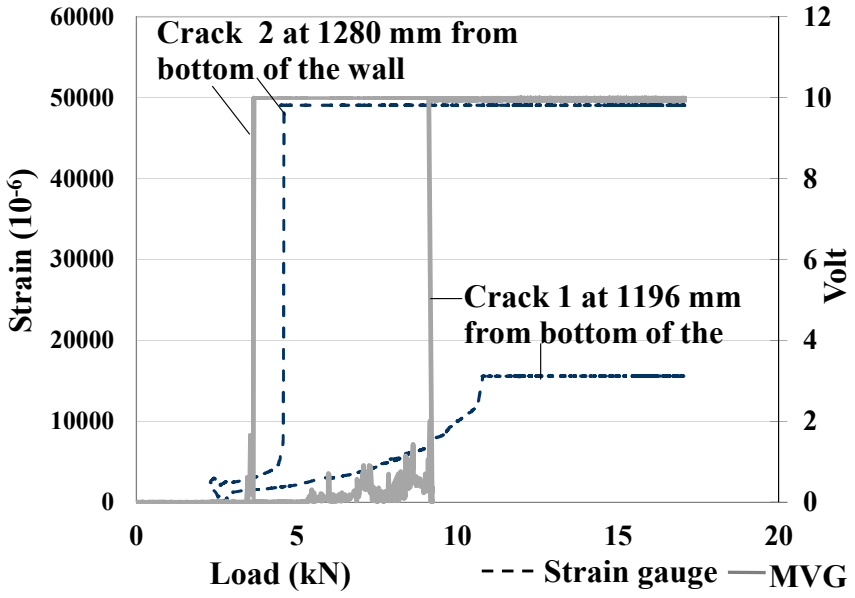

Figure 6-18: Crack development in wall 5

6.2.6. Wall 6

This wall was retrofitted on its tension face with two 4.8x7.5 mm FRP strips. The FRP reinforcement ratio used in wall 6 was same as wall 5 (0.061%) but the strips were spaced symmetrical about the wall centerline 535 mm apart. . Wall 6 had maximum recorded values for ε_{max} = 10989 με; Δ_{ult} = 70 mm and F_{max} = 27 kN which were all noticeably higher than for wall 5. The maximum strain recorded during the test was observed to be approximately 67% of ε_{rup} indicating much better use of reinforcement as compared to wall 5.

As can be seen from Figure 6-19, IC debonding from masonry started at a flexural crack at wall mid-height and propagated towards the support with the usual herringbone cracking pattern (Figure 6-19(a)). The debonded strip had some masonry residue attached to it (Figure 6-19(d)) show that debonding failure was at FRP-masonry interface. While the other failure mechanisms observed during testing for wall 5 were also seen for wall 6, they were significantly less pronounced. For example, perpend shear failure was limited to just a few bricks (Figure 6-19(b)).

Figure 6-20 shows the load-displacement response for wall 6. In comparison to wall 5, distribution of FRP along the wall resulted in a stiffer load-displacement response with a significant increase in strength (from 17 to 27 kN) and maximum displacement (from 49 to 70 mm). The overall improved behaviour compared to wall 5 was due to the reduced strip spacing and strip cross-section (> Lper in wall 6). As shown in Figure 6-20, the onset of debonding was approximated at the point (20-23 kN) where the load-displacement response changes slope (i.e. starts to soften). This is comparable to the predicted value of the IC debonding load (22 kN). Refer to Appendix §E.4.2 for calculations.

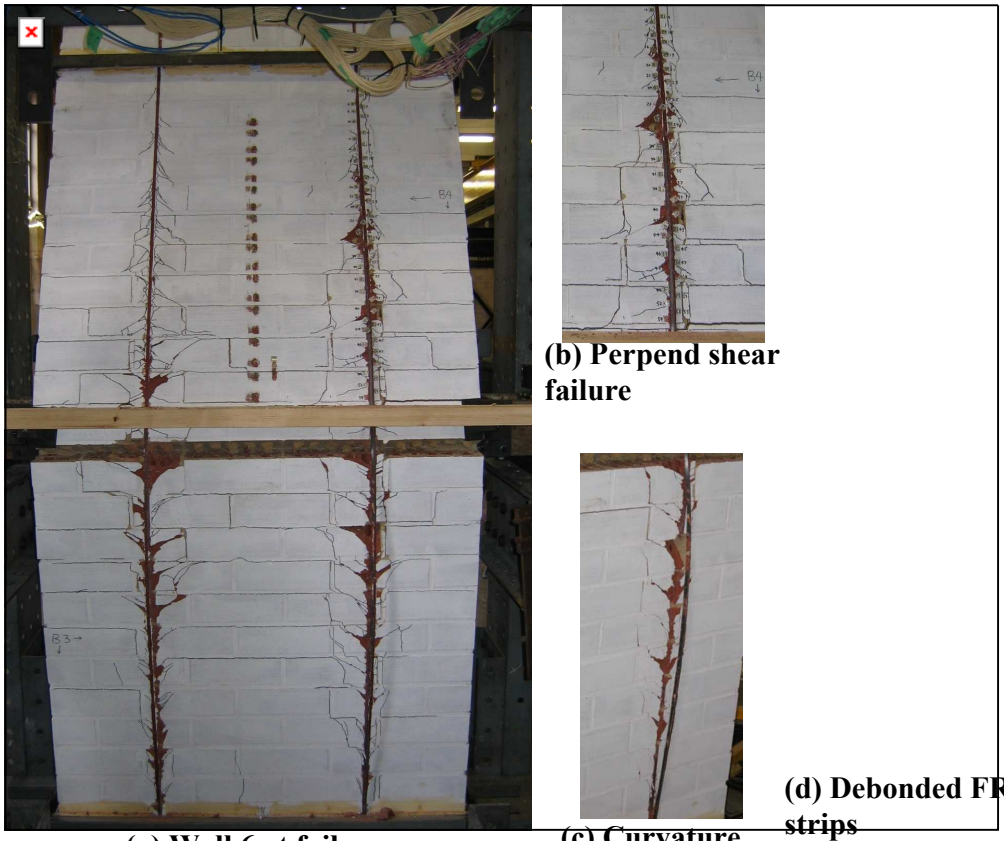

Figure 6-19: Failure pattern for wall 6

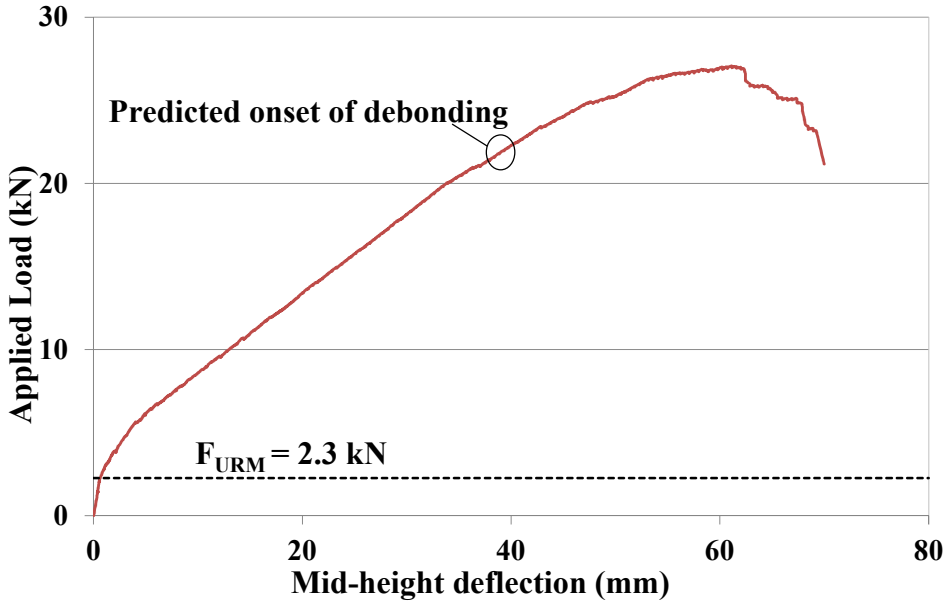

Figure 6-20: Load displacement response for wall 6

Figure 6-21 and Figure 6-22 show the strain and shear stress distribution for wall 6. It can be noted that considerable strain and stress was developed along the FRP-masonry interface at early stages of loading (5-10 kN) except over the few bricks near the support brick where the bond had not yet been fully engaged.

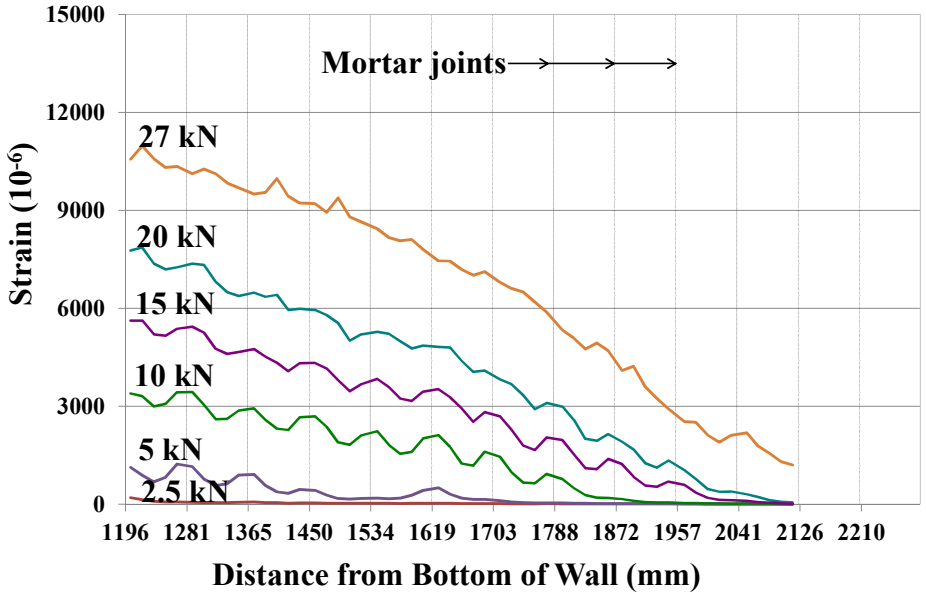

Figure 6-21: Strain distribution for wall 6

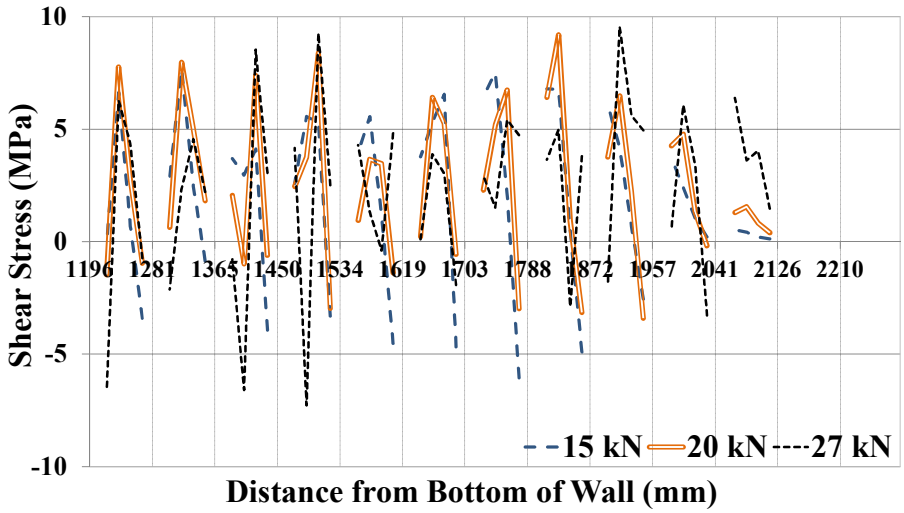

Figure 6-22: Shear stress distribution for wall 6

As the load increased, strain variations within a brick decreased (Figure 6-21) with the corresponding stress profile (Figure 6-22) showing unidirectional shear with propagation of micro-cracking and softening towards the support. At peak load, the strain profile (Figure 6-21) shows a mostly linear change of force in the FRP

indicating more or less full debonding. The maximum shear stress was noted as 9.15 MPa. This was noticeably lower than the 13.5 MPa calculated from the corresponding pull test with similar strip dimensions.

6.2.7. Wall 7

This wall was retrofitted on the tension face with three FRP strips each having a cross-section of 3.6 mm (i.e. three 1.2 mm layers adhered together) x 10 mm. The FRP reinforcement ratio used in wall 7 (0.092%) was 50% higher than in wall 6 (0.061%) and the strip spacing was 357 mm. As can be seen from Figure 6-23, wall 7 failed by IC debonding with herringbone cracking patterns along all three strips. At the final failure, the strip popped out of the wall (Figure 6-23) as seen in wall 5 and wall 6. The maximum recorded values for wall 7 were ε_{max} = 11889 με; Δ_{ult} = 75.7 mm and F_{max} = 41 kN. The maximum strain recorded during the tests was observed to be approximately 72% of the rupture strain indicating more efficient use of reinforcement than for wall 5. This is further discussed in §6.3.2.

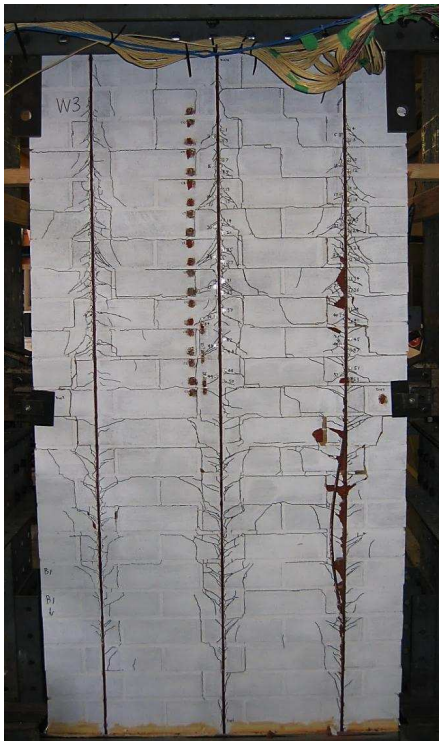

Figure 6-23: Failure pattern for wall 7

As shown in Figure 6-24, stiffness of the load-displacement response changed as debonding initiated at 35-38 kN (matches with the predicted F_{IC} of 35 kN – refer to Appendix §E.4.3) and the specimen starts to soften with diagonal cracking and debonding progressing from the mid-span flexural crack towards the supports, resulting in strength and stiffness reductions of the member. After reaching a load of 41 kN at a displacement of 75 mm the final failure occurred. Although, this wall had a 50% higher reinforcement ratio compared to wall 5 and 6, its much improved behaviour in terms of strength and displacement capacity and other failure mechanisms can also be attributed to the reduced strip spacing.

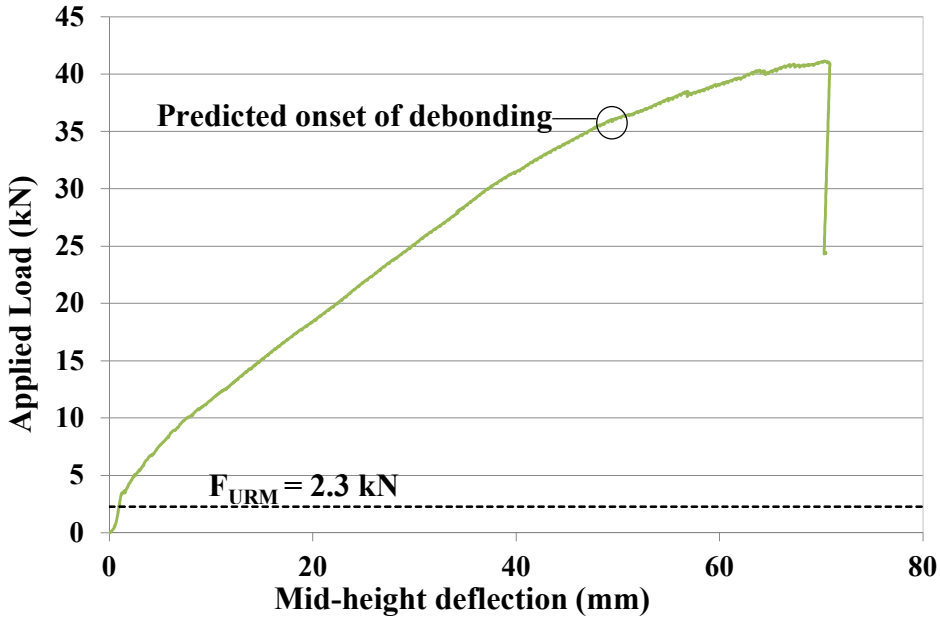

Figure 6-24: Load displacement response for wall 7

Figure 6-25 and Figure 6-26 shows the strain and stress distributions for wall 7 along the outer and central FRP strip. As can be seen from Figure 6-25, the strain distribution for the central strip is not continuous. This is because one of the strain gauges was faulty. It can be noted that the strain profiles along the outer and central strip match reasonably well, indicating more or less uniform bending across the wall's width. Peaks in strain at the mortar joints and troughs within the brick units can be noted at early stages of loading. However, as only three strain gauges per brick were used the peaks are not very clear. As the load increased and approached its peak, debonding progressed along the strip indicated by a nearly linear strain profile.

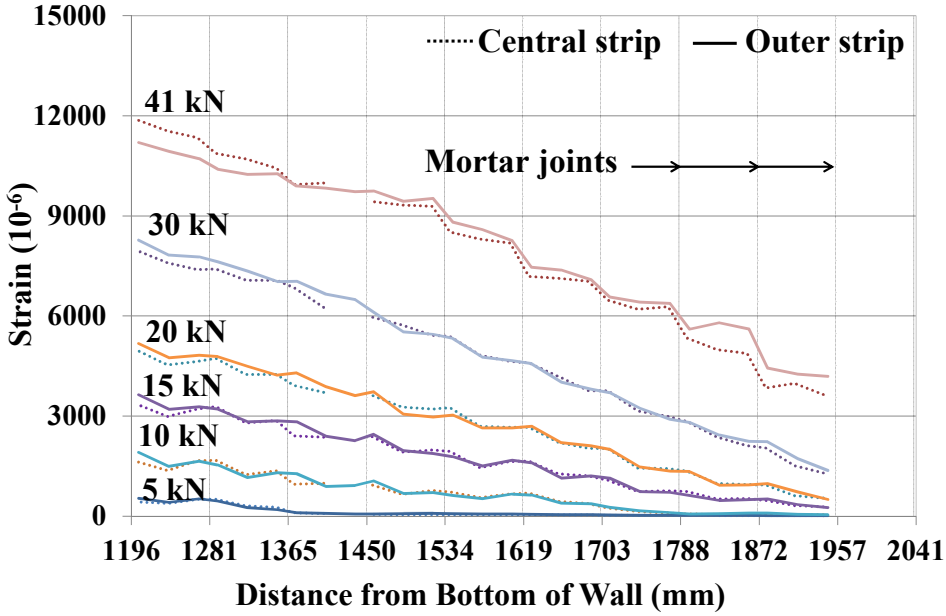

Figure 6-25: Strain distribution for wall 7

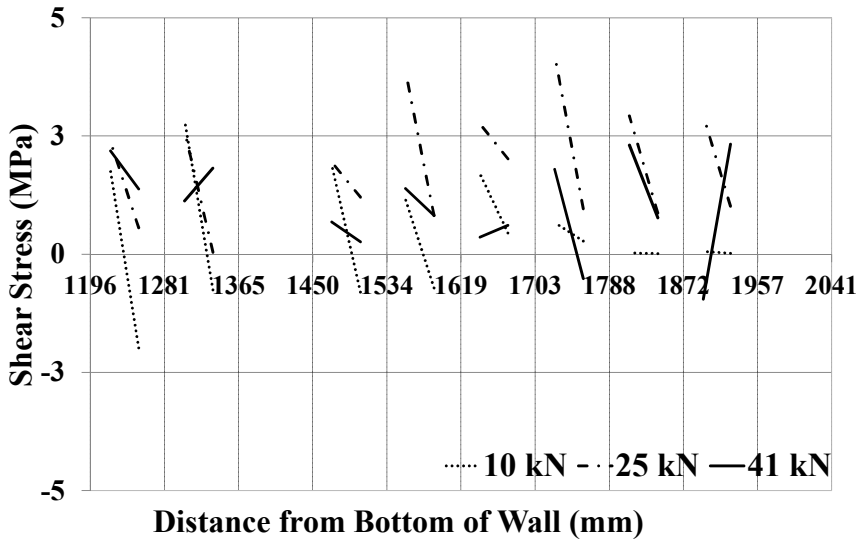

Figure 6-26: Shear stress distribution for wall 7

Figure 6-26 shows the shear stress distribution for wall 7. Signs of shear stress reversals were observed at early loads along the length of FRP except over the last few bricks which had not yet been fully engaged. As the load increased, stress reversal progressed towards the support indicating debonding propagation from mid-height to the support. Ultimately, signs of micro-cracking could not be captured as only three strain gauges per brick were used giving only two calculated shear stress values per brick.

6.2.8. Wall 8

This wall was retrofitted on the tension face with three 4.8 mm (i.e. four 1.2 mm layers adhered together) x 5 mm FRP strips. Hence, this wall had the same reinforcement ratio (0.061%) as walls 5 and 6. Figure 6-27 shows the test specimen at failure where it can be seen that the main failure mechanism for wall 8 was IC debonding at the FRP-masonry interface. However, an in-plane shear crack, parallel to the FRP strip and aligned with the perpend joints nearest to the strip, developed during this test. This was very noticeable, particularly in the top half of the wall for the strip at the centre (Figure 6-27(a)). These cracks spanned the thickness of the wall, and were also observed on the compression face (Figure 6-27(b)).

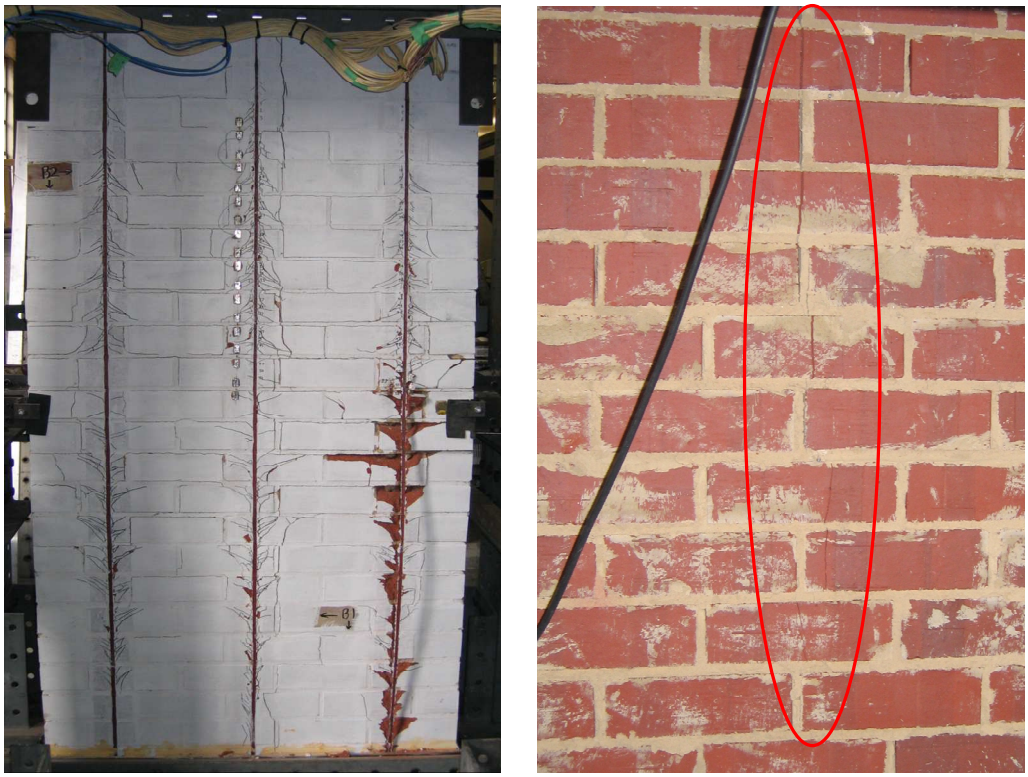

(a) Front view **(b) Compression face**

Figure 6-27: Failure pattern for wall 8

Wall 8 had maximum recorded values of ε_{max} = 12445 με; Δ_{ult} = 78.9 mm and F_{max} = 36.6 kN. The maximum strain recorded during the tests was observed to be approximately 76% of the rupture strain indicating efficient use of reinforcement. As seen in Figure 6-28, the load-displacement response for wall 8 showed a reduction in

strength and stiffness as the load increased and debonding progressed along the FRP strip.

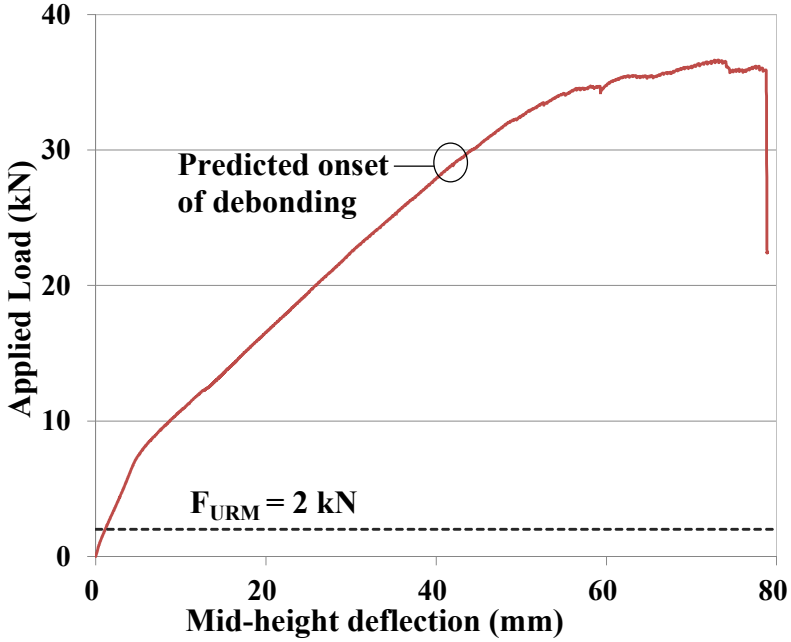

Figure 6-28: Load displacement response for wall 8

As the load approached the peak value (36.6 kN), the load-displacement curve plateaued with very little increment in load from displacement of 65 mm to Δ_{ult} = 79 mm indicating complete debonding. Although, this wall had the same total amount of reinforcement as walls 5 and 6, its much improved behaviour in terms of stiffness, strength and displacement capacity can be attributed to the reduced strip spacing.

6.2.9. Wall 9

This wall was retrofitted on its tension face with a single 3.6 mm (i.e. three 1.2 mm layers adhered together) x 10 mm FRP strip corresponding to a reinforcement ratio of 0.031%. The maximum recorded values for Wall 9 were ε_{max} = 9473 με; Δ_{ult} = 61.2 mm and F_{max} = 12.4 kN. (Figure 6-29).

As can be seen from Figure 6-29, the failure mechanism was through IC debonding although the herringbone cracking pattern had not fully developed. In the upper half of the wall, some perpend shear failure was observed whereas in the lower half stepped cracking was observed. Such wall behavior was considered to be due to the

large strip spacing used. The effect of strip spacing is discussed in §6.3.2.The maximum strain for wall 9 was observed to be approximately 58% of ε_{rup}. Note that this was higher than maximum strain recorded for wall 5 (43% of ε_{rup}) which had double the reinforcement ratio (0.061%). This is discussed further in §6.3.5.

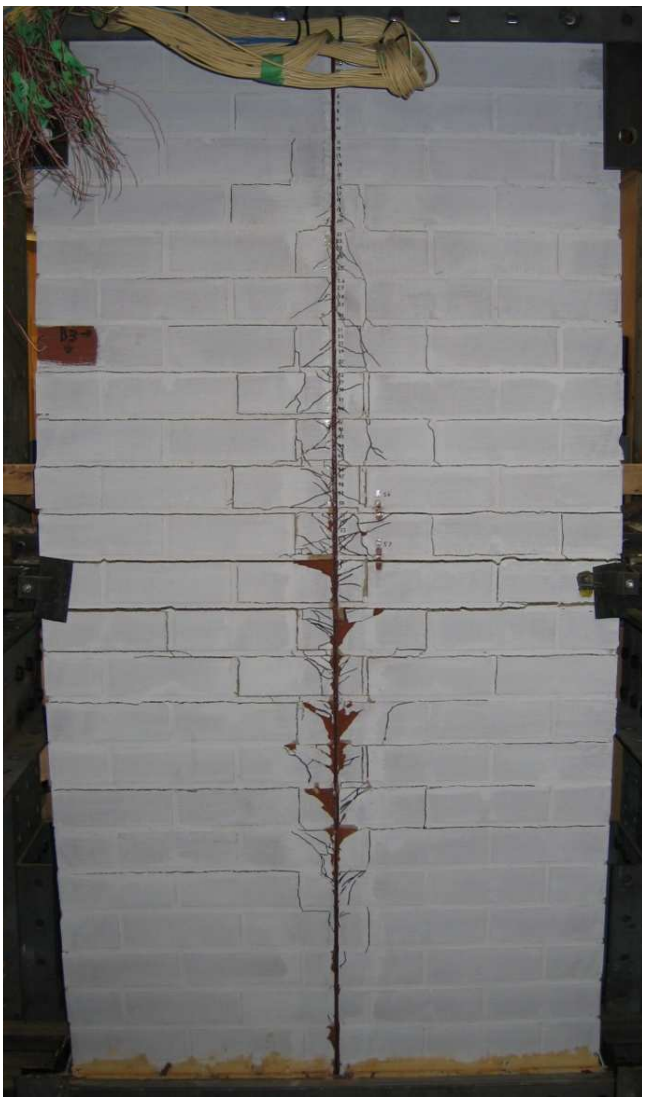

Figure 6-29: Failure pattern for wall 9

Figure 6-30 shows the load-displacement response for wall 9. Similar to the previous walls there was considerable reduction in stiffness after the initial tensile crack at mid-height occured in the masonry at approximately 2 kN. The overall response was less stiff than for wall 5 which also had a single strip but had twice the reinforcement. This is discussed in detail in §6.3.5. The cross-sectional analysis

predicted the onset of debonding at about 12 kN which is the maximum load for wall 9. This was probably due to the fact that the wall did not attain its full debonding capacity due to the single strip configuration resulting in other failure modes as discussed earlier.

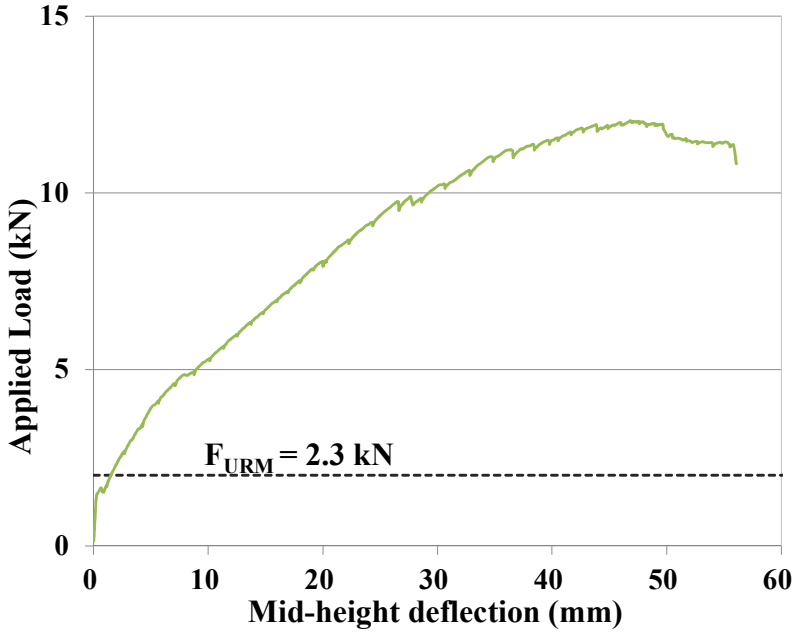

Figure 6-30: Load displacement response for wall 9

Figure 6-31 and Figure 6-32 show the strain and shear stress distributions for wall 9, respectively. As can be seen from these plots, some readings are missing due to strain gauge malfunction so could not be used for shear stress calculations. At 5 kN signs of shear reversals (Figure 6-32) can be noted for few bricks near wall mid-height. As load increases (10 kN), strain variation within a brick happens at decreased rate with corresponding stress profile showing unidirectional shear. At peak load (12 kN) linear change of force in the FRP and reduced shear stress can be observed for few bricks near wall mid-height region.

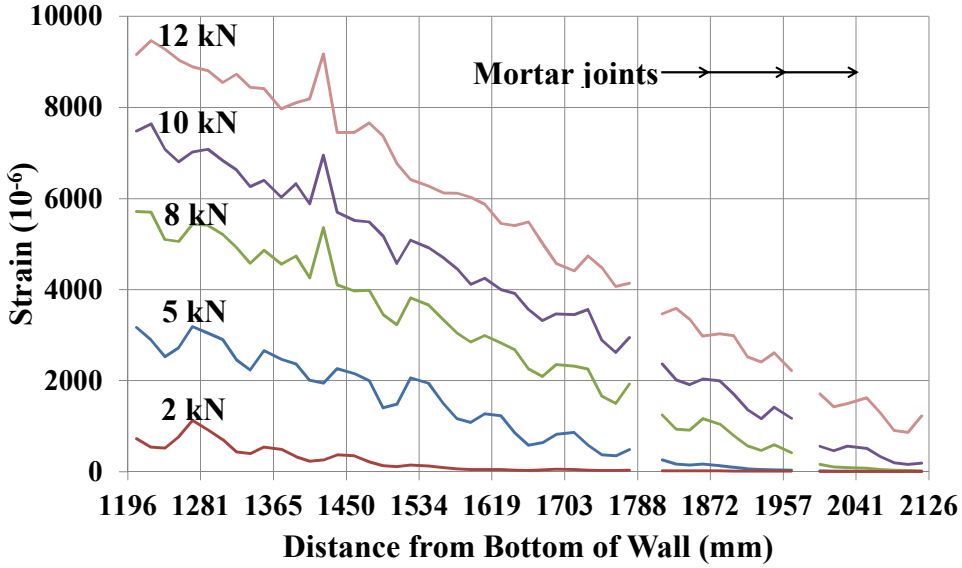

Figure 6-31: Strain distribution for wall 9

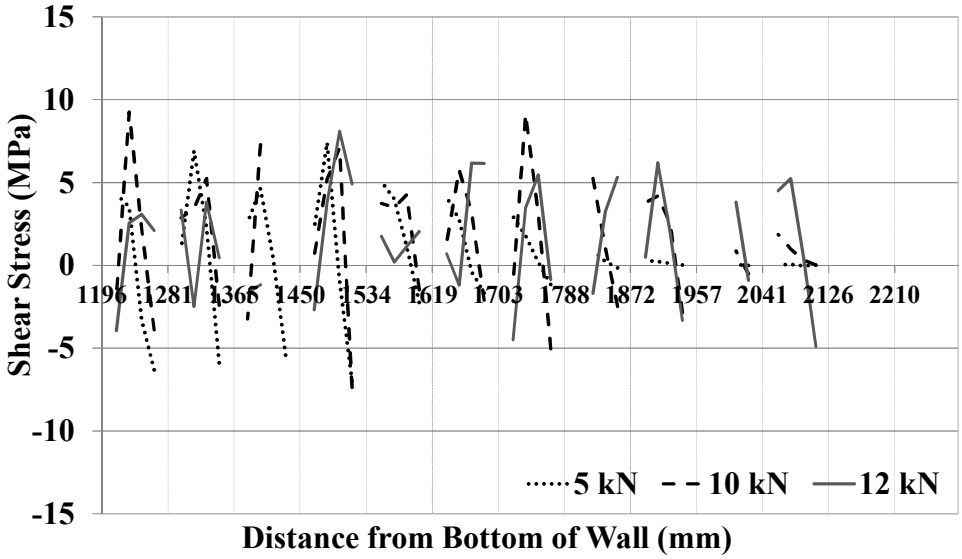

Figure 6-32: Stress distribution for wall 9

6.2.10. Wall 10

For walls 10-15, the reinforcement ratio was kept constant at 0.071% with all walls retrofitted with two FRP strips, each having a cross-sectional dimension of 4.2 mm (i.e. three 1.4 mm layers adhered together) x 10 mm. Wall 10 was subjected to a vertical pre-compression load of 0.1 MPa and monotonically loaded to failure . Wall 10 failed by IC debonding at the FRP-masonry interface as shown in Figure 6-33(a) although some tensile splitting of masonry units was also observed along a vertical

line on the compression force of the wall opposite to the NSM strip (Figure 6-33(b)). This was thought to be due to the plane of weakness caused by the FRP strip on opposite face.

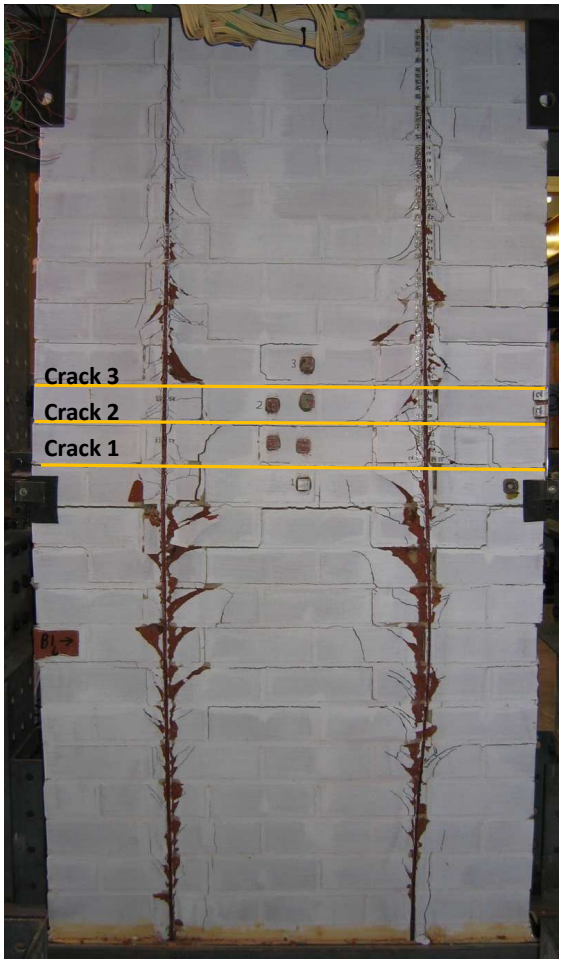

(a)Tension face

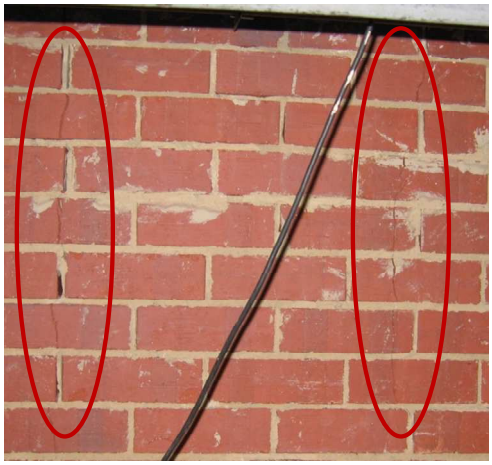

(b) Compression face

(c) Side view showing crack height

Figure 6-33: Failure pattern for wall 10

Maximum values recorded during the test for wall 10 were ε_{max} = 11092 με; Δ_{ult} = 69.3 mm and F_{max} = 30.8 kN. The maximum strain recorded during the tests was approximately 68% of the ε_{rup}. Figure 6-34 shows the load-displacement response for wall 10. In comparison to wall 6, the vertical axial load resulted in a stiffer load-displacement response with a slight increase in strength (about 15%) and a small reduction in maximum displacement (5%). For all walls 10-15, initiation of full debonding was predicted at a load of about 21 kN as similar strip configuration (i.e. two 4.2 x10 mm strips) was used for these walls.

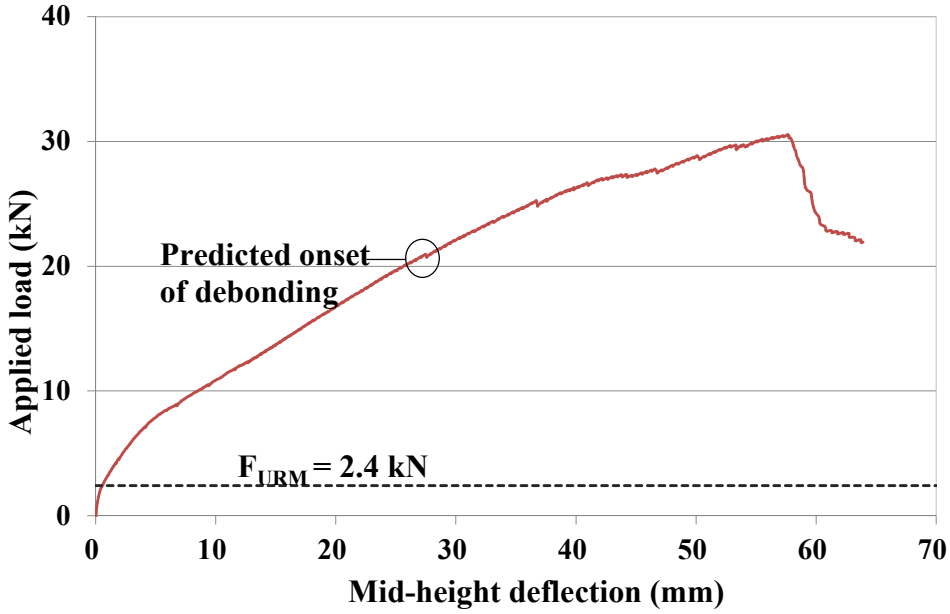

Figure 6-34: Load displacement response for wall 10

Figure 6-35 and Figure 6-36 show the strain and shear stress distributions for wall 10. Considerable strain and stress was developed along the FRP-masonry interface at early stages of loading (<10 kN) except over the few bricks near support brick where the bond had not yet been fully engaged. At a load of 15-20 kN , the strain and shear profiles show signs of softening stage for the almost entire wall length. At the peak load of 30kN there is noticeable degradation in the FRP-to-masonry bond with almost linear strain (Figure 6-35) and no shear reversals (Figure 6-36) indicating full debonding.

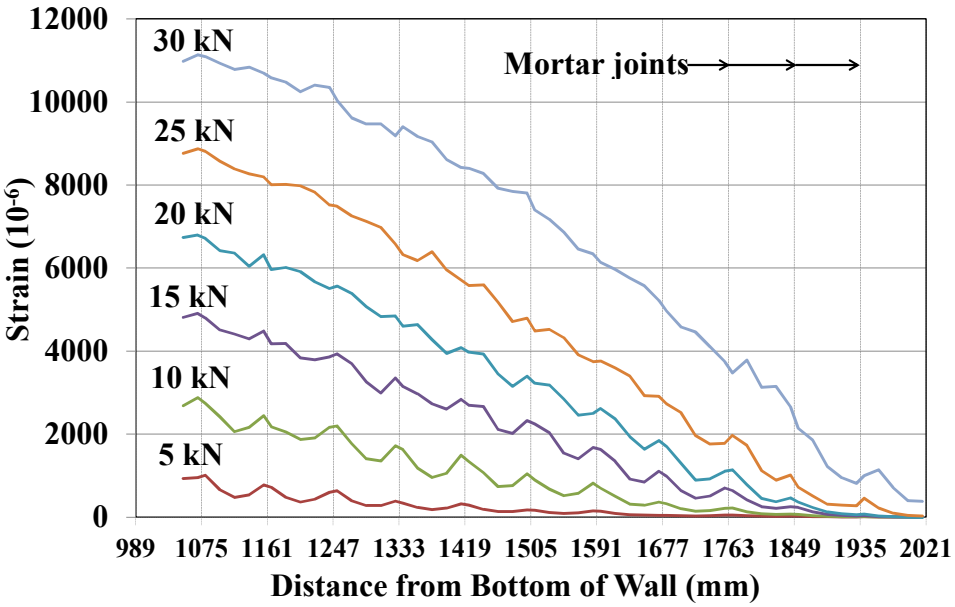

Figure 6-35: Strain distribution for wall 10

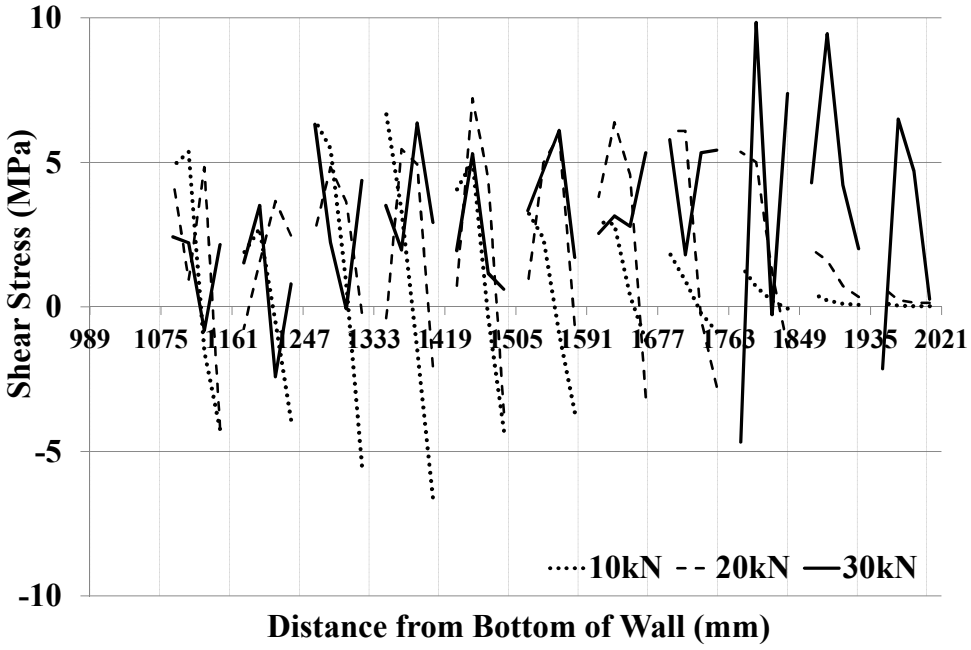

Figure 6-36: Shear stress distribution for wall 10

Figure 6-37 shows force in the strip vs. crack width plot at different bed joints near wall mid-height. The FRP force was calculated from the recorded strains in the FRP strip. As mentioned earlier in §5.6.2, the MVGs used in previous walls did not provide information about crack behavior after opening and so these were replaced by LVDTs. Three LVDTs were used in wall 10 for the first time and were placed at the three bed joints above the central brick (wall mid-height). Here crack 1 refers to

the bed joint crack immediately above the wall mid-height, crack 2 refers to the bed joint crack above crack 1 and so on (refer Figure 6-33). The secondary axis in Figure 6-37 shows the applied load on the wall.

Global load-slip pull test data was compared to the experimental crack width data for wall 10 (Figure 6 37). This investigation led to the important conclusion that a strong correlation exists between the force in an FRP strip vs. crack width at a bed joint in the wall and the corresponding pull test load-slip response up to δ_{max}. From Figure 6 37, it can be seen that the stiffness of the pull test curve closely matches the initial wall crack stiffness with the pull test result giving a lower bound estimate of the IC debonding force for the FRP in the wall test.

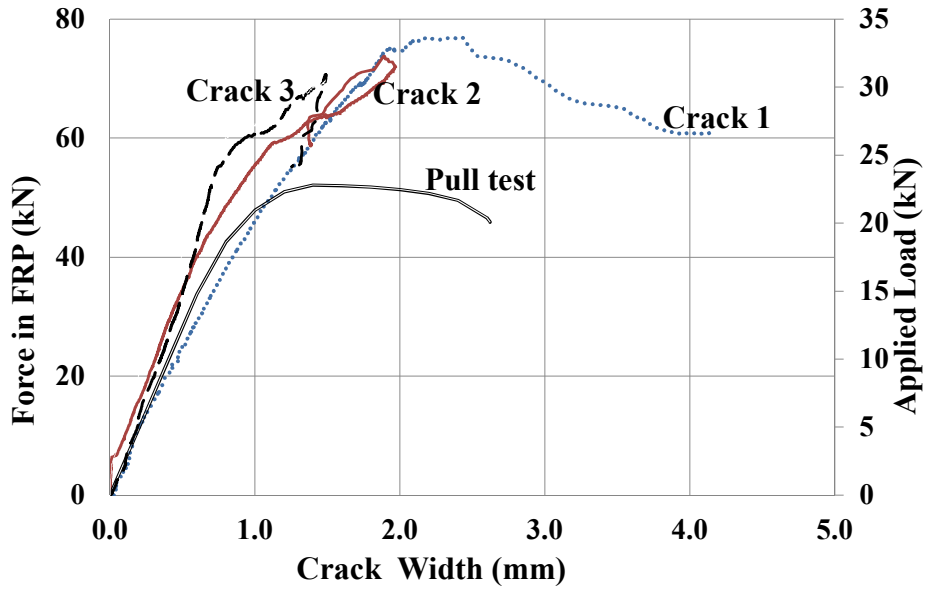

Figure 6-37: Load-slip behavior at bed joint for wall 10

It can be noted from Figure 6-37 that cracks 2 and 3 had similar initial stiffness and were slightly stiffer than crack 1. This difference in stiffness is probably just due to material variability. As the applied load approached its peak value of 30.8 kN, the crack at bed joint one (crack 1) opened up rapidly whereas cracks 2 and 3 began to close indicating full debonding (Figure 6-38). It is interesting to note that the width of the central crack (crack 1) was almost twice the width of the other cracks. This behavior was further studied in other walls.

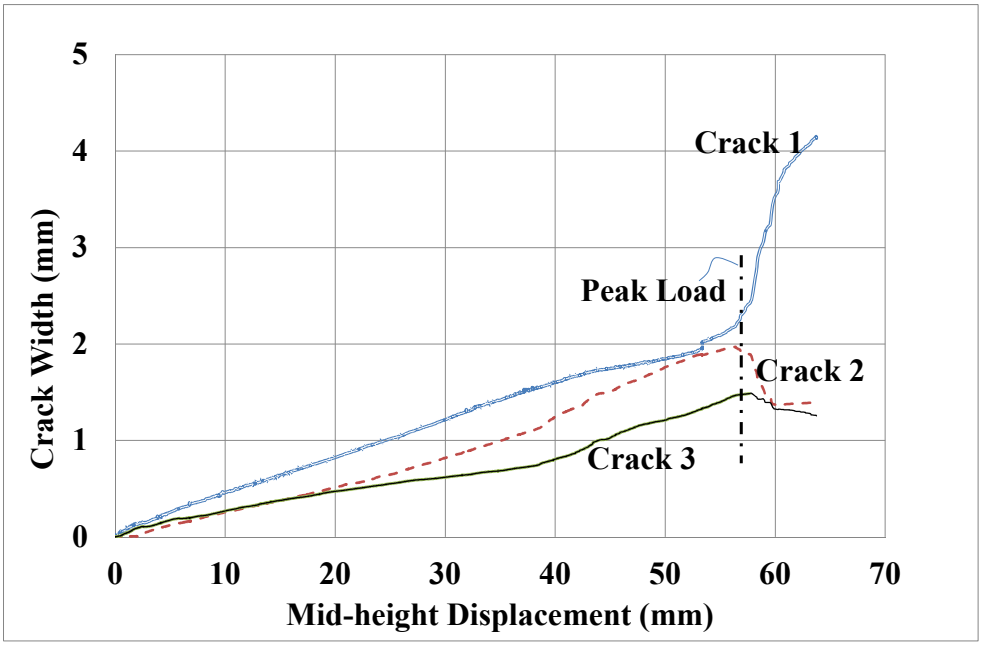

Figure 6-38: Crack width vs. Mid-height Displacement for wall 10

6.2.11. Wall 11

Wall 11 was subjected to cyclic loading and as Figure 6-39 shows, failed by IC debonding although some evidence of perpend shear failure was noticed near the left FRP strip on both faces and was more prominent in the top half of front face (Figure 6-39(a)). At failure, once debonding cracks had propagated towards the supports, a small portion of the right-hand strip popped out of the wall. The maximum recorded values were ε_{max} = 9951 με; Δ_{ult} = +53.7/-64.5 mm and F_{max} = +27.3/-27.6 kN. The maximum strain recorded during the tests was approximately 61% of the ε_{rup}.

Figure 6-40 shows the load-displacement response for wall 11. Degradation of stiffness was observed after each cycle of loading however, very little degradation of the bond was observed until the peak load of 27.5kN was reached. After the peak load, rapid bond degradation occurred. This is more clear in Figure 6-41, where each line represents the force in the FRP strip versus crack width for successive cycles in the positive direction. As can be seen from Figure 6-41 , minimal bond degradation was observed before the peak load was applied, as indicated by the closely spaced hysteresis loading lines to the left of peak load line.

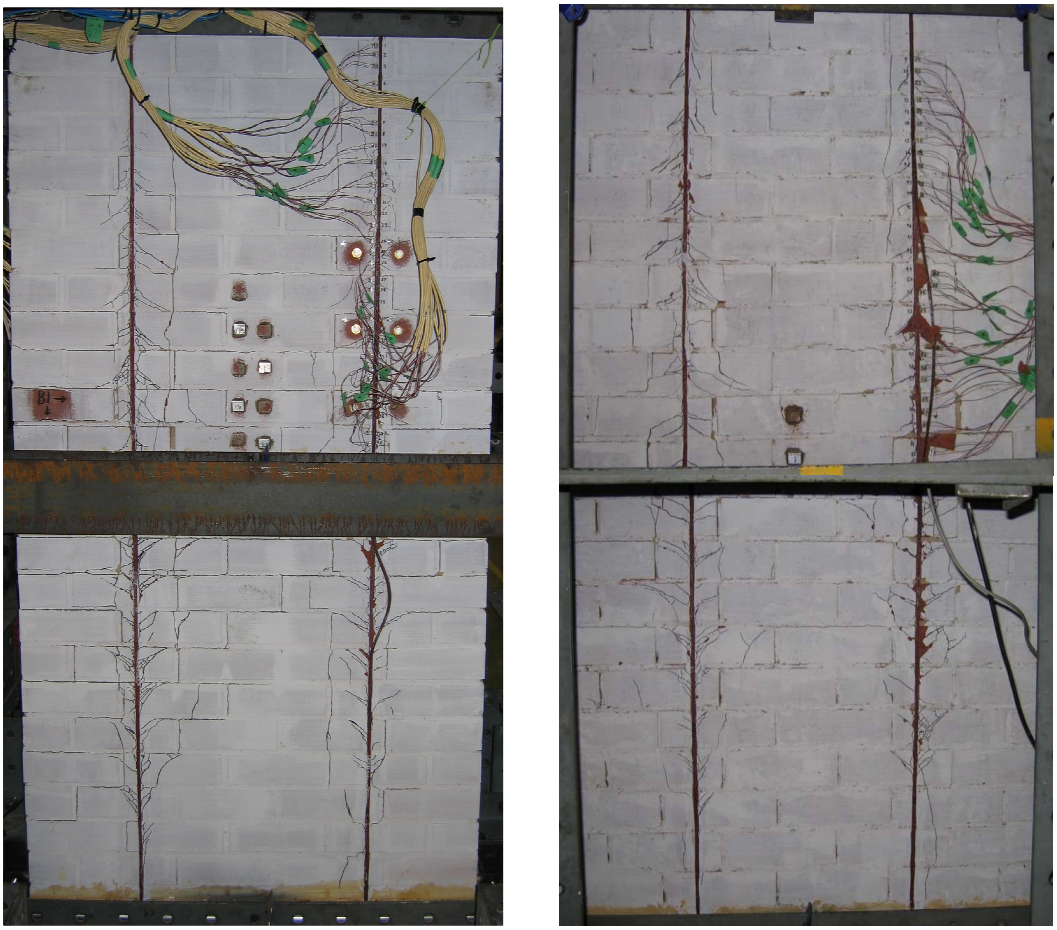

(a) Front of wall (b) Back of wall

Figure 6-39: Failure pattern for wall 11

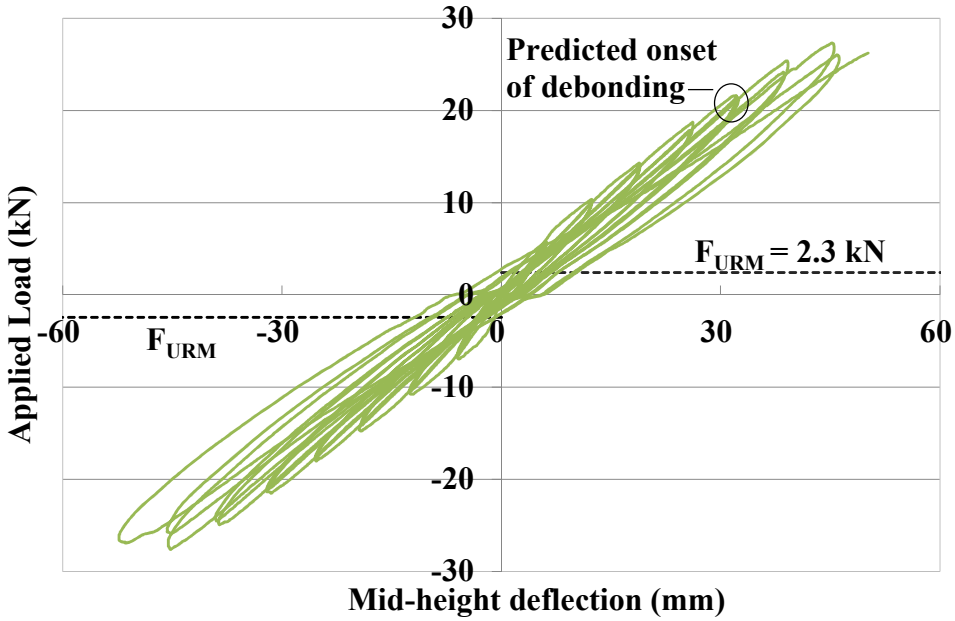

Figure 6-40: Load displacement response for wall 11

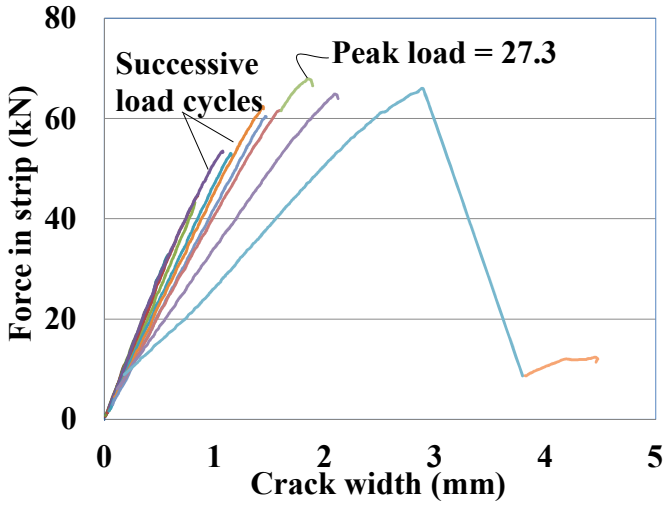

Figure 6-41: Force in the strip vs. crack width at crack 1 for wall 11

As mentioned in §5.6.1, in the top half of wall 11 alternate strips on each face were strain gauged with three gauges per brick which allowed the behaviour of the strips on both faces of the wall to be monitored. Figure 6-42 shows the comparison of strain values for equivalent loads but opposing deflections (e.g., 3kN and -3kN for two different displacement cycles of wall 11. As indicated from these plots, minimal differences were found between strip strains on the front and back face throughout all stages of loading. This confirmed that similar debonding process occurred on both sides of the walls subjected to cyclic loading.

As can be seen in Figure 6-43, all cracks had similar initial stiffness (up to 15 kN applied load). Similar to wall 10, the bed-joint crack width at crack 1 kept increasing as the peak load (27.3 kN) was approached whereas the other cracks (2-5) started closing. Furthermore, the crack at bed joint 2 on front and back (crack 2-B) of the wall showed similar behaviour indicating little difference between the debonding process of the strips on either face.

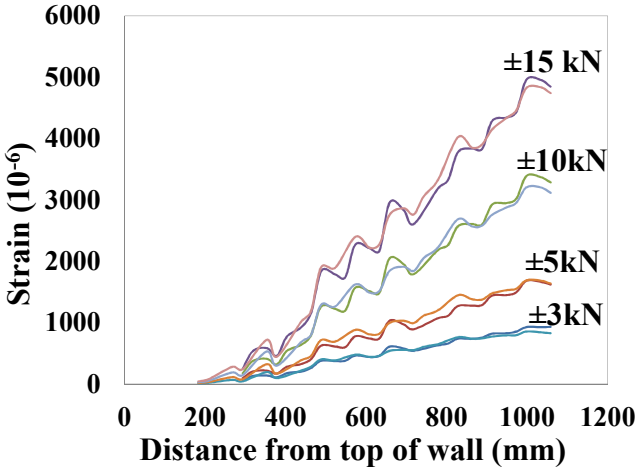

a) Δ = 28 mm – Cycle 1

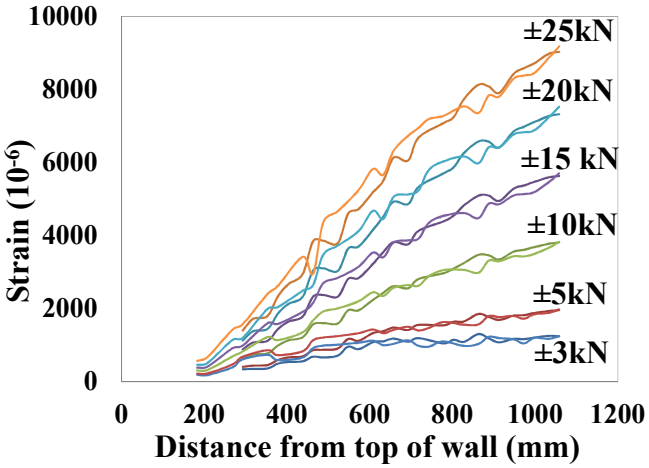

b) Δ = 56 mm - Cycle 1

Figure 6-42: Strain comparison between the front and back strips–Wall 11

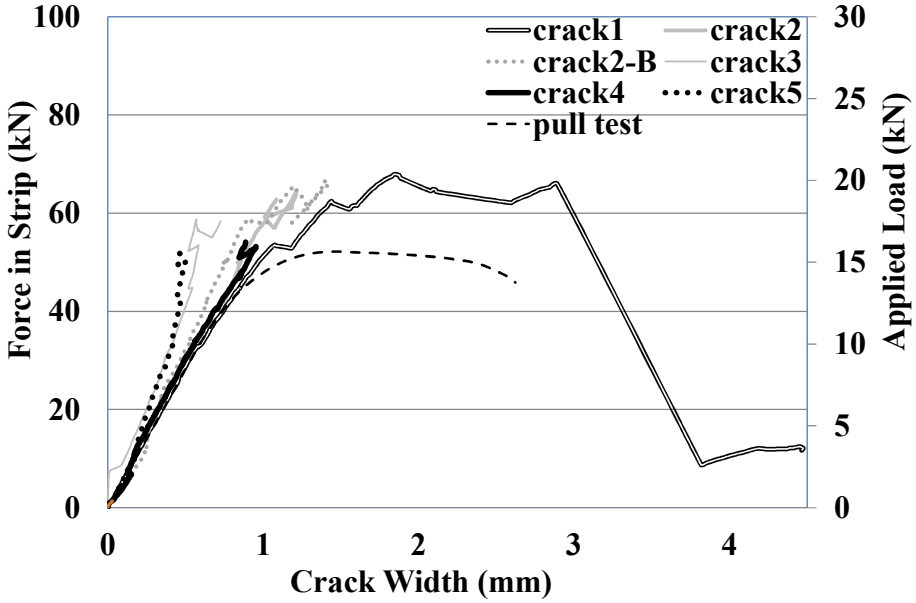

Figure 6-43: Load-slip behavior at bed joints for wall 11

6.2.12. Wall 12

Wall 12 was subjected to cyclic loading under a vertical pre-compression of 0.1MPa. As Figure 6-44 shows, wall 12 failed by IC debonding while onset of perpend shear failure was also noticed on both faces of the wall. As the load approached its peak value of 29 kN, debonding progressed towards the supports, and one FRP strip completely debonded, popping out of the wall resulting in a sudden explosive failure of the specimen. The recorded maximum values were ε_{max} = 9531 με; Δ_{ult} = +56.8/-53 mm and F_{max} = +28.9/-29.1 kN. The maximum strain recorded during the tests was approximately 58% of ε_{rup}.

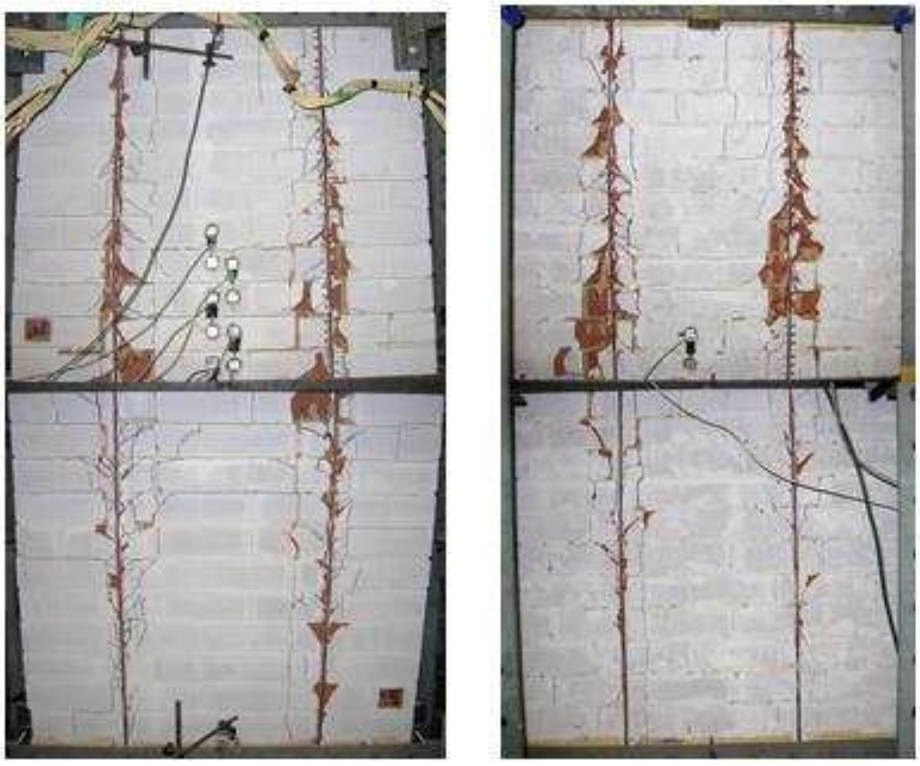

(a) Front of wall **(b) Back of wall**

Figure 6-44: Failure pattern for wall 12

Figure 6-45 shows the load-displacement response of wall 12. Similar to wall 11, only a small degradation of the bond was observed until peak load after which the bond degradation increased rapidly causing larger displacement without much increase in applied load.

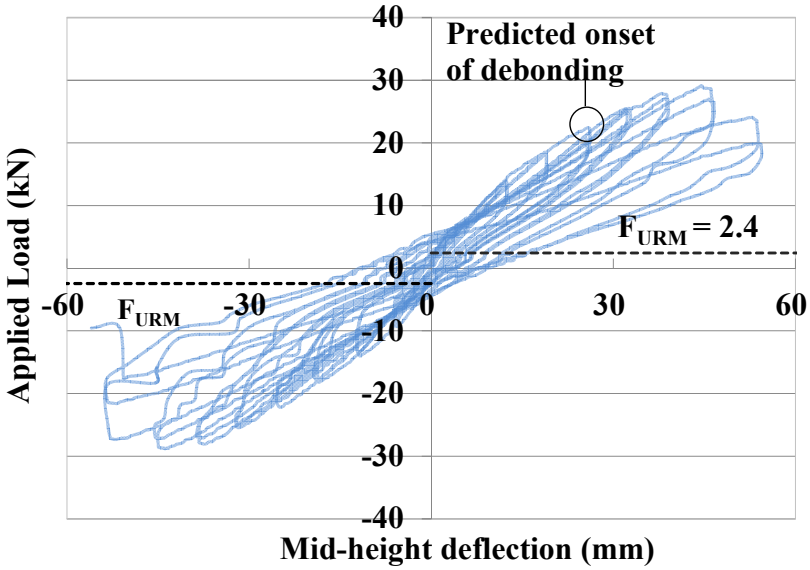

Figure 6-45: Load displacement response for wall 12

Figure 6-46 shows the crack development in wall 12. The LVDT placed on bed-joint 2 was broken and hence, no readings could be recorded for crack 2. Similar to walls 10 and 11, the central crack opened up significantly more than the other cracks with them reducing in width once the peak load was reached. As for previous walls, the corresponding bond pull-test provided a good, lower bound estimate of the FRP force vs. crack width response in the wall.

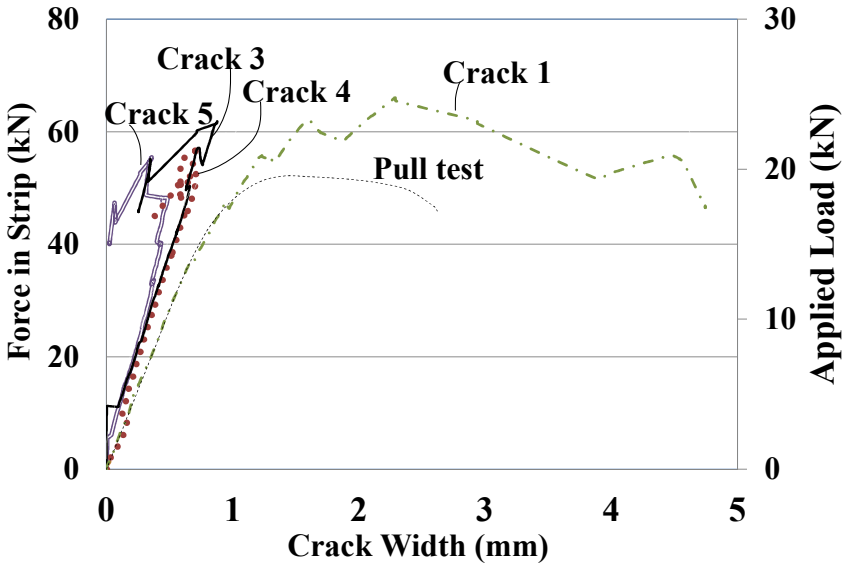

Figure 6-46: Load-slip behavior at bed joints for wall 12

6.2.13. Wall 13

Wall 13 was unique in the sense that it was tested with cyclic loading even though it only had NSM reinforcement on one face of the wall. It was tested like this in order to show the wall's behaviour in its 'strong' and 'weak' direction. Similar to wall 10, wall 13 failed by IC debonding (Figure 6-47(a)) with vertical cracks observed on the compressive face directly behind the FRP strips on the tension face (Figure 6-47(b)) with significant cracks at bed joints (Figure 6-47(c-i)). The crack height as seen from Figure 6-47(c-ii) was almost equal to the wall thickness. The recorded test values were ε_{max} = 11175 με; Δ_{ult} = 69.4/-57 mm and F_{max} = +30.2/-1.5 kN.

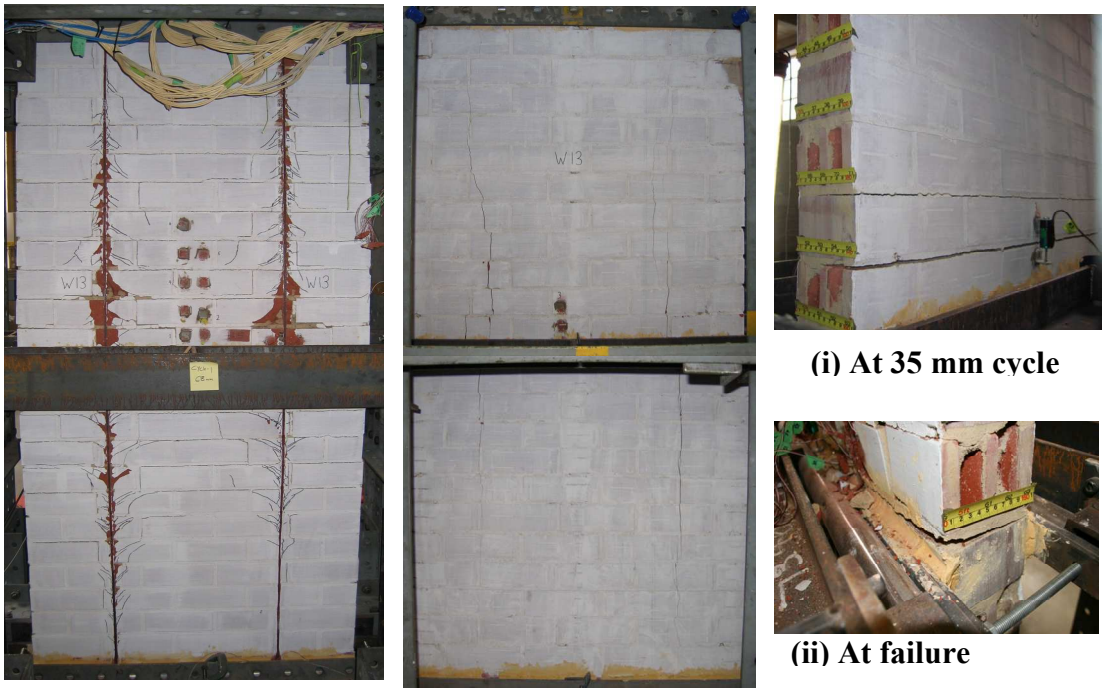

(a) Front face **(b) Back face** **(i) At 35 mm cycle** **(ii) At failure** **(c) Back face**

Figure 6-47: Failure pattern for wall 13

The load-displacement response of wall 13 (Figure 6-48) shows the difference between the strong and weak direction strength and is representative of the amount of strength increase that was achieved for all of the NSM CFRP reinforced walls. This wall could also be representative of one leaf a cavity wall where the reinforcement may be applied to the outer face of each leaf. In spite of being cyclically loaded and reinforced on one side only, the strength and displacement capacity of wall 13 was higher than wall 11 which was reinforced on both sides.

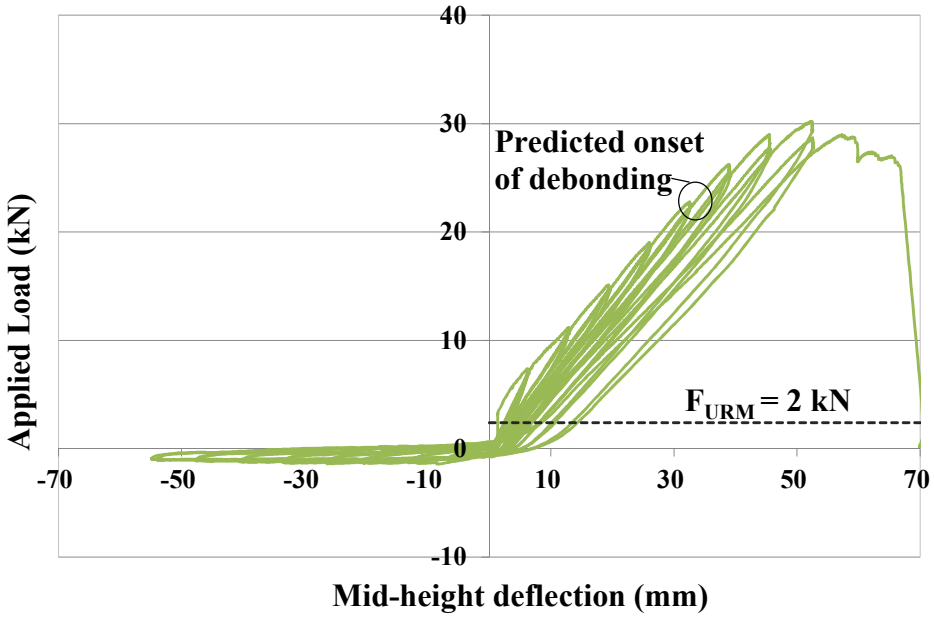

Figure 6-48: Load displacement response for wall 13

Wall 13 was instrumented with 5 strain gauges per brick (§5.6.1). Figure 6-49 and Figure 6-50 show the strain and stress distributions. As seen for the other walls, these plots show clear signs of shear stress reversals within bricks at low load, softening as the loading progresses with initiation of debonding occurring at approximately 20-25 kN (Figure 6-50). At peak load the strain profile (Figure 6-49) near the mid-height was almost constant and linear for the remaining portion of the wall indicating that the strip had debonded for the entire wall length except for the last brick near support. This can also be noted from the stress profile (Figure 6-50). As seen from Figure 6-50, the maximum shear stress was 8 MPa during first cycle of peak load.

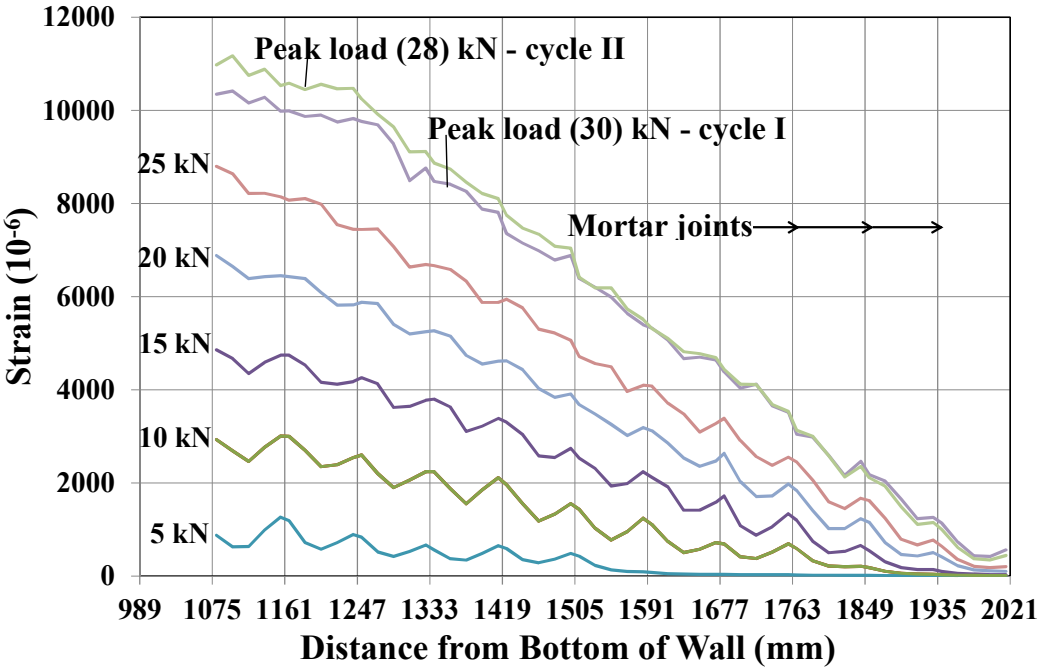

Figure 6-49: Strain distribution of wall 13

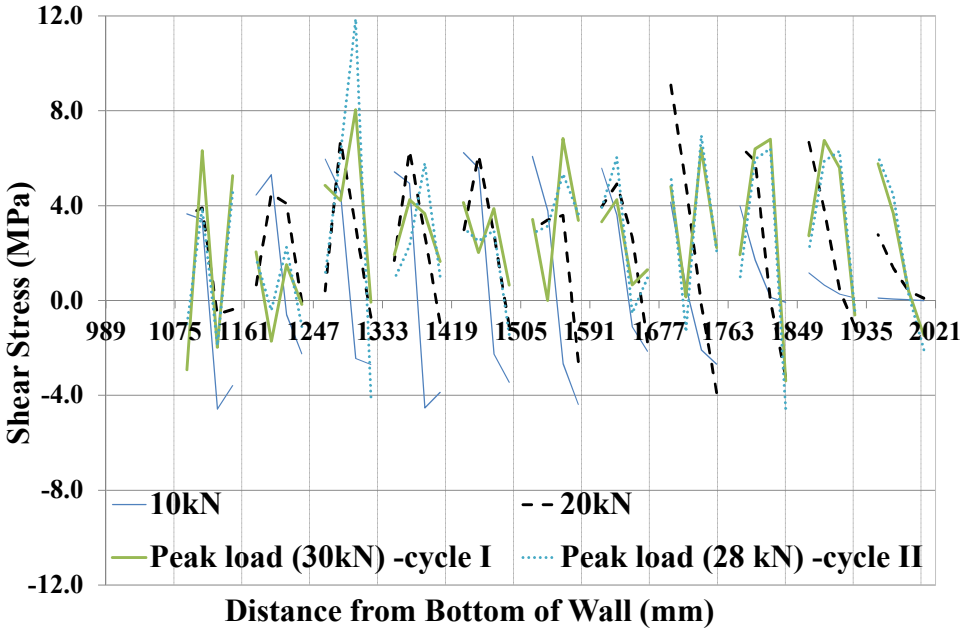

Figure 6-50: Stress distribution of wall 13

Figure 6-51 shows the crack development in wall 13. Overall, the crack behavior was similar to that for the previous walls except that the crack at bed-joint 1 started to close after peak load and had much lower stiffness compared to the other cracks. This could be attributed to fact that wall 13 was reinforced only on one side. Notably,

comparison between crack 2 on the front and back faces demonstrates the effectiveness of the NSM CFRP reinforcement (Figure 6-51).

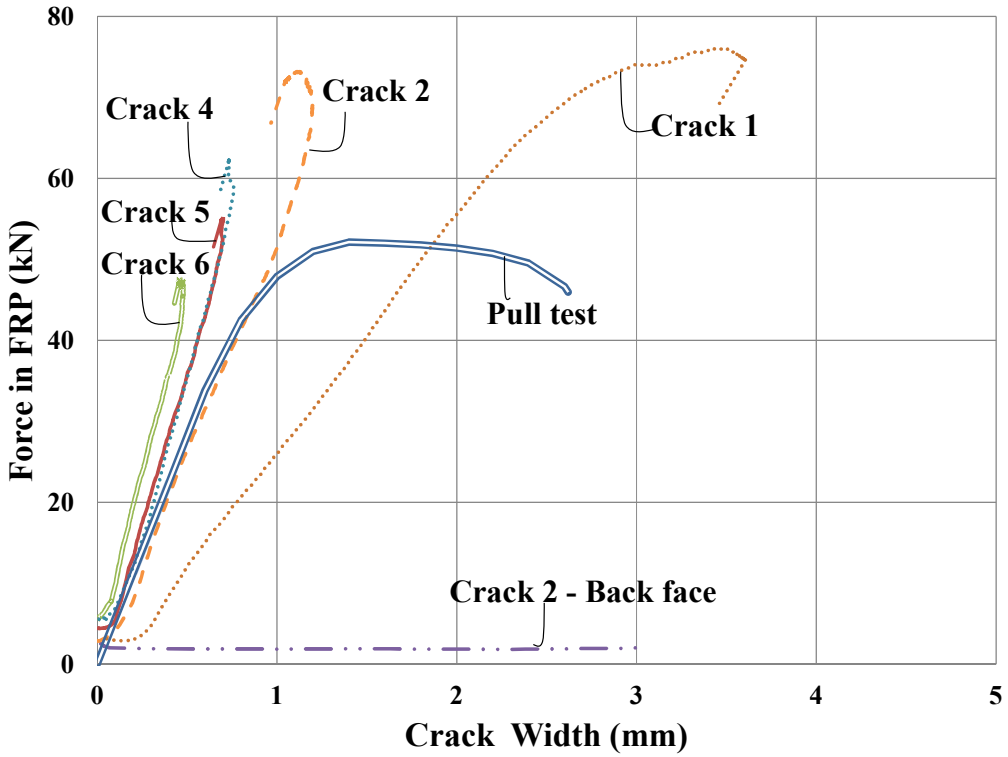

Figure 6-51: Load-slip behavior at bed joints for wall 13

6.2.14. Wall 14

Wall 14 was monotonically loaded and subjected to vertical pre-compression of 0.2 MPa. Wall 14 failed by IC debonding as shown in Figure 6-52(a). The maximum recorded test values were ε_{max} = 10552 με; Δ_{ult} = 52 mm and F_{max} = 29.7 kN with the maximum strain observed to be approximately 64% of ε_{rup}. Unlike walls 6 and 10, herringbone debonding cracking in wall 14 was limited to 4-5 brick courses above and below the mid-height. This was probably due to the higher applied axial load resulting in stiffer member due to delayed tensile cracking. This is further discussed in §6.3.3. However, tensile splitting was still observed on the compression face (Figure 6-52(b)) as was noted for walls 6 and 10.

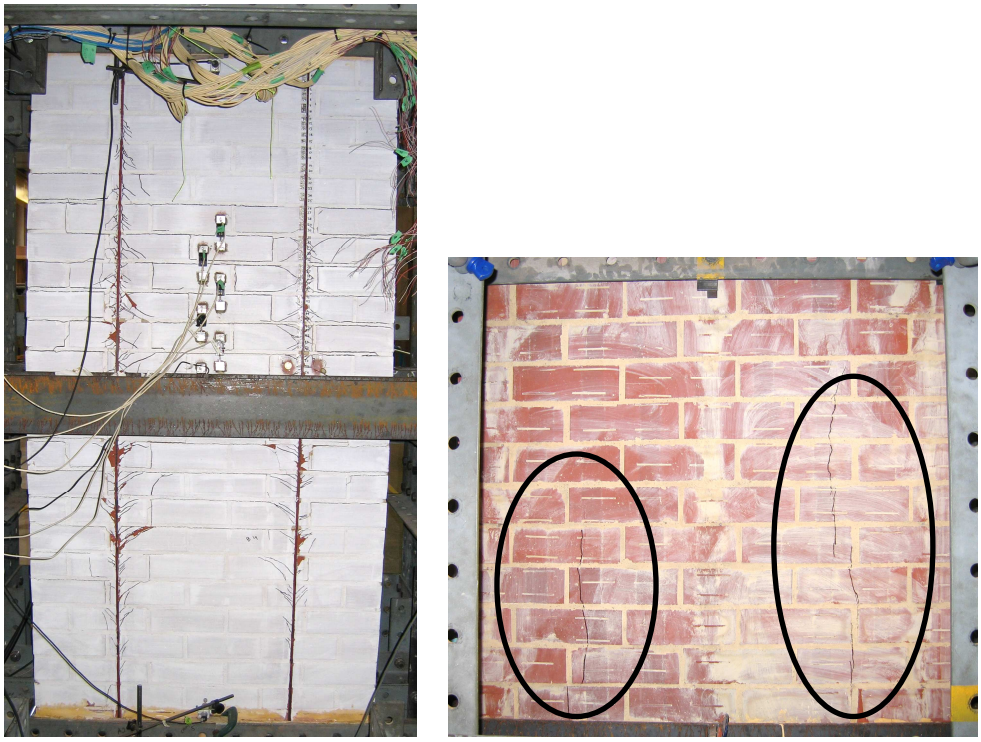

(a) Tension face **(b) Compression face**

Figure 6-52: Failure pattern for wall 14

As shown in Figure 6-53, the load-displacement response for wall 14 was not very ductile. In comparison to wall 6 (axial load = 0), Wall 14 with an axial load of 0.2 MPa had a stiffer load-displacement response with a 10% increase in strength and approximately 25% reduction in displacement in comparison to wall 6. The change in slope at a load of 20-25 kN was thought to correspond to the onset of debonding.

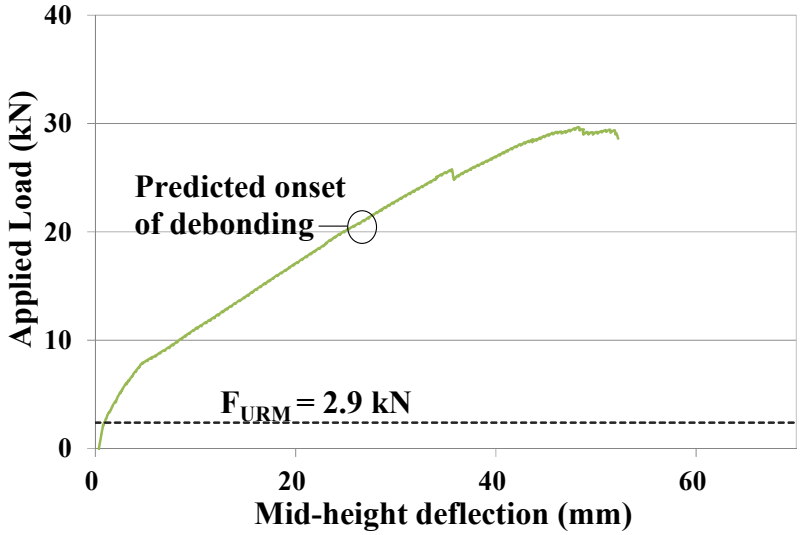

Figure 6-53: Load displacement response for wall 14

Figure 6-54 and Figure 6-55 show the strain and shear stress distributions for wall 14. Shear reversals were seen at early stages of loading due to cracks occurring at every bed joint except over the few bricks near support brick. With increasing loads (20-25 kN), signs of softening and debonding can be seen in Figure 6-54 and Figure 6-55.

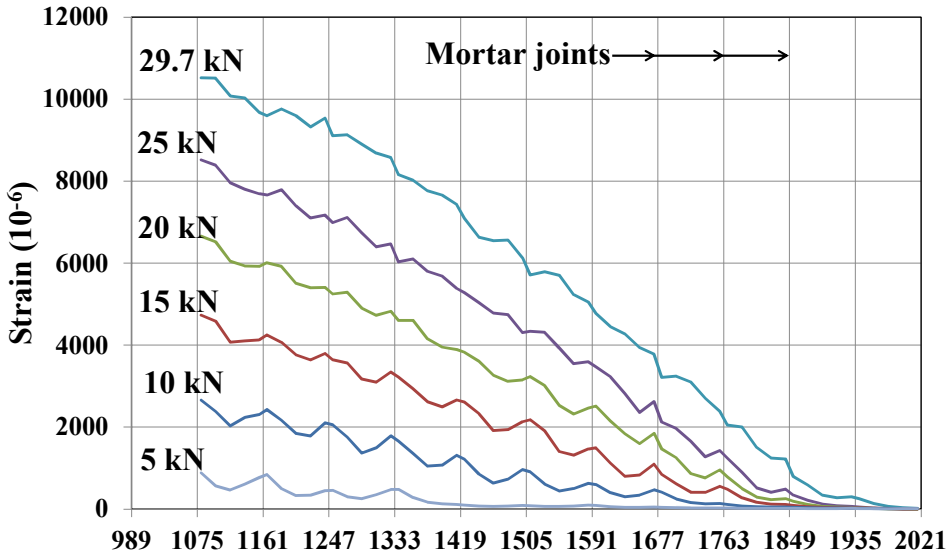

Figure 6-54: Strain distribution for wall 14

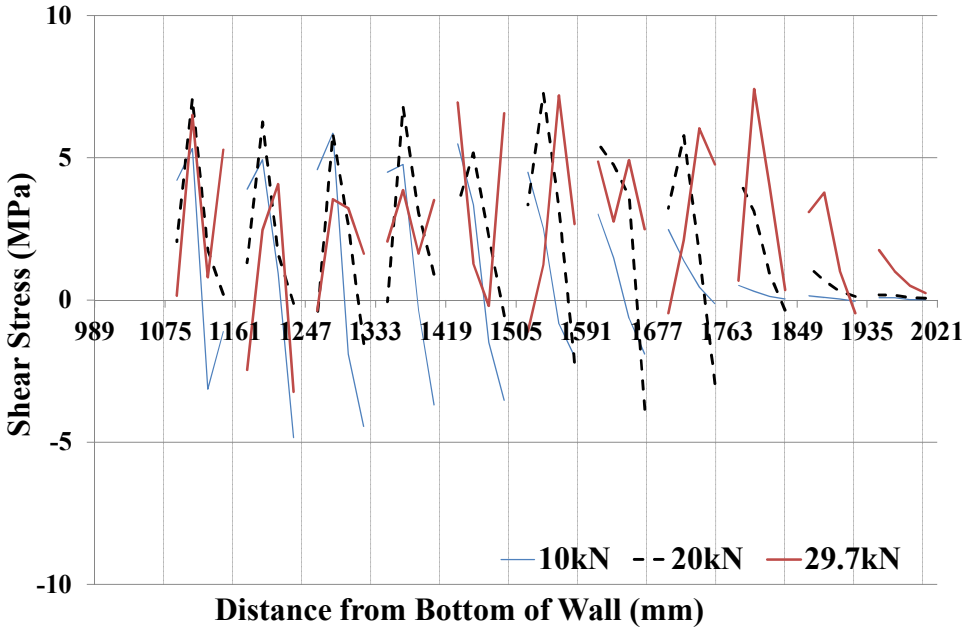

Figure 6-55: Shear stress distribution for wall 14

Figure 6-56 shows the force in the FRP strip vs. crack width for wall 14 from six LVDTs placed at the bed joints above the central brick (Figure 6-52). As can be seen in Figure 6-56, all cracks had similar initial stiffness. Further, as the load approached its peak value (29.7 kN), the crack widths at bed-joints 1 and 2 kept increasing whereas the other cracks start closing. It is interesting to note that width of crack 1 in wall 14 was almost twice that of crack 1 in wall 10. This could be possibly due to the increased pre-compression for wall 14.

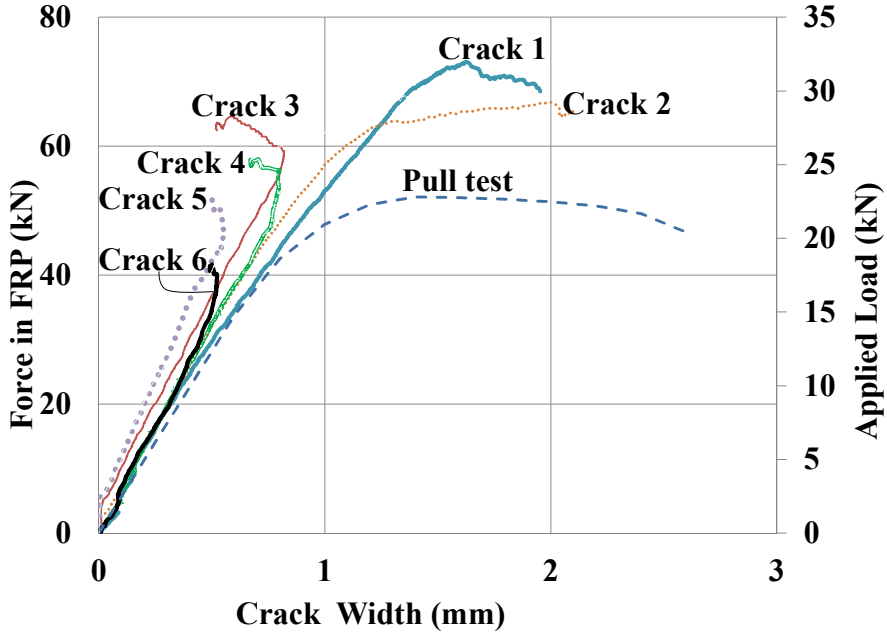

Figure 6-56 Load-slip behavior at bed joints for wall 14

As before it can be seen (Figure 6-56), that the stiffness of the pull test curve closely matches the initial crack stiffness with the pull test giving a lower bound estimate of the IC debonding resistance for FRP strips in a wall.

6.2.15. Wall 15

Wall 15 was loaded with a vertical pre-compression of 0.2MPa and then subjected to cyclic loading. As shown in Figure 6-57, wall 15 failed by IC debonding. The maximum recorded test values were ε_{max} = 8212 με; Δ_{ult} = +57/-51.8 mm and F_{max} = +27.8/-26.6 kN with the maximum strain observed to be approximately 50% of ε_{rup} hence indicating that reinforcement was not used very efficiently.

(a) Tension face **(b) Compression face**

Figure 6-57: Failure pattern for wall 15

Figure 6 58 shows the load-displacement response of wall 15. Similar to the other cyclic tests, very small degradation of the bond was observed until peak load. However, it was noted that the increased pre-compression did not have much effect on the wall's behavior.

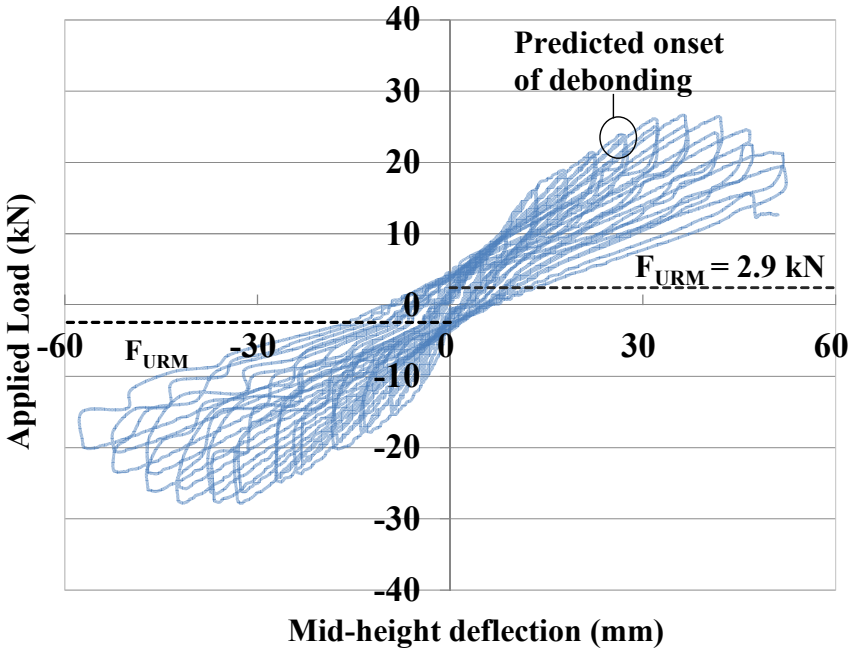

Figure 6-58: Load displacement response for wall 15

Figure 6-59 shows the crack development in wall 15. Notably, the responses of crack 2 on the front and back faces were quite comparable indicating similar behavior on either face. Similar to walls 10 , 11, 12 and 14, the central crack was almost four to five times wider than the other cracks while the others cracks started closing after the peak load was attained. Unlike other walls, the maximum force recorded in the strip was similar to the pull test load-slip data and had the lowest failure load for all three cyclic tests.

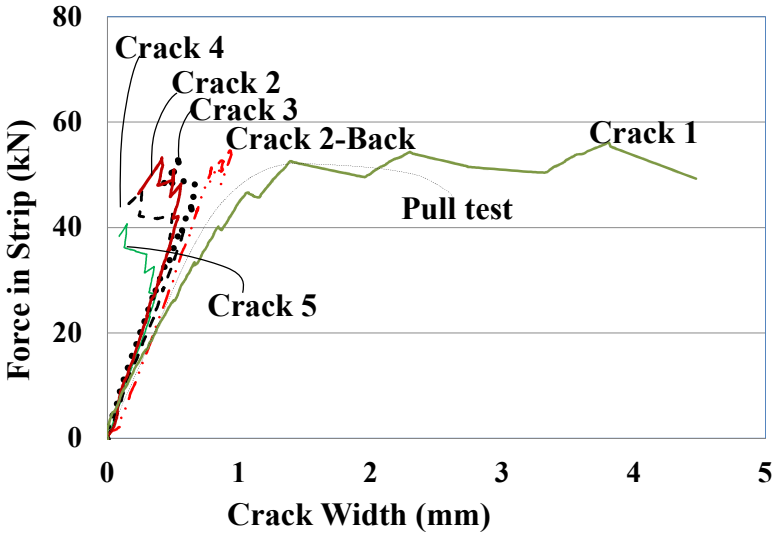

Figure 6-59: Load-slip behavior at bed joints for wall 15

6.3. Discussion of Test Results

The wall bending tests results are summarised in Table 6-1 where F_{max} refers to the maximum applied load, ε_{max} refers to the maximum strain recorded in the FRP strip during the test; Δ_{ult} refers to the maximum displacement; P_{exp} is the maximum force measured in the FRP strips during tests; and a_{exp} refers to the equivalent horizontal acceleration, to cause F_{max} and a_{urm} is the horizontal acceleration corresponding to the unreinforced flexural strength of each wall, F_{urm}. The observations and data relating to the research objectives are discussed in detail in the following sections.

Table 6-1: Tests results

Wall *S/C (1)	Strip size (mm) (2)	ε_{max} (με) (3)	F_{max} (kN) (4)	Δ_{ult} (+ve) (mm) (5)	$\varepsilon_{max}/\varepsilon_{rupt}$ (%) (6)	a_{exp}/a_{URM} (7)	L_{per}/strip (mm) (8)	Total L_{per} (mm) (9)	P_{exp}/strip (kN) (10)	P_{exp}/L_{per} (kN/mm (11)	Failure mode**
1S	3.6x10	0.00983	18.6	-	60.0	14.3	27.6	27.6	58.4	2.1	IC+MC
2S	3.6x10	0.00998	18.5	36.6	60.9	14.2	27.6	27.6	59.3	2.1	IC+MC
3C	3.6x10	0.00829	15.6	30.3	50.6	12.0	27.6	27.6	49.3	1.8	IC+MC
4S	3.6x10	0.00818	15.6	27.6	49.9	18.6	27.6	27.6	48.6	1.8	IC+MC
5S	7.2x10	0.00699	17.1	49.2	42.7	7.5	31.2	31.2	83.1	2.7	IC+VS
6S	4.8x7.5	0.01098	27.0	70.0	67.0	11.9	23.8	47.6	65.3	2.7	IC+VS
7S	3.6x10	0.01188	41.0	75.7	72.5	18.1	27.6	82.8	70.6	2.6	IC+VS
8S	4.8x5.0	0.01245	36.6	78.9	75.9	18.2	18.8	56.4	49.3	2.6	IC+VS
9S	3.6x10	0.00947	12.4	61.2	57.8	6.2	27.6	27.6	56.3	2.0	IC+VS
10S	4.2x10	0.01109	30.8	69.3	67.6	12.7	28.2	56.4	76.9	2.7	IC+VS
11C	4.2x10	0.00995	27.3/-27.6	53.7/-64.5	60.7	13.6	28.2	56.4	69.0	2.4	IC+VS
12C	4.2x10	0.00953	28.9/-29.1	56.8/-53.0	58.1	11.9	28.2	56.4	66.0	2.3	IC+VS
13C	4.2x10	0.01117	30.2/-1.4	69.4/-57.0	68.1	15.0	28.2	56.4	77.4	2.7	IC+VS
14S	4.2x10	0.01055	29.7	52.0	64.3	10.4	28.2	56.4	73.1	2.6	IC+VS
15C	4.2x10	0.00821	27.8/-26.6	57.0/-51.8	50.1	9.5	28.2	56.4	56.9	2.0	IC+VS

* S – monotonic loading; C – quasi-static cyclic loading

** IC - intermediate crack debonding; MC – masonry crushing; VS – vertical in-plane shear failure

The efficiency in use of the CFRP material for each wall was determined using the recorded ε_{max} during the tests expressed as a % of the rupture strain (Column 6 in Table 6-1). In all tests, wall failure was by IC debonding. Due to the high reinforcement ratios used in walls 1-4, their failure mechanism was a combination of masonry crushing and IC debonding.

6.3.1. Comparison with Vertical Bending Capacity of URM

Based on the applied axial load conditions for the retrofitted walls, the unreinforced flexural strength of each wall, M_{urm} was calculated along with the equivalent horizontal acceleration, a_{urm} that would be needed to cause the respective moment. The vertical bending moment capacity of an unreinforced masonry section, M_{urm}, is defined by Eq. 6-1(where: Φ = capacity reduction factor ; k_{mt} = bending moment capacity factor; f'_{mt} = characteristic flexural tensile strength of the masonry; f_d = design compressive stress; and, Z_d = section modulus of the bedded area). This also accounts for the different specimen widths. Using mean instead of characteristic values, and setting Φ and k_{mt} = 1.0, the values of M_{urm} and a_{urm} (Eq. 6-2) for the walls were calculated. Refer Appendix §E.5 for detailed calculations.

$$M_{urm} = \phi k_{mt} f'_{mt} Z_d + f_d Z_d \qquad \text{Eq. 6-1}$$

$$a_{urmx} = \frac{8M_{urm}}{H^2 t \gamma W} \qquad \text{Eq. 6-2}$$

As can be seen from Column 7 in Table 6-1, a significant increase of approximately 6 to 20 times in flexural strength is possible even with the very small reinforcement ratios used in these URM walls. This can also be noted from result of wall 13 which had a 30 kN strength in its 'strong' direction whereas its 'weak' direction strength was only 1.4 kN. Further, a_{exp} in all the walls is substantially higher than that required for normal seismic design situations and hence, highlights the effectiveness of the retrofitting scheme used for the bending tests. The increase in the strength due to retrofitting varied depending on the other test variables such as reinforcement

ratio, applied axial load and strip spacing. The effect of these test variables is discussed in the following sections §6.3.2 to §6.3.5.

6.3.2. Effect of FRP Strip Spacing

Three walls (5, 6 and 8) were tested covering three different effective strip spacings. The same total amount of FRP reinforcement (72 mm^2) was used in each of the three test walls. The load versus mid-height displacement response for these three walls is given in Figure 6-60. As can be seen, the only difference was that Wall 5 had a single CFRP strip (7.2 mm x 10 mm) in the 1070 mm wide wall, Wall 6 had two (4.8 mm x 7.5 mm) CFRP strips spaced at 535 mm, and wall 8 had three (4.8 mm x 5 mm) CFRP strips spaced at 357 mm.

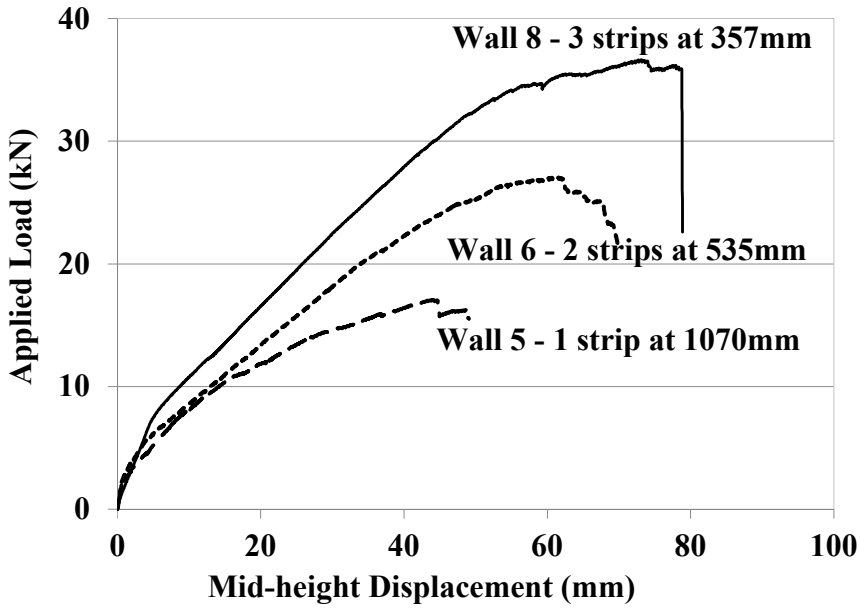

Figure 6-60: Load-displacement response showing effect of FRP strip spacing

From the test results (Table 6-1), it can be seen that there was a significant increase in both strength (approximately 17 to 37 kN) and displacement capacity (approximately 45 to 79 mm) when the FRP reinforcement was distributed more evenly. That is, using three strips with 24 mm^2 each spaced evenly (357 mm) across the width of wall 8 was much more efficient use of the 72 mm^2 total of FRP than for wall 5 which lumped all 72 mm^2 of FRP into a single strip. Further, wall 5 had a single strip which is harder to engage the entire width of the wall on the compression

face compared to wall 6 and wall 8 due to the smaller effective width i.e. the width of the compressive zone which results in a total force equal to the tensile force in the FRP.

The total surface area of FRP that was bonded to the masonry for wall 8 (L_{per} = 56.4 mm) was nearly double that for wall 5 (L_{per} = 31.2 mm) (see column 9, Table 6.1). Notably, the maximum force measured in the FRP strips during tests (P_{exp}/strip) are given in column 10, Table 6-1where the strip forces are smaller for the smaller strips due to the strip cross-section but when normalized by the bonded length L_{per}, the value of P_{exp}/L_{per} is fairly consistent for all three walls ranging between 2.62 and 2.74 kN/mm (Column 11, Table 6-1). Finally, the most efficient use of the CFRP material was also achieved in wall 8 where the maximum tensile strain recorded during the tests was observed to be 76% of the rupture strain (Column 6, Table 6-1).

As mentioned in section §6.2, vertical in-plane shear failure and curvature incompatibility were also observed. Notably, wall 5 was more susceptible to these failure mechanisms because of the larger strip cross-section resulting in higher flexural rigidity and greater force in strip (83.1 kN) than either of the other two walls (65.3 and 49.3 kN) (see Column 10, Table 6-1). Fewer large strips at greater spacing can lead to inefficient use of the reinforcement and can change the failure mode from intermediate crack debonding to one where an in-plane shear crack, parallel to the strip develops in line with the perpend joints nearest to the CFRP strip. It was concluded that for any larger strip spacings, this failure mechanism would govern.

6.3.3. Effect of vertical Pre-Compression

Effects under Static Loading Conditions

To investigate the effects of an applied pre-compression on the behaviour of FRP retrofitted masonry under monotonic loading, three walls (walls 6, 10 and 14) were tested with pre-compression ranging from zero to 0.2 MPa. As seen from the global load-displacement response for the walls (Figure 6-61), increasing the axial load resulted in the increased stiffness and approximately 10-15% increase in flexural strength. However, there was about 15-30% reduction in the displacement capacity.

This was expected as the applied axial load makes the member stiffer as the flexural cracks are restrained by the combinations of the bond strength and the applied compressive load and hence, delaying the crack propagation. As discussed in §2.5.3, a study by Korany and Drysdale (2006) also showed similar results but the amount of strength increase was much higher compared to this study which was probably due to their higher applied pre-compression as well as the fact that the walls were laterally supported on all four edges.

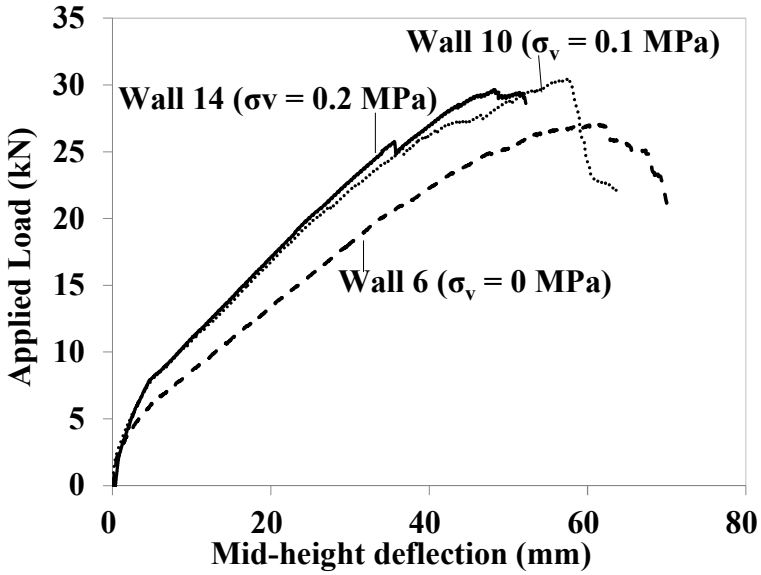

Figure 6-61: Effect of variable axial loads under static loading

Further, in order to study the effects of an axial load on the bond behaviour, the measured crack widths for walls 10 and 14 were compared (Figure 6-62). There was no crack width data recorded for wall 6. All cracks had similar initial stiffness except the first crack for wall 10 which had slightly lower stiffness and had twice the width of the other cracks. Notably, for wall 14 both crack 1 and crack 2 opened further after the peak load was attained compared to only one crack for wall 10 ((Figure 6-62). This could explain the difference in the crack widths for wall 10 and wall 14 as the sum of the first and second crack widths at failure is 4.0 mm for wall 14 was similar to the width of central crack of wall 10 (4.1mm).

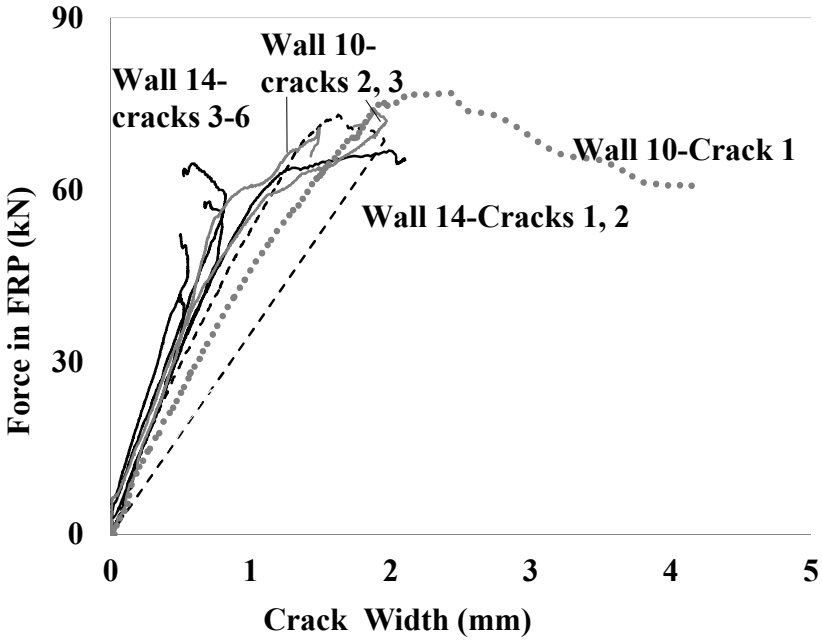

Figure 6-62: Crack width comparison for wall 10 and wall 14

Effects under Cyclic Loading Conditions

To investigate the effects of pre-compression on the behaviour of FRP retrofitted masonry under cyclic loading, three walls (walls 11, 12 and 15) were tested under pre-compression ranging from zero to 0.2 MPa. The envelope of the cyclic load displacement plots for the three walls are shown in Figure 6-63. The cyclic test results were consistent with the static tests, showing a similar increase in stiffness due to increased axial load. However, its effect on the strength and displacement capacity was negligible. Figure 6-64 shows the crack comparison for walls 11, 12 and 14. Similar to the static tests all cracks had similar initial stiffness. Further, from Figure 6-64 it can be noted that the force in the strip decreased with increased applied axial load. Also, width of the central crack of wall 11 (σ_v=0 MPa) was lowest in all three cyclic tests. This was different to that observed for static tests where the crack width decreased with increase in axial load. Hence, effect of pre-compression under cyclic loading was not very conclusive.

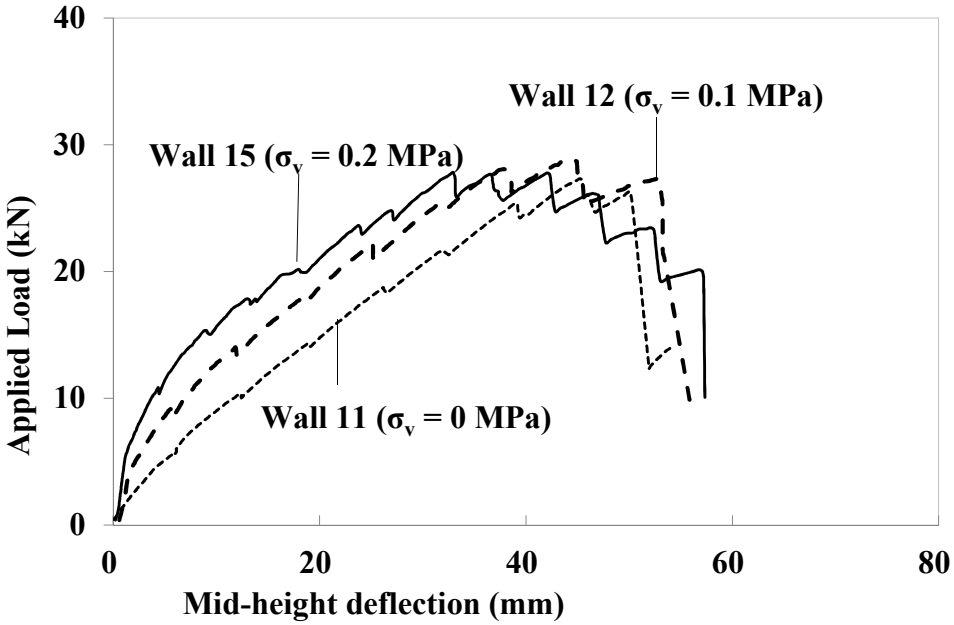

Figure 6-63: Effect of variable axial loads under cyclic loading

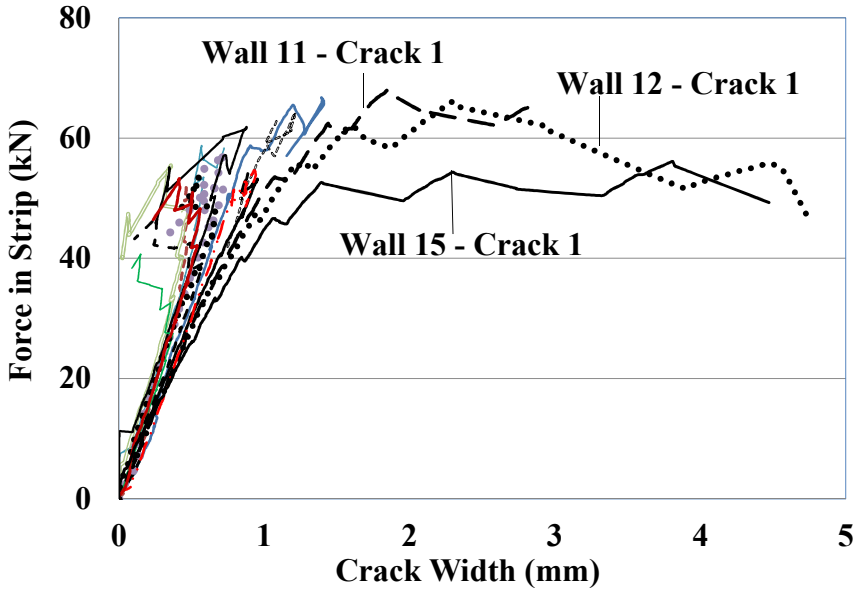

Figure 6-64: Crack behaviour of wall 11, 12 and 14

6.3.4. Effect of cyclic loading

In Figure 6-65, mirror images of the static load-displacement curve in the negative direction have been used for comparison with the cyclic hysteresis plots. The static curves envelope the cyclic test curves closely which suggest that cyclic load effects are not substantial. This is in agreement with the findings from the literature (Kuzik

et al. 2003; Ghobarah and Galal 2004; Korany and Drysdale 2006), as discussed in §2.5.2.

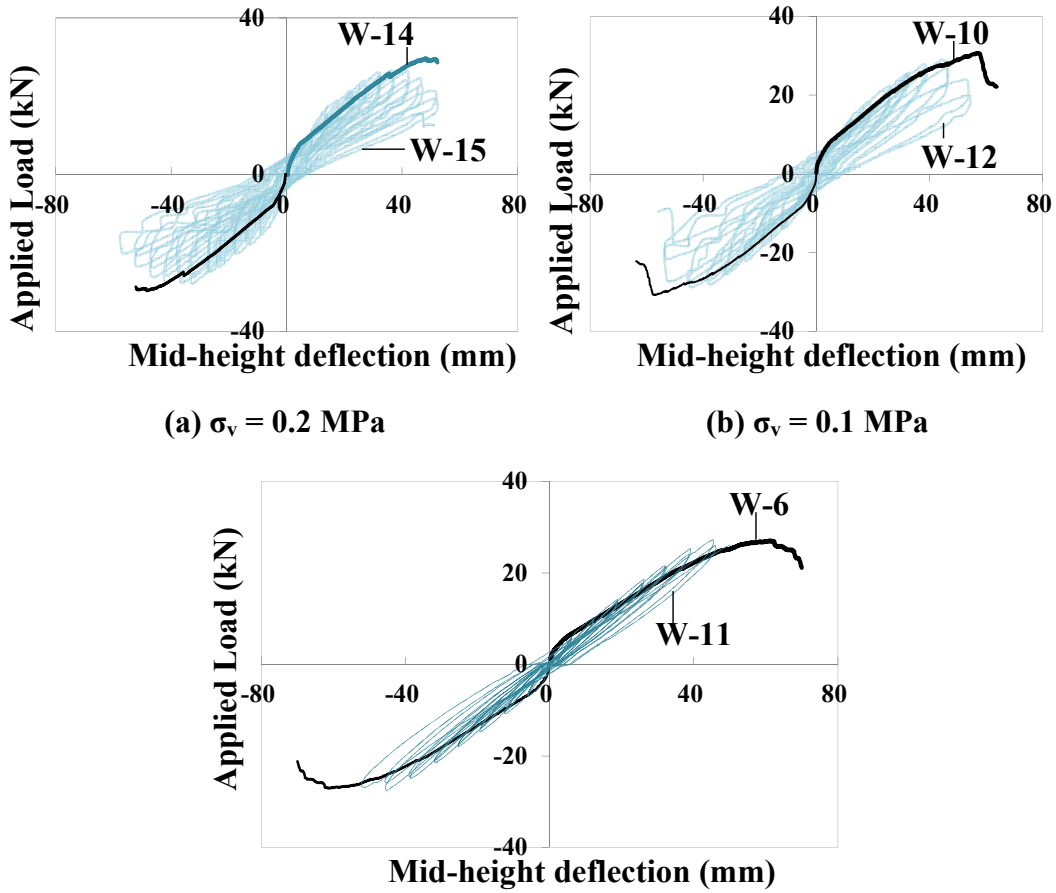

Figure 6-65: Effect of cyclic loading under different applied pre-compression

Overall, cyclic loading resulted only in small decrease in both strength and displacement capacity, by 6-8% and 15-20%, respectively. This was attributed to bond degradation due to cyclic loading as it destroys the mechanical interlock between the FRP and the masonry. Notably, increased pre-compression resulted in higher strength reduction but a smaller displacement reduction with increasing axial loads (Figure 6-65).

6.3.5. Effect of reinforcement ratio

Figure 6-66 shows that the amount of FRP reinforcement used affects the overall stiffness, strength and displacement capacity of a wall.

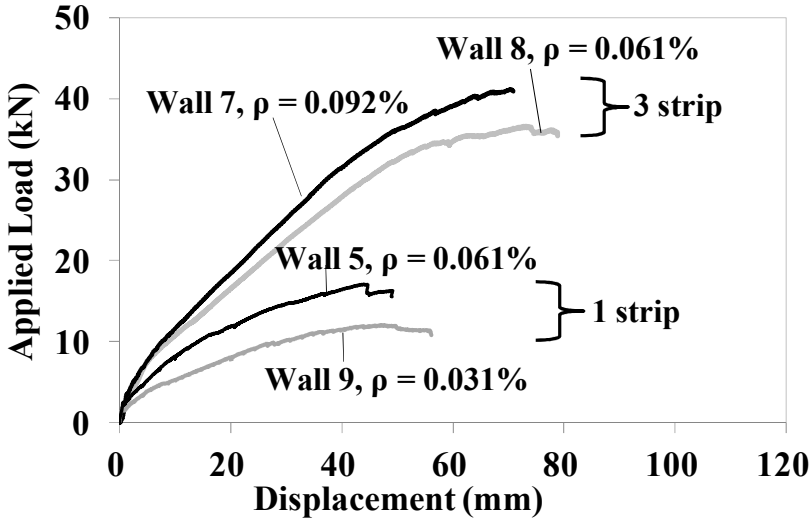

(a) Load-displacement response

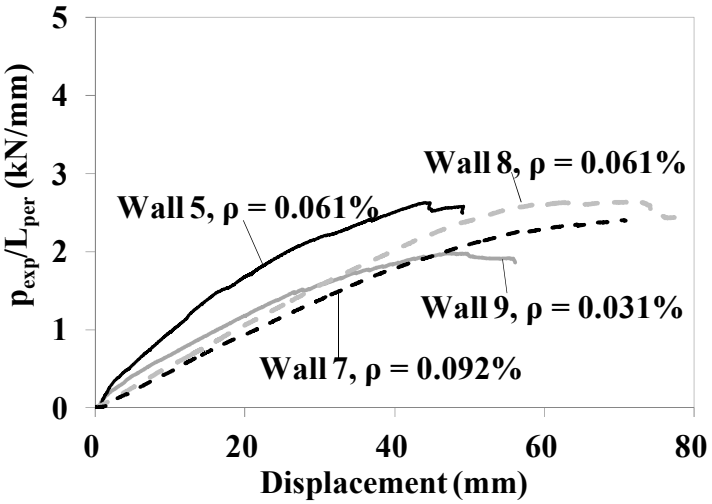

(b) Effect of L_{per}

Figure 6-66: Influence of reinforcement ratio

While evaluating the influence of reinforcement ratio, walls were selected such that other variables were constant. As can be seen in Figure 6-66(a), for the one strip configuration (walls 5 and 9), doubling the reinforcement ratio led to a 42% increase in strength whereas for the three strip configuration (walls 7 & 8), a 50% increase in reinforcement ratio resulted in only a 12% gain in strength. No linear co-relation was observed. Further, it was noted that depending on strip spacing, an increase in reinforcement ratio can affect the wall's failure mechanism and ductility of the load-displacement response of walls.

Notably, P_{exp}/strip (Column 10, Table 6-1) was smaller for walls with lower reinforcement ratios but when normalized by the bonded perimeter, L_{per}, the value of P_{exp}/L_{per} (Column 11, Table 6-1) was virtually constant for all walls ranging between 2.0-2.6 kN/mm, as shown in Figure 6-66(b). From Figure 6-66(a) it can also be noted that the spacing of FRP strips has a greater influence on overall behavior of walls compared to reinforcement ratio and hence, is a key factor for efficient use of CFRP for retrofitting URM walls. For example, walls 5 and 8 in Figure 6-66(b) both have the same reinforcement ratio (0.061%) but the three strip configuration (wall 8) is roughly twice as strong as the single strip configuration (wall 5). This can also be observed from Column 6 of Table 6-1, where $\varepsilon_{max}/\varepsilon_{rup}$ is not strongly correlated to reinforcement ratio but was significantly affected by strip spacing.

6.4. Summary

The results of this experimental study have demonstrated that NSM CFRP strips designed to fail by IC debonding can provide substantial increases in strength of up to 20 times the strength of the URM wall even with the very small reinforcement ratios used in these walls (0.031% – 0.142%). The equivalent horizontal acceleration, aexp corresponding to the failure load for the weakest of the FRP strengthened walls was nearly 2.3g, well in excess of maximum acceleration of 0.5g required (by AS1170.4) for out-of-plane loaded URM walls. Hence, these results highlight the effectiveness of the NSM retrofitting scheme used for these wall bending tests. However, the increase in the strength, efficient use of the CFRP material and failure mode for retrofitted walls varied depending on the test variables such as reinforcement ratio, cyclic loading, applied axial load and strip spacing. Further, it should be noted that in FRP strengthened walls with rigid supports and low slenderness ratio arching mechanism may occur. Due to arching effect, the increase of wall capacity due to the FRP reinforcement may be considerably less than expected. (Galati et al. 2007).

It was found that spacing of FRP strips has a greater influence on overall behavior of walls than reinforcement ratio, cyclic loading and vertical pre-compression. Importantly, a significant increase in strength and displacement capacity and hence,

more efficient use of reinforcement was achieved when the FRP strips were distributed more evenly (i.e. closer spacing). The test results for walls 5, 6 and 8 suggest that the maximum practical spacing (1070 mm) for the reinforcement ratio of $\rho = 0.061\%$ was achieved as the failure mechanism showed signs of changing from IC debonding mechanism to vertical in-plane shear failure through the perpends or horizontal bending failure of the masonry between the FRP strips. Hence, for a given reinforcement ratio there is a clear benefit in terms of strength and displacement capacity by having more strips, in terms of decreased spacing.

Test results also showed that an increase in the amount of fiber reinforcement increases the strength capacity but also slightly reduces the displacement capacity. As expected the high reinforcement ratios used in walls 1-4 caused failure due to a combination of masonry crushing and IC debonding. It is recommended to use reinforcement ratios and spacings for strengthening URM walls that will avoid failure mechanisms such as compressive failure of the masonry and tensile FRP rupture.

The effects of increased axial pre-compression on flexural response of FRP strengthened masonry were found to be minimal. Although, the axial load increased the flexural stiffness of walls and the static strength capacity, it had a negligible effect on strength and displacement capacity of walls under cyclic loading. Further investigation into the effect of cyclic loading under different axial loads indicated that compared to the monotonic tests, cyclic loading caused only slight reduction in the strength and displacement capacity due to gradual FRP-to-masonry bond degradation.

Finally, the use of LVDTs to measure the crack widths along with the strain gauge data along the strip indicated a strong correlation between the FRP force-crack width response in the flexural wall tests and the global FRP force-displacement response reported for the shear bond pull tests in Chapter 4. Comparison of the strip force vs. crack width plots (at the bed joints) from wall tests with the pull test P-Δ curve showed that the pull tests give a close lower bound estimate of the IC debonding

force in the FRP strip. Moreover, these plots illustrated that the bond behavior in walls and pull test specimens match reasonably well with each other up to $\Delta = \delta_{max}$.

CHAPTER 7
DESIGN METHODOLOGY

7.1. Introduction

The experimental wall bending tests results described in Chapter 6 have demonstrated the effectiveness of the NSM FRP retrofit technique for URM walls under flexural loading. This chapter presents a design procedure to retrofit masonry walls with vertical CFRP strips with IC debonding as the preferred failure mechanism. Also, some key design considerations are presented along with recommendations based on the experimental observations discussed in Chapter 6. Finally, the design methodology was verified using the results of NSM CFRP retrofitted walls tested in this study.

7.2. Design objectives and Assumptions

As discussed in §2.3, IC debonding is the preferred failure mechanisms as it controls both the flexural capacity as well as the sectional ductility of the plated member (Oehlers and Seracino 2004; Xia and Oehlers 2006). Hence, the design procedure is based on the premise that the preferred failure mode will be IC debonding rather than other more brittle failure modes such as (1) masonry crushing; (2) horizontal bending failure of the masonry between the FRP strips; (3) tensile FRP rupture; or (4) out-of-plane shear failure

Generally, the three main design questions that need to be addressed are: (1) what FRP material (e.g. Carbon, glass or aramid) and retrofit technique (e.g. NSM, EB) should be used?; (2) what FRP strip size should be chosen?; and (3) at what spacing should the FRP strips be placed? The design methodology outlined in this chapter will provide solutions for choosing the FRP strip dimensions (b_p and t_p) and spacing

(S) (Figure 7-1). The methodology is generic in the sense that it can be used for any type of FRP material and both EB and NSM retrofit techniques.

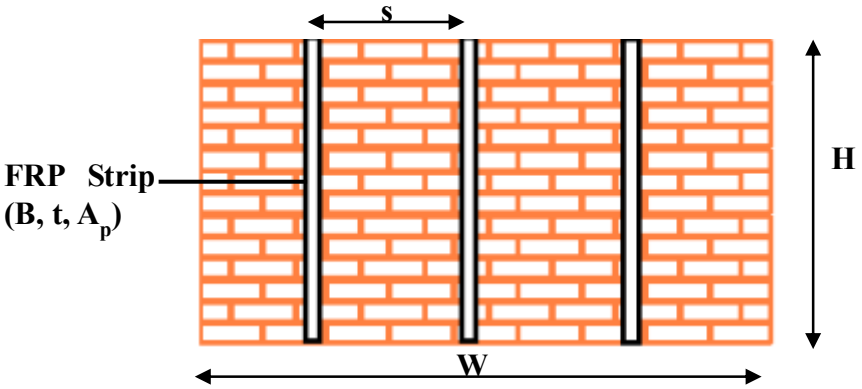

Figure 7-1: Important design parameters

The proposed design procedure is based on the cross-sectional analysis of an FRP reinforced section (Figure 7-2) using conventional "beam theory" and the following assumptions:

a) The wall is "simply-supported" at its top and bottom edges;
b) Plane sections remain plane after bending;
c) Full composite action exists between the FRP strip and the masonry interface;
d) The tensile resistance of the masonry is neglected for calculating the flexural strength;
e) IC debonding occurs prior to masonry crushing, so that the stress-strain relationship for masonry is assumed to be within the elastic range. Hence, a triangular stress block distribution is used for the masonry in compression. (Figure 7-2); and
f) The strain in the FRP is equal to the strain at the onset of debonding, ε_{db} and the force in the FRP strip is therefore equal to P_{IC} (Figure 7-2).

7.3. Prediction of IC debonding resistance

To determine the IC debonding resistance (P_{IC}), the generic analytical model (Eq. 4-3) developed in §4.2.1 is used. The model was validated against a large pull test database from the literature along with the pull test conducted as a part of this study.

$$(P_{IC})_{Generic} = 1.99\varphi_f^{0.19} f_{ut}^{0.47} \sqrt{L_{per}(EA)_p} \quad \text{Eq. 4.3}$$

7.4. Neutral axis location

The neutral axis location, c in Eq. 7-1 is determined by satisfying axial force equilibrium and strain compatibility for the section, as shown in Figure 7-2. In Eq. 7-1, N_s is self-weight of the wall; N_a is the applied axial load and C_m is the masonry compressive force.

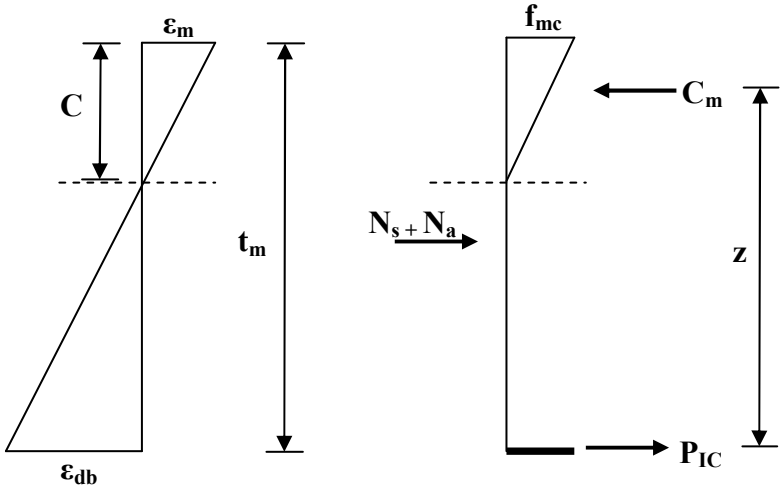

Figure 7-2: Strain and stress profiles at cross-section

$$P_{IC} + N_s + N_a = C_m = \frac{1}{2} c \varepsilon_m E_m S \quad \text{Eq. 7-1}$$

$$\text{Hence, } c = \frac{P_{IC} + N_s + N_a}{\frac{1}{2}\varepsilon_m E_m S} \quad \text{Eq. 7-2}$$

$$\varepsilon_m = \frac{c}{\left(z - \frac{2}{3}c\right)} \varepsilon_{db} \quad \text{Eq. 7-3}$$

where, the lever arm, $z = t_m - \frac{b_p}{2} - \frac{c}{3}$ for NSM and $z = t_m + \frac{t_p}{2} - \frac{c}{3}$ for EB applications.

As the strip dimensions are very small compared to t_m, therefore, $z = t_m - \frac{c}{3}$ and substituting in Eq. 7-3 yields:

$$\varepsilon_m = \frac{c}{(t_m - c)}\varepsilon_{db} \quad \text{Eq. 7-4}$$

Now, Eq. 7-4 can be substituted in Eq. 7-1 to give:

$$c = \frac{-\alpha + \sqrt{\alpha^2 + 4\alpha t_m}}{2} \quad \text{Eq. 7-5}$$

where, $\alpha = \frac{2(P_{IC} + N_s + N_a)}{\varepsilon_{db} E_m S}$; and $\varepsilon_{db} = \frac{P_{IC}}{(EA)_p}$

7.5. Calculation of vertical moment demand (M_d) of FRP reinforced section

The response a wall subjected to the out-of-plane loading depends on the amount of lateral load the wall is subjected to and its capacity to sustain that load. Considering the wall being subjected to a uniformly distributed lateral load (w_d) and spanning vertically between top and bottom supports, the required flexural strength for wall, M_d is given by Eq. 7-6

$$M_d = \frac{w_d h^2}{8} \quad \text{Eq. 7-6}$$

Eq. 7-6 can be written in terms of the demand acceleration (a_d) as shown in

$$M_d = \frac{a_{de} t_m S \gamma h^2}{8} \quad \text{Eq. 7-7}$$

where,

a_{de} is the demand acceleration in units of acceleration due to gravity, g;

h is the clear height of URM wall (i.e. vertical distance between the top and bottom support of the wall);

S is the horizontal spacing between the vertical FRP strips;

t_m is thickness of masonry wall; and,

γ is specific weight of the masonry.

7.6. Calculation of horizontal bending capacity (M_{ch}) of FRP reinforced section

The FRP strip spacing should be sufficiently close to prevent horizontal bending failure of the masonry by out-of-plane loading. The horizontal bending capacity (M_{ch}) of a section of the masonry wall spanning between two FRP strips (per metre height of wall) can be calculated using provisions given by the relevant national design codes. In this study, equations given in AS 3700 (2001) have been used to determine the horizontal bending capacity, M_{ch} which is given by the lesser of:

$$M_{ch} = 2.0\phi k_p \left(\sqrt{f'_{mt}}\right)\left(1+\frac{f_d}{f'_{mt}}\right) z_d \le 4.0\phi k_p \left(\sqrt{f'_{mt}}\right) z \qquad \text{(stepped failure) Eq. 7-8}$$

and

$$M_{ch} = \phi(0.44 f'_{ut} Z_u + 0.56 f'_{mt} Z_p) \qquad \text{(line failure) Eq. 7-9}$$

where,

Φ is the capacity reduction factor = 0.6;

k_p is a perpend factor to allow for the degree of stretcher overlap (for normal stretcher bond, $k_p = 1$)

f'_{mt} is the characteristic flexural tensile bond strength of the masonry, in MPa;

f_d is the minimum design compressive stress on the bed joint at the cross-section, in MPa;

f'_{ut} is the characteristic lateral modulus of rupture of the brick units, in MPa;

z_d is the section modulus of the bedded area, in mm^3/m for a 1m wide section of masonry;

Z_u is the lateral section modulus of the masonry units, in mm^3/m; and

Z_p is the lateral section modulus of the perpends, in mm^3/m.

7.7. Design procedure

The following design flowchart explains the basic steps to be followed.

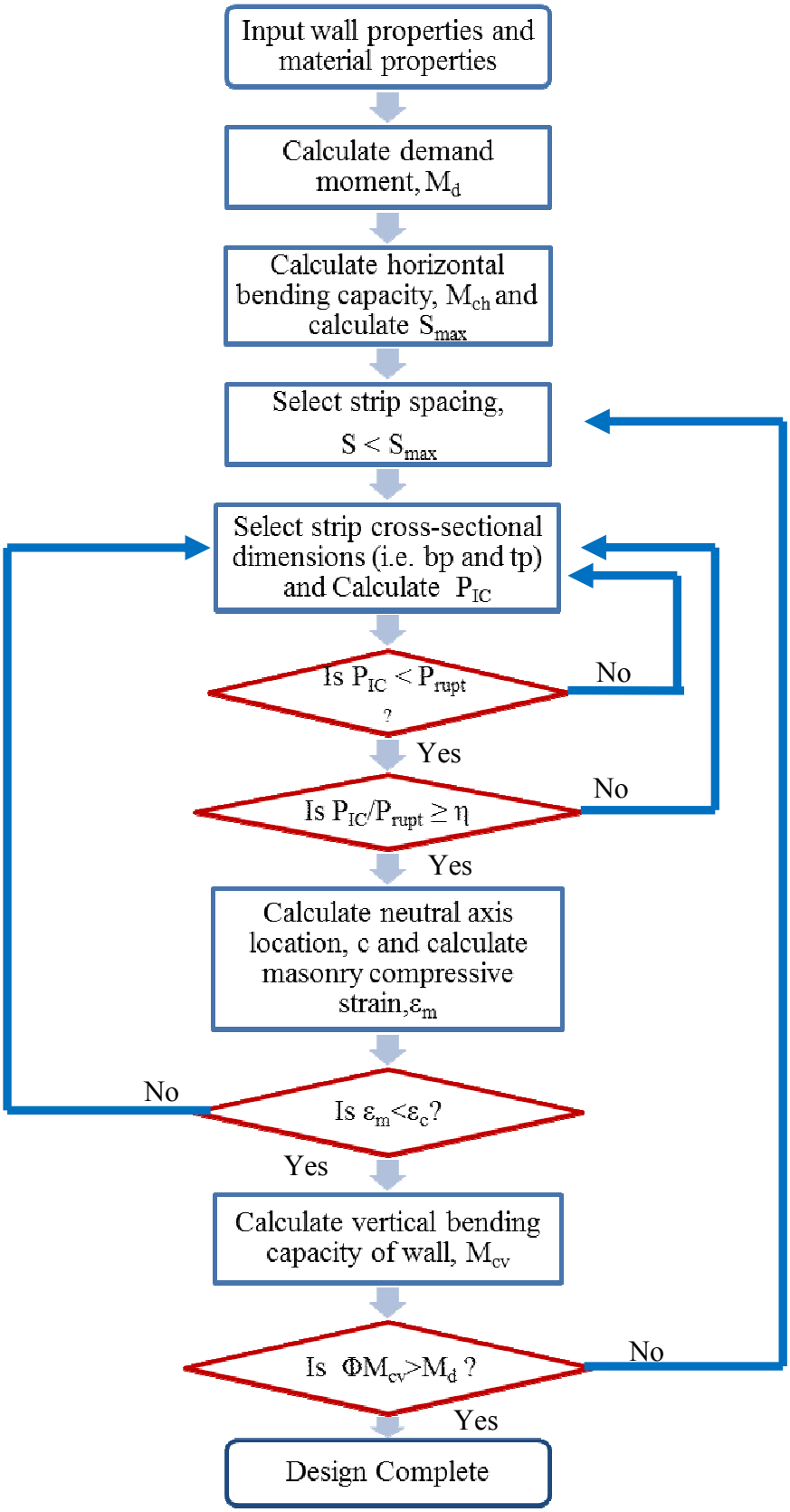

Figure 7-3: Design procedure

Step 1: Calculate the design moment, M_d using Eq. 7-6.

Step 2: Calculate horizontal bending moment capacity, M_{ch} using Eq. 7.8 and Eq. 7.9

Step 3: Calculate the maximum horizontal strip spacing (S_{max}) using Eq. 7-11, such that strengthened wall does not fail by horizontal bending of masonry between the strips due to a_{de}.

$$M_{ch} \geq M_d = \frac{w_d S_{Max}^{\ 2}}{8} \qquad \text{Eq. 7-10}$$

$$S_{\max} \leq \sqrt{\frac{8M_{ch}}{a_{de} t_m \gamma}} \qquad \text{Eq. 7-11}$$

Step 4: Assume cross-sectional dimensions (i.e. b_p and t_p) for the FRP strip and strip spacing, S, such that $S < S_{max}$.

Step 5: Calculate P_{IC} using Eq. 4-3. Check that P_{IC} is less than the tensile rupture capacity of the FRP strip, P_{rupt}, which is given by Eq. 7-12. If not, Go to Step 4 and adjust the strip cross-section.

$$P_{rupt} = f_{rupt} A_p \qquad \text{Eq. 7-12}$$

Step 6: For efficient use of FRP, P_{IC} should not be drastically smaller than P_{rupt}. Designer may wish to specify a minimum "efficiency factor, $\eta = P_{IC} / P_{rupt}$", say 0.8.

Check $1 \geq \eta \geq 0.8$. If not, Go to Step 4 and adjust the strip cross-section.

Step 7: Calculate the neutral axis location, *c* using Eq. 7-5.

Step 8: Calculate the strain in masonry, ε_m using Eq. 7-4. Check that the masonry compressive stress, $f_m = \varepsilon_m E_m$ is less than the masonry strength capacity, $f'_{mc} = \varepsilon_{mc} E_m$. If not, go to Step 4 and adjust the FRP cross-section or strip spacing.

Step 9: Calculate the vertical bending capacity of the section per FRP strip, M_{cv} using Eq. 7-13.

$$M_{cv} = \phi(P_{IC} + N_s + N_a)z \qquad \text{Eq. 7-13}$$

Step 10: Calculate number of FRP strips required, n_p, using Eq. 7-14 and check the spacing between the strips, $S = B/n_p < S_{max}$. If not, go to Step 4 and decrease the strip

spacing, and /or increase the strip cross-section and follow Steps 5-10. If OK, then retrofit the wall with 'n_p' FRP strips with strip spacing of 'S' on both sides.

$$n_p = \frac{M_d}{M_{cv}} \quad \text{Eq. 7-14}$$

7.8. Verification of design procedure using experimental results

The design procedure outlined in §7.7 has been verified against the wall bending tests results presented in Chapter 6. The flexural strength of walls 5-15 were predicted according to Eq. 7.13 with Φ equal to 1 using the material properties given in Table 3-2 and the retrofit details from Table 5-1. The results are summarised in Table 7-1 (Refer to Appendix §F.1 for detailed calculations), where it can be seen that the predictions of flexural strength of NSM CFRP retrofitted walls using the proposed design procedure were, on average, 79 % of the experimental result with a COV of 16 %.

Table 7-1: Comparison of experimental and predicted moment capacity of walls

Wall **S/C** **(1)**	**M_{exp}** **(kN-m)** **(2)**	**M_{pred}** **(kN-m)** **(3)**	**M_{pred}/M_{exp} or (F_{pred}/F_{exp})** **(4)**
5S	8.82	7.37	0.84
6S	13.93	9.13	0.66
7S	21.16	15.74	0.74
8S	18.89	9.29	0.49
9S	6.21	5.52	0.89
10S	15.89	12.57	0.79
11C	14.16	11.37	0.80
12C	14.96	12.57	0.84
13C	15.58	11.37	0.73
14S	15.33	13.77	0.90
15C	14.04	13.77	0.98
Mean			0.79
COV			0.16

Importantly, the design procedure includes the effect of strip spacing which greatly influences the overall flexural response of the retrofitted wall (§6.3.2). The design methodology also accounts for the effect of axial loading which includes self-weight of the wall and any additional applied axial load at the top of the wall. From the theoretical results it has been noted that the increase in moment capacity due to self-weight ranged approximately between 0.5 to 5% while applied pre-compression resulted in increases of about 10% (for 0.1MPa) to 22 % (for 0.2MPa).

Retrofitted walls (walls 5-15) were analysed using the proposed design methodology to check for the possible failure mode such as FRP rupture, masonry crushing and horizontal bending failure of masonry between the FRP strips. Refer to Appendix §F.3 for detailed calculations. The design check revealed that all the walls could withstand the aforementioned failure modes.

7.9. Further verification of the design procedure

The design procedure was further verified using walls tested by Yang (2006) refer to Appendix §F.2). Eight full-scale URM walls were tested under two-way reversed-cyclic loading (Griffith and Vaculik 2005). Four of the most severely damaged walls (with window openings) were subsequently retrofitted using vertical FRP strips with no anchorage and subjected to two way bending. Details of the tests can be found in Yang (2006). Test results indicated that wall A retrofitted using EB CFRP, failed primarily due to IC debonding whereas walls B and C retrofitted using the EB GFRP strips, exhibited horizontal bending failure. Wall D was retrofitted using NSM CFRP strips and it failed prematurely by displacement induced (DI) debonding mechanism and hence is not included in the present analysis. Table 7-2 shows the comparison of predicted and experimental results for walls A to C. It can be seen that predictions of moment capacity are suitably conservative and agree reasonably well with experimental results with mean M_{pred}/M_{exp} ratio of 0.73 and COV of 0.12.

Table 7-2: Prediction of moment capacity for Yang's (2006) wall tests

Wall	t_p x b_p (mm x mm)	# of Strips	Strip spacing (mm)	w_{exp}* (kPa)	M_{exp} (kN-m)	M_{pred} (kN-m)	M_{pred} / M_{exp}
A	1.2 x 50	4	650	9.7	26.68	22.51	0.83
B	2 x 100	4	650	10.5	28.88	19.37	0.67
C	2 x 77	5	500	8.9	24.48	16.64	0.68

Width of wall = 4m

Height of wall = 2.5m

*- experimental lateral load capacity of wall

7.10.Summary

A simple design methodology has been developed for FRP strengthened masonry walls subjected to out-of-plane bending. The predictions from the proposed design procedure compared well with the test results. The design methodology enables the FRP retrofit to be optimised in terms of both the strip spacing and cross-section. From the analysis of the retrofitted walls it was observed that in order to avoid horizontal bending failure of the masonry between the FRP strips, spacing between FRP strips is an important design factor. This suggests that evenly distributed strips result in better performance of wall but the limit to this is rupture strength of the FRP strip.

CHAPTER 8
CONCLUSIONS AND RECOMMENDATIONS

8.1. Introduction

URM buildings are most vulnerable to flexural out-of-plane failure as it endangers the gravity-load-carrying capability of a wall causing the most serious life-safety hazard for this type of construction (Ingham and Griffith 2010). URM structures constitute both a significant portion of the world's heritage buildings and modern residential building stock. Therefore, it is important not only to considerably reduce the seismic risk posed to these structures but also to preserve where possible their architectural appearance. This research was part of a collaborative project between the Universities of Adelaide, Newcastle and Auckland which was aimed at developing an invovative and cost effective retrofit technique for masonry buildings.

The research reported here investigated the performance of NSM CFRP strengthened clay brick masonry walls under monotonic and cyclic out-of-plane bending with particular attention to the FRP-to-masonry bond behaviour. This chapter summarises the important findings of this study as well as recommendations for further research.

8.2. Summary and conclusions

This section presents a brief summary of the research undertaken to accomplish the objectives outlined in §1.2 and also highlights the significant results of this study. The section is divided into two major parts namely, FRP-to-masonry bond behaviour and FRP strengthened masonry walls.

8.2.1. FRP-to-masonry bond behaviour

Part I – Pull tests experimental study (§1.2 - Aim 1)

Fourteen NSM carbon FRP-to-masonry pull tests were conducted to study the FRP-to-masonry bond behaviour and to investigate the effect that cyclic loading and FRP strip dimensions have on the debonding resistance of a NSM FRP-to-masonry joint. The global load-slip response and FRP-to-masonry interface behaviour were studied in depth (Kashyap et al. 2012a). The following conclusions were made:

- All specimens failed by IC debonding with the ultimate failure plane near the masonry-to-adhesive interface FRP-masonry interface indicating that the bonding characteristics of FRP-to-masonry are closely related to the tensile strength of the masonry unit.
- The pull test results indicated that increasing the depth of the NSM FRP strips was more effective for enhancing the debonding resistance of FRP-to-masonry joint than increasing the width of the FRP strip, primarily because of the increase in L_{per} for specimens with a deeper strip and hence providing more efficient confinement of the surrounding masonry. Importantly, the investigation into the effects of cyclic loading on load-slip behaviour of FRP-to-masonry bonded joints indicated that cyclic loading does not significantly affect the overall behaviour of the FRP-to-masonry bond.

Part II –Empirical bond strength model (§1.2 - Aim 2)

The pull tests results were then incorporated into a large database of EB and NSM FRP retrofitted masonry pull test results by various researchers over the past 10 years. Local bond-slip parameters such as the maximum interface shear stress, τ_{max}, and the maximum slip, δ_{max}, were then investigated to determine correlations between these values and masonry material properties. Fifteen existing concrete and masonry bond strength models in the literature were assessed for their use with masonry by comparing these models against the results in the pull test database. Based on the comparative statistics of the test-to-predicted bond strength it was concluded that a new FRP-to-masonry bond model was required to give more

accurate predictions (Kashyap et al. 2012a). The important research outcomes are listed below.

- An analytical model was derived for the IC debonding resistance of FRP-to-masonry joints using a large set of test data from the open literature. A new generic model that is applicable to both EB and NSM techniques was derived. This model is a function of the usual geometric and material design variables such as the FRP strip aspect ratio, the axial rigidity of the FRP strip and the masonry unit tensile strength. For the range of experimental parameters investigated as part of this study, the predicted values from the new model correlated reasonably well with the experimental values.
- Empirical expressions were developed for the key local bond-slip (τ-δ) parameters such as peak interface shear-stress and maximum slip. These bond characteristics are necessary to determine the critical bond length of FRP-to-masonry joints and for analysing the behaviour of FRP strengthened structures.

Part III – Prediction of load-slip behaviour of FRP retrofitted masonry (§1.2 - Aim 2)

In order to predict the global load-slip response of FRP-to-masonry pull tests using various local bond-slip relationships two analytical procedures, namely a new generic numerical procedure and a closed-form mathematical solution, were developed which account for the partial-interaction response at the FRP-masonry interface (Kashyap et al. 2011). Key results are summarised below.

- Validation of both the analytical prodedures against the test data showed that both methods can predict the experimental behaviour well.
- The results of the homogeneous numerical procedure were similar to those of the heterogeneous numerical procedure for all three τ-δ models. Particularly, the difference between the peak loads was observed to be negligible, hence, for simplicity the homogeneous procedure can be used for pull test analysis.
- For both predictive procedures, the elastic-softening τ-δ model gave better correlation with the experimental results than the rigid-softening and

nonlinear models for the overall *P*-Δ response. However, the peak load (P_{IC}) only varied slightly when using either the rigid-softening or nonlinear model.

8.2.2. FRP strengthened masonry walls

Part I - FRP strengthened masonry walls (§1.2 - Aim 3)

Fifteen "walls" specimens were tested in this study to investigate the behaviour of NSM CFRP retrofitted masonry walls under out-of-plane bending and to study the IC debonding failure mechanism in them. Also, the effects of typical design variables such as reverse cyclic loading, axial pre-compression, FRP strip spacing and reinforcement ratio on the stiffness, displacement capacity and ultimate strength of FRP retrofitted masonry walls were studied (Kashyap et al. 2012b). The main outcomes of the experiment wall tests are given below.

- The test results demonstrated that NSM CFRP strips designed to fail by IC debonding can provide an increase in strength of up to 20 times the strength of the corresponding unreinforced wall.
- With respect to the test variables under investigation, it was found that FRP strip spacing and reinforcement ratio most strongly affect wall performance whereas cyclic loading and vertical pre-compression had little effect.
- Optimal spacing of FRP strips was found to be beneficial not only in terms of strength and displacement capacity but was also helpful in avoiding the vertical in-plane shear failure or the horizontal bending failure of the masonry between the FRP strips. For the same reinforcement ratio, smaller strips at closer spacing gave better strength and displacement response but the limit to this is rupture strength of the FRP strip.
- An increase in reinforcement ratio resulted in increased strength but also a corresponding reduction in displacement capacity. Clearly, over reinforced walls can also induce compressive failure of the masonry.
- An applied axial load was seen to increase the flexural stiffness of walls but it had a minimal effect on the strength and displacement capacity of walls.

- The load-displacement behaviour under cyclic load was, in general, very close to the response measured for corresponding monotonically tested walls indicating that monotonic tests may be used to reliably evaluate the effectiveness of the NSM FRP technique for enhancement of out-of-plane seismic resistance.

- Investigation into measured crack widths and the global load-slip of a pull test led to the important conclusion that a strong correlation exists between the force in an FRP strip vs. crack width at a bed joint in the wall and the corresponding pull test load-slip response up to δ_{max}. It was found that the stiffness of the pull test curve closely matches the initial crack stiffness with the pull test giving a lower bound estimate of the IC debonding resistance for FRP strips in a wall.

Part II - FRP strengthened masonry walls (§1.2 - Aim 4)

A simple design methodology was developed for masonry walls retrofitted with vertical CFRP strips with IC debonding as the preferred failure mechanism. This design methodology provides solutions for choosing the FRP strip dimensions (b_p and t_p) and spacing (S). Key conclusions are outlined below.

- The design methodology developed is generic in the sense that it can be used for any type of FRP material and both EB and NSM retrofit techniques.
- It enables the FRP retrofit to be optimised in terms of both the strip spacing and cross-section and thus, allow reliable and economic design to be undertaken.
- The predictions from the proposed design procedure compared well with the test results.

From the results summarised in §8.2.1 and §8.2.2, it was concluded that the proposed NSM technique is structurally efficient and viable for seismic retrofitting of URM walls. Moreover, implementation of the proposed technique could have a significant impact in strengthening of masonry structures including conservation of the heritage buildings with considerable historical importance.

8.3. Future research recommendations

Research into the use of NSM as a retrofitting technique for masonry structures is only in early stages. Although, a range of different parameters were investigated in this study, some related aspects require further research.

Although the bond strength model (Eq. 4-3) proposed in Chapter 3 (§4.2.1) of this study is reasonably accurate there is further scope for improvement by adding more FRP-to-masonry pull test results to the present database. In addition, a significant number of test results were excluded from the test database due to insufficient information available for analysis. The exclusion of some data, points to the need for standardised reporting of test results as well as standardised testing procedures. Further, as reported in Chapter 2 the NSM FRP-masonry pull test database is relatively small hence, more tests should be conducted. Additionally, the local bond-slip parameters, τ_{max} and $\delta_{max,}$ from the pull test data are the principal parameters for the numerical investigation of FRP strengthened structures. The expressions developed for τ_{max} (Eq. 4-8) and δ_{max} (Eq. 4-9) are based on small data set available. Therefore, a wider experimental base is needed to refine these expressions.

Further research should be undertaken on the effects of environmental factors such as moisture, extreme temperatures on the FRP-to-masonry interface. These aspects have received little attention to date. Additionally, it should be noted that for pull tests conducted in this study the FRP strip is pulled only in one direction which does not allow shear stress reversals to occur. However, in flexural walls tests cracking occurs at almost every bed joint causing to the strip to be pulled in both directions. Therefore, it is recommended that the behaviour of the FRP-to-masonry bond when the strip is pulled from both directions should be investigated.

Also, it should be noted that presence of cores in the brick unit may negatively impact the debonding resistance due to stress concentrations, and which may also encourage the longitudinal splitting of observed on the compression face of the walls behind the FRP. The possible effect and influence of this on the prediction of the debonding resistance, and the performance of the system in a wall, should be studied.

The walls tested in this study were accessible from both sides for retrofitting. However, this is not the case for cavity walls. Therefore, experimental investigation on cavity walls is needed to determine if it is possible to transfer the load across the wall ties. Additionally, other influential parameters such as different support conditions, size and location openings need further investigation.

References

ACI 440.7R (2010) "Guide for the design and construction of externally bonded fiber-reinforced polymer systems for strengthening unreinforced masonry structures", American Concrete Institute, Farmington Hills, MI.

Albert, M.L., Elwi, A.E., Cheng, J.J.R. (2001) "Strengthening of unreinforced masonry walls using FRPs", Journal of Composites for Construction, 5(2):76-84.

Aiello, M.A., Sciolti, M.S. Triantafillou, T.C. (2007) "FRP strengthened masonry: Bond aspects", 8th International Symposium on Fiber Reinforced Polymer Reinforcement for Concrete Structures (FRPRCS)-8, Patras, Greece, July 16-18.

Bajpai, K.K., Duthinh, D. (2003) "Flexural Strengthening of Masonry Walls with External composite Bars", The Masonry Society, TMS Journal, 21(1):69-80.

Blaschko, M. (2003) "Bond behavior of CFRP strips glued into slits", 6th International Symposium on Fiber Reinforced Polymer Reinforcement for Concrete Structures (FRPRCS)-6, Singapore, 205-214.

Brosens, K., van Gemert, D. (1999) "Anchorage design for externally bonded carbon fiber reinforced polymer laminates", 4th International Symposium on Fiber Reinforced Polymer Reinforcement for Concrete Structures (FRPRCS)-4, Farmington Hills (MI), SP-188:635–645.

Bruneau, M. (1994) "Seismic evaluation of unreinforced masonry buildings - A state-of-the-art report", Canadian Journal of Civil Engineering, 21:512-539.

Camli, U.S., Binici, B. (2006) "Strength of carbon fiber reinforced polymers bonded to concrete and masonry", Construction and Building Material, 21:1431–1446.

Capozucca R. (2009) "Experimental FRP/SRP–historic masonry delamination", Composite Structures, 92:891-903.

Carloni, C. and Subramaniam, K. (2012) “FRP-Masonry Debonding: Numerical and Experimental Study of the Role of Mortar Joints” Journal of Composites for Construction, 16(5): 581-589.

Carloni, C., Subramanium, K.V. (2010) “Investigation of the interface fracture during debonding between FRP and masonry”, Advances in Structural Engineering, 12(5):731-743.

Chaallal, O., Nollet, M.J., Perraton, D. (1998) “Strengthening of reinforced concrete beams with externally bonded fiber-reinforced-plastic plates: Design guidelines for shear and flexure”, Canadian Journal of Civil Engineering, 25(4): 692-704.

Christensen, J.B., Gilstrap, J., Dolan, C. (1996) “Composites material reinforcement of existing masonry walls”, Journal of Architectural Engineering, ASCE, 2(2):63-70.

Chuang, Y., Zhuge, Y., (2005) “Seismic retrofitting of unreinforced masonry – A literature review”, Australian Journal of Structural Engineering, 6(1):25-36.

Chen, J.F., Teng, J.G. (2001) “Anchorage strength models for FRP and steel plates bonded to concrete”, Journal of Structural Engineering, ASCE, 127(7):784–791.

Dai, J., Ueda, T. (2003) “Local bond stress slip relations for FRP sheets-concrete interfaces”, 6th International Symposium on FRP Reinforcement for Concrete Structures (FRPRCS), 143-152.

Dai J., Ueda T., Sato Y. (2005) “Development of nonlinear bond stress slip model of fiber reinforced plastics sheet-concrete interfaces with a simple method", Journal of Composites for Construction, 9(1):52-62.

Dai, J., Ueda, T., Sato, Y. (2006) “Unified analytical approaches for determining shear bond characteristics of FRP-concrete interfaces through pull out tests”, Journal of Advanced Concrete Technology, 4(1):133-145.

De Lorenzis L., Tinazzi D., Nanni A. (2000) “Near-surface mounted FRP rods for masonry strengthening: Bond and flexural testing”, Proceedings of the Mechanics of

Masonry Structures Strengthened with FRP- materials, modeling, testing, design, control, Venice, Italy, 7-18.

De Lorenzis L., Nanni A. (2002) "Bond Between Near Surface Mounted FRP Rods and Concrete in Structural Strengthening", ACI Structures Journal, 99(2):123-133.

De Lorenzis, L., Teng, J.G. (2006) "Near-surface mounted FRP reinforcement - An emerging technique for strengthening structures", Composites Part B: Engineering, 28:119-143.

Dizhur, D., Derakhshan, H., Griffith, M., Ingham, J. (2010) "In-situ testing of a low intervention NSM seismic strengthening technique for historic URM buildings", International Journal of Materials and Structural Integrity, 5(2-3):168-191.

Drysdale, R.G., Hamid, A., Baker, L.R. "Masonry structures – Behavior and design", Prentice-Hall Inc: Englewood Cliffs, NJ, 1994.

Doherty, K.T. (2000) "An investigation of the weak links in the seismic load path of URM", Ph.D. Thesis, School of Civil and Environmental Engineering, The University of Adelaide.

Ehsani, M.R., Saadatmanesh, H., Velazquez-Dimas, J.I. (1999) "Behavior of Retrofitted Walls Under Simulated Earthquake Loading", Journal of Composites for Construction, 3(3):134-142.

ElGawady, M., Lestuzzi, P., Badoux, M. (2004) "A review of conventional seismic retrofitting techniques for URM", 13th International Brick and Block Masonry Conference, Amsterdam, Holland.

ElGawady, M. A., Lestuzzi, P., Badoux, M. (2005) "In-plane seismic response of URM walls upgraded with FRP", Journal of Composites for Construction, ASCE, 9(6):524-535.

Erdal, M. (2010) "Improving out-of-plane strength and ductility of unreinforced masonry walls in low-rise buildings by centrally applied FRP strip", International Journal of the Physical Sciences, 5(2):116–131.

Galati, N., Garbin, E., Tumialan, J.G., Nanni, A. (2005) "Design guidelines for masonry structures:Out of plane loads", ACI Special Publication, Farmington Hills, Michigan, SP-230-16:269–288.

Galati, N., Tumialan, G., Nanni, A. (2006) "Strengthening with FRP bars of URM walls subject to out-of-plane loads", Construction and Building Materials, 20:101-110.

Galati, N., Hrynyk, T., Tumialan, J.G., Bell, G.N., Myers, J.J., Nanni, A. (2007) "A simplified design methodology accounting for the arching effects in masonry walls strengthened with FRP materials and subject to out-of-plane loads", 10th Northern American Masonry conference, 3-5 June, St. Louis, Missouri, USA.

Ghiassi, B., Marcari1, G., Oliveira, D., Lourenco, P. (2012) "Numerical analysis of bond behavior between masonry bricks and composite materials", Engineering Structures, 43:210-220.

Gravina, R.J., Smith, S.T. (2008) 'Flexural Behaviour of Indeterminate concrete beams reinforced with FRP bars", Engineering Structures, 30(9):2370–2380.

Ghobarah, A., Galal, K.E.M. (2004) "Out-of-plane strengthening of unreinforced masonry walls with openings", Journal of Composites for Construction, 8(4):298-305.

Gilstrap, J.M., C.W. Dolan. (1998) "Out-of-plane Bending of FRP-reinforced Masonry Walls", Composites Science and Technology, 58:1277-1284.

Griffith, M. C., Vaculik, J. (2005) "Flexural strength of unreinforced clay brick masonry walls", 10th Canadian Masonry Symposium, Banff, Alberta.

Hamilton III, H.R., Dolan, C.W. (2001) "Flexural Capacity of Glass FRP Strengthened Concrete Masonry Walls", Journal of Composites for Construction, 5(3):170-178.

Hamoush, S.A., McGinley, M.W., Mlakar, P., Scott, D., Murray, K. (2001) “Out-of-plane strengthening of masonry walls with reinforced composites”, Journal of Composites for Construction, 5(3):139-145.

Hamed, E., Rabinovitch, O. (2007) "Out-of-plane behavior of unreinforced masonry walls strengthened with FRP strips", Composites Science and Technology, 67(3-4): 489-500.

Hamed, E., Rabinovitch, O. (2011) “Free Out-of-Plane vibrations of masonry walls strengthened with composite materials”, Journal of Engineering Mechanics, ASCE. 137(2):125-137.

Haskett, M., Oehlers, D.J., Mohamed Ali, M.S. (2008) “Local and global bond characteristics of steel reinforcing bars”, Engineering Structures, 30:376-383.

Hiroyuki Y., Wu Z. (1997) “Analysis of debonding fracture properties of CFS strengthened member subject to tension”, 3rd International Symposium on Non-metallic (FRP) Reinforcement for Concrete Structures, 284–294.

Ingham, J., M., Griffith, M.C. (2011) “Performance of unreinforced masonry buildings during the 2010 Darfield (Christchurch, NZ) earthquake”, Australian Journal of Structural Engineering, 11(3):207-224.

Ismail, N. and Ingham, J. (2012) “Cyclic Out-of-Plane Behavior of Slender Clay Brick Masonry Walls Seismically Strengthened Using Posttensioning”, Journal of Structural Engineering, 138(10): 1255-1266.

Kashyap, J., Griffith, M. C., Mohamed Ali, M. S., Oehlers, D. J. (2011) “Prediction of load-slip behavior of FRP retrofitted masonry”, Journal of Composites for Construction, 5(6):943-951.

Kashyap J., Willis C.R., Griffith M.C., Ingham J.M., Masia M. (2012a) “Debonding resistance of FRP-to-masonry joints”, Engineering structures, 41(8):186–198.

Kashyap J., Griffith M.C., and Mohamed Ali M.S. (2012b) "Experimental study on flexural behaviour of FRP retrofitted masonry walls," Proceedings, FRP Composites in Construction (CICE) conference, Rome, Italy, 13-15 June.

Karbhari, V. M., Niu H., Sikorsky, C. (2006) "Review and comparison of fracture mechanics-based bond strength models for FRP-strengthened structures", Journal of Reinforced Plastics and Composites, 25(17):1757-1794.

Khalifa, A., Gold, W.J., Nanni, A., Abdel Aziz, M.I. (1988) "Contribution of externally bonded FRP to shear capacity of RC flexural members", Journal of Composites for Construction 1998, 2(4):195-202.

Kiss, R.M., Laszlo, P.K., Jai, J., Krawinkler, H. (2002) "FRP strengthened masonry beams- Part I", Journal of Composite Materials, 36:521-536.

Klopp, G.M. (1996) "Seismic design of unreinforced masonry structures", Ph.D. Thesis, School of Civil and Environmental Engineering, The University of Adelaide.

Konthesingha, K.M.C., Masia, M.J., Petersen, R.B., Page, A.W. (2009) "Bond behaviour of NSM FRP strips to modern clay brick masonry prisms under cyclic loading", 11th Canadian Masonry Symposium, McMaster University/Canadian Masonry Design Centre, Toronto, Ontario, Canada, 665-674.

Korany, Y., Drysdale, R., (2004) "New FRP rehabilitation technique for historic masonry buildings. Masonry Society Journal, 22(1):27-38.

Korany, Y., Drysdale, R., (2006) "Rehabilitation of masonry walls using unobtrusive FRP techniques for enhanced out-of-plane seismic resistance", Journal of Composites for Construction, ASCE, 10(3):213-222.

Kuzik, M.D., Elwi, A.E., Cheng, J.J.R. (2003) "Cyclic flexure tests of masonry walls reinforced with glass fibre reinforced polymer sheets", Journal of Composites for Construction, 7(1): 20-30.

Lam C. (2009) "Finite element study of bond-slip behaviour of CFRP and GFRP laminates on brick masonry", MSc. Thesis, University of Padova.

Lillistone, D., Jolly, C.K. (1998) "Strengthening of masonry walls with FRP composite materials", 7th International Conference on Fibre Reinforced Composites, Newcastle Upon Tyne, UK,15-17 April.

Liu, I.S.T. (2005) “Intermediate crack debonding of plated RC beams”, Ph.D. Thesis, School of Civil and Environmental Engineering, The University of Adelaide.

Liu, I.S.T., Oehlers, D.J., Seracino, R. (2007) “Study of intermediate crack debonding in adhesively plated beams”, Journal of Composites for Construction, 11(2):175-183.

Lu, X. Z., Teng, J. G., Ye, L. P., Jiang, J. J. (2005) "Bond-slip models for FRP sheets/plates bonded to concrete", Engineering Structures, 27(6): 920-937.

Luccioni, B., Rougier, V. (2010) “Shear behaviour of brick–mortar interface in CFRP retrofitted or repaired masonry”, International Journal of Mechanical Sciences, 52(4):602-611.

MacGregor, J.G. (1988) “Reinforced concrete: mechanics and design”, New Jersey: Prentice Hall.

Milani, G. and Lourenço, P. (2012) “Simple Homogenized Model for the Nonlinear Analysis of FRP-Strengthened Masonry Structures”, II: Structural Applications. Journal of Engineering Mechanics, 2012. 139(1): 77-93.

Milani, G., Bucchi, A. (2010) “Kinematic FE homogenized limit analysis model for masonry curved structures strengthened by near surface mounted FRP bars”, Composite Structures, 93(1): 239-258.

Milani, G., Milani, E., Tralli, A. (2009) “Upper bound limit analysis model for FRP-reinforced masonry curved structures - Part II: Structural analyses”, Computers and structures, 87(23-24): 1534-1558.

Milani G. (2010), “FE homogenized limit analysis model for masonry strengthened by near surface FRP bars”, Composite Structures; 92(2): 330-338.

Monti, M., Renzelli, M., Luciani, P. (2003) “FRP adhesion in uncracked and cracked concrete zones”, 6th international symposium on FRP reinforcement for concrete structures, Singapore, 183–192.

Mohamed Ali, M. S., Oehlers, D. J., Griffith, M. C., Seracino R. (2008) “Interfacial stress transfer of near surface-mounted FRP-to-concrete joints”, Engineering Structures, 30(7):1861-1868.

Mosallam, A.S. (2007) “Out-of-plane flexural behavior of unreinforced red brick walls strengthened with FRP composites”, Composites, Part B: Engineering, 38:559-574.

Nakaba, K., Kanakubo, T., Furuta, T., Yoshizawa, H. (2001) “Bond behavior between fiber-reinforced polymer laminates and concrete”, ACI Structural Journal, 98(3): 359-367.

Neubauer, U., Rostasy, F. S. (1997) “Design aspects of concrete structures strengthened with externally bonded CFRP plates”, 7th International Conference on Structural Faults and Repairs, Edinburgh, Scotland, July.

Oehlers, D. J., Seracino, R. (2004). "Design guideline for RC structures retrofitted with FRP and metal plates: Beams and slabs”, Elsevier, UK.

Oehlers, D.J., Bradford, M. A. (1995) “Composite steel and concrete structural members: Fundamental behaviour”, Pergamon, Oxford, U.K.

Oehlers, D.J., Seracino R. (2004) “Design of FRP and steel plated RC structures: Retrofitting of beams and slabs for strength, stiffness and ductility”, Elsevier, Kidlington, Oxford, UK.

Oehlers, D.J., Haskett, M., Wu, C., Seracino, R. (2008) Embedding NSM FRP plates for improved IC debonding resistance”, Journal of Composites for Construction, 12(6): 635-642.

Oliveira, D.V., Basilio, I., Lourenço, P.B. (2010) "Experimental bond behavior of FRP sheets glued on brick masonry", Journal of Composites for Construction, 15(1): 32-41.

Paquette, J., Bruneau, M., Filiatrault, A. (2001) "Out-of-plane seismic behavior of brick Masonry walls of Turn-of-the-Century Residential Buildings", Journal of Structural Engineering, 127(5): 561–569.

Petersen, R.B., Masia, M.J., Seracino, R. (2009) "Bond behaviour of NSM FRP strips bonded to modern clay brick masonry prisms: Influence of strip orientation and compression perpendicular to the strip", Journal of Composites for Construction, 13(3):169-178.

Rahimi, H., Hutchinson, A. (2001) "Concrete beams strengthened with externally bonded FRP plates", Journal of Composites for Construction, 5(1):44-56.

Saadatmanesh, H. (1997) "Extending Service Life of Concrete and Masonry Structures with Fiber Composites", International Journal of Construction and Building Materials, Elsevier Science Ltd., 11(5-6):327-335.

Sayari, A., Donchev, T., Limbachiya, M.C., Kew, H.Y. (2010) "Out-of-Plane Behaviour of FRP Strengthened Masonry Walls", 8th International Masonry Conference, International Masonry Society, Dresden, Germany, 4-7 July.

Sayed-Ahmed, E.Y., Bakay, R., Shrive, N.G. (2009) "Bond strength of FRP laminates to concrete: State-of-the-art review" Electronic Journal of Structural Engineering, 9:45-61.

Schwegler, G. (1995) "Masonry construction strengthened with fiber composites in seismically endangered zones", 10th European Conference on Earthquake Engineering, Rotterdam, 28 August-2 September.

Shrive, N.G. (2006) "The use of fibre reinforced polymers to improve seismic resistance of masonry", Construction and Building Materials, 20(4):269-277.

Standards Australia (2001) “AS 3700-2001: Masonry Structures (including Amendment 3, August 2007)”, Standards Australia, Sydney.

Seracino R., Jones, N.M., Ali, M.S.M., Page, M.W., Oehlers, D.J. (2007a) “Bond strength of near-surface mounted FRP strip-to-concrete joints”, Journal of Composites for Construction; 11(4):401- 409.

Seracino, R., Saifulnaz, M.R.R., Oehlers, D.J. (2007b) "Generic debonding resistance of EB and NSM plate-to-concrete joints", Journal of Composites for Construction, 11(1):62-70.

Soric, Z., Tulin, L.G. (1989) “Bond stress/deformation in pull-out masonry specimens”, Journal of Structural Engineering, 115(10):2588-2602.

Standards Australia, AS/NZS 4456.15 (2003): Masonry units, segmental pavers and flags— Methods of test Method 15: Determining lateral modulus of rupture, Sydney.

Tan, K.H. and Patoary, M.K.H. (2004) “Strengthening of masonry walls against out-of–plane loads using fibre-reinforced polymer reinforcement”, Journal of Composites for Construction, ASCE, 8(1):79-87.

Teng, J.G., Chen, J.F., Smith, S.T., Lam, L. (2002) “FRP strengthened RC structures,” Chichester, England, John Wiley and Sons Ltd.

Tinazzi, D., Nanni A. (2000) "Assessment of technologies of masonry retrofitting with FRP", Center for Infrastructure Engineering Studies, University of Missouri-Rolla.

Triantafillou, T. (1998) “Strengthening of masonry structures using epoxy bonded FRP laminates”, Journal of Composites for Construction, ASCE, 2(2):96-104.

Tumialan, J.G., Galati, N., Nanni, A. (2003) “Field assessment of unreinforced masonry walls strengthened with fiber reinforced polymer laminates”, Journal of Structural Engineering, 129(8):1047-1056.

Tumialan, G., Vatovec, M., Kelly, P. (2009) "FRP composites for masonry retrofitting: Review of engineering issues, limitations and practical issues", Structure Magazine, 12-14.

Turco, V.N. Galati, L., De Lorenzis, L., Modena C, Nanni A. (2003) "Bond between near surface mounted FRP rods and masonry in structural strengthening", Advancing with Composites, Plastics, Ed. I: Crivelli-Visconti, Milan, Italy, 209-217.

Ueda, T., Dai, J.G., Sato, Y. (2003) "A nonlinear bond stress–slip relationship for FRP sheet–concrete interface", International symposium on latest achievement of technology and research on retrofitting concrete structures, 113–120.

Ueda, T. and Dai, J. (2005) "Interface bond between FRP sheets and concrete substrates: properties, numerical modeling and roles in member behaviour," Progress in Structural Engineering and Materials, 7(1): 27-43.

Vasquez, D., Seracino, R. (2010) "Assessment of the predictive performance of existing analytical models for debonding of near-surface mounted FRP strips", Advances in Structural Engineering, 13(2), 299-308.

Velazquez-Dimas, J.I., Ehsani, M.R. (2000) "Modeling out-of-plane behavior of URM walls retrofitted with fiber composites", Journal of Composites for Construction, 4(4):172-181.

Vandergrift, Gergely, Young (2002) "CFRP retrofit of masonry walls" 3rd International Conference on Composites in Infrastructure, , San Francisco, CA, 10-12 June.

Wakabayashi, M. (198**6)** "Design of earthquake-resistant buildings", McGraw-Hill, New York.

Willis, C.R., Yang, Q., Seracino, R., Griffith, M.C. (2009a) "Damaged masonry walls in two-way bending retrofitted with vertical FRP strips", Construction and Building Materials, 23(4): 1591-1604.

Willis, C.R., Yang, Q., Seracino, R., Griffith M.C. (2009b) “Bond behaviour of FRP-to-clay brick masonry joints” Engineering Structures, 31(11):2580-2587.

Wu, Z.S., Yuan, H., Niu, H.D. (2002) “Stress transfer and fracture propagation in different kinds of adhesive joints” Journal of Engineering Mechanics, ASCE, 128(5):562–73.

Xia, S., Oehlers, D.J. (2006) “Debonding mechanisms in FRP plated unreinforced masonry under out-of-plane loading”, Advances in Structural Engineering, 9(5):619-637.

Yang, Q. (2006) “Out-of-plane strengthening of unreinforced masonry walls using FRP techniques”, Masters Thesis, School of Civil and Environmental Engineering, The University of Adelaide.

Yuan, H., Teng, J. G., Seracino, R., Wu, Z. S., Yao, J. (2004) "Full-range behaviour of FRP-to-concrete bonded joints", Engineering Structures, 26(5):553-565.

Yuan, H., Wu, Z. (1999) “Interfacial fracture theory in structures strengthened with composite of continuous fibre”, Symposium of China and Japan, Science and Technology of 21st Century, Tokyo, Japan, 142-155.

Appendices

Notations

b_c	width of concrete section
$b_{p/FRP/f}$	width of FRP strip/plate
b_a	width of adhesive
C_1	experimental coefficient (0.015 – 0.030)
$E_{FRP/p/f}$	FRP Young modulus
E_a	adhesive Young modulus
$f_{dff,rid}$	reduced value of the design bond strength
f_{fdd}	design bond strength
f'_c	compressive strength of masonry
f_{mk}	characteristic compressive strength of masonry
f_{mtm}	average tensile strength of masonry
f_{rupt}	rupture stress of FRP strip
f_t	concrete surface tensile strength
G_f	fracture energy
k_p	geometric factor
L, l_b	bond length of FRP elements
L_e, l_e	optimal bond length of FRP
$P_{u/max/IC}$	bond strength of joint
t_a	thickness of adhesive
$t_{FRP/p/f}$	thickness of FRP strip/plate
$\tau_{max/f/p/u}$	maximum FRP-substrate interfacial shear stress
$\delta_{max/f/p/u}$	slip at which macro cracking occurs
δ_1	slip corresponding to maximum shear stress
β_L	geometric bond length coefficient
β_p	geometric width coefficient
φ_f	IC debonding failure plane aspect ratio
Γ_{fd}	safety factor (1.20)
Γ_M	partial safety factor for masonry (1.0)

APPENDIX A: PULL TEST NUMERICAL STUDY

A.1 Existing bond strength models

This section provides details of the sixteen bond strength models assessed in §2.4.2 of Chapter 2.

[1] Sato et al. model (from Sayed-Ahmed et al. 2009)

$$\tau_u = 2.68x10^{-5}(f'_c)^{0.2} E_p t_p$$

$$P_u = \tau_u L_e (b_p + 7.4)$$

$$L_e = 1.89(E_p t_p)^{0.4} \quad \text{if L > Le: Le = L}$$

[2] Iso model (from Sayed-Ahmed et al. 2009)

$$\tau_u = 0.93(f'_c)^{0.44}$$

$$P_u = \tau_u L_e b_p$$

$$L_e = 0.125(E_p t_p)^{0.57} \quad \text{if L > Le: Le = L}$$

[3] Yang et al. model (from Sayed-Ahmed et al. 2009)

$$Pu = \left(0.5 + 0.08\sqrt{0.01E_p t_p / f_t}\right) b_p L_e \tau_u$$

$$Le = 100mm$$

$$\tau_u = 0.5 f_t$$

[4] Meada et al. model (from Sayed-Ahmed et al. 2009)

$$\tau_u = \left(110.2x10^{-6}\right) E_p t_p$$

$$P_u = \tau_u L_e b_p$$

$$L_e = e^{2.1235 - 0.580\ln(E_p t_p)}$$

[5] Tanaka model (from Sayed-Ahmed et al. 2009)

$$\tau_u = 6.13 - \ln(L)$$

$$P_u = \tau_u L\, b_p$$

[6] Hiroyuki and Wu model (from Sayed-Ahmed et al. 2009)

$$\tau_u = 0.27 L^{-0.669}$$

$$P_u = \tau_u L_e b_p$$

[7] Khalifa et al. model (1998)

$$\tau_u = \left(110.2x10^{-6}\right)\left(f'_c / 42\right) E_p t_p$$

$$P_u = \tau_u L_e b_p$$

$$L_e = e^{2.1235 - 0.580\ln(E_p t_p)}$$

[8] Nebauer & Rostasy model (from Sayed-Ahmed et al. 2009)

$$P_u = 0.64 k_p b_p \sqrt{E_p t_p f_t} \qquad \text{if } L \geq Le$$

$$P_u = 0.64 k_p b_p \sqrt{E_p t_p f_t}\,\alpha \qquad \text{if } L < Le$$

where, $\alpha = \left(\frac{L}{L_e}\right)\left(2 - \frac{L}{L_e}\right)$; $L_e = \sqrt{\frac{E_p t_p}{2 f_t}}$; $G_f = c_f f_t$

[9] Karbhari et al. model (2006)

This model is based on the model proposed by Nakaba et al. (2001).

$$p_{\max} = b_p \sqrt{2 G_f E_p t_p}$$

$$G_f = 0.644 f'^{0.19}_c$$

$$\tau_{\max} = 3.5 f'^{0.19}_c$$

$$L_e \approx \frac{P_{\max}}{b_p \tau_{\max} / 2}$$

$$L_e \approx \frac{P_{\max}}{b_p \tau_{\max}/2}$$

$$\approx \frac{2b_p\sqrt{2G_f E_p t_p}}{b_p \tau_{\max}} = \frac{0.6485\sqrt{E_p t_p}}{f'^{0.095}_c}$$

[10] Lu et al. model (2005)

$$p_u = \beta_l b_f \sqrt{2G_f E_f t_f}$$

$$L_e = a + \frac{1}{2\lambda_1}\ln\frac{\lambda_1 + \lambda_2 \tan\lambda_2 a}{\lambda_1 - \lambda_2 \tan\lambda_2 a}$$

Where

$$\lambda_1 = \sqrt{\frac{\tau_{\max}}{s_0 E_f t_f}}$$

$$\lambda_2 = \sqrt{\frac{\tau_{\max}}{(s_f - s_0)E_f t_f}}$$

$$a = \frac{1}{\lambda_2}\arcsin\left[0.99\sqrt{\frac{s_f - s_0}{s_f}}\right]$$

$$\tau_{\max} = \alpha_1 \beta_w f_t$$

$$s_0 = 0.0195\,\beta_w f_t$$

$$G_f = 0.308\beta_w^2\sqrt{f_t}$$

$$\beta_w = \sqrt{\frac{2.25 - b_f/b_c}{1.25 + b_f/b_c}}$$

Bond length factor, β_l

$= 1$ if $L > Le$

$= \sin\left(\frac{\Pi L}{2Le}\right)$ if $L \le L_e$

[11] Chen and Teng (2001)

$$p_u = 0.427\beta_p\beta_L\sqrt{f'_c}\,b_p L_e$$

$$L_e = \sqrt{\frac{E_p t_p}{\sqrt{f'_c}}}$$

$$\beta_p = \sqrt{\frac{2 - b_p / b_c}{1 + b_p / b_c}}$$

$$\beta_L \begin{cases} = 1 & \text{if } L \geq Le \\ = \sin\left(\frac{\Pi L}{2Le}\right) & \text{if } L < L_e \end{cases}$$

[12] Camli and Binici (2006)

$$p_u = \alpha t_{frp} b_{frp} f_{frp}$$

α is equal to 0.35 and 0.50 for specimens with and without plaster finish, respectively.

[13] Monti et al. (2003)

$$\sigma_{\max} = \beta \sqrt{\frac{E_p \tau_{\max}}{3 t_p}}$$

$$\beta \begin{cases} = 1 & \text{if } L \geq Le \\ = \sin\left(\frac{\Pi L}{2Le}\right) & \text{if } L < L_e \end{cases}$$

$$L_e = \sqrt{\frac{E_p t_p}{4 \tau_{\max}}}$$

$$\tau_{\max} = 1.8 k_b f_t$$

$$k_p = \sqrt{\frac{1.5(2 - b_p / b_c)}{1 + (b_p / 100)}}$$

[14] Milani et al. (2009)

$$f_{fdd} = \frac{1}{\Gamma_{fd}\sqrt{\Gamma_M}}\sqrt{\frac{2E_{FRP}\Gamma_{Fk}}{t_{FRP}}} \qquad \text{if } l_b > l_e$$

$$f_{fdd,rid} = f_{fdd}\frac{l_b}{l_e}\left(2-\frac{l_b}{l_e}\right) \qquad \text{if } l_b < l_e$$

$$\Gamma_{Fd} = C_1\sqrt{f_{mk}f_{mtm}}$$

$$l_e = \sqrt{\frac{E_{FRP}t_{FRP}}{2f_{mtm}}}$$

[15] Seracino et al. (2007b)

$$P_{IC} = \alpha\beta\sqrt{f_c}\,d_p^{1.36}b_p^{0.21} \le f_{rupt}b_p d_p$$

where, α is taken as 0.19 and 0.16 for mean and characteristic values, respectively; β = 1.0 for L ≥ 200 mm and β = L/200 for L < 200 mm

[16] Willis et al. 2009

$$P_{IC} = 0.988\varphi_f^{0.263}\left(\frac{f_{ut}}{0.53}\right)^{0.6}\sqrt{L_{per}(EA)_p}$$

$$EB: \varphi_f = \frac{1}{2+b_p}$$

$$NSM: \varphi_f = \frac{1+b_p}{2+t_p}$$

$$L_{per} = 2d_f + b_f$$

A.2 FRP-to-masonry pull tests database

Table A-1: Existing pull test database

Reference	Specimen	EB/ NSM	t_p (mm)	b_p (mm)	E_p (GPa)	L_b (mm)	f_{ut} (MPa)	b_m (mm)	P_{exp} (kN)
Turco et al. [30]	E-10-SS	NSM	6.35	6.35	40.8	254	1.93	230	19.17
	E-15-SS	NSM	6.35	6.35	40.8	381	1.93	230	18.55
Liu et al. [31]	CM50(A)	EB	1.00	25.00	22.3	50	2.05	400	4.88
	CM50(B)	EB	1.00	25.00	22.3	50	2.05	400	5.63
	CM50(C)	EB	1.00	25.00	22.3	50	2.05	400	4.25
	CM50(D)	EB	1.00	25.00	22.3	50	2.05	400	3.75
	CM50(E)	EB	1.00	25.00	22.3	50	2.05	400	5.13
	CM75(A)	EB	1.00	25.00	22.3	75	2.05	400	5.81
	CM75(B)	EB	1.00	25.00	22.3	75	2.05	400	5.44
	CM75(C)	EB	1.00	25.00	22.3	75	2.05	400	6.38
	CM75(D)	EB	1.00	25.00	22.3	75	2.05	400	3.94
	CM75(E)	EB	1.00	25.00	22.3	75	2.05	400	7.13
	CM100(A)	EB	1.00	25.00	22.3	100	2.05	400	4.75
	CM100(B)	EB	1.00	25.00	22.3	100	2.05	400	5.00
	CM100(C)	EB	1.00	25.00	22.3	100	2.05	400	6.50
	CM100(D)	EB	1.00	25.00	22.3	100	2.05	400	7.25
	CM100(E)	EB	1.00	25.00	22.3	100	2.05	400	7.25
	CM100(F)	EB	1.00	25.00	22.3	100	2.05	400	8.50
	BM50(A)	EB	1.00	25.00	22.3	50	2.73	200	9.25
	BM50(B)	EB	1.00	25.00	22.3	50	2.73	200	7.38
	BM50(C)	EB	1.00	25.00	22.3	50	2.73	200	8.63
	BM50(D)	EB	1.00	25.00	22.3	50	2.73	200	6.88
	BM75(A)	EB	1.00	25.00	22.3	75	2.73	200	10.69
	BM75(B)	EB	1.00	25.00	22.3	75	2.73	200	8.44
	BM75(C)	EB	1.00	25.00	22.3	75	2.73	200	9.38
	BM75(D)	EB	1.00	25.00	22.3	75	2.73	200	9.56
	BM75(E)	EB	1.00	25.00	22.3	75	2.73	200	8.25
	BM100(A)	EB	1.00	25.00	22.3	100	2.73	200	8.50
	BM100(B)	EB	1.00	25.00	22.3	100	2.73	200	10.00
	BM100(C)	EB	1.00	25.00	22.3	100	2.73	200	10.00
	BM100(D)	EB	1.00	25.00	22.3	100	2.73	200	9.00
	BM100(E)	EB	1.00	25.00	22.3	100	2.73	200	10.00
	CSG100	EB	1.00	25.00	22.3	100	2.05	400	5.58
	BSG100	EB	1.00	25.00	22.3	100	2.73	200	9.40

Reference	Specimen	EB/ NSM	t_p (mm)	b_p (mm)	E_p (GPa)	L_b (mm)	f_{ut} (MPa)	b_m (mm)	P_{exp} (kN)
Camli and Binici [32]	TS-4	EB	1.00	25.00	61.0	125	1.30	280	4.06
	TS-7	EB	1.00	50.00	61.0	100	1.30	280	5.90
	TS-8	EB	1.00	50.00	61.0	125	1.30	280	5.14
Xia and Oehlers [18]	Pull 3	EB	1.20	50.00	165	210	2.75	230	25.25
	Pull 4	EB	1.20	50.00	165	280	2.75	230	28.40
Konthesingha et al. [24]	1A	NSM	2.80	15.00	207	355	3.57	230	61.60
	2A	NSM	2.80	15.00	207	355	3.57	230	65.24
	2B	NSM	2.80	15.00	207	355	3.57	230	63.53
	2C	NSM	2.80	15.00	207	355	3.57	230	66.52
Lam [33]	C1	EB	0.17	50.00	230	200	3.35	250	15.94
	C2	EB	0.17	50.00	230	200	3.35	250	17.12
	C3	EB	0.17	50.00	230	200	3.35	250	17.66
	C4	EB	0.17	50.00	230	200	3.35	250	19.61
	C5	EB	0.17	50.00	230	200	3.35	250	20.15
	G1	EB	0.23	50.00	65.0	200	3.35	250	11.69
	G2	EB	0.23	50.00	65.0	200	3.35	250	13.97
	G3	EB	0.23	50.00	65.0	200	3.35	250	13.65
	G4	EB	0.23	50.00	65.0	200	3.35	250	13.20
	G5	EB	0.23	50.00	65.0	200	3.35	250	14.18
Petersen et al. [6]	S1-A-NG-1	NSM	2.80	15.00	207	336	3.57	230	83.45
	S1-A-NG-2	NSM	2.80	15.00	207	336	3.57	230	71.09
	S1-A-SG	NSM	2.80	15.00	207	336	3.57	230	81.48
	S1-B-NG-1	NSM	2.80	15.00	207	336	3.57	230	70.36
	S1-B-NG-2	NSM	2.80	15.00	207	336	3.57	230	59.41
	S1-C-NG-1	NSM	2.80	15.00	207	336	3.57	230	63.88
	S1-C-NG-2	NSM	2.80	15.00	207	336	3.57	230	69.41
	S1-C-SG	NSM	2.80	15.00	207	336	3.57	230	84.50
Willis et al. [5]	St1.0-3-15-1/2-NSG	NSM	1.20	15.00	162	241	3.55	230	46.80
	HO1.5-4-15-1/4	NSM	1.20	15.00	162	328	3.55	230	44.00
	HO1.0-4-15-0	NSM	1.20	15.00	162	328	3.55	230	38.30
	HO1.0-4-15-0-NSG	NSM	1.20	15.00	162	334	3.55	230	46.70
	St1.0-4-20-AC	NSM	1.20	20.00	162	328	3.55	230	50.00
	St1.0-4-20-BC	NSM	1.20	20.00	162	328	3.55	230	51.20
	GP-5-Ne-M-1	EB	2.00	50.00	65.0	420	3.55	230	22.10
	GP-5-Ne-Q-1	EB	2.00	50.00	65.0	395	3.55	230	21.50
	GP-5-Ne-M-2	EB	2.00	50.00	65.0	419	3.55	230	21.90
	GP-5-Ne-Q-2	EB	2.00	50.00	65.0	396	3.55	230	18.10
	GP-5-Sa-Q	EB	2.00	50.00	65.0	394	3.55	230	24.70
	GP-5-Gr-Q	EB	2.00	50.00	65.0	393	3.55	230	24.30
	GD-5-Sa-Q-1	EB	0.62	50.00	73.0	386	3.55	230	19.90
	GD-5-Sa-Q-2	EB	0.62	50.00	73.0	386	3.55	230	18.60
	CP-2-Ne-M	EB	1.20	50.00	162	140	3.55	230	26.80
	CP-3-Ne-M	EB	1.20	50.00	162	210	3.55	230	24.90
	CP-4-Ne-M	EB	1.20	50.00	162	280	3.55	230	28.40

Reference	Specimen	EB/ NSM	t_p (mm)	b_p (mm)	E_p (GPa)	L_b (mm)	f_{ut} (MPa)	b_m (mm)	P_{exp} (kN)
Oliveria et al. [34]	G150RS-1	EB	0.15	25.00	80.2	150	1.57	235	3.48
	G150RS-2	EB	0.15	25.00	80.2	150	1.57	235	4.81
	G150RS-3	EB	0.15	25.00	80.2	150	1.57	235	4.69
	G150RS-5	EB	0.15	25.00	80.2	150	1.57	235	4.64
	G100RS-1	EB	0.15	25.00	80.2	100	1.57	235	3.66
	G100RS-2	EB	0.15	25.00	80.2	100	1.57	235	3.17
	G100RS-3	EB	0.15	25.00	80.2	100	1.57	235	2.85
	G100RS-4	EB	0.15	25.00	80.2	100	1.57	235	3.68
	G100RS-5	EB	0.15	25.00	80.2	100	1.57	235	3.79
	G200RS-2	EB	0.15	25.00	80.2	200	1.57	235	4.48
	G200RS-3	EB	0.15	25.00	80.2	200	1.57	235	5.06
	G150RI-5	EB	0.15	25.00	80.2	150	1.57	235	5.27
	G150RT-1	EB	0.15	25.00	80.2	150	1.57	235	4.20
	G150RT-2	EB	0.15	25.00	80.2	150	1.57	235	4.89
	G150RT-3	EB	0.15	25.00	80.2	150	1.57	235	5.60
	G150RT-4	EB	0.15	25.00	80.2	150	1.57	235	4.34
	G150RT-5	EB	0.15	25.00	80.2	150	1.57	235	5.49
	G150ES-1	EB	0.15	25.00	80.2	150	1.57	235	3.52
	G150ES-2	EB	0.15	25.00	80.2	150	1.57	235	4.83
	G150ES-4	EB	0.15	25.00	80.2	150	1.57	235	4.53
	G150ES-5	EB	0.15	25.00	80.2	150	1.57	235	5.46
	G150XS-1	EB	0.15	25.00	80.2	150	1.57	235	4.55
	G150XS-2	EB	0.15	25.00	80.2	150	1.57	235	3.73
	G150XS-3	EB	0.15	25.00	80.2	150	1.57	235	3.82
	G150XS-4	EB	0.15	25.00	80.2	150	1.57	235	4.54
	G150XS-5	EB	0.15	25.00	80.2	150	1.57	235	4.06
	C150RS-1	EB	0.12	25.00	216	150	1.57	235	4.78
	C150RS-2	EB	0.12	25.00	216	150	1.57	235	4.29
	C150RS-3	EB	0.12	25.00	216	150	1.57	235	4.02
	C150RS-4	EB	0.12	25.00	216	150	1.57	235	4.33
	C150RS-5	EB	0.12	25.00	216	150	1.57	235	4.26

APPENDIX B: MATERIAL TESTS

B.1 Introduction

This section presents details of the tests conducted to determine the masonry material properties used in this research. Three types of material tests were conducted in accordance with Australian Standards: (1) Lateral modulus of rupture tests to estimate the tensile strength of brick units (f_{ut}), (2) Bond wrench tests to determine the flexural strength of masonry perpendicular to bed joints (f_{mt}), and (3) Compressive strength tests to determine the compressive strength of masonry (f_{mc}) and the elastic modulus of brick (E_b), mortar (E_m) and masonry (E). Also, the material specifications and CFRP and adhesive properties are presented.

B.2 Material tests results

B.2.1 Lateral modulus of rupture of brick unit test (AS/NZS 4456.15:2003)

Table B-1: Lateral modulus of rupture test results

1st Batch

Specimen Number	f_{ut} (MPa)
1*	5.15
2	2.31
3	3.48
4*	0.73
5	2.9
6	2.55
7*	6.84
8	3.37
9	3.1
10	3.23
11	1.79
12	2.62
Mean (MPa)	2.82
Std. dev.	0.55
COV	0.20

2nd Batch

Specimen Number	f_{ut} (MPa)
1*	2.52
2	3.62
3	2.82
Mean (MPa)	2.99
Std. dev.	0.57
COV	0.19

3rd Batch

Specimen Number	f_{ut} (MPa)
1	4.5
2*	2.57
3	4.56
4*	5.39
5	4.53
6	1.60
7	3.06
8	3.89
9	2.53
10	3.02
Mean (MPa)	3.46
Std. dev.	1.09
COV	0.31

* Results from specimens were rejected because the failure occurred outside of the constant moment region and consequently these values were not used in the calculation of fut.

B.2.2 Bond wrench

Table B-2: Bond wrench test results

1st Batch	
specimen number	f_{mt} (Mpa)
1_1	0.63
1_2	0.47
1_3	0.56
1_4	0.54
1_5	0.66
1_6	0.27
1_7	0.68
1_8	0.51
1_9	0.75
1_10	0.51
1_11	0.54
1_12	0.28
2-1	0.36
2-2	0.52
2-3	0.46
2-4	0.68
2-5	0.32
2-6	0.37
2-7	0.35
2-8	0.31
2-9	0.46
2-10	0.47
2-11	0.32
2-12	0.49
Mean (MPa)	0.48
Std. dev.	0.14
COV	0.28

2nd Batch	
specimen number	f_{mt} (Mpa)
1-1	0.40
1-2	0.43
1-3	0.34
2-1	0.64
2-2	0.48
2-3	0.66
3-1	0.25
3-2	0.48
4-1	0.80
4-2	0.67
4-3	0.67
5-1	0.47
5-2	0.54
5-3	0.40
Mean (MPa)	0.52
Std. dev.	0.15
COV	0.30

3rd Batch	
specimen number	f_{mt} (Mpa)
1-1	0.34
1-2	0.32
1-3	0.34
2-1	0.44
2-2	0.37
2-3	0.56
3-1	0.41
3-2	0.42
3-3	0.40
4-1	0.35
4-2	0.62
4-3	0.44
5-1	0.36
5-2	0.28
5-3	0.38
6-1	0.53
6-2	0.35
6-3	0.55
7-1	0.43
7-2	0.37
7-3	0.49
8-1	0.60
8-2	0.59
8-3	0.64
9-1*	1.01
9-2	0.56
9-3	0.67
10-1	0.30
10-2	0.47
10-3	0.58
11-1	0.51
11-2	0.45
11-3	0.50
Mean (MPa)	0.46
Std. dev.	0.11
COV	0.24

B.2.3 Compression Tests

Table B-3: Compression test results – 1st batch

Specimen no	f_{mc} (Mpa)	E_m(MPa)	E_b (MPa)	E_{mo} (MPa)
1_1*	19.50	NA	NA	NA
1_2	17.65	13925	18589	4079
1_3	19.45	10309	16730	2639
2_1	20.75	11320	20913	2425
2_2	20.10	10350	15750	2370
2_3	23.05	6059	26141	1677
Mean (MPa)	20.20	10393	19625	2638
Std. dev.	1.78	2834	4141	883
COV	0.09	0.27	0.21	0.33

*Rejected result due to errors in strain measurement

Table B-4: Compression test results – 2nd batch

Specimen no	f_{mc} (Mpa)	E_m(MPa)	E_b (MPa)	E_{mo} (MPa)
1	13.40	8700	13317	2711
2	14.44	10100	15685	1253
3	14.19	7200	13840	1840
4	16.10	11400	21388	2215
5	12.97	8800	17645	1619
Mean (MPa)	14.22	9240	16375	1928
Std. dev.	1.21	1585	3279	560
COV	0.08	0.17	0.20	0.29

Table B-5: Compression test results – 3rd batch

Specimen no	f_{mc} (Mpa)	E_m(MPa)	E_b (MPa)	E_{mo} (MPa)
1_1	10.00	7800	16510	1210
1_2	12.75	10900	22230	1987
1_3	14.01	13200	20608	2696
1_4	15.13	9500	19606	1629
2_1	15.51	15500	23430	3662
2_2	18.73	12500	22230	3162
2_3	18.98	13500	22953	2869
2_4	17.42	12500	16656	3668
2_5	20.08	10500	25321	1607
2_6	19.18	8500	22953	1177
2_7	16.46	12000	17268	1261
Mean (MPa)	16.83	11491	20888	2266
Std. dev.	3.11	2306	3002	974
COV	0.18	0.20	0.14	0.43

B.3 Assessment of material test results

The test results from three different batches were assessed to check if there were significant differences between the groups. The assessment was done using: (1) the rejection criteria from AS3700-2001: Appendix H and (2) The analysis of variance (ANOVA) test statistics (or Single factor ANOVA test).

B.3.1 Lateral modulus of rupture of brick unit test

(1) Rejection criteria from AS3700-2001: Appendix H

	Serial No.	Specimen	f_{ut} (Mpa)	Y=ln(f_{ut})
1st batch	1*	1*		
	2	2	2.31	0.84
	3	3	3.48	1.25
	4*	4*		
	5	5	2.90	1.06
	6	6	2.55	0.94
	7*	7*		
	8	8	3.37	1.21
	9	9	3.10	1.13
	10	10	3.23	1.17
	11	11	1.79	0.58
	12	12	2.62	0.96
2nd batch	13*	1*		
	14	2	3.62	1.29
	15	3	2.82	1.04
3rd batch	16	1	4.50	1.50
	17*	2*		
	18	3	4.56	1.52
	19*	4*		
	20	5	4.52	1.51
	21	6	1.60	0.47
	22	7	3.06	1.12
	23	8	3.89	1.36
	24	9	2.53	0.93
	25	10	3.02	1.11
	Mean (MPa)		**3.13**	
	Std. dev.		**0.84**	
	COV		**0.27**	

* Results from specimens were rejected because the failure occurred outside of the constant moment region and consequently these values were not used in the calculation of f_{ut}.

Table B-6: Assessment using rejection criteria (AS3700-2001: Appendix H)

	Check for rejection				
Serial No. of Suspect result	**11**	**21**	**18**	**16**	**20**
Mean	1.13	1.14	1.08	1.08	1.08
Std. Dev.	0.26	0.25	0.27	0.28	0.28
Lower Rejection Limit, Yl	0.34	0.40	0.26	0.25	0.25
Upper Rejection Limit, Yu	1.92	1.88	1.91	1.91	1.91
Assessment result	keep	keep	keep	keep	keep

(2) Single factor ANOVA test

Table B-7: ANOVA results

Source of Variation	SS[1]	df[2]	MS[3]	F	P-value	F crit
Between Groups	2.640	2	1.320	1.536	0.242	6.013
Within Groups	15.461	18	0.859			
Total	18.101	20				

[1] - sum of squares; [2] – degree of freedom; [3] – mean square

Assuming significance level, $\alpha = 0.01$ and considering two tailed test gives 0.005 in each tail of the distribution of the test statistic. As P-value > 0.005 and F value < Fcrit (Table B-7), it can be concluded that there is no significant difference between the groups.

B.3.2 Bond wrench test

(1) Rejection criteria from AS3700-2001: Appendix H

	serial no	specimen no.	f_{mt} (Mpa)	$Y=\ln(f_{ut})$
1st batch	1	1_1	0.63	-0.46
	2	1_2	0.47	-0.76
	3	1_3	0.56	-0.58
	4	1_4	0.54	-0.62
	5	1_5	0.66	-0.41
	6	1_6	0.27	-1.30
	7	1_7	0.68	-0.39
	8	1_8	0.51	-0.68
	9	1_9	0.75	-0.29
	10	1_10	0.51	-0.67
	11	1_11	0.54	-0.62
	12	1_12	0.28	-1.28
	13	2-1	0.36	-1.02
	14	2-2	0.52	-0.65
	15	2-3	0.46	-0.77
	16	2-4	0.68	-0.38
	17	2-5	0.32	-1.14
	18	2-6	0.37	-1.00
	19	2-7	0.35	-1.04
	20	2-8	0.31	-1.16
	21	2-9	0.46	-0.77
	22	2-10	0.47	-0.76
	23	2-11	0.32	-1.13
	24	2-12	0.49	-0.71
2nd batch	25	1-1	0.40	-0.91
	26	1-2	0.43	-0.84
	27	1-3	0.34	-1.06
	28	2-1	0.64	-0.45
	29	2-2	0.48	-0.74
	30	2-3	0.66	-0.41
	31	3-1	0.25	-1.39
	32	3-2	0.48	-0.73
	33	4-1	0.80	-0.22
	34	4-2	0.67	-0.41
	35	4-3	0.67	-0.41
	36	5-1	0.47	-0.76
	37	5-2	0.54	-0.61
	38	5-3	0.40	-0.92

	serial no	specimen no.	f_{mt} (Mpa)	$Y=\ln(f_{ut})$
3rd batch	39	1-1	0.34	-1.07
	40	1-2	0.32	-1.14
	41	1-3	0.34	-1.09
	42	2-1	0.44	-0.83
	43	2-2	0.37	-1.00
	44	2-3	0.56	-0.58
	45	3-1	0.41	-0.90
	46	3-2	0.42	-0.88
	47	3-3	0.40	-0.90
	48	4-1	0.35	-1.04
	49	4-2	0.62	-0.48
	50	4-3	0.44	-0.82
	51	5-1	0.36	-1.01
	52	5-2	0.28	-1.26
	53	5-3	0.38	-0.96
	54	6-1	0.53	-0.63
	55	6-2	0.35	-1.05
	56	6-3	0.55	-0.60
	57	7-1	0.43	-0.85
	58	7-2	0.37	-1.00
	59	7-3	0.49	-0.71
	60	8-1	0.60	-0.51
	61	8-2	0.59	-0.52
	62	8-3	0.64	-0.44
	63	9-2	0.56	-0.57
	64	9-3	0.67	-0.40
	65	10-1	0.30	-1.22
	66	10-2	0.47	-0.74
	67	10-3	0.58	-0.54
	68	11-1	0.51	-0.68
	69	11-2	0.45	-0.81
	70	11-3	0.50	-0.69
		Mean (MPa)	**0.48**	
		Std. dev.	**0.13**	
		COV	**0.27**	

Table B-8: Assessment using rejection criteria (AS3700-2001: Appendix H)

Check for rejection		
Serial No. of Suspect result	**31**	**33**
Mean	-0.77	-0.79
Std. Dev.	0.27	0.27
Lower Rejection Limit, Yl	-1.59	-1.59
Upper Rejection Limit, Yu	0.05	0.02
Assessment result	keep	keep

(2) Single factor ANOVA test

Table B-9: ANOVA results

Source of Variation	SS[1]	df[2]	MS[3]	F	P-value	F crit
Between Groups	0.035	2	0.017	1.063	0.351	4.937
Within Groups	1.098	67	0.016			
Total	1.133	69				

[1] - sum of squares; [2] – degree of freedom; [3] – mean square

Assuming significance level, $\alpha = 0.01$ and considering two tailed test gives 0.005 in each tail of the distribution of the test statistic. As P-value > 0.005 and F value < Fcrit (Table B-9), it can be concluded that there is no significant difference between the groups.

B.3.3 Compression test

(1) Rejection criteria from AS3700-2001: Appendix H

	Serial no	Specimen no.	f_{mc} (Mpa)	Em (Mpa)	Eb (Mpa)	Emo (Mpa)
1st batch	1*	1_1*		NA	NA	NA
	2	1_2	17.65	13925	18589	4079
	3	1_3	19.45	10309	16730	2639
	4	2_1	20.75	11320.05	20913	2425
	5	2_2	20.10	10349.69	15750	2370
	6	2_3	23.05	6059	26141	1677
2nd batch	7	1	13.40	8700	13317	2711
	8	2	14.44	10100	15685	1253
	9	3	14.19	7200	13840	1840
	10	4	16.10	11400	21388	2215
	11	5	12.97	8800	17645	1619
3rd batch	12	1*		7800	16510	1210
	13	2	12.75	10900	22230	1987
	14	3	14.01	13200	20608	2696
	15	4	15.13	9500	19606	1629
	16	1	15.51	15500	23430	3662
	17	2	18.73	12500	22230	3162
	18	3	18.98	13500	22953	2869
	19	4	17.42	12500	16656	3668
	20	5	20.08	10500	25321	1607
	21	6	19.18	8500	22953	1177
	22	7	16.46	12000	17268	1261
		Mean (MPa)	**17.02**	**10693**	**19513**	**2274**
		Std. dev.	**2.95**	**2381**	**3687**	**870**
		COV	**0.17**	**0.22**	**0.19**	**0.38**

Natural Log, Y				
Serial no	fmc	Em	Eb	Emo
1*				
2	2.87	9.54	9.83	8.31
3	2.97	9.24	9.72	7.88
4	3.03	9.33	9.95	7.79
5	3.00	9.24	9.66	7.77
6	3.14	8.71	10.17	7.42
7	2.60	9.07	9.50	7.90
8	2.67	9.22	9.66	7.13
9	2.65	8.88	9.54	7.52
10	2.78	9.34	9.97	7.70
11	2.56	9.08	9.78	7.39
12*		8.96	9.71	7.10
13	2.55	9.30	10.01	7.59
14	2.64	9.49	9.93	7.90
15	2.72	9.16	9.88	7.40
16	2.74	9.65	10.06	8.21
17	2.93	9.43	10.01	8.06
18	2.94	9.51	10.04	7.96
19	2.86	9.43	9.72	8.21
20	3.00	9.26	10.14	7.38
21	2.95	9.05	10.04	7.07
22	2.80	9.39	9.76	7.14

Table B-10: Assessment using rejection criteria (AS3700-2001: Appendix H)

	Check for rejection						
	fmc	Em		Eb		Emo	
Serial No. of Suspect result	6	6	16	7	6	21	2
Mean	2.80	9.28	9.23	9.88	9.85	7.69	7.63
Std. Dev.	0.18	0.20	0.22	0.18	0.18	0.37	0.37
Lower Rejection Limit, Yl	2.27	8.67	8.57	9.34	9.29	6.57	6.53
Upper Rejection Limit, Yu	3.34	9.89	9.90	10.42	10.40	8.80	8.72
Assessment result	keep	keep	keep	keep	keep	keep	keep

(2) Single factor ANOVA test

Table B-11: ANOVA results

(a) For fmc

Source of Variation	SS[1]	df[2]	MS[3]	F	P-value	F crit
Between Groups	90.135	2	45.067	6.161	0.006	8.112
Within Groups	75.401	17	4.435			
Total	165.535	19				

(b) For Em

Source of Variation	SS[1]	df[2]	MS[3]	F	P-value	F crit
Between Groups	18010641	2	9005321	1.700	0.211	6.013
Within Groups	95368027	18	5298224			
Total	113378669	20				

(c) For Eb

Source of Variation	SS[1]	df[2]	MS[3]	F	P-value	F crit
Between Groups	70086947	2	35043474	3.127	0.068	6.013
Within Groups	201727518	18	11207084			
Total	271814465	20				

(d) For Emo

Source of Variation	SS[1]	df[2]	MS[3]	F	P-value	F crit
Between Groups	1262879	2	631440	0.820	0.456	6.013
Within Groups	13866923	18	770385			
Total	15129803	20				

[1] - sum of squares; [2] – degree of freedom; [3] – mean square

Assuming significance level, $\alpha = 0.01$ and considering two tailed test gives 0.005 in each tail of the distribution of the test statistic. As P-value > 0.005 and F value < Fcrit (Table B-11), it can be concluded that there is no significant difference between the groups for fmc, Em, Eb and Emo values.

APPENDIX C: PULL TEST EXPERIMENTAL STUDY

C.1 Pull test specimen design

For the design of pull test specimens, length of bonded region of the strip, L was designed to be greater than the effective bond length, L_{eff} in order to develop full IC debonding resistance force, P_{IC}. From Table C-1, it can be seen that the pull test specimen height (L = 420mm) exceeded the maximum L_{eff} of 399 mm.

$$L_{eff} = \frac{\pi}{2\lambda}$$

where, $\lambda = \sqrt{\frac{\tau_{\max} L_{per}}{\delta_{\max} (EA)_p}}$.

Perimeter of debonding failure plane, $L_{per} = 2d_f + b_f$

aspect ratio, $\varphi_f = \frac{1 + b_p}{2 + t_p}$

maximum interface slip, $\delta_{\max} = \frac{0.976\varphi_f^{0.526}}{0.802 + 0.078\varphi_f}$;

maximum interface shear stress, $\tau_{\max} = (0.802 + 0.078\varphi_f) fc^{0.6}$;

The above equation can be modified for masonry using the relation between splitting tensile strength of concrete f_{ct} and concrete cylinder compressive strength f_c' by MacGregor (1988) as shown below.

$$\sqrt{f_c'} = \frac{f_{ct}}{0.53}$$

It was assumed that a similar relationship exists between the compressive and tensile strength for a clay brick masonry unit. Therefore,

$$\tau_{\max} = (0.802 + 0.078\varphi_f)\left(\frac{f_{ut}}{0.53}\right)^{1.2}$$

The IC debonding resistance, was calculated using equation given by Willis et al. (2009) and was checked against rupture.

$$P_{IC} = 0.988\varphi_f^{0.263}\left(\frac{f_{ut}}{0.53}\right)^{0.6}\sqrt{L_{per}(EA)_p}$$

Table C-1: Pull test specimen design

Depth of FRP strip, bp	10.00	10.00	7.50	5.00	10.00
Thickness of FRP strip, tp	3.60	7.20	4.80	4.80	4.20
FRP rupture stress, f_{rup}	2700	2700	2700	2700	2700
Elastic modulus of masonry, E_p	165000	165000	165000	165000	165000
Lateral modulus of rupture, f_{ut}	2.82	3.22	3.22	3.56	3.56
d_f	11.00	11.00	8.50	6.00	11.00
b_f	5.60	9.20	6.80	6.80	6.20
Perimeter of debonding failuire plane, L_{per}	27.60	31.20	23.80	18.80	28.20
c/s area of FRP strip, A_p	36.00	72.00	36.00	24.00	42.00
Debonding failure plane aspect ratio, φ_f	1.96	1.20	1.25	0.88	1.77
IC debonding resistance, P_{IC} =	**41.19**	**58.86**	**36.78**	**25.86**	**50.35**
FRP rupture force, $P_{rup} = f_{rp.} A_p$	**97.2**	**194.4**	**97.2**	**64.8**	**113.4**
Maximum interfacial shear stress, τ_{max}	6.08	7.07	7.07	7.95	8.02
Maximum interfacial slip, δ_{max}	1.46	1.20	1.22	1.05	1.40
λ^2	1.94E-05	1.55E-05	2.32E-05	3.60E-05	2.33E-05
Effective bond length, L_{eff}	*357*	*399*	*326*	*262*	*326*

C.2 Pull test results

P1 results are included in Chapter 3.

C.2.1 P2 (M-SG 3.6-10-2)

Figure C-1: Failed specimen P2

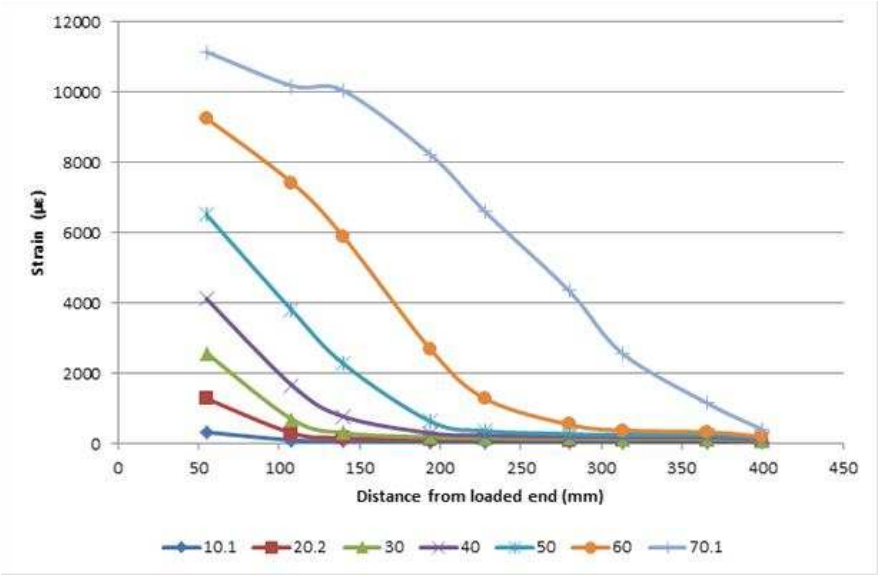

Figure C-2: Strain distribution of P2

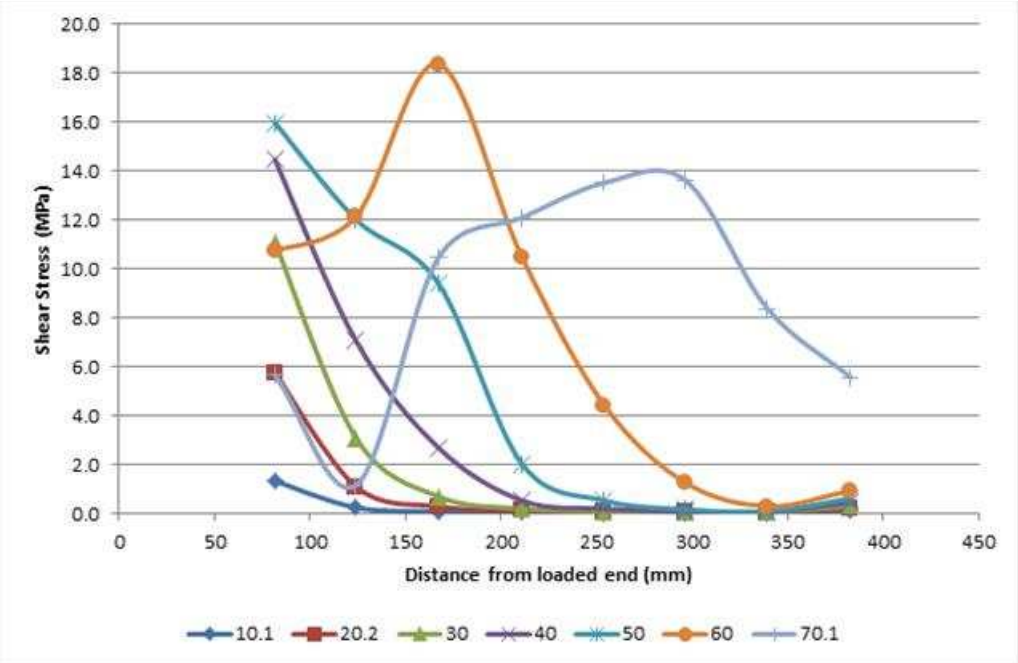

Figure C-3: Stress distribution of P2

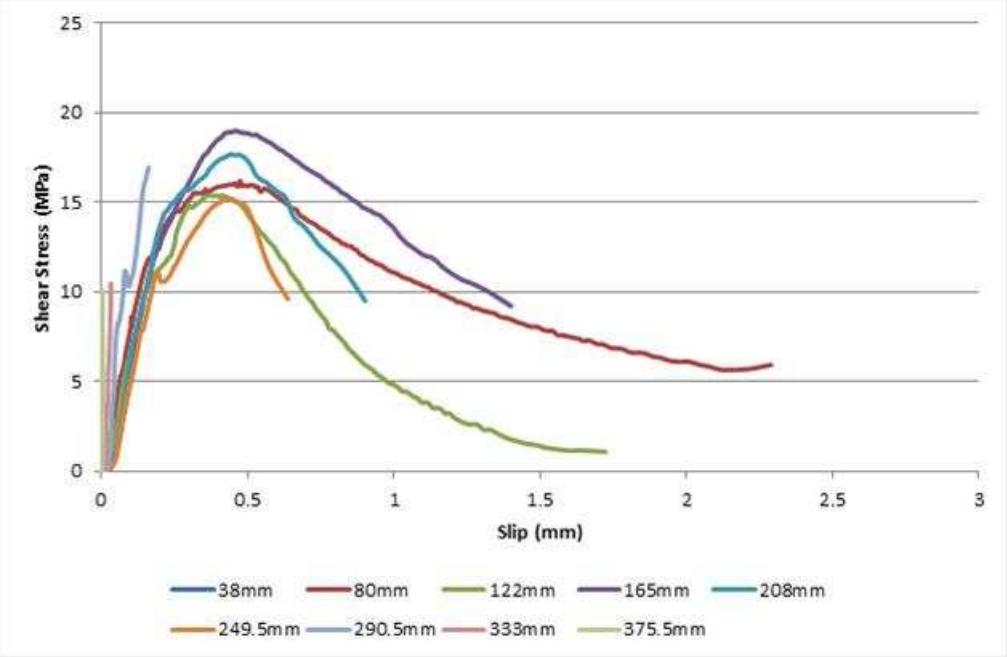

Figure C-4: Local bond-slip relation (P2)

C.2.2 P3 (M-SG-3.6-10-3)

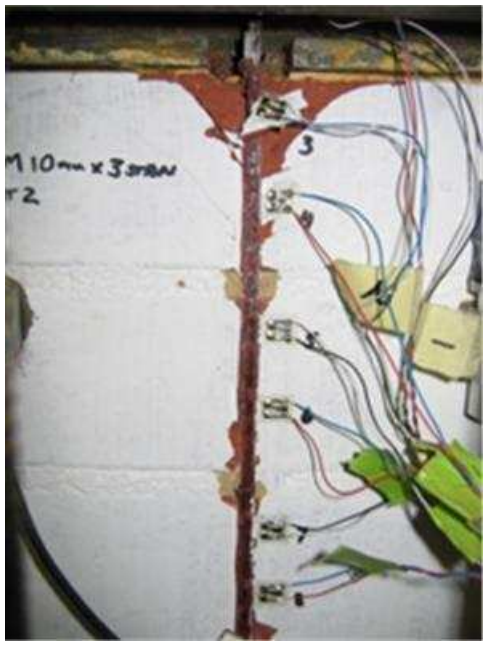

Figure C-5: Failed specimen P3

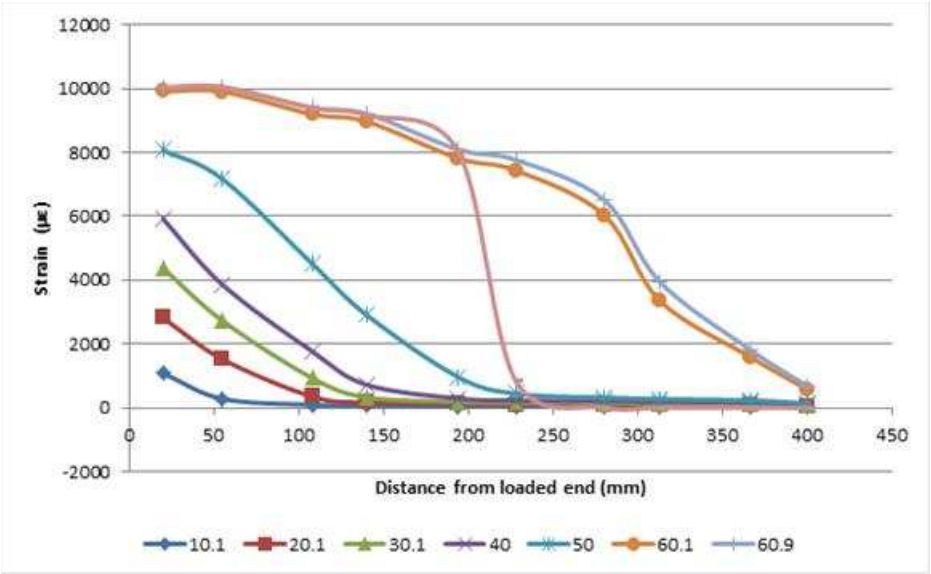

Figure C-6: Strain distribution of P3

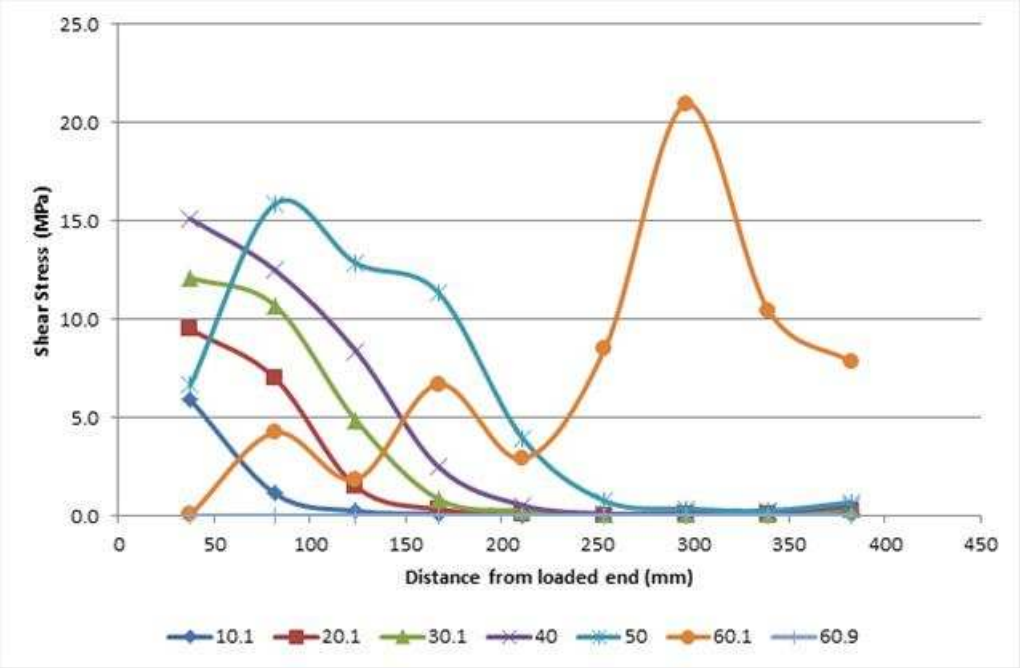

Figure C-7: Stress distribution of P3

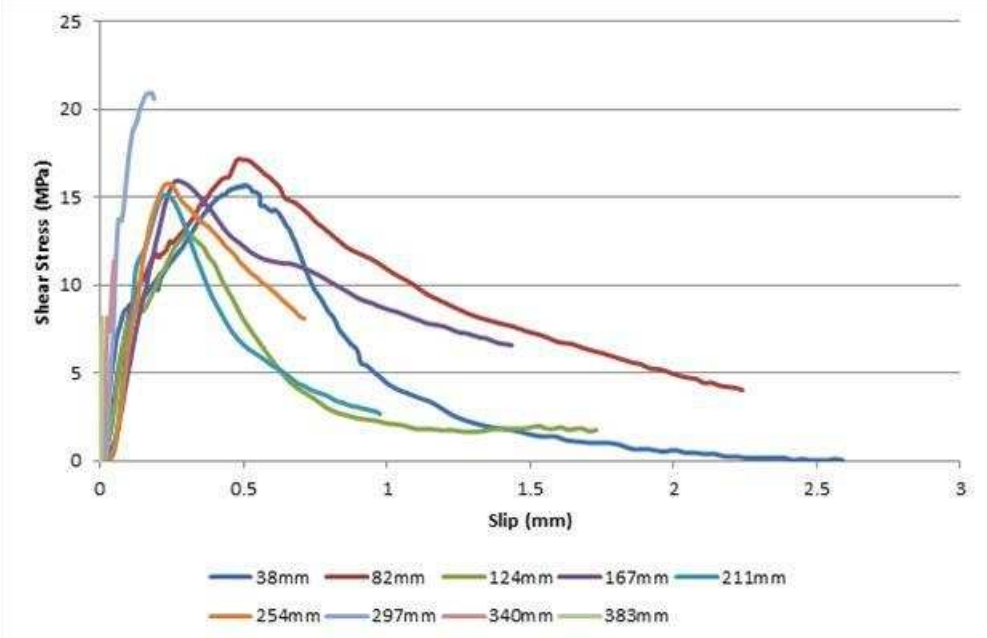

Figure C-8: Local bond-slip (P3)

C.2.3 P4 (M-SG-3.6-10-4)

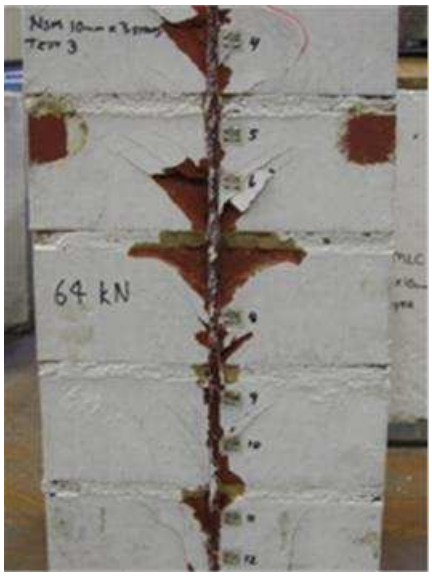

Figure C-9: Failed specimen P4

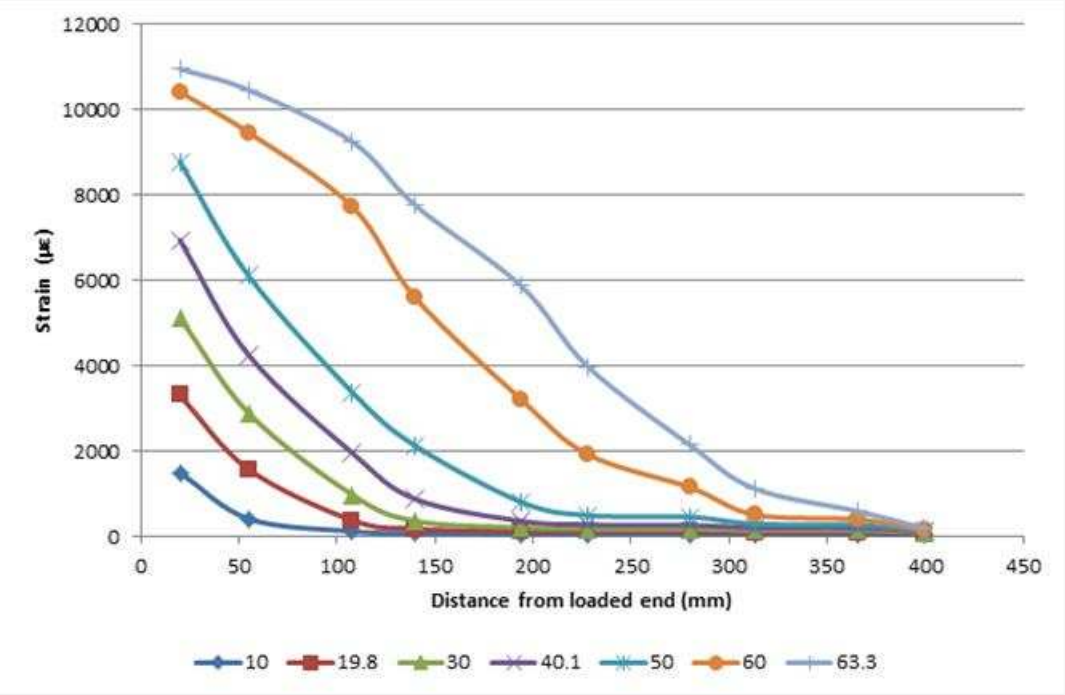

Figure C-10: Strain distribution of P4

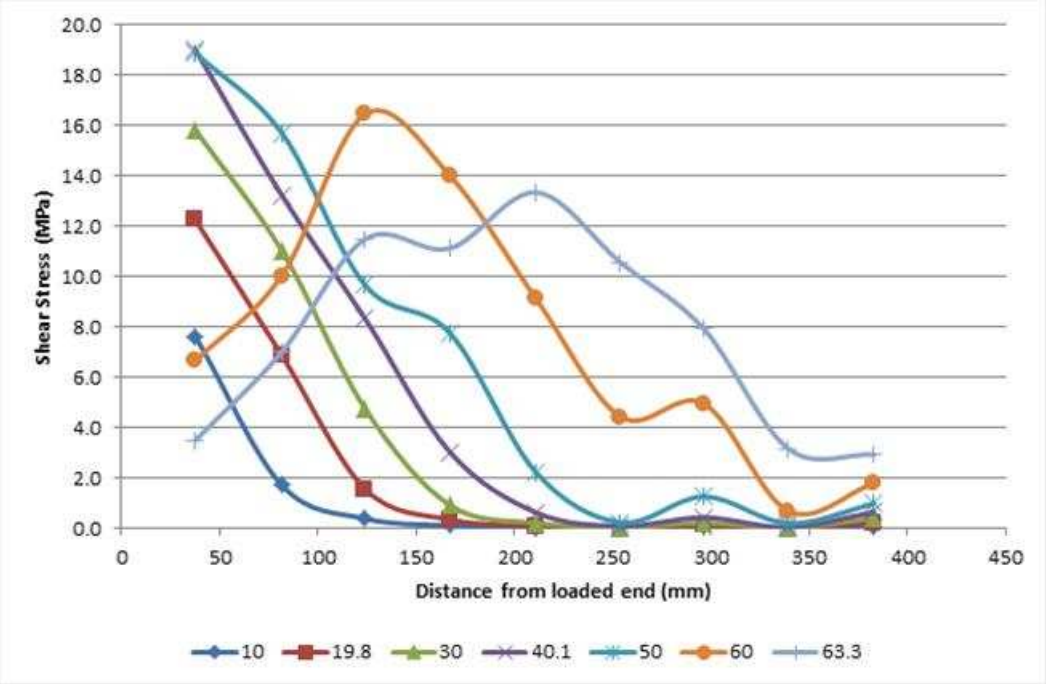

Figure C-11: Stress distribution of P3

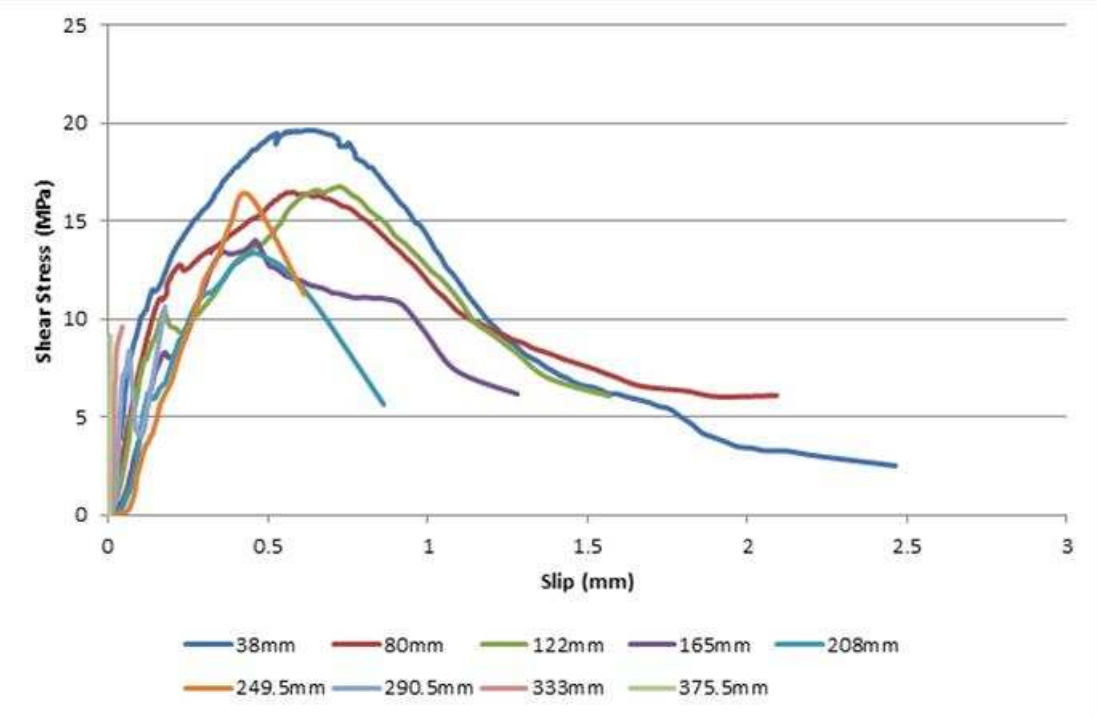

Figure C-12: Local bond-slip (P4)

C.2.4 P5 (C-SG-3.6-10-5)

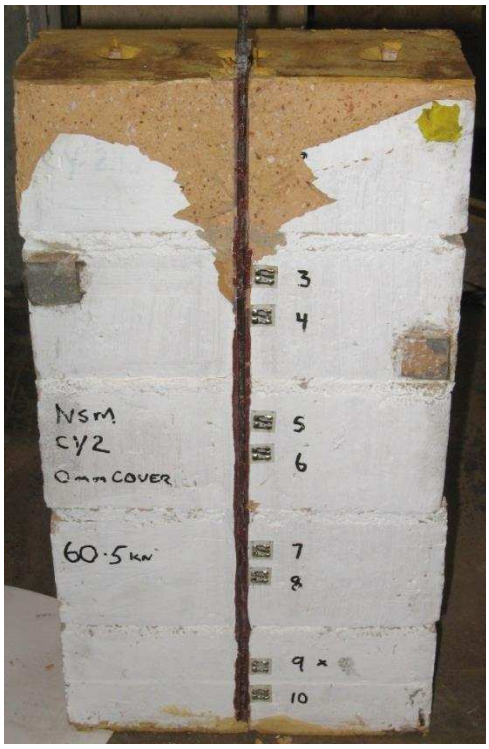

Figure C-13: Failed specimen P5

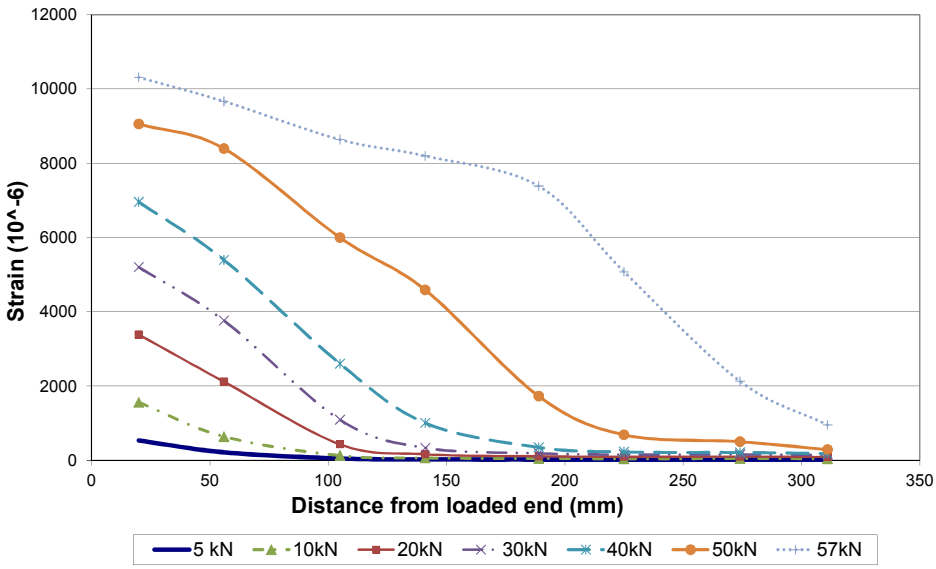

Figure C-14: Strain distribution of P5

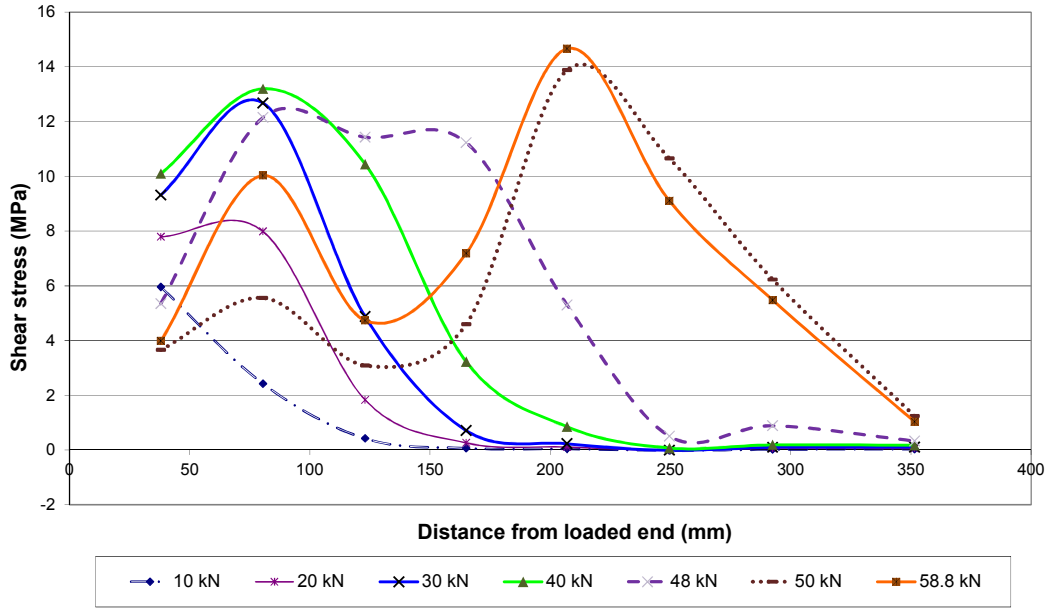

Figure C-15: Stress distribution of P5

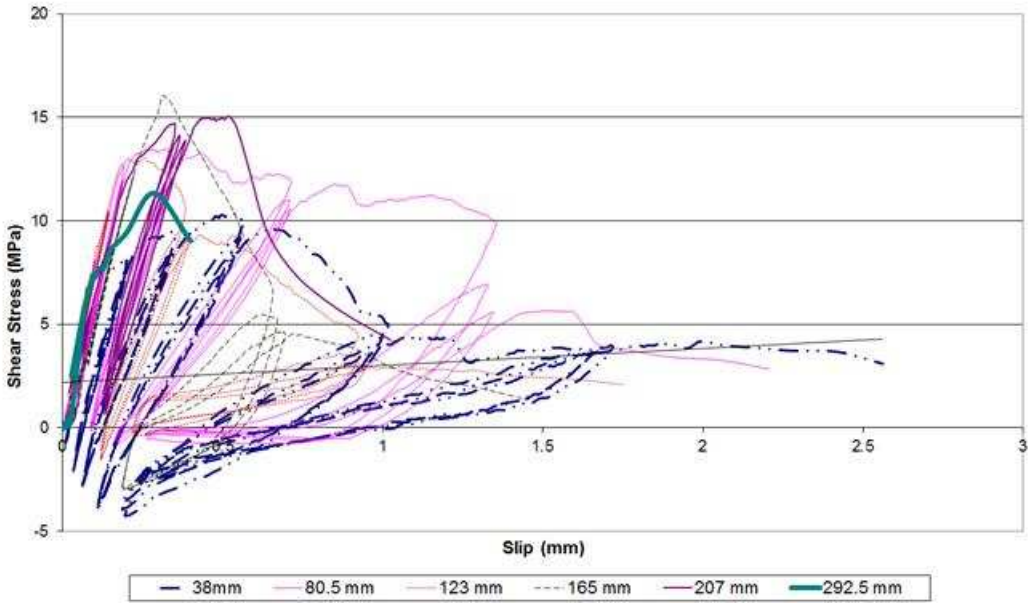

Figure C-16: Local bond-slip (P5)

C.2.5 P6 (C-SG-3.6-10-6)

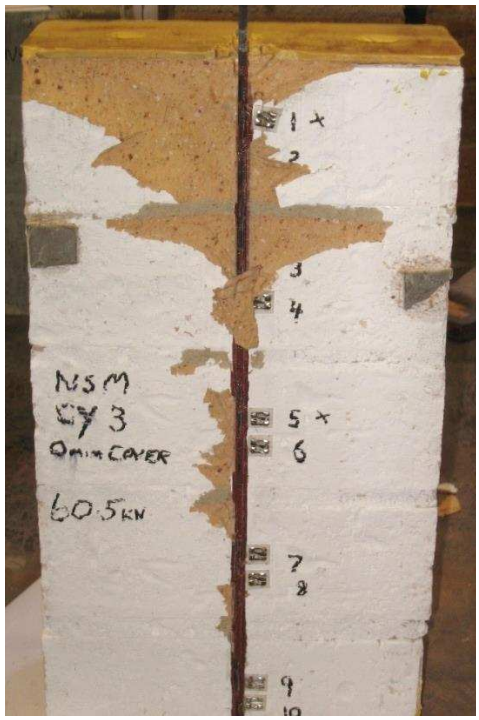

Figure C-17: Failed specimen P6

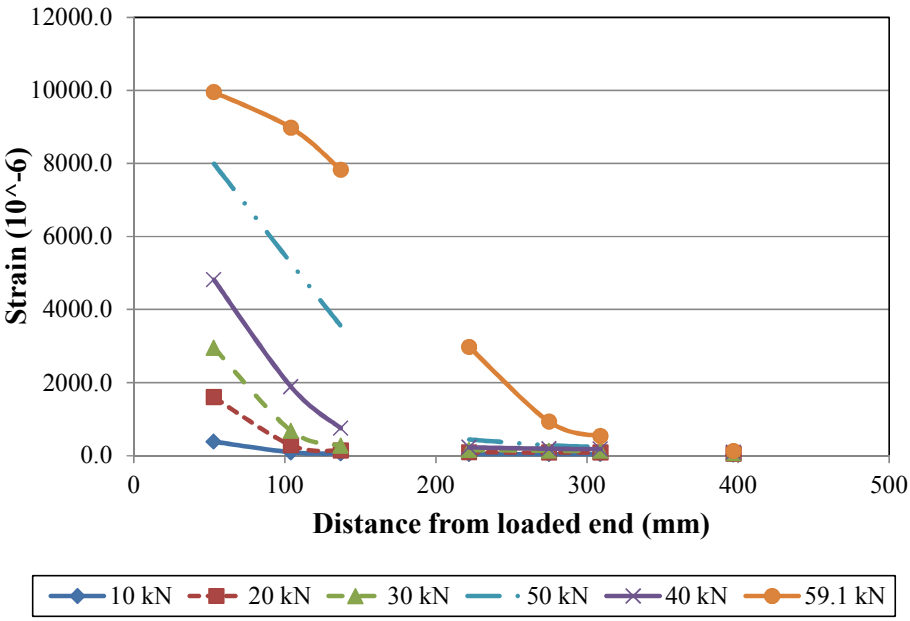

Note: 2 strain gauges were not working

Figure C-18: Strain distribution for P6

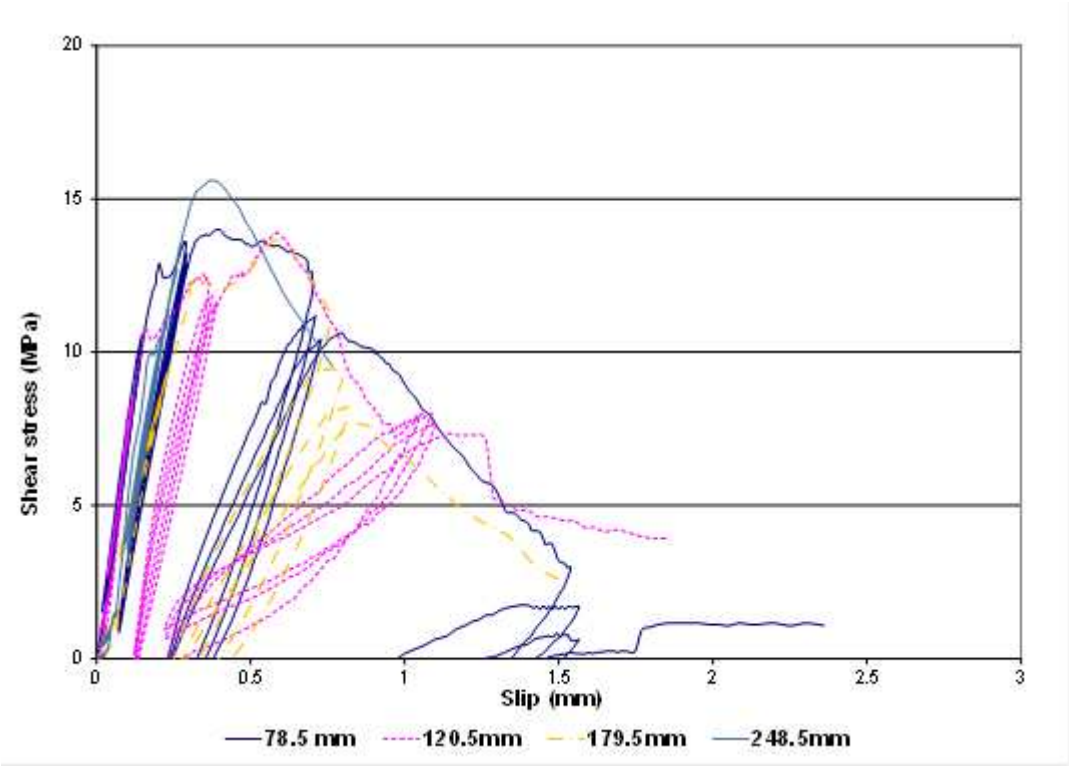

Figure C-19: Local bond-slip for P6

C.2.6 Test Specimen P7 – P14

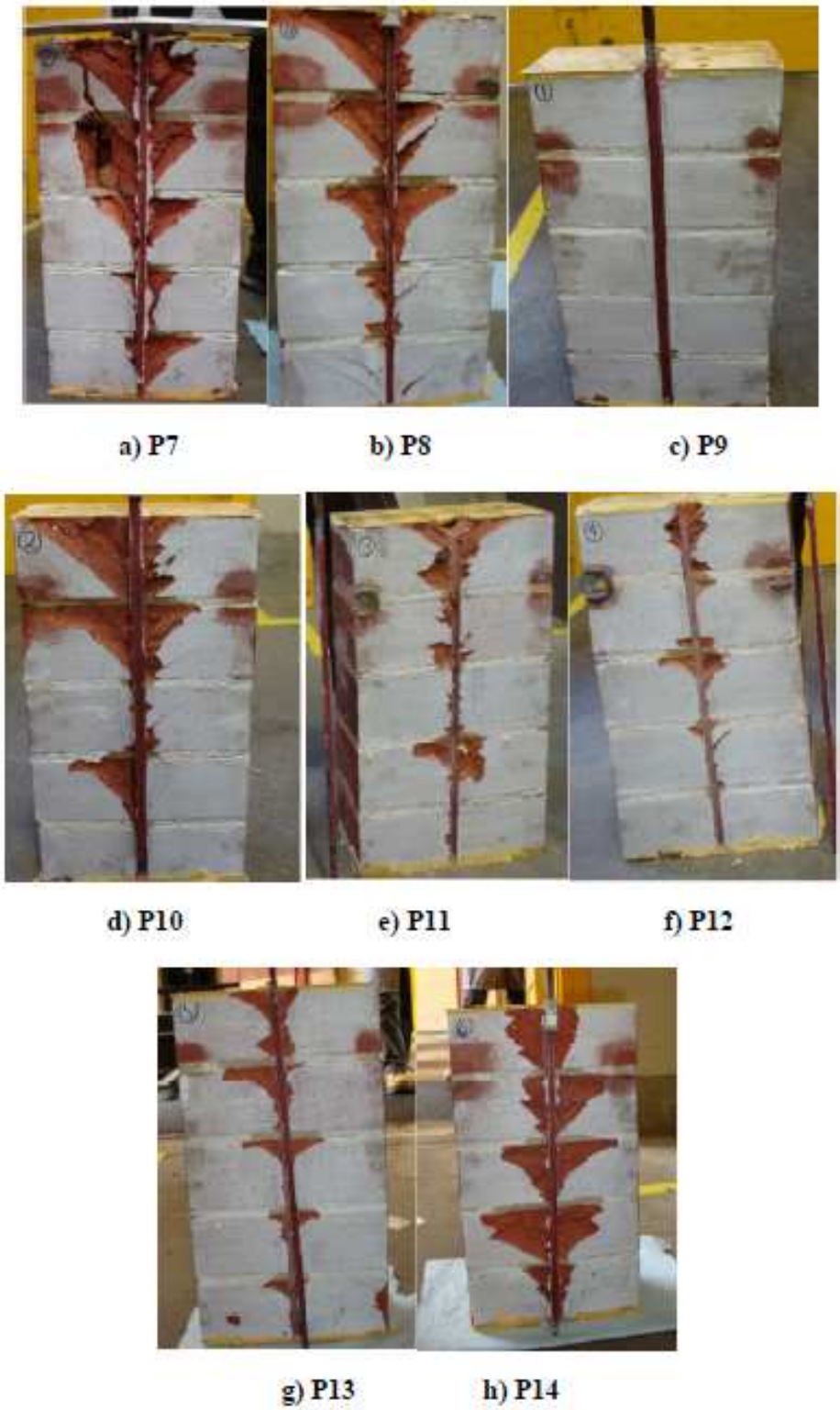

Figure C-20: Failed specimen P7 – P14

APPENDIX D*:* PULL TEST NUMERICAL STUDY

D.1 Bond strength models: Statistical analysis details

D.1.1 New EB specific model

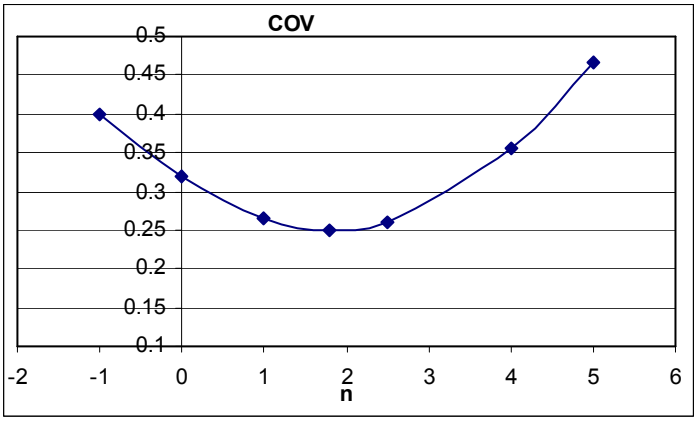

Figure D-1: Determining exponent of f_{ut} (n) by comparison with COV

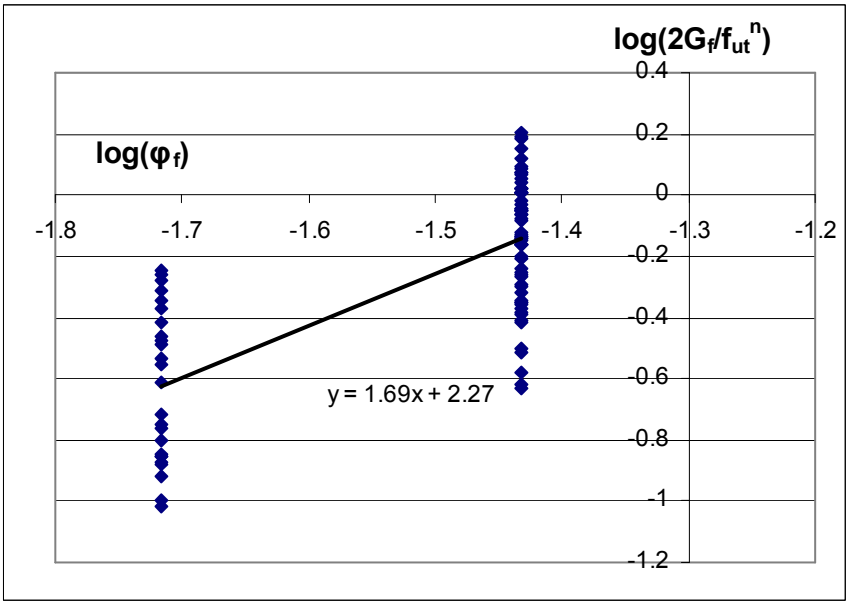

Figure D-2: Statistical analysis for key bond-slip parameters

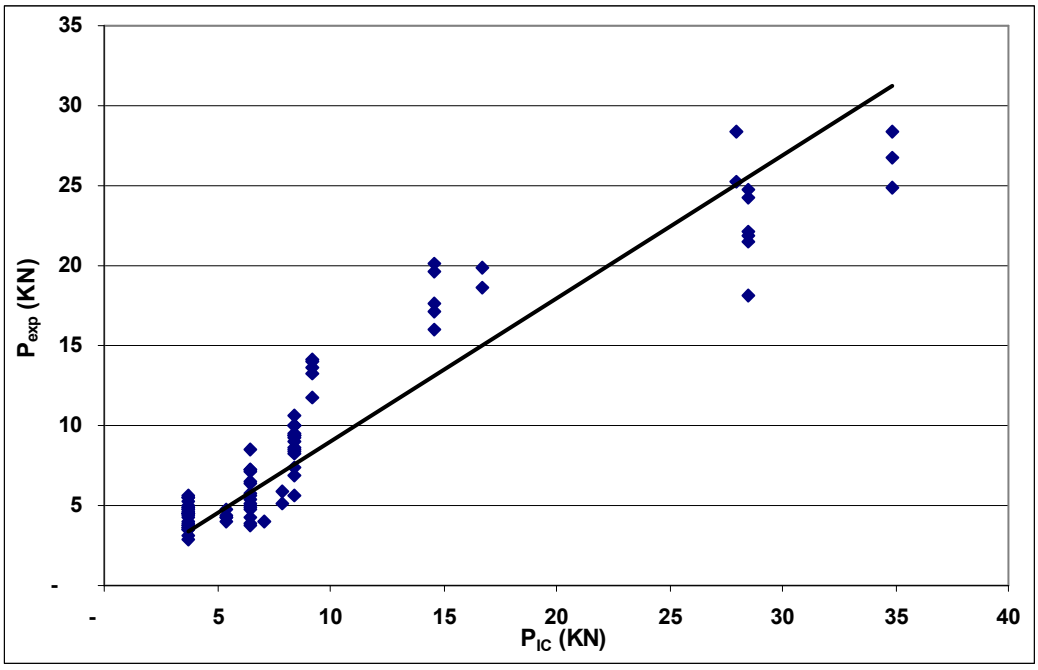

Figure D-3: Comparison of experimental and predicted IC debonding resistance

D.1.2 New NSM Specific model

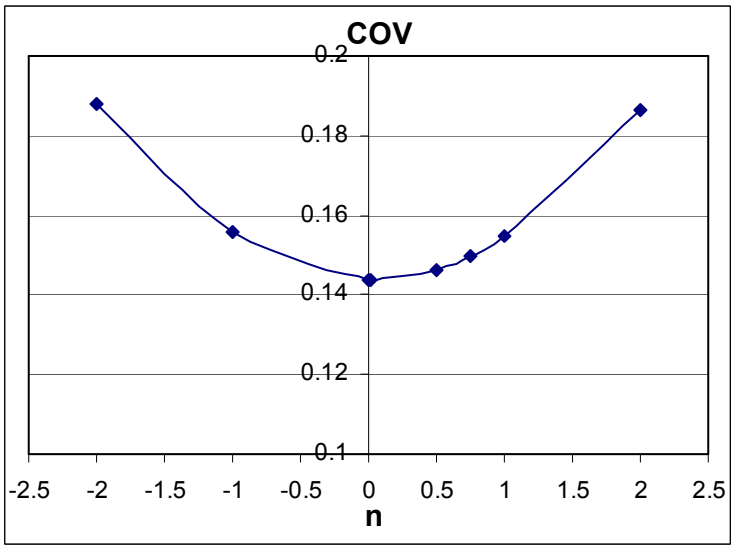

Figure D-4: Determining exponent of fut (n) by comparison with COV

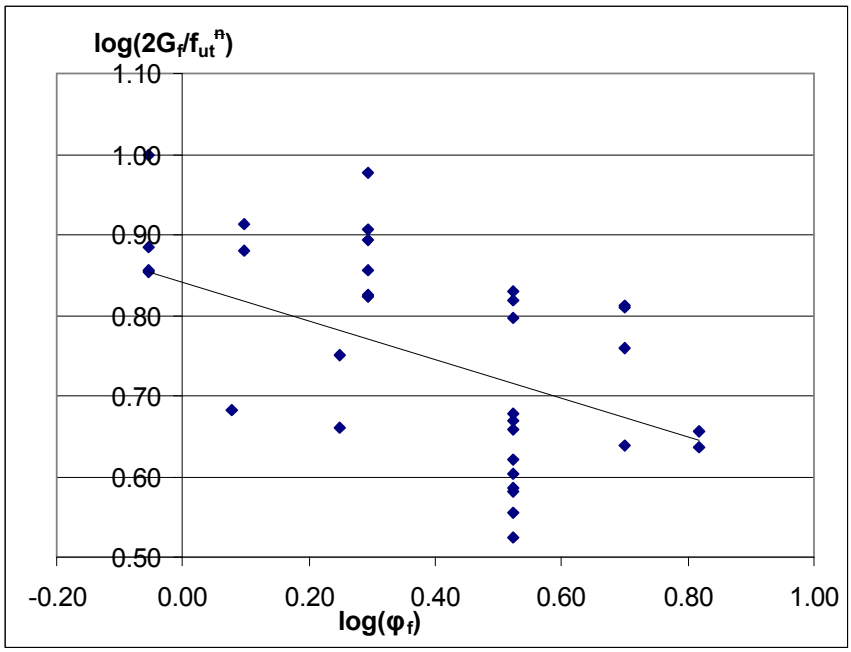

Figure D-5: Determining exponent of f_{ut} (n) by comparison with COV

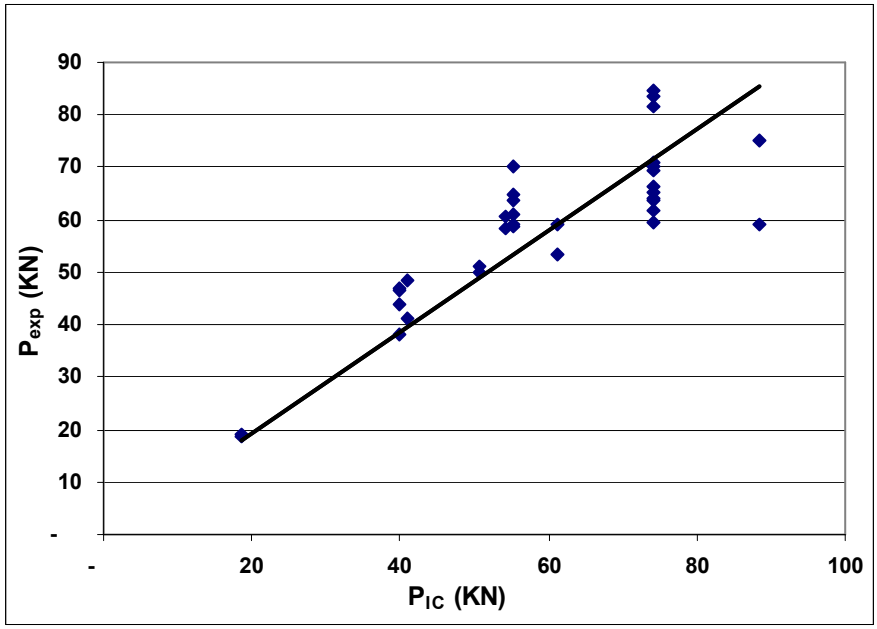

Figure D-6: Comparison of experimental and predicted IC debonding resistance

D.2 Example of numerical procedure

The numerical procedure described §4.3.2 is explained in this section through a step-by-step calculation for the sample test specimen results of which have been used to demonstrate the reliability of the predictive procedures. Geometric and material properties for this specimen are given in Table 3-2and the local τ-δ properties are shown in Table 3-4. Assuming that t_b=t_d=1 mm (Figure 2-7), L_{per} = 28.2 mm. Also, A_m = 230 x 110 = 25300 mm^2 and A_p = 10 x 4.2 = 42 mm^2. Take segment length dx = 1 mm. As the specimen is 420 mm long (igure 3-1), there are total 420 segments.

- Fix strain in FRP at loaded end at Position 0, $\varepsilon_p(0)$ = 0.005
- Therefore, force in FRP, $P(0) = \varepsilon_p(0)(EA)_p$= 0.005 x (165000 x 42)/1000 = 34.65 kN
- The corresponding compression strain in the masonry at Position 0 , $\varepsilon_m(0) = -P(0)/(EA)_m$ = -34.65 x 1000 / (11491 x 25300) = -0.00012
- The slip strain over the first segment, $ds(0)/dx = \varepsilon_p(0)-\varepsilon_m(0)$ = 0.005 – (-0.00012) = 0.00512
- By integration, the change in slip over the first segment, $\Delta s(0) = \int \frac{ds(0)}{dx} dx$ = 0.00256 mm
- Guess a slip at the loaded end, = $\Delta(0) = \delta(0)$ = 0.40 mm
- The bond stress, $\tau_m(0)$, corresponding to the guessed slip is derived from local τ-δ model for masonry = 11.27MPa
- The bond force acting over the first segment length, $B(0) = \tau_m(0) L_{per} dx$ = 11.27 x 28.2 x 1/1000 = 0.32 kN
- Therefore, the load in the FRP at end of the first segment, $P(1) = P(0) – B(0)$ = 34.65 – 0.32 = 34.33 kN
- The strain in the FRP at end of the first segment, $\varepsilon_p(1) = P(1)/(EA)_p$ = 34.33 x 1000 / (165000 x 42) =0.00495
- The strain in the masonry at end of the first segment, $\varepsilon_m(1) = -P(1)/(EA)_m$ = -34.33 x 1000 / (11491 x 25300) = -0.000118

- Hence, the slip at beginning of the second segment, $\delta(1) = \delta(0) - \Delta s(0) = 0.4 - 0.00512 = 0.39744$ mm

The numerical procedure is repeated over the subsequent segments to determine the axial strain *ε,* interface slip *δ* and slip strain *ds/dx.* Two boundary conditions at the unloaded end are used to solve the initial guess of *Δ(0):*

ds(420)/dx = 0 and δ(420) = 0.

D.3 Example of mathematical model

The closed form mathematical solution described in this paper is explained in this section through a step-by-step calculation for the sample test specimen results of which have been used to demonstrate the reliability of the predictive procedures. Geometric and material properties for this specimen are given in Table 3-1and Table 3-2, respectively and the local *τ-δ* properties are shown in Table 3-4. Assuming that t_b=t_d=1 mm (igure 3-1), L_{per} = 28.2 mm.

D.3.1 Calculation for Rigid-softening *τ-δ* model

- Using $\lambda = \sqrt{\frac{\tau_{\max} L_{per}}{\delta_{\max} (EA)_p}}$, gives λ = .00652.
- Using $L_e = \frac{\pi}{2\lambda}$ gives Le = 240.85 mm.
- Now, as L > L_e, Eq. 4-19 gives P_{IC} = 53.99 kN. This compares well with 53.10 kN from test.
- At the end of debonding stage, Δ = 2.57 mm from Eq. 4-20 and the corresponding magnitude from the test was 2.75 mm.

D.3.2 Calculation for elastic-softening *τ-δ* model

- Calculate the values of β_0, β_1, β_2, using $\beta_2 = \beta_1 \beta_0, \beta_1 = L_{per} / A_p$, $\beta_0 = \left(1/E_p + A_p/(EA)_m\right)$. β_0= 6.205 x 10^{-6}, β_1= 0.671 and β_2 = 4.166 x 10^{-6}.
- The P-Δ solution during the elastic stage can be derived using Eq. 4-21 with λ_1= 0.0124. At the end of this stage that is Δ = δ_1 = 0.33 mm, the load is 27.75 kN.

- Using Eq. 4-22and Eq. 4-23 solution for the softening stage can be derived and λ_2 = 0.0075.
- When debonding initiates the peak load is attained and $\Delta = \delta_{max}$. Therefore, a_d = 135.22mm from Eq. 4-25. As L> a_d, hence, softening will fully develop. Eq. 4-24, gives P_{IC} = 53.34 kN which agrees well with the test value.
- At the end of debonding stage, P = 45.58 kN, a_u = 207.6, and Δ = 2.65 mm from Eq. 4-27 and Eq. 4-28. The corresponding magnitude of slip at this stage from the test is 2.75.

D.3.3 Calculation for non-linear τ-δ model

- Calculate $G_f = 0.5*\tau_{max}\delta_{max}$ = 7.46 N/mm and k = 3.28 mm^{-1} using Eq. 4-29. From Eq. 4-35, P_{IC} = 53.35 kN. This is in close agreement with experimental result.

APPENDIX E: WALL TESTS DETAILS

E.1 Test Specimen design

E.1.1 Walls 1-3

IC debonding Check				
Elastic modulus of FRP, E_p	165000	MPa		
Plate Thickness, tp	3.6	mm		
Plate depth, bp	10	mm		
No. of strips	1			
Lateral modulus of rupture, f_{ut}	2.82	MPa		
Elastic modulus of masonry, E_m	10400	MPa		
Height of masonry wall, H	1710	mm		
Width of masonry wall, b	355	mm		
Wall thickness, tm	110	mm		
C/s area of FRP plate, Ap (per strip)	36	mm^2		
Perimeter of failure plane, L_{per}	27.6	mm		
FRP rupture stress, f_{rupt}	2700.00	MPa		
FRP rupture strain, ε_{rup}	0.0164			
Masonry compressive strength, fmc	20.2	MPa		
Masonry crushing strain, ε_{mc}	0.00194			
IC debonding resistance per strip, PIC	41.19	KN	(Seracino et al.2007a)	
Total PIC	41.19	KN		
Debonding strain in FRP, ε_{db}	0.00693	< εrup ←	**FRP Rupture check**	
Assumed NA. Depth, c	16.84	mm →	**Goal seek to get ΣF= 0**	
Strain at extreme compressive side, ε_m	0.00132	< εmc ←	**Masonry crushing**	
			Check	
Tensile force, F1	41191	N		
Compressive force, F2	41191	N		
Check Force equilibrium				
ΣF=	0.00			

E.1.2 Wall 4

IC debonding Check				
Elastic modulus of FRP, E_p	165000	MPa		
Plate Thickness, tp	3.6	mm		
Plate depth, bp	10	mm		
No. of strips	1			
Lateral modulus of rupture, f_{ut}	2.82	MPa		
Elastic modulus of masonry, E_m	10400	MPa		
Height of masonry wall, H	1710	mm		
Width of masonry wall, b	230	mm		
Wall thickness, tm	110	mm		
C/s area of FRP plate, Ap (per strip)	36	mm^2		
Perimeter of failure plane, L_{per}	27.6	mm		
FRP rupture stress, f_{rupt}	2700.00	MPa		
FRP rupture strain, ε_{rup}	0.0164			
Masonry compressive strength, fmc	20.2	MPa		
Masonry crushing strain, ε_{mc}	0.00194			
IC debonding resistance per strip, PIC	41.19	KN	(Seracino et al.2007a)	
Total PIC	41.19	KN		
Debonding strain in FRP, ε_{db}	0.00693	**< εrup** ←	**FRP Rupture check**	
Assumed NA. Depth, c	20.49	mm →	**Goal seek to get ΣF= 0**	
Strain at extreme compressive side, ε_m	0.00168	**< εmc** ←	**Masonry crushing**	
			Check	
Tensile force, F1	41190.92	N		
Compressive force, F2	41190.92	N		
Check Force equilibrium				
ΣF=	0.00			

E.1.3 Wall 5

IC debonding Check				
Elastic modulus of FRP, E_p	165000	MPa		
Plate Thickness, tp	7.2	mm		
Plate depth, bp	10	mm		
No. of strips	1			
Lateral modulus of rupture, f_{ut}	3.22	MPa		
Elastic modulus of masonry, E_m	9240	MPa		
Height of masonry wall, H	2310	mm		
Distance between the support	2064	mm		
Width of masonry wall, b	1070	mm		
Wall thickness, tm	110	mm		
C/s area of FRP plate, Ap (per strip)	72	mm^2		
Perimeter of failure plane, L_{per}	31.2	mm		
FRP rupture stress, f_{rupt}	2700.00	MPa		
FRP rupture strain, ε_{rup}	0.0164			
Masonry compressive strength, fmc	14.2	MPa		
Masonry crushing strain, ε_{mc}	0.00154			
IC debonding resistance per strip, PIC	58.86	KN	(Seracino et al.2007a)	
Total PIC	58.86	KN		
Debonding strain in FRP, ε_{db}	0.00495	**< εrup** ←	**FRP Rupture check**	
Assumed NA. Depth, c	14.73	mm →	**Goal seek to get ΣF= 0**	
Strain at extreme compressive side, ε_m	0.00081	**< εmc** ←	**Masonry crushing**	
			Check	
Tensile force, F1	58857.33	N		
Compressive force, F2	58857.33	N		
Check Force equilibrium				
ΣF=	0.00			

E.1.4 Wall 6

IC debonding Check				
Elastic modulus of FRP, E_p	165000	MPa		
Plate Thickness, tp	4.8	mm		
Plate depth, bp	7.5	mm		
No. of strips	2			
Lateral modulus of rupture, f_{ut}	3.22	MPa		
Elastic modulus of masonry, E_m	9240	MPa		
Height of masonry wall, H	2310	mm		
Distance between the support	2064	mm		
Width of masonry wall, b	1070	mm		
Wall thickness, tm	110	mm		
C/s area of FRP plate, Ap (per strip)	36	mm^2		
Perimeter of failure plane, L_{per}	23.8	mm		
FRP rupture stress, f_{rupt}	2700.00	MPa		
FRP rupture strain, ε_{rup}	0.0164			
Masonry compressive strength, fmc	14.22	MPa		
Masonry crushing strain, ε_{mc}	0.00154			
IC debonding resistance per strip, PIC	36.78	KN	(Seracino et al.2007a)	
Total PIC	73.55	KN		
Debonding strain in FRP, ε_{db}	0.00619	< εrup ←	**FRP Rupture check**	
Assumed NA. Depth, c	14.82	mm →	**Goal seek to get ΣF= 0**	
Strain at extreme compressive side, ε_m	0.00100	< εmc ←	**Masonry crushing**	
			Check	
Tensile force, F1	73553.61	N		
Compressive force, F2	73553.61	N		
Check Force equilibrium				
ΣF=	0.00			

E.1.5 Wall 7

IC debonding Check				
Elastic modulus of FRP, E_p	165000	MPa		
Plate Thickness, tp	3.6	mm		
Plate depth, bp	10	mm		
No. of strips	3			
Lateral modulus of rupture, f_{ut}	3.22	MPa		
Elastic modulus of masonry, E_m	9240	MPa		
Height of masonry wall, H	2310	mm		
Distance between the support	2064	mm		
Width of masonry wall, b	1070	mm		
Wall thickness, tm	110	mm		
C/s area of FRP plate, Ap (per strip)	36	mm^2		
Perimeter of failure plane, L_{per}	27.6	mm		
FRP rupture stress, f_{rupt}	2700.00	MPa		
FRP rupture strain, ε_{rup}	0.0164			
Masonry compressive strength, fmc	14.2	MPa		
Masonry crushing strain, ε_{mc}	0.00154			
IC debonding resistance per strip, PIC	44.60	KN	(Seracino et al.2007a)	
Total PIC	133.81	KN		
Debonding strain in FRP, ε_{db}	0.00751	< εrup ←	**FRP Rupture check**	
Assumed NA. Depth, c	17.74	mm →	**Goal seek to get ΣF= 0**	
Strain at extreme compressive side, ε_m	0.00153	< εmc ←	**Masonry crushing**	
			Check	
Tensile force, F1	133809.45	N		
Compressive force, F2	133809.45	N		
Check Force equilibrium				
ΣF=	0.00			

E.1.6 Wall 8

IC debonding Check				
Elastic modulus of FRP, E_p	165000	MPa		
Plate Thickness, tp	4.8	mm		
Plate depth, bp	5	mm		
No. of strips	3			
Lateral modulus of rupture, f_{ut}	3.56	MPa		
Elastic modulus of masonry, E_m	11490.0	MPa		
Height of masonry wall, H	2310	mm		
Distance between the support	2064	mm		
Width of masonry wall, b	1070	mm		
Wall thickness, tm	110	mm		
C/s area of FRP plate, Ap (per strip)	24	mm^2		
Perimeter of failure plane, L_{per}	18.8	mm		
FRP rupture stress, f_{rupt}	2700.00	MPa		
FRP rupture strain, ε_{rup}	0.0164			
Masonry compressive strength, fmc	16.83	MPa		
Masonry crushing strain, ε_{mc}	0.00146			
IC debonding resistance per strip, PIC	25.86	KN	(Seracino et al.2007a)	
Total PIC	77.59	KN		
Debonding strain in FRP, ε_{db}	0.00653	**< εrup** ←	**FRP Rupture check**	
Assumed NA. Depth, c	13.48	mm →	**Goal seek to get ΣF= 0**	
Strain at extreme compressive side, ε_m	0.00094	**< εmc** ←	**Masonry crushing**	
			Check	
Tensile force, F1	77591.32	N		
Compressive force, F2	77591.32	N		
Check Force equilibrium				
ΣF=	0.00			

E.1.7 Wall 9

IC debonding Check				
Elastic modulus of FRP, E_p	165000	MPa		
Plate Thickness, tp	3.6	mm		
Plate depth, bp	10	mm		
No. of strips	1			
Lateral modulus of rupture, f_{ut}	3.56	MPa		
Elastic modulus of masonry, E_m	11490.0	MPa		
Height of masonry wall, H	2310	mm		
Distance between the support	2064	mm		
Width of masonry wall, b	1070	mm		
Wall thickness, tm	110	mm		
C/s area of FRP plate, Ap (per strip)	36	mm^2		
Perimeter of failure plane, L_{per}	27.6	mm		
FRP rupture stress, f_{rupt}	2700.00	MPa		
FRP rupture strain, ε_{rup}	0.0164			
Masonry compressive strength, fmc	16.83	MPa		
Masonry crushing strain, ε_{mc}	0.00146			
IC debonding resistance per strip, PIC	47.37	KN	(Seracino et al.2007a)	
Total PIC	47.37	KN		
Debonding strain in FRP, ε_{db}	0.00798	**< εrup** ←	**FRP Rupture check**	
Assumed NA. Depth, c	9.60	mm →	**Goal seek to get ΣF= 0**	
Strain at extreme compressive side, ε_m	0.00080	**< εmc** ←	**Masonry crushing**	
			Check	
Tensile force, F1	47372.03	N		
Compressive force, F2	47372.03	N		
Check Force equilibrium				
ΣF=	0.00			

E.1.8 Wall 10

IC debonding Check				
Elastic modulus of FRP, E_p	165000	MPa		
Plate Thickness, tp	4.2	mm		
Plate depth, bp	10	mm		
No. of strips	2			
Lateral modulus of rupture, f_{ut}	3.56	MPa		
Elastic modulus of masonry, E_m	11490.0	MPa		
Height of masonry wall, H	2310	mm		
Distance between the support	2064	mm		
Width of masonry wall, b	1070	mm		
Wall thickness, tm	110	mm		
C/s area of FRP plate, Ap (per strip)	42	mm^2		
Perimeter of failure plane, L_{per}	28.2	mm		
FRP rupture stress, f_{rupt}	2700.00	MPa		
FRP rupture strain, ε_{rup}	0.0164			
Masonry compressive strength, fmc	16.83	MPa		
Masonry crushing strain, ε_{mc}	0.00146			
IC debonding resistance per strip, PIC	50.35	KN	(Seracino et al.2007a)	
Total PIC	100.71	KN		
Debonding strain in FRP, ε_{db}	0.00727	**< εrup** ←	**FRP Rupture check**	
Assumed NA. Depth, c	14.30	mm →	**Goal seek to get ΣF= 0**	
Strain at extreme compressive side, ε_m	0.00115	**< εmc** ←	**Masonry crushing**	
			Check	
Tensile force, F1	100709.36	N		
Compressive force, F2	100709.36	N		
Check Force equilibrium				
ΣF=	0.00			

E.2 Test set up details

Figure E-1: Mecano frame support system

Figure E-2: Wall specimen test set-up

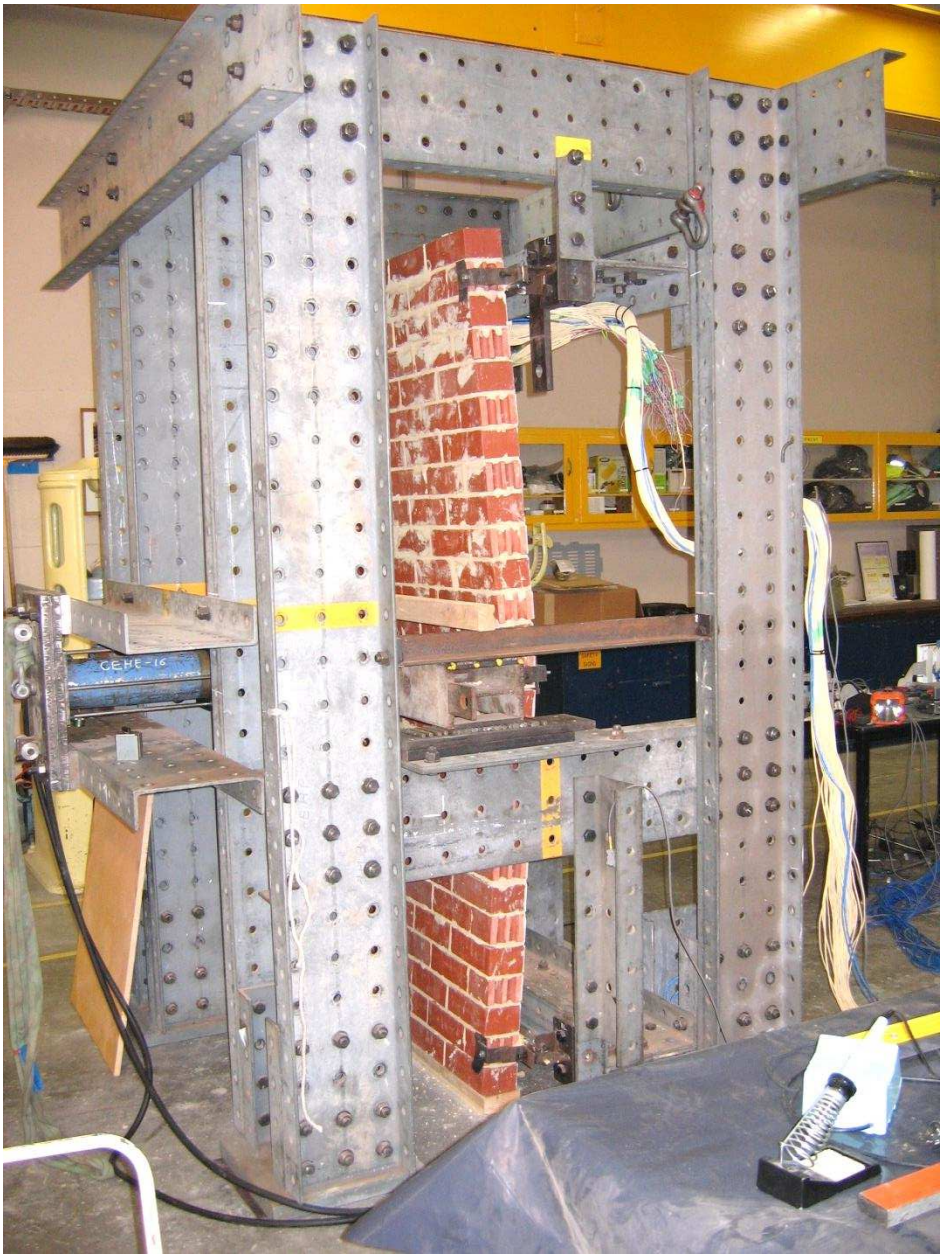

Figure E-3: Side view of wall test specimen

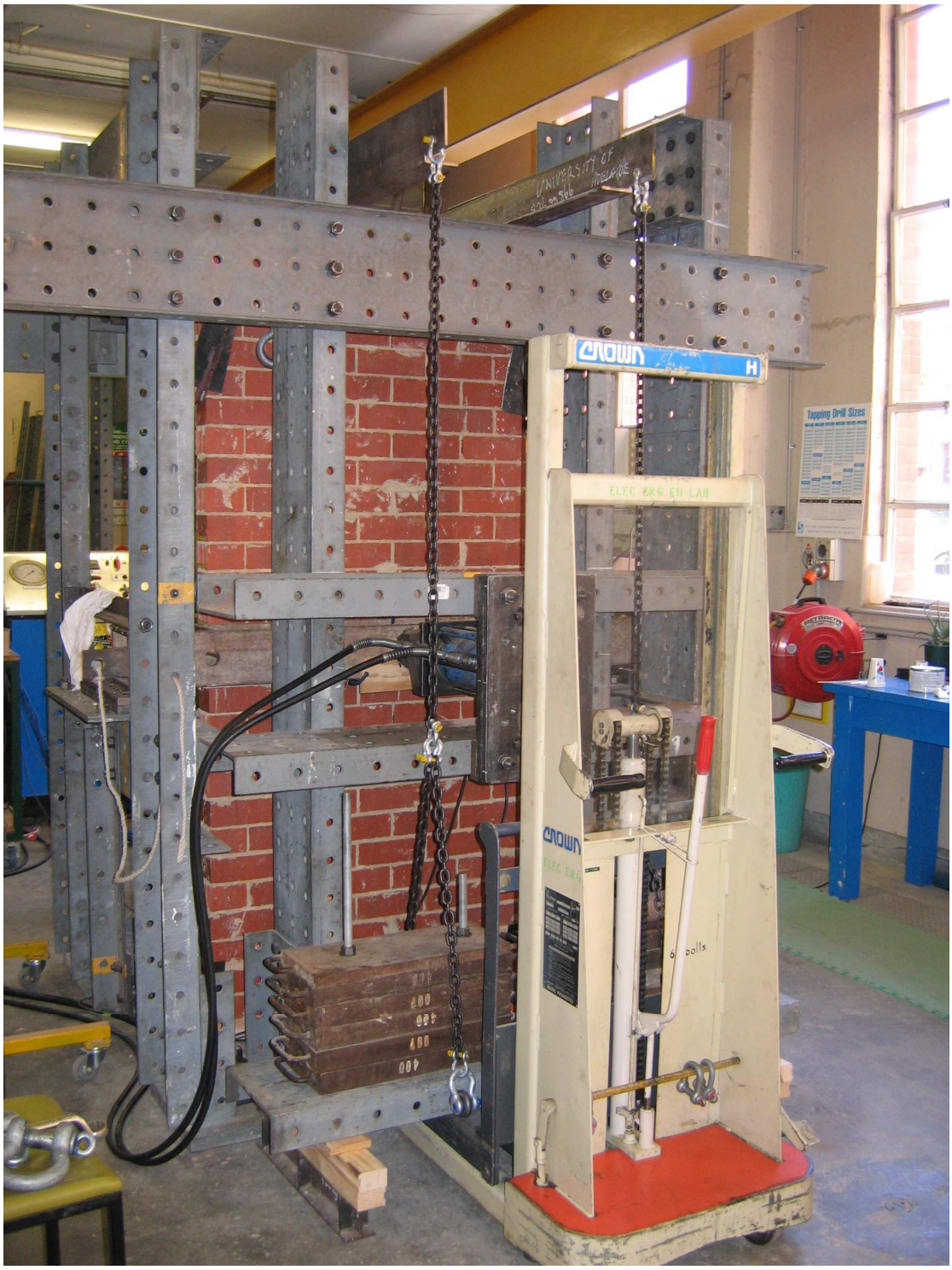

Figure E-4: Axial load set up for wall test

E.3 Masonry crushing check

E.3.1 Wall 1

Input Data			
Elastic modulus of FRP, E_p	165000	MPa	
Plate Thickness, t	3.6	mm	
Plate Width, bp	10	mm	
c/s area of FRP plate, Ap	36	mm^2	
Strain in FRP, ε_1	**0.009837**		
Elastic modulus of masonry, E_m	10700	MPa	
Width of masonry beam, b	355	mm	
Depth of beam, d	110	mm	
fmc	17		
Assumed NA. Depth, c	16.63	mm	
Masonry crushing strain, εmc	0.00159		
Calculations			
Strain in FRP, ε_2	0.00878		
Strain at extreme compressive side, ε_3	0.00175	**> εmc**	**Masonry Crushing check**
Tensile force, F1	55302.89678	N	
Compressive force, F2	55302.89678	N	
Check Force equilibrium			
ΣF=	**0.00**		

E.3.2 Wall 2

Input Data			
Elastic modulus of FRP, E_p	165000	MPa	
Plate Thickness, t	3.6	mm	
Plate Width, bp	10	mm	
c/s area of FRP plate, Ap	36	mm^2	
Strain in FRP, ε_1	**0.009987**		
Elastic modulus of masonry, E_m	10700	MPa	
Width of masonry beam, b	355	mm	
Depth of beam, d	110	mm	
fmc	17		
Assumed NA. Depth, c	16.63	mm	
Masonry crushing strain, εmc	0.00159		
Calculations			
Strain in FRP, ε_2	0.00892		
Strain at extreme compressive side, ε_3	0.00178	**> εmc**	**Masonry Crushing check**
Tensile force, F1	56146.18584	N	
Compressive force, F2	56146.18584	N	
Check Force equilibrium			
ΣF=	**0.00**		

E.3.3 Wall 3

Input Data				
Elastic modulus of FRP, E_p	165000	MPa		
Plate Thickness, t	3.6	mm		
Plate Width, bp	10	mm		
c/s area of FRP plate, Ap	36	mm^2		
Strain in FRP, ε_1	**0.008298**			
Elastic modulus of masonry, E_m	10700	MPa		
Width of masonry beam, b	355	mm		
Depth of beam, d	110	mm		
fmc	17			
Assumed NA. Depth, c	16.63	mm		
Masonry crushing strain, εmc	0.00159			
Calculations				
Strain in FRP, ε_2	0.00741			
Strain at extreme compressive side, ε_3	0.00148	**< εmc**	**Masonry Crushing check**	
Tensile force, F1	46650.75099	N		
Compressive force, F2	46650.75099	N		
Check Force equilibrium				
ΣF=	**0.00**			

E.3.4 Wall 4

Input Data				
Elastic modulus of FRP, E_p	165000	MPa		
Plate Thickness, t	3.6	mm		
Plate Width, bp	10	mm		
c/s area of FRP plate, Ap	36	mm^2		
Strain in FRP, ε_1	**0.008189**			
Elastic modulus of masonry, E_m	10700	MPa		
Width of masonry beam, b	230	mm		
Depth of beam, d	110	mm		
fmc	17			
Assumed NA. Depth, c	20.23	mm		
Masonry crushing strain, εmc	0.00159			
Calculations				
Strain in FRP, ε_2	0.00728			
Strain at extreme compressive side, ε_3	0.00185	**> εmc**	**Masonry Crushing check**	
Tensile force, F1	45933.39435	N		
Compressive force, F2	45933.3946	N		
Check Force equilibrium				
ΣF=	**0.00**			

E.3.5 Wall 5

Input Data			
Elastic modulus of FRP, E_p	165000	MPa	
Plate Thickness, t	7.2	mm	
Plate Width, bp	10	mm	
c/s area of FRP plate, Ap	72	mm^2	
Strain in FRP, ε_1	**0.006998**		
Elastic modulus of masonry, E_m	10700	MPa	
Width of masonry beam, b	1070	mm	
Depth of beam, d	110	mm	
fmc	17		
Assumed NA. Depth, c	13.76	mm	
Masonry crushing strain, εmc	0.00159		
Calculations			
Strain in FRP, ε_2	0.00627		
Strain at extreme compressive side, ε_3	0.00100	**< εmc**	**Masonry Crushing check**
Tensile force, F1	78817.00749	N	
Compressive force, F2	78817.00758	N	
Check Force equilibrium			
ΣF=	**0.00**		

E.3.6 Wall 6

Input Data			
Elastic modulus of FRP, E_p	165000	MPa	
Plate Thickness, t	4.8	mm	
Plate Width, bp	7.5	mm	
c/s area of FRP plate, Ap	36	mm^2	
Strain in FRP, ε_1	**0.010989**		
Elastic modulus of masonry, E_m	10700	MPa	
Width of masonry beam, b	1070	mm	
Depth of beam, d	110	mm	
fmc	17		
Assumed NA. Depth, c	9.99	mm	
Masonry crushing strain, εmc	0.00159		
Calculations			
Strain in FRP, ε_2	0.01016		
Strain at extreme compressive side, ε_3	0.00110	**< εmc**	**Masonry Crushing check**
Tensile force, F1	62827.00764	N	
Compressive force, F2	62827.00764	N	
Check Force equilibrium			
ΣF=	**0.00**		

E.4 Initiation of IC debonding

E.4.1 Wall 5

Elastic modulus of FRP, E_p	165000	MPa			
Plate Thickness, t	7.2	mm			
Plate Width, bp	10	mm			
No. of strips	1				
Elastic modulus of masonry, E_m	10700	MPa			
fmc	17	MPa			
Masonry crushing strain, εmc	0.00159				
Height of masonry Wall, H	2310	mm			
Distance between the supports	2064	mm			
Width of masonry beam, b	1070	mm			
Depth of beam, d	110	mm			
c/s area of FRP plate, Ap (per strip)	72	mm^2			
L_{per}	31.2	mm			
PIC per strip (exp-from pull test)	67.20	KN			
Total PIC	67.20	KN			
Strain in FRP, ε_p	**0.0057**				
Assumed NA. Depth, c	13.76	mm →	**Goal seek to get ΣF= 0**		
Strain at extreme compressive side, ε_m	0.00085	**< εmc**			
Tensile force, F1	67200.00	N			
Compressive force, F2	67200.00	N			
Check Force equilibrium					
ΣF=	**0.00**				
MIC	6439534	N-mm			
	6.44	**kN-m**			
Load cell, P applied	12480	N			
	12.48	**kN**			

E.4.2 Wall 6

Elastic modulus of FRP, E_p	165000	MPa			
Plate Thickness, t	4.8	mm			
Plate Width, bp	7.5	mm			
No. of strips	2				
Elastic modulus of masonry, E_m	10700	MPa			
fmc	17	MPa			
Masonry crushing strain, εmc	0.00159				
Height of masonry Wall, H	2310	mm			
Distance between the supports	2064	mm			
Width of masonry beam, b	1070	mm			
Depth of beam, d	110	mm			
c/s area of FRP plate, Ap (per strip)	36	mm^2			
L_{per}	23.8	mm			
Strip spacing	535.00	mm			
PIC per strip (exp-from pull test)	59.40	KN			
Total PIC	**118.80**	**KN**			
Strain in FRP, ε_p	0.01				
Assumed NA. Depth, c	13.84779447	mm →	Goal seek to get ΣF= 0		
Strain at extreme compressive side, ε_m	0.00	**< εmc**			
Tensile force, F1	118800.00	N			
Compressive force, F2	118800	N			
Check Force equilibrium					
ΣF=	5.78344E-06				
MIC	**11525754.68**	**N-mm**			
	11.53	kN-m			
Load cell, P applied	**22336.73**	**N**			
	22.34	kN			

E.4.3 Wall 7

Elastic modulus of FRP, E_p	165000	MPa			
Plate Thickness, t	3.6	mm			
Plate Width, bp	10	mm			
No. of strips	3				
Elastic modulus of masonry, E_m	10700	MPa			
fmc	17	MPa			
Masonry crushing strain, εmc	0.00159				
Height of masonry Wall, H	2310	mm			
Distance between the supports	2064	mm			
Width of masonry beam, b	1070	mm			
Depth of beam, d	110	mm			
c/s area of FRP plate, Ap (per strip)	36	mm^2			
L_{per}	27.6	mm			
Strip spacing	357.00	mm			
PIC per strip (exp-from pull test)	65.00	KN			
Total PIC	**195.00**	**KN**			
Strain in FRP, ε_p	0.0109				
Assumed NA. Depth, c	16.59	mm →	Goal seek to get ΣF= 0		
Strain at extreme compressive side, ε_m	0.00	**> εmc**			
Tensile force, F1	195000.00	N			
Compressive force, F2	195000.0	N			
Check Force equilibrium					
ΣF=	0.000242158				
MIC	**18318348.21**	**N-mm**			
	18.32	kN-m			
Load cell, P applied	**35500.67**	**N**			
	35.50	kN			

E.4.4 Wall 8

Elastic modulus of FRP, E_p	165000	MPa			
Plate Thickness, t	4.8	mm			
Plate Width, bp	5	mm			
No. of strips	3				
Elastic modulus of masonry, E_m	10700	MPa			
fmc	17	MPa			
Masonry crushing strain, εmc	0.00159				
Height of masonry Wall, H	2310	mm			
Distance between the supports	2064	mm			
Width of masonry beam, b	1070	mm			
Depth of beam, d	110	mm			
c/s area of FRP plate, Ap (per strip)	24	mm^2			
L_{per}	18.8	mm			
Strip spacing	357	mm			
PIC per strip (exp-from pull test)	44.80	KN			
Total PIC	**134.40**	**KN**			
Strain in FRP, ε_p	0.0113				
Assumed NA. Depth, c	13.93	mm →	Goal seek to get ΣF= 0		
Strain at extreme compressive side, ε_m	0.00	**> εmc**			
Tensile force, F1	134400.00	N			
Compressive force, F2	134400.0	N			
Check Force equilibrium					
ΣF=	0				
MIC	**13199452.95**	**N-mm**			
	13.20	kN-m			
Load cell, P applied	**25580.34**	**N**			
	25.58	kN			

E.4.5 Wall 9

Elastic modulus of FRP, E_p	165000	MPa			
Plate Thickness, t	3.6	mm			
Plate Width, bp	10	mm			
No. of strips	1				
Elastic modulus of masonry, E_m	10700	MPa			
fmc	17	MPa			
Masonry crushing strain, εmc	0.00159				
Height of masonry Wall, H	2310	mm			
Distance between the supports	2064	mm			
Width of masonry beam, b	1070	mm			
Depth of beam, d	110	mm			
c/s area of FRP plate, Ap (per strip)	36	mm^2			
L_{per}	27.6	mm			
Strip spacing	1070	mm			
PIC per strip (exp-from pull test)	65.00	KN			
Total PIC	**65.00**	**KN**			
Strain in FRP, ε_p	0.0109				
Assumed NA. Depth, c	9.93	mm →	Goal seek to get ΣF= 0		
Strain at extreme compressive side, ε_m	0.00	**< εmc**			
Tensile force, F1	65000.00	N			
Compressive force, F2	65000.0	N			
Check Force equilibrium					
ΣF=	0				
MIC	**6394608.71**	**N-mm**			
	6.39	kN-m			
Load cell, P applied	**12392.65**	**N**			
	12.39	kN			

E.4.6 Walls 10 - 15

Elastic modulus of FRP, E_p	165000	MPa			
Plate Thickness, t	4.2	mm			
Plate Width, bp	10	mm			
No. of strips	2				
Elastic modulus of masonry, E_m	10700	MPa			
fmc	17	MPa			
Masonry crushing strain, εmc	0.00159				
Height of masonry Wall, H	2310	mm			
Distance between the supports	2064	mm			
Width of masonry beam, b	1070	mm			
Depth of beam, d	110	mm			
c/s area of FRP plate, Ap (per strip)	42	mm^2			
L_{per}	28.2	mm			
Strip spacing	535	mm			
PIC per strip (exp-from pull test)	56.20	KN			
Total PIC	**112.40**	**KN**			
Strain in FRP, ε_p	0.0081				
Assumed NA. Depth, c	14.78	mm →	Goal seek to get ΣF= 0		
Strain at extreme compressive side, ε_m	0.00	**< εmc**			
Tensile force, F1	112400.00	N			
Compressive force, F2	112400.0	N			
Check Force equilibrium					
ΣF=	0				
MIC	**10694509.35**	**N-mm**			
	10.69	kN-m			
Load cell, P applied	**20725.79**	**N**			
	20.73	kN			

E.5 Unreinforced masonry strength calculations

E.5.1 Walls 1-4

Wall 1-3		
density of masonry, γ	19	KN/m
weight of wall	0.634	KN
height of wall, H	1710	mm
distance between Supports	1462	mm
width of wall	355	mm
wall thickness	110	mm
section modulus of the bedded area, Zd	715917	mm3
applied axial compressive stress	0	MPa
design compressive stress, fd	0.016	MPa
flexural tensile strength of masonry perpendicular to bed joints, fmt	0.53	MPa
bending moment capacity factor, kmt	1	
capacity reduction factor, Φ	1	
URM vertical bending capacity		
(a)	0.39	
(b)	1.14	
Murm	**0.39**	kN-m
	(lesser of (a) and (b))	
maximum applied load, F_{URM}	1.299	KN
equivalent horizontal acceleration, a_{URM}	1.02	g

Wall 4		
density of masonry, γ	19	KN/m
weight of wall	0.411	KN
height of wall, H	1710	mm
distance between Supports	1462	mm
width of wall	230	mm
wall thickness	110	mm
section modulus of the bedded area, Zd	463833	mm3
applied axial compressive stress	0	MPa
design compressive stress, fd	0.016	MPa
flexural tensile strength of masonry perpendicular to bed joints, fmt	0.53	MPa
bending moment capacity factor, kmt	1	
capacity reduction factc	1	
URM vertical bending capacity	0.25	
(a)	0.74	
(b)		
Murm	**0.25**	kN-m
	(lesser of (a) and (b))	
maximum applied load, F_{URM}	0.842	KN
equivalent horizontal acceleration, a_{URM}	1.02	g

E.5.2 Walls 5 -15

Walls 5-7		
density of masonry, γ	19	KN/m3
weight of wall	2.583	KN
height of wall, H	2310	mm
distance between Supports	2064	mm
width of wall	1070	mm
wall thickness	110	mm
section modulus of the bedded area, Zd	2157833	mm3
applied axial compressive stress	0	MPa
design compressive stress, fd	0.022	MPa
flexural tensile strength of masonry perpendicular to bed joints, fmt	0.52	MPa
bending moment capacity factor, kmt	1	
capacity reduction factc	1	
URM vertical bending capacity	1.17	
(a)	3.37	
(b)		
Murm	**1.17**	kN-m
	(lesser of (a) and (b))	
maximum applied load, F_{URM}	2.266	KN
equivalent horizontal acceleration, a_{URM}	0.44	g

Walls 8-15 (No axial load)		
density of masonry, γ	19	KN/m
weight of wall	2.583	KN
height of wall, H	2310	mm
distance between Supports	2064	mm
width of wall	1070	mm
wall thickness	110	mm
section modulus of the bedded area, Zd	2157833	mm3
applied axial compressive stress	0	MPa
design compressive stress, fd	0.022	MPa
flexural tensile strength of masonry perpendicular to bed joints, fmt	0.46	MPa
bending moment capacity factor, kmt	1	
capacity reduction factc	1	
URM vertical bending capacity	1.04	
(a)	2.98	
(b)		
Murm	**1.04**	kN-m
	(lesser of (a) and (b))	
maximum applied load, F_{URM}	2.015	KN
equivalent horizontal acceleration, a_{URM}	0.39	g

Walls 8-15 (Axial load = 0.1MPa)		
density of masonry, γ	19	KN/m3
weight of wall	2.583	KN
height of wall, H	2310	mm
distance between Supports	2064	mm
width of wall	1070	mm
wall thickness	110	mm
section modulus of the bedded area, Zd	2157833	mm3
applied axial compressive stress	0.1	MPa
design compressive stress, fd	0.122	MPa
flexural tensile strength of masonry perpendicular to bed joints, fmt	0.46	MPa
bending moment capacity factor, kmt	1	
capacity reduction factc	1	
URM vertical bending capacity	1.26	
(a)	2.98	
(b)		
Murm	**1.26**	kN-m
	(lesser of (a) and (b))	

Walls 8-15 (Axial load = 0.2MPa)		
density of masonry, γ	19	KN/m3
weight of wall	2.583	KN
height of wall, H	2310	mm
distance between Supports	2064	mm
width of wall	1070	mm
wall thickness	110	mm
section modulus of the bedded area, Zd	2E+06	mm3
applied axial compressive stress	0.2	MPa
design compressive stress, fd	0.222	MPa
flexural tensile strength of masonry perpendicular to bed joints, fmt	0.46	MPa
bending moment capacity factor, kmt	1	
capacity reduction factc	1	
URM vertical bending capacity	1.47	
(a)	2.98	
(b)		
Murm	**1.47**	kN-m
	(lesser of (a) and (b))	

maximum applied load, F_{URM}	2.434	KN
equivalent horizontal acceleration, a_{URM}	0.47	g

maximum applied load, F_{URM}	2.852	KN
equivalent horizontal acceleration, a_{URM}	0.55	g

APPENDIX F: WALL DESIGN CALCULATIONS

F.1 Prediction of moment capacity of retrofitted walls

F.1.1 Wall 5

Input Data			
Masonry Wall			
Specific weight,γm		19	kN/m3
Wall Height, H		2.31	m
Distance between the supports, Hs		2.064	m
Wall width, B		1.07	m
Wall Thickness, tm		110	mm
characteristic lateral modulus of rupture of masonry, f'ut		3.13	MPa
Elastic modulus of nasonry, Em		10700	MPa
Perpend factor, kp		1	
Axial stress on wall		0	MPa
FRP Strip			
Elastic modulus of FRP, Ep		165000	Mpa
FRP tesnsile strength, frupt		2700	Mpa
Actual strip spacing, s		1070	mm
No. of strips		1	
Depth of FRP strip, bp		10	mm
Thickness of FRP strip, tp		7.2	mm
Calculations			
Cross-sectional area of FRP strip, Ap		72	mm2
Perimeter of debonding failure plane, Lper		31.2	mm
FRP strip aspect ratio, Φf		1.195652	
IC debonding resistance, PIC		67.76	kN
Wall self-weight, Pself		2.31	kN
Force in plate due to applied axial load, Papplied		0	kN
Tensile force, T		70.07	kN
Debonding strain, εdb		0.005704	
constant, α		2.145971	
Neutral axis depth, c		14.32858	mm
Lever arm. z		105.2238	mm
Predicted moment, Mcv		7.37	kN-m
Predicted load, Ppred		14.29	kN

F.1.2 Wall 6

Input Data			
Masonry Wall			
Specific weight,γm		19	kN/m3
Wall Height, H		2.31	m
Distance between the supports, Hs		2.064	m
Wall width, B		1.07	m
Wall Thickness, tm		110	mm
characteristic lateral modulus of rupture of masonry, f'ut		3.13	MPa
Elastic modulus of nasonry, Em		10700	MPa
Perpend factor, kp		1	
Axial stress on wall		0	MPa
FRP Strip			
Elastic modulus of FRP, Ep		165000	Mpa
FRP tesnsile strength, frupt		2700	Mpa
Actual strip spacing, s		535	mm
No. of strips		2	
Depth of FRP strip, bp		7.5	mm
Thickness of FRP strip, tp		4.8	mm
Calculations			
Cross-sectional area of FRP strip, Ap		36	mm2
Perimeter of debonding failure plane, Lper		23.8	mm
FRP strip aspect ratio, Φf		1.25	
IC debonding resistance, PIC		42.20	kN
Wall self-weight, Pself		1.15	kN
Force in plate due to applied axial load, Papplied		0	kN
Tensile force, T		43.36	kN
Debonding strain, εdb		0.007105	
constant, α		2.132032	
Neutral axis depth, c		14.2852	mm
Lever arm. z		105.2383	mm
Predicted moment, Mcv		9.13	kN-m
Predicted load, Ppred		17.69	kN

F.1.3 Wall 7

Input Data			
Masonry Wall			
Specific weight,γm		19	kN/m3
Wall Height, H		2.31	m
Distance between the supports, Hs		2.064	m
Wall width, B		1.07	m
Wall Thickness, tm		110	mm
characteristic lateral modulus of rupture of masonry, f'ut		3.13	MPa
Elastic modulus of nasonry, Em		10700	MPa
Perpend factor, kp		1	
Axial stress on wall		0	MPa
FRP Strip			
Elastic modulus of FRP, Ep		165000	Mpa
FRP tesnsile strength, frupt		2700	Mpa
Actual strip spacing, s		357	mm
No. of strips		3	
Depth of FRP strip, bp		10	mm
Thickness of FRP strip, tp		3.6	mm
Calculations			
Cross-sectional area of FRP strip, Ap		36	mm2
Perimeter of debonding failure plane, Lper		27.6	mm
FRP strip aspect ratio, Φf		1.964286	
IC debonding resistance, PIC		49.52	kN
Wall self-weight, Pself		0.77	kN
Force in plate due to applied axial load, Papplied		0	kN
Tensile force, T		50.29	kN
Debonding strain, εdb		0.008337	
constant, α		3.158384	
Neutral axis depth, c		17.12685	mm
Lever arm. z		104.291	mm
Predicted moment, Mcv		15.74	kN-m
Predicted load, Ppred		30.50	kN

F.1.4 Wall 8

Input Data			
Masonry Wall			
Specific weight,γm		19	kN/m3
Wall Height, H		2.31	m
Distance between the supports, Hs		2.064	m
Wall width, B		1.07	m
Wall Thickness, tm		110	mm
characteristic lateral modulus of rupture of masonry, f'ut		3.13	MPa
Elastic modulus of nasonry, Em		10700	MPa
Perpend factor, kp		1	
Axial stress on wall		0.1	MPa
FRP Strip			
Elastic modulus of FRP, Ep		165000	Mpa
FRP tesnsile strength, frupt		2700	Mpa
Actual strip spacing, s		357	mm
No. of strips		3	
Depth of FRP strip, bp		5	mm
Thickness of FRP strip, tp		4.8	mm
Calculations			
Cross-sectional area of FRP strip, Ap		24	mm2
Perimeter of debonding failure plane, Lper		18.8	mm
FRP strip aspect ratio, Φf		0.882353	
IC debonding resistance, PIC		28.67	kN
Wall self-weight, Pself		0.77	kN
Force in plate due to applied axial load, Papplied		3.927	kN
Tensile force, T		33.36	kN
Debonding strain, εdb		0.007239	
constant, α		2.413085	
Neutral axis depth, c		15.13038	mm
Lever arm. z		104.9565	mm
Predicted moment, Mcv		10.50	kN-m
Predicted load, Ppred		20.36	kN

F.1.5 Wall 9

Input Data			
Masonry Wall			
Specific weight,γm		19	kN/m3
Wall Height, H		2.31	m
Distance between the supports, Hs		2.064	m
Wall width, B		1.07	m
Wall Thickness, tm		110	mm
characteristic lateral modulus of rupture of masonry, f'ut		3.13	MPa
Elastic modulus of nasonry, Em		10700	MPa
Perpend factor, kp		1	
Axial stress on wall		0.1	MPa
FRP Strip			
Elastic modulus of FRP, Ep		165000	Mpa
FRP tesnsile strength, frupt		2700	Mpa
Actual strip spacing, s		1070	mm
No. of strips		1	
Depth of FRP strip, bp		10	mm
Thickness of FRP strip, tp		3.6	mm
Calculations			
Cross-sectional area of FRP strip, Ap		36	mm2
Perimeter of debonding failure plane, Lper		27.6	mm
FRP strip aspect ratio, Φf		1.964286	
IC debonding resistance, PIC		49.52	kN
Wall self-weight, Pself		2.31	kN
Force in plate due to applied axial load, Papplied		11.77	kN
Tensile force, T		63.60	kN
Debonding strain, εdb		0.008337	
constant, α		1.33261	
Neutral axis depth, c		11.45933	mm
Lever arm. z		106.1802	mm
Predicted moment, Mcv		6.75	kN-m
Predicted load, Ppred		13.09	kN

F.1.6 Walls 10, 12

Input Data			
Masonry Wall			
Specific weight,γm		19	kN/m3
Wall Height, H		2.31	m
Distance between the supports, Hs		2.064	m
Wall width, B		1.07	m
Wall Thickness, tm		110	mm
characteristic lateral modulus of rupture of masonry, f'ut		3.13	MPa
Elastic modulus of nasonry, Em		10700	MPa
Perpend factor, kp		1	
Axial stress on wall		0.1	MPa
FRP Strip			
Elastic modulus of FRP, Ep		165000	Mpa
FRP tesnsile strength, frupt		2700	Mpa
Actual strip spacing, s		535	mm
No. of strips		2	
Depth of FRP strip, bp		10	mm
Thickness of FRP strip, tp		4.2	mm
Calculations			
Cross-sectional area of FRP strip, Ap		42	mm2
Perimeter of debonding failure plane, Lper		28.2	mm
FRP strip aspect ratio, Φf		1.774194	
IC debonding resistance, PIC		53.03	kN
Wall self-weight, Pself		1.15	kN
Force in plate due to applied axial load, Papplied		5.885	kN
Tensile force, T		60.07	kN
Debonding strain, εdb		0.007653	
constant, α		2.742518	
Neutral axis depth, c		16.05164	mm
Lever arm. z		104.6495	mm
Predicted moment, Mcv		12.57	kN-m
Predicted load, Ppred		24.37	kN

F.1.7 Walls 11, 13

Input Data			
Masonry Wall			
Specific weight,γm		19	kN/m3
Wall Height, H		2.31	m
Distance between the supports, Hs		2.064	m
Wall width, B		1.07	m
Wall Thickness, tm		110	mm
characteristic lateral modulus of rupture of masonry, f'ut		3.13	MPa
Elastic modulus of nasonry, Em		10700	MPa
Perpend factor, kp		1	
Axial stress on wall			MPa
FRP Strip			
Elastic modulus of FRP, Ep		165000	Mpa
FRP tesnsile strength, frupt		2700	Mpa
Actual strip spacing, s		535	mm
No. of strips		2	
Depth of FRP strip, bp		10	mm
Thickness of FRP strip, tp		4.2	mm
Calculations			
Cross-sectional area of FRP strip, Ap		42	mm2
Perimeter of debonding failure plane, Lper		28.2	mm
FRP strip aspect ratio, Φf		1.774194	
IC debonding resistance, PIC		53.03	kN
Wall self-weight, Pself		1.15	kN
Force in plate due to applied axial load, Papplied		0	kN
Tensile force, T		54.19	kN
Debonding strain, εdb		0.007653	
constant, α		2.473852	
Neutral axis depth, c		15.30556	mm
Lever arm. z		104.8981	mm
Predicted moment, Mcv		11.37	kN-m
Predicted load, Ppred		22.03	kN

F.1.8 Walls 14, 15

Input Data			
Masonry Wall			
Specific weight,γm		19	kN/m3
Wall Height, H		2.31	m
Distance between the supports, Hs		2.064	m
Wall width, B		1.07	m
Wall Thickness, tm		110	mm
characteristic lateral modulus of rupture of masonry, f'ut		3.13	MPa
Elastic modulus of nasonry, Em		10700	MPa
Perpend factor, kp		1	
Axial stress on wall		0.2	MPa
FRP Strip			
Elastic modulus of FRP, Ep		165000	Mpa
FRP tesnsile strength, frupt		2700	Mpa
Actual strip spacing, s		535	mm
No. of strips		2	
Depth of FRP strip, bp		10	mm
Thickness of FRP strip, tp		4.2	mm
Calculations			
Cross-sectional area of FRP strip, Ap		42	mm2
Perimeter of debonding failure plane, Lper		28.2	mm
FRP strip aspect ratio, Φf		1.774194	
IC debonding resistance, PIC		53.03	kN
Wall self-weight, Pself		1.15	kN
Force in plate due to applied axial load, Papplied		11.77	kN
Tensile force, T		65.96	kN
Debonding strain, εdb		0.007653	
constant, α		3.011183	
Neutral axis depth, c		16.75631	mm
Lever arm. z		104.4146	mm
Predicted moment, Mcv		13.77	kN-m
Predicted load, Ppred		26.69	kN

F.2 Yang's (2007) wall tests

F.2.1 Wall A

Input Data			
Masonry Wall			
Specific weight,γm		19	kN/m3
Wall Height, H		2.5	m
Distance between the supports, Hs		2.5	m
Wall width, B		4	m
Wall Thickness, tm		110	mm
characteristic lateral modulus of rupture of masonry, f'ut		3.55	MPa
Elastic modulus of nasonry, Em		3539	MPa
Perpend factor, kp		1	
Axial stress on wall		0	MPa
FRP Strip			
Elastic modulus of FRP, Ep		165000	Mpa
FRP tesnsile strength, frupt		2700	Mpa
Actual strip spacing, s		650	mm
No. of strips		4	
Depth of FRP strip, bp		50	mm
Thickness of FRP strip, tp		1.2	mm
Calculations			
Cross-sectional area of FRP strip, Ap		60	mm2
Perimeter of debonding failure plane, Lper		104	mm
FRP strip aspect ratio, Φf		0.019231	
IC debonding resistance, PIC		54.67	kN
Wall self-weight, Pself		1.70	kN
Force in plate due to applied axial load, Papplied		0	kN
Tensile force, T		56.37	kN
Debonding strain, εdb		0.005522	
constant, α		8.87474	
Neutral axis depth, c		27.1207	mm
Lever arm. z		100.9598	mm
Predicted moment, Mcv		22.51	kN-m
Predicted load, Ppred		8.19	kN

F.2.2 Wall B

Input Data			
Masonry Wall			
Specific weight,γm		19	kN/m3
Wall Height, H		2.5	m
Distance between the supports, Hs		2.5	m
Wall width, B		4	m
Wall Thickness, tm		110	mm
characteristic lateral modulus of rupture of masonry, f'ut		3.55	MPa
Elastic modulus of nasonry, Em		3539	MPa
Perpend factor, kp		1	
Axial stress on wall		0.1	MPa
FRP Strip			
Elastic modulus of FRP, Ep		16000	Mpa
FRP tesnsile strength, frupt		202	Mpa
Actual strip spacing, s		650	mm
No. of strips		4	
Depth of FRP strip, bp		100	mm
Thickness of FRP strip, tp		2	mm
Calculations			
Cross-sectional area of FRP strip, Ap		200	mm2
Perimeter of debonding failure plane, Lper		204	mm
FRP strip aspect ratio, Φf		0.009804	
IC debonding resistance, PIC		38.30	kN
Wall self-weight, Pself		1.70	kN
Force in plate due to applied axial load, Papplied		7.15	kN
Tensile force, T		47.15	kN
Debonding strain, εdb		0.011969	
constant, α		3.424904	
Neutral axis depth, c		17.77272	mm
Lever arm. z		104.0758	mm
Predicted moment, Mcv		19.37	kN-m
Predicted load, Ppred		7.04	kN

F.2.3 Wall C

Input Data			
Masonry Wall			
Specific weight,γm		19	kN/m3
Wall Height, H		2.5	m
Distance between the supports, Hs		2.5	m
Wall width, B		4	m
Wall Thickness, tm		110	mm
characteristic lateral modulus of rupture of masonry, f'ut		3.55	MPa
Elastic modulus of nasonry, Em		3539	MPa
Perpend factor, kp		1	
Axial stress on wall		0	MPa
FRP Strip			
Elastic modulus of FRP, Ep		16000	Mpa
FRP tesnsile strength, frupt		202	Mpa
Actual strip spacing, s		500	mm
No. of strips		5	
Depth of FRP strip, bp		77	mm
Thickness of FRP strip, tp		2	mm
Calculations			
Cross-sectional area of FRP strip, Ap		154	mm2
Perimeter of debonding failure plane, Lper		158	mm
FRP strip aspect ratio, Φf		0.012658	
IC debonding resistance, PIC		31.05	kN
Wall self-weight, Pself		1.31	kN
Force in plate due to applied axial load, Papplied		0	kN
Tensile force, T		32.36	kN
Debonding strain, εdb		0.012601	
constant, α		2.902129	
Neutral axis depth, c		16.47489	mm
Lever arm. z		104.5084	mm
Predicted moment, Mcv		16.65	kN-m
Predicted load, Ppred		6.05	kN

F.3 Verification of proposed design methodology

F.3.1 Wall 5

Input Data					
Masonry Wall					
Specific weight, γm	19	kN/m3			
Wall Height, H	2.31	m			
Distance between the supports, Hs	2.06	m			
Wall width, W	1.07	m			
Wall Thickness, tm	110	mm			
Compressive strength of masonry, f'mc	17.00	MPa			
Characteristic flexural tensile strength, f'mt	0.48	MPa			
Characteristic lateral modulus of rupture of masonry, f'ut	3.13	MPa			
Elastic modulus of nasonry, Em	10700	MPa			
Perpend factor, kp	1				
Capacity reduction factor,φ	1				
Axial stress on wall	0	MPa			
FRP Strip					
Elastic modulus of FRP, Ep	165000	Mpa			
FRP tensile strength, frupt	2700	Mpa			
Step 1					
Weight of wall	5.17	kN			
Design acceleration, a_{de}	3.31	g			
Design weight, wd	17.10	kN			
Demand moment, Md	8.82	kN-m			
Step 2					
Section modulus of the bedded area, zd	2016666.67	mm3/m			
Lateral section modulus of the masonry units, Zu	2016666.67	mm3/m			
Lateral section modulus of the perpends, Zp	2016666.67	mm3/m			
Horizontal bending mmt, Mch	2.79	kN-m/m			
b)	5.59	kN-m/m			
c)	3.32	kN-m/m			
Mch	2.79	kN-m/m			
Step 3					
Maximum strip spacing, s_{max}	1797.63	mm			
Step 4					
Select strip spacing, s	1070	mm	OK	**Horizontal bending**	
No of strips	2			**failure check**	
Select, depth of wall, bp	10	mm			
Select thickness of wall, tp	7.2	mm			
Cross-sectional area of FRP strip, Ap	72	mm2			
Step 5					
Perimeter of debonding failure plane, Lper	31.20	mm			
FRP strip aspect ratio, Φf	1.20				
IC debonding resistance, PIC	67.76	kN			
Self weight of Wall, Pself	2.31	kN			
Force in FRP strip due to applied axial load, Papplied	0.00	kN			
Tensile force, T	70.07	kN			
FRP strip rupture force, Prupt	194.40	kN	OK	**Rupture check**	
Step 6					
Strip debonding strain, εdb	0.0057				
Constant, α	2.15				
Depth of neutral axis, c	14.33	mm			
Step 7					
Strain in masonry, εm	0.0009				
Stress in masonry, σm	9.14	MPa	OK	**crushing check**	

F.3.2 Wall 6

Input Data						
Masonry Wall						
Specific weight, γ_m	19	kN/m3				
Wall Height, H	2.31	m				
Distance between the supports, Hs	2.06	m				
Wall width, W	1.07	m				
Wall Thickness, tm	110	mm				
Compressive strength of masonry, f'mc	17.00	MPa				
Characteristic flexural tensile strength, f'mt	0.48	MPa				
Characteristic lateral modulus of rupture of masonry, f'ut	3.13	MPa				
Elastic modulus of nasonry, Em	10700	MPa				
Perpend factor, kp	1					
Capacity reduction factor,ϕ	1					
Axial stress on wall	0	MPa				
FRP Strip						
Elastic modulus of FRP, Ep	165000	Mpa				
FRP tensile strength, frupt	2700	Mpa				
Step 1						
Weight of wall	5.17	kN				
Design acceleration, a_{de}	5.23	g				
Design weight, wd	27.02	kN				
Demand moment, Md	13.94	kN-m				
Step 2						
Section modulus of the bedded area, zd	2016666.67	mm3/m				
Lateral section modulus of the masonry units, Zu	2016666.67	mm3/m				
Lateral section modulus of the perpends, Zp	2016666.67	mm3/m				
Horizontal bending mmt, Mch a)	2.79	kN-m/m				
b)	5.59	kN-m/m				
c)	3.32	kN-m/m				
Mch	2.79	kN-m/m				
Step 3						
Maximum strip spacing, s_{max}	1430.09	mm				
Step 4						
Select strip spacing, s	535	mm	OK	**Horizontal bending**		
No of strips	2			**failure check**		
Select, depth of wall, bp	7.5	mm				
Select thickness of wall, tp	4.8	mm				
Cross-sectional area of FRP strip, Ap	36	mm2				
Step 5						
Perimeter of debonding failure plane, Lper	23.80	mm				
FRP strip aspect ratio, Φf	1.25					
IC debonding resistance, PIC	42.20	kN				
Self weight of Wall, Pself	1.15	kN				
Force in FRP strip due to applied axial load, Papplied	0.00	kN				
Tensile force, T	43.36	kN				
FRP strip rupture force, Prupt	97.20	kN	OK	**Rupture check**		
Step 6						
Strip debonding strain, εdb	0.0071					
Constant, α	2.13					
Depth of neutral axis, c	14.29	mm				
Step 7						
Strain in masonry, εm	0.0011					
Stress in masonry, σm	11.35	MPa	OK	**crushing check**		

F.3.3 Wall 7

Input Data					
Masonry Wall					
Specific weight, γm	19	kN/m3			
Wall Height, H	2.31	m			
Distance between the supports, Hs	2.06	m			
Wall width, W	1.07	m			
Wall Thickness, tm	110	mm			
Compressive strength of masonry, f'mc	17.00	MPa			
Characteristic flexural tensile strength, f'mt	0.48	MPa			
Characteristic lateral modulus of rupture of masonry, f'ut	3.13	MPa			
Elastic modulus of nasonry, Em	10700	MPa			
Perpend factor, kp	1				
Capacity reduction factor,φ	1				
Axial stress on wall	0	MPa			
FRP Strip					
Elastic modulus of FRP, Ep	165000	Mpa			
FRP tensile strength, frupt	2700	Mpa			
Step 1					
Weight of wall	5.17	kN			
Design acceleration, a_{de}	7.94	g			
Design weight, wd	41.02	kN			
Demand moment, Md	21.16	kN-m			
Step 2					
Section modulus of the bedded area, zd	2016667	mm3/m			
Lateral section modulus of the masonry units, Zu	2016667	mm3/m			
Lateral section modulus of the perpends, Zp	2016667	mm3/m			
Horizontal bending mmt, Mch a)	2.79	kN-m/m			
b)	5.59	kN-m/m			
c)	3.32	kN-m/m			
Mch	2.79	kN-m/m			
Step 3					
Maximum strip spacing, s_{max}	1161	mm			
Step 4					
Select strip spacing, s	357	mm	OK	**Horizontal bending**	
No of strips	3			**failure check**	
Select, depth of wall, bp	10	mm			
Select thickness of wall, tp	3.6	mm			
Cross-sectional area of FRP strip, Ap	36	mm2			
Step 5					
Perimeter of debonding failure plane, Lper	27.60	mm			
FRP strip aspect ratio, Φf	1.96				
IC debonding resistance, PIC	49.52	kN			
Self weight of Wall, Pself	0.77	kN			
Force in FRP strip due to applied axial load, Papplied	0.00	kN			
Tensile force, T	50.29	kN			
FRP strip rupture force, Prupt	97.20	kN	OK	**Rupture check**	
Step 6					
Strip debonding strain, εdb	0.0083				
Constant, α	3.16				
Depth of neutral axis, c	17.13	mm			
Step 7					
Strain in masonry, εm	0.0015				
Stress in masonry, σm	16.45	MPa	OK	**Crushing check**	

F.3.4 Wall 8

Input Data					
Masonry Wall					
Specific weight, γm	19	kN/m3			
Wall Height, H	2.31	m			
Distance between the supports, Hs	2.06	m			
Wall width, W	1.07	m			
Wall Thickness, tm	110	mm			
Compressive strength of masonry, f'mc	17.00	MPa			
Characteristic flexural tensile strength, f'mt	0.48	MPa			
Characteristic lateral modulus of rupture of masonry, f'ut	3.13	MPa			
Elastic modulus of nasonry, Em	10700	MPa			
Perpend factor, kp	1				
Capacity reduction factor,ϕ	1				
Axial stress on wall	0	MPa			
FRP Strip					
Elastic modulus of FRP, Ep	165000	Mpa			
FRP tensile strength, frupt	2700	Mpa			
Step 1					
Weight of wall	5.17	kN			
Design acceleration, a_{de}	7.08	g			
Design weight, wd	36.57	kN			
Demand moment, Md	18.87	kN-m			
Step 2					
Section modulus of the bedded area, zd	2016667	mm3/m			
Lateral section modulus of the masonry units, Zu	2016667	mm3/m			
Lateral section modulus of the perpends, Zp	2016667	mm3/m			
Horizontal bending mmt, Mch	2.79	kN-m/m			
b)	5.59	kN-m/m			
c)	3.32	kN-m/m			
Mch	2.79	kN-m/m			
Step 3					
Maximum strip spacing, s_{max}	1229	mm			
Step 4					
Select strip spacing, s	357	mm	OK	**Horizontal bending**	
No of strips	3			**failure check**	
Select, depth of wall, bp	5	mm			
Select thickness of wall, tp	4.8	mm			
Cross-sectional area of FRP strip, Ap	24	mm2			
Step 5					
Perimeter of debonding failure plane, Lper	18.80	mm			
FRP strip aspect ratio, Φf	0.88				
IC debonding resistance, PIC	28.67	kN			
Self weight of Wall, Pself	0.77	kN			
Force in FRP strip due to applied axial load, Papplied	0.00	kN			
Tensile force, T	29.44	kN			
FRP strip rupture force, Prupt	64.80	kN	OK	**Rupture check**	
Step 6					
Strip debonding strain, εdb	0.0072				
Constant, α	2.13				
Depth of neutral axis, c	14.28	mm			
Step 7					
Strain in masonry, εm	0.0011				
Stress in masonry, σm	11.55	MPa	OK	**crushing check**	

F.3.5 Wall 9

Input Data					
Masonry Wall					
Specific weight, γm	19	kN/m3			
Wall Height, H	2.31	m			
Distance between the supports, Hs	2.06	m			
Wall width, W	1.07	m			
Wall Thickness, tm	110	mm			
Compressive strength of masonry, f'mc	17.00	MPa			
Characteristic flexural tensile strength, f'mt	0.48	MPa			
Characteristic lateral modulus of rupture of masonry, f'u	3.13	MPa			
Elastic modulus of nasonry, Em	10700	MPa			
Perpend factor, kp	1				
Capacity reduction factor,ϕ	1				
Axial stress on wall	0	MPa			
FRP Strip					
Elastic modulus of FRP, Ep	165000	Mpa			
FRP tensile strength, frupt	2700	Mpa			
Step 1					
Weight of wall	5.17	kN			
Design acceleration, a_{de}	2.33	g			
Design weight, wd	12.04	kN			
Demand moment, Md	6.21	kN-m			
Step 2					
Section modulus of the bedded area, zd	2016667	mm3/m			
Lateral section modulus of the masonry units, Zu	2016667	mm3/m			
Lateral section modulus of the perpends, Zp	2016667	mm3/m			
Horizontal bending mmt, Mch	2.79	kN-m/m			
b)	5.59	kN-m/m			
c)	3.32	kN-m/m			
Mch	2.79	kN-m/m			
Step 3					
Maximum strip spacing, s_{max}	2143	mm			
Step 4					
Select strip spacing, s	1070	mm	OK	**Horizontal bending**	
No of strips	1			**failure check**	
Select, depth of wall, bp	10	mm			
Select thickness of wall, tp	3.6	mm			
Cross-sectional area of FRP strip, Ap	36	mm2			
Step 5					
Perimeter of debonding failure plane, Lper	27.60	mm			
FRP strip aspect ratio, Φf	1.96				
IC debonding resistance, PIC	49.52	kN			
Self weight of Wall, Pself	2.31	kN			
Force in FRP strip due to applied axial load, Papplied	0.00	kN			
Tensile force, T	51.83	kN			
FRP strip rupture force, Prupt	97.20	kN	OK	**Rupture check**	
Step 6					
Strip debonding strain, εdb	0.01				
Constant, α	1.09				
Depth of neutral axis, c	10.40	mm			
Step 7					
Strain in masonry, εm	0.0009				
Stress in masonry, σm	9.32	MPa	OK	**crushing check**	

F.3.6 Wall 10

Input Data					
Masonry Wall					
Specific weight, γm	19	kN/m3			
Wall Height, H	2.31	m			
Distance between the supports, Hs	2.06	m			
Wall width, W	1.07	m			
Wall Thickness, tm	110	mm			
Compressive strength of masonry, f'mc	17.00	MPa			
Characteristic flexural tensile strength, f'mt	0.48	MPa			
Characteristic lateral modulus of rupture of masonry, f'ut	3.13	MPa			
Elastic modulus of nasonry, Em	10700	MPa			
Perpend factor, kp	1				
Capacity reduction factor,ϕ	1				
Axial stress on wall	0.1	MPa			
FRP Strip					
Elastic modulus of FRP, Ep	165000	Mpa			
FRP tensile strength, frupt	2700	Mpa			
Step 1					
Weight of wall	5.17	kN			
Design acceleration, a_{de}	5.96	g			
Design weight, wd	30.79	kN			
Demand moment, Md	15.89	kN-m			
Step 2					
Section modulus of the bedded area, zd	2016667	mm3/m			
Lateral section modulus of the masonry units, Zu	2016667	mm3/m			
Lateral section modulus of the perpends, Zp	2016667	mm3/m			
Horizontal bending mmt, Mch a)	2.79	kN-m/m			
b)	5.59	kN-m/m			
c)	3.32	kN-m/m			
Mch	2.79	kN-m/m			
Step 3					
Maximum strip spacing, s_{max}	1340	mm			
Step 4					
Select strip spacing, s	535	mm	OK	**Horizontal bending**	
No of strips	2			**failure check**	
Select, depth of wall, bp	10	mm			
Select thickness of wall, tp	4.2	mm			
Cross-sectional area of FRP strip, Ap	42	mm2			
Step 5					
Perimeter of debonding failure plane, Lper	28.20	mm			
FRP strip aspect ratio, Φf	1.77				
IC debonding resistance, PIC	53.03	kN			
Self weight of Wall, Pself	1.15	kN			
Force in FRP strip due to applied axial load, Papplied	5.89	kN			
Tensile force, T	60.07	kN			
FRP strip rupture force, Prupt	113.40	kN	OK	**Rupture check**	
Step 6					
Strip debonding strain, εdb	0.0077				
Constant, α	2.74				
Depth of neutral axis, c	16.05	mm			
Step 7					
Strain in masonry, εm	0.0013				
Stress in masonry, σm	13.99	MPa	OK	**Crushing check**	

F.3.7 Wall 11

Input Data					
Masonry Wall					
Specific weight, γm	19	kN/m3			
Wall Height, H	2.31	m			
Distance between the supports, Hs	2.06	m			
Wall width, W	1.07	m			
Wall Thickness, tm	110	mm			
Compressive strength of masonry, f'mc	17.00	MPa			
Characteristic flexural tensile strength, f'mt	0.48	MPa			
Characteristic lateral modulus of rupture of masonry, f'ut	3.13	MPa			
Elastic modulus of nasonry, Em	10700	MPa			
Perpend factor, kp	1				
Capacity reduction factor,ϕ	1				
Axial stress on wall	0	MPa			
FRP Strip					
Elastic modulus of FRP, Ep	165000	Mpa			
FRP tensile strength, frupt	2700	Mpa			
Step 1					
Weight of wall	5.17	kN			
Design acceleration, a_{de}	5.31	g			
Design weight, wd	27.45	kN			
Demand moment, Md	14.16	kN-m			
Step 2					
Section modulus of the bedded area, zd	2016666.7	mm3/m			
Lateral section modulus of the masonry units, Zu	2016666.7	mm3/m			
Lateral section modulus of the perpends, Zp	2016666.7	mm3/m			
Horizontal bending mmt, Mch a)	2.79	kN-m/m			
b)	5.59	kN-m/m			
c)	3.32	kN-m/m			
Mch	2.79	kN-m/m			
Step 3					
Maximum strip spacing, s_{max}	1419	mm			
Step 4					
Select strip spacing, s	535	mm	OK	**Horizontal bending**	
No of strips	2			**failure check**	
Select, depth of wall, bp	10	mm			
Select thickness of wall, tp	4.2	mm			
Cross-sectional area of FRP strip, Ap	42	mm2			
Step 5					
Perimeter of debonding failure plane, Lper	28.20	mm			
FRP strip aspect ratio, Φf	1.77				
IC debonding resistance, PIC	53.03	kN			
Self weight of Wall, Pself	1.15	kN			
Force in FRP strip due to applied axial load, Papplied	0.00	kN			
Tensile force, T	54.19	kN			
FRP strip rupture force, Prupt	113.40	kN	OK	**Rupture check**	
Step 6					
Strip debonding strain, εdb	0.0077				
Constant, α	2.47				
Depth of neutral axis, c	15.31	mm			
Step 7					
Strain in masonry, εm	0.0012				
Stress in masonry, σm	13.24	MPa	OK	**crushing check**	

F.3.8 Wall 12

Input Data					
Masonry Wall					
Specific weight, γm	19	kN/m3			
Wall Height, H	2.31	m			
Distance between the supports, Hs	2.06	m			
Wall width, W	1.07	m			
Wall Thickness, tm	110	mm			
Compressive strength of masonry, f'mc	17.00	MPa			
Characteristic flexural tensile strength, f'mt	0.48	MPa			
Characteristic lateral modulus of rupture of masonry, f'ut	3.13	MPa			
Elastic modulus of nasonry, Em	10700	MPa			
Perpend factor, kp	1				
Capacity reduction factor,ϕ	1				
Axial stress on wall	0.1	MPa			
FRP Strip					
Elastic modulus of FRP, Ep	165000	Mpa			
FRP tensile strength, frupt	2700	Mpa			
Step 1					
Weight of wall	5.17	kN			
Design acceleration, a_{de}	5.61	g			
Design weight, wd	29	kN			
Demand moment, Md	14.96	kN-m			
Step 2					
Section modulus of the bedded area, zd	2016667	mm3/m			
Lateral section modulus of the masonry units, Zu	2016667	mm3/m			
Lateral section modulus of the perpends, Zp	2016667	mm3/m			
Horizontal bending mmt, Mch a)	2.79	kN-m/m			
b)	5.59	kN-m/m			
c)	3.32	kN-m/m			
Mch	2.79	kN-m/m			
Step 3					
Maximum strip spacing, s_{max}	1380	mm			
Step 4					
Select strip spacing, s	535	mm	OK	**Horizontal bending**	
No of strips	2			**failure check**	
Select, depth of wall, bp	10	mm			
Select thickness of wall, tp	4.2	mm			
Cross-sectional area of FRP strip, Ap	42	mm2			
Step 5					
Perimeter of debonding failure plane, Lper	28.20	mm			
FRP strip aspect ratio, Φf	1.77				
IC debonding resistance, PIC	53.03	kN			
Self weight of Wall, Pself	1.15	kN			
Force in FRP strip due to applied axial load, Papplied	5.89	kN			
Tensile force, T	60.07	kN			
FRP strip rupture force, Prupt	113.40	kN	OK	**Rupture check**	
Step 6					
Strip debonding strain, εdb	0.0077				
Constant, α	2.74				
Depth of neutral axis, c	16.05	mm			
Step 7					
Strain in masonry, εm	0.0013				
Stress in masonry, σm	13.99	MPa	OK	**crushing check**	

F.3.9 Wall 13

Input Data						
Masonry Wall						
Specific weight, γm		19	kN/m3			
Wall Height, H		2.31	m			
Distance between the supports, Hs		2.06	m			
Wall width, W		1.07	m			
Wall Thickness, tm		110	mm			
Compressive strength of masonry, f'mc		17.00	MPa			
Characteristic flexural tensile strength, f'mt		0.48	MPa			
Characteristic lateral modulus of rupture of masonry, f'ut		3.13	MPa			
Elastic modulus of nasonry, Em		10700	MPa			
Perpend factor, kp		1				
Capacity reduction factor,ϕ		1				
Axial stress on wall		0	MPa			
FRP Strip						
Elastic modulus of FRP, Ep		165000	Mpa			
FRP tensile strength, frupt		2700	Mpa			
Step 1						
Weight of wall		5.17	kN			
Design acceleration, a_{de}		5.85	g			
Design weight, wd		30.20	kN			
Demand moment, Md		15.58	kN-m			
Step 2						
Section modulus of the bedded area, zd		2016667	mm3/m			
Lateral section modulus of the masonry units, Zu		2016667	mm3/m			
Lateral section modulus of the perpends, Zp		2016667	mm3/m			
Horizontal bending mmt, Mch	a)	2.79	kN-m/m			
	b)	5.59	kN-m/m			
	c)	3.32	kN-m/m			
	Mch	2.79	kN-m/m			
Step 3						
Maximum strip spacing, s_{max}		1353	mm			
Step 4						
Select strip spacing, s		535	mm	OK	**Horizontal bending**	
No of strips		2			**failure check**	
Select, depth of wall, bp		10	mm			
Select thickness of wall, tp		4.2	mm			
Cross-sectional area of FRP strip, Ap		42	mm2			
Step 5						
Perimeter of debonding failure plane, Lper		28.20	mm			
FRP strip aspect ratio, Φf		1.77				
IC debonding resistance, PIC		53.03	kN			
Self weight of Wall, Pself		1.15	kN			
Force in FRP strip due to applied axial load, Papplied		0.00	kN			
Tensile force, T		54.19	kN			
FRP strip rupture force, Prupt		113.40	kN	OK	**Rupture check**	
Step 6						
Strip debonding strain, εdb		0.0077				
Constant, α		2.47				
Depth of neutral axis, c		15.31	mm			
Step 7						
Strain in masonry, εm		0.0012				
Stress in masonry, σm		13.24	MPa	OK	**crushing check**	

F.3.10 Wall 14

Input Data					
Masonry Wall					
Specific weight, γm	19	kN/m3			
Wall Height, H	2.31	m			
Distance between the supports, Hs	2.06	m			
Wall width, W	1.07	m			
Wall Thickness, tm	110	mm			
Compressive strength of masonry, f'mc	17.00	MPa			
Characteristic flexural tensile strength, f'mt	0.48	MPa			
Characteristic lateral modulus of rupture of masonry, f'ut	3.13	MPa			
Elastic modulus of nasonry, Em	10700	MPa			
Perpend factor, kp	1				
Capacity reduction factor,ϕ	1				
Axial stress on wall	0.2	MPa			
FRP Strip					
Elastic modulus of FRP, Ep	165000	Mpa			
FRP tensile strength, frupt	2700	Mpa			
Step 1					
Weight of wall	5.17	kN			
Design acceleration, a_{de}	5.75	g			
Design weight, wd	29.7	kN			
Demand moment, Md	15.53	kN-m			
Step 2					
Section modulus of the bedded area, zd	2016667	mm3/m			
Lateral section modulus of the masonry units, Zu	2016667	mm3/m			
Lateral section modulus of the perpends, Zp	2016667	mm3/m			
Horizontal bending mmt, Mch a)	2.79	kN-m/m			
b)	5.59	kN-m/m			
c)	3.32	kN-m/m			
Mch	2.79	kN-m/m			
Step 3					
Maximum strip spacing, s_{max}	1364	mm			
Step 4					
Select strip spacing, s	535	mm	OK	**Horizontal bending**	
No of strips	2			**failure check**	
Select, depth of wall, bp	10	mm			
Select thickness of wall, tp	4.2	mm			
Cross-sectional area of FRP strip, Ap	42	mm2			
Step 5					
Perimeter of debonding failure plane, Lper	28.20	mm			
FRP strip aspect ratio, Φf	1.77				
IC debonding resistance, PIC	53.03	kN			
Self weight of Wall, Pself	1.15	kN			
Force in FRP strip due to applied axial load, Papplied	11.77	kN			
Tensile force, T	65.96	kN			
FRP strip rupture force, Prupt	113.40	kN	OK	**Rupture check**	
Step 6					
Strip debonding strain, εdb	0.0077				
Constant, α	3.01				
Depth of neutral axis, c	16.76	mm			
Step 7					
Strain in masonry, εm	0.0014				
Stress in masonry, σm	14.72	MPa	OK	**crushing check**	

F.3.11 Wall 15

Input Data					
Masonry Wall					
Specific weight, γm	19	kN/m3			
Wall Height, H	2.31	m			
Distance between the supports, Hs	2.06	m			
Wall width, W	1.07	m			
Wall Thickness, tm	110	mm			
Compressive strength of masonry, f'mc	17.00	MPa			
Characteristic flexural tensile strength, f'mt	0.48	MPa			
Characteristic lateral modulus of rupture of masonry, f'ut	3.13	MPa			
Elastic modulus of nasonry, Em	10700	MPa			
Perpend factor, kp	1				
Capacity reduction factor,ϕ	1				
Axial stress on wall	0.2	MPa			
FRP Strip					
Elastic modulus of FRP, Ep	165000	Mpa			
FRP tensile strength, frupt	2700	Mpa			
Step 1					
Weight of wall	5.17	kN			
Design acceleration, a_{de}	5.27	g			
Design weight, wd	27.22	kN			
Demand moment, Md	14.04	kN-m			
Step 2					
Section modulus of the bedded area, zd	2016667	mm3/m			
Lateral section modulus of the masonry units, Zu	2016667	mm3/m			
Lateral section modulus of the perpends, Zp	2016667	mm3/m			
Horizontal bending mmt, Mch a)	2.79	kN-m/m			
b)	5.59	kN-m/m			
c)	3.32	kN-m/m			
Mch	2.79	kN-m/m			
Step 3					
Maximum strip spacing, s_{max}	1425	mm			
Step 4					
Select strip spacing, s	535	mm	OK	**Horizontal bending**	
No of strips	2			**failure check**	
Select, depth of wall, bp	10	mm			
Select thickness of wall, tp	4.2	mm			
Cross-sectional area of FRP strip, Ap	42	mm2			
Step 5					
Perimeter of debonding failure plane, Lper	28.20	mm			
FRP strip aspect ratio, Φf	1.77				
IC debonding resistance, PIC	53.03	kN			
Self weight of Wall, Pself	1.15	kN			
Force in FRP strip due to applied axial load, Papplied	11.77	kN			
Tensile force, T	65.96	kN			
FRP strip rupture force, Prupt	113.40	kN	OK	**Rupture check**	
Step 6					
Strip debonding strain, εdb	0.0077				
Constant, α	3.01				
Depth of neutral axis, c	16.76	mm			
Step 7					
Strain in masonry, εm	0.0014				
Stress in masonry, σm	14.72	MPa	OK	**crushing check**	